NMR Studies of Emulsions in Porous Media and Applications to Fischer-Tropsch Synthesis

Léonard R. van Thiel

Department of Chemical Engineering and Biotechnology
University of Cambridge

This dissertation is submitted for the degree of
Doctor of Philosophy

Corpus Christi College
September 2019

Declarations

Declaration of Originality

The work presented in this dissertation was carried out at the Magnetic Resonance Research Centre (MRRC) in the Department of Chemical Engineering and Biotechnology, University of Cambridge, between October 2015 and October 2019. This thesis is the result of my own work and includes nothing which is the outcome of work done in collaboration except as declared in the Preface and specified in the text. It is not substantially the same as any that I have submitted, or, is being concurrently submitted for a degree or diploma or other qualification at the University of Cambridge or any other University or similar institution except as declared in the Preface and specified in the text. I further state that no substantial part of my thesis has already been submitted, or, is being concurrently submitted for any such degree, diploma or other qualification at the University of Cambridge or any other University or similar institution except as declared in the Preface and specified in the text. This thesis does not exceed 65,000 words and contains less than 150 figures.

Copyright Declaration

Abstract

NMR Studies of Emulsions in Porous Media and Applications to Fischer-Tropsch Synthesis

Léonard R. van Thiel

As global reserves of conventional fossil fuels are dwindling, Fischer-Tropsch (FT) is a promising and greener method to convert natural gas into liquid fuels. However, it is highly complex and remains thus far poorly understood. The work presented in this thesis employs nuclear magnetic resonance (NMR) and magnetic resonance imaging (MRI) to gain insight into and elucidate the multiphase behaviour and transport processes of Fischer-Tropsch Synthesis (FTS) reactants and products. In order to achieve this, the world's first *operando* NMR compatible reactor was designed, commissioned and built to ultimately optimise the conversion of Gas-to-Liquids (GTL) through the FT process. A particular focus of this work lies on the application of a pulsed-field gradient (PFG) NMR emulsion detection technique to characterise hydrocarbon-in-water emulsions and study their droplet size distribution (DSD) inside porous media under *operando* conditions (≥180 °C and ≥36 bar).

The initial study into droplet formation was done on θ-Al_2O_3 pellets by relaxometry and PFG NMR measurements at ambient conditions, where dodecane and water were model compounds for FT products. The relaxation results indicated that water was the surface wetting phase, while dodecane was isolated from the pore surface. Spontaneous dodecane-in-water droplets formed, suggested by the restrictive diffusion behaviour for dodecane in the binary mixture. This trend was confirmed in Q-silica beads as well as in Ru-based FT catalyst pellets. Subsequently, the influence of (i) temperature, (ii) pore size, (iii) surfactant and (iv) surface modification on emulsion formation was investigated. Little impact of temperature and pore size was found for the ranges studied. However, a longer alcohol chain length lead to a small increase in droplet size. Furthermore, if the catalyst surface became hydrophobic with stearic acid, spontaneous emulsion formation did no longer occur.

Studying FTS *in situ* can be very complex due to its high P and T. This thesis contains the first ever reported *operando* study of FT under real operating conditions. This work

resulted in spatially-resolved MRI measurements of the diffusion and spatial mapping of product formation inside catalysts. These results can be used to validate numerical reactor simulations and optimise catalyst development.

Finally, the phase behaviour of wax and water was studied post-FTS *in situ* in 1 wt% Ru/TiO_2 catalysts at both 180 and 220 °C. Emulsion formation was detected by slowly increasing the water partial pressure between 0.3 - 0.95. At $P/P_0 \leq 0.5$, both water and wax diffused freely. However, at $P/P_0 \geq 0.8$, capillary condensation of water inside the catalyst pores was reported. This resulted in the formation of a water-rich, surface-wetting layer, located in between the pore surface and the wax layer. The wax species were displaced and became isolated from the pore space, which was confirmed by the significant increase in both T_1 and D values. For $P/P_0 \geq 0.9$, wax-in-water emulsions spontaneously formed. This was concluded from the sudden drop in the diffusion behaviour for wax.

Acknowledgements

Firstly, I would very much like to thank and acknowledge my supervisor, Professor Lynn F. Gladden, for giving me the incredible opportunity of undertaking my PhD in her research group. I am greatly indebted to Lynn for all her guidance, advice and patience throughout the last four years. I am especially grateful for everything I learned from her while being under her supervision. Many thanks also go to Dr Mick Mantle and Dr Andrew Sederman for their daily supervision, their help in the lab when working on the spectrometers and sharing their expertise while setting up the Zeton rig. The many useful discussions during the Shell-Cambridge meetings at the MRRC were invaluable.

A special thank you goes to Dr Qingyuan Zheng for his endless support and help during the experiments and the subsequent analysis. I also want to acknowledge Jack Williams for all his help and fun during the reactor commissioning; Dr Camilla Terenzi, Dr Nicholas Ramskill, Dr Andi Reci and the other MRRC members for their input and collaboration. Particular thanks go to the Shell collaborators, Dr Constant Guédon, Dr Tim Baart, Hans Smits and Heiko Oosterbeek, at Shell Technology Centre Amsterdam (STCA), for their advice and providing us with the necessary samples and characterisation work. Thank you for the opportunity of the 2016 R&D internship at STCA, which was very insightful.

I am also indebted to all my new friends I made while being at Corpus Christi College, in my Department or elsewhere, for the moments of laughter in between the hard work and for making Cambridge such a special place. My experience in Cambridge has been an extraordinarily enriching journey, I enjoyed every moment of it and I will always carry those incredible memories with me.

I gratefully acknowledge Shell, Corpus Christi College, the Cambridge Philosophical Society, Hendrik Muller Fonds and the Prins Bernhard Cultuurfonds for their financial contribution. Without their financial support, this PhD work would not have been possible.

Above all, I want to express my special gratitude to my amazing mother and father, oma, Mariella, Menno, Françoise and the girls, the Loprestos, the Steins and my family for their unconditional support, unfailing encouragements and faith. Most importantly, I want to thank my girlfriend Dora for always being there for me with her permanent kindness and love. I will always be extremely grateful for bumping into her at the Porter's Lodge at Corpus Christi College in February 2016 as I would not be who I am today without her. Thank you Dora for being an infinite source of happiness for me.

Contents

List of Figures

List of Tables

Acronyms

1D	1-dimensional
2D	2-dimensional
3D	3-dimensional
APGSTE	alternating pulsed-gradient stimulated echo
ASF	Anderson-Schulz-Flory
BET	Brunauer-Emmett-Teller
BJH	Barrett-Joyner-Halenda
BPP	Bloembergen-Purcell-Pound
C&E	Causes & Effects
CEM	controlled evaporative mixer
CMC	critical micelle concentration
COSHH	Control of Substances Hazardous to Health
CPMG	Carr-Purcell-Meiboom-Gill
CSTR	continuous-stirred tank reactor
CT	computerised tomography
DFT	density functional theory
DLBPR	dome loaded back-pressure regulator
DSD	droplet size distribution
DSEAR	Dangerous Substances and Explosive Atmospheres Regulations
EOR	enhanced oil recovery
EPR	Electron Paramagnetic Resonance Spectroscopy
FAT	Factory Acceptance Testing
F-I-D	flame ionisation detector
FID	free induction decay
FOV	field of view
FT	Fischer-Tropsch
FTS	Fischer-Tropsch Synthesis
FWHM	full width at half maximum
GC	gas chromatograph
GC-MS	gas chromatography - mass spectrometer
GTL	Gas-to-Liquids
HDS	hydrodesulfurisation
HLB	hydrophilic-lipophilic balance
HPLC	high-performance liquid chromatography

HT-FT	high-temperature FT
ID	internal diameter
IR	Infrared Spectroscopy
LT-FT	low-temperature FT
MD	molecular dynamic
MES	Mössbauer emission spectroscopy
MFC	mass flow controller
MR	magnetic resonance
MRI	magnetic resonance imaging
MRRC	Magnetic Resonance Research Centre
MS	Mass Spectroscopy
MSD	mean square displacement
MTGV	Modified Total Generalized Variation
NMR	nuclear magnetic resonance
NS	number of scans
PFG	pulsed-field gradient
PFR	plug flow reactor
PGSE	pulsed-gradient spin echo
PGSTE	pulsed-gradient stimulated echo
ppm	parts-per-million
RARE	Rapid Acquisition with Relaxation Enhancement
RF	radio frequency
RGA	refinery gas analyser
RG	receiver gain
RMSD	root mean squared displacement
RO	restriction orifice
RS	Raman Spectroscopy
SAXS	small angle X-ray scattering
SGPM	Short Gradient Pulse Method
SMDS	Shell Middle Distillate Synthesis
SNR	signal-to-noise ratio
SOP	Standard Operating Procedures
SP	set point
SSITKA	Steady-State Isotopic Transient Kinetic Analysis
ST	Stejskal-Tanner
STCA	Shell Technology Centre Amsterdam
STE	stimulated echo
SW	sweep width
SWB	super-wide-bore
TCD	thermal conductivity detector
TMS	tetramethylsilane
TOS	time-on-stream
TPD	temperature programmed desorption
TPR	temperature programmed reduction

UV-VIS	Ultraviolet-Visible Spectroscopy
VD	Variable Delay
VLE	vapour-liquid equilibrium
WGFM	water-gas flow-meter
WGSR	water-gas shift reaction
WHSV	weight hourly space velocity, units of weight of feed per hour per unit of catalyst weight
XRD	X-Ray diffraction

Symbols

Latin symbols

ΔA	Increase in interfacial area due to the formation of droplets	[m^2]
a	Droplet radius	[m]
b	$\boldsymbol{b}$-factor [equal to $\gamma^2 g^2 \delta^2 (\Delta - \frac{\delta}{3})$]	[s m^{-2}]
$\boldsymbol{B}_0$	Static magnetic field	[T]
$\boldsymbol{B}_1$	Superimposed magnetic field	[T]
$\boldsymbol{B}_{\mathsf{eff}}$	Effective magnetic field	[T]
$\Delta\boldsymbol{B}_0$	Inhomogeneities of the static magnetic field	[T]
D_0	Self diffusion coefficient of a pure liquid	[m^2 s^{-1}]
$D_{\mathsf{eff}\,(\infty)}$	Diffusion coefficient as measured by PFG NMR	[m^2 s^{-1}]
dw	Dwell time	[s]
D_x, D_y, D_z	Diffusion constants in the x-, y- and z-directions	[m^2 s^{-1}]
E	Energy of a nucleus	[J]
g	Strength of applied magnetic field gradient	[G cm^{-1}]
G	Magnetic field gradient	[G cm^{-1}]
h	Planck's constant	[m^2 ks s^{-1}]
$\hbar$	Reduced Planck's constant	[m^2 ks s^{-1}]
I	Angular momentum quantum number	[-]
k	Mass transport coefficient	[m s^{-1}]
k_B	Boltzmann constant	[m^2 kg s^{-2} K^{-1}]
m	Magnetic or directional quantum number	[-]
$\boldsymbol{M}_0$	Macroscopic magnetisation vector in the static field $\boldsymbol{B}_0$	[A m^{-1}]
M_x, M_y	Transverse magnetisation in the x- and y-directions	[A m^{-1}]
M_z	Longitudinal magnetisation in the z-direction	[A m^{-1}]
N_{s}	Number of spins in a sample	[-]
n	Degrees of aggregation for amphipathic species	[-]
P	Nuclear angular momentum	[Js]

R_p	Chain growth rate	[C min^{-1}]
R_t	Chain termination rate	[C min^{-1}]
S	Echo signal intensity	[a.u.]
sw	Sweep width	[Hz]
τ_c	Rotational correlation time	[s]
t_g	Time between opposite gradient pulses in APGSTE	[s]
T_1	Spin-lattice relaxation time	[s]
T_2	Spin-spin relaxation time	[s]
T	Temperature	[K]
x_n	Mole fraction distribution	[-]
x, y, z	Cartesian coordinates	[-]

Greek symbols

α	Low energy spin state	[-]
α	Chain growth probability	[-]
β	Regularisation Parameter	[-]
β	High energy spin state	[-]
γ	Gyromagnetic ratio	[rad s^{-1} T^{-1}]
γ_{12}	Interfacial tension between the two liquids	[kg s^{-2} m^{-1}]
δ	Gradient pulse duration	[s]
δ	Chemical shift	[ppm]
Δ	Observation time	[s]
ξ	Ratio used to characterise restricted diffusion time scales	[-]
Θ	Pulse angle	[°]
μ	Magnetic momentum vector	[J T^{-1}]
v_1	Electromagnetic waves frequency	[Hz or rad s^{-1}]
v	Nucleus resonance frequency	[Hz or rad s^{-1}]
ρ	Spin density	[mol $^{-3}$]
τ	Delay time	[s]
τ_E	Echo time	[s]
τ_P	Pulse duration	[s]
ϕ	Phase shift	[-]
ω	Larmor frequency	[Hz or rad s^{-1}]

Exposure of this Work

Conferences

L.F. Gladden, L.R. van Thiel, Q. Zheng, J. Williams, C. Terenzi, M.D. Mantle and A.J. Sederman, *Operando* Magnetic Resonance Studies of Fischer-Tropsch Catalysis in a Fixed-Bed Reactor, *The 25th International Symposium on Chemical Reaction Engineering (ISCRE25)*, Florence, Italy, May 2018. *(Keynote talk)*

Chapter 1

Introduction

1.1 Background and Scientific Motivation

It is generally accepted that FT is an attractive, clean and alternative approach to catalytically convert synthesis gas into premium liquid fuels [1]. The GTL process has commercially been operated by Shell and other large oil companies for several decades [2]. However, in the literature there still exists major disagreement about the fundamental science behind GTL, specifically regarding the reaction mechanisms and phase behaviour phenomena [3]. One of the main hurdles that contributed to this lack of consensus is the complexity of the mechanisms involved. Moreover, it simply remains technically very challenging to study FT *in situ*, which is reflected by the absence of *operando* studies performed at elevated pressure and temperature in the literature [4]. Live monitoring of FT reactors and on-line characterisation of products formed inside the catalysts has traditionally not been possible. Many FT reactors are treated as a “black-box”, whereby many scientific studies are performed off-line and post-synthesis. Therefore, more *in situ* studies are required to bridge the gap between theoretical models and optimisation of numerical simulations.

NMR is a very powerful technique to study heterogeneous catalytic processes. The advantage of magnetic resonance (MR) in this application is that it is non-invasive and can acquire 2-dimensional (2D) and 3-dimensional (3D) images of optically opaque media [5]. NMR relaxometry and diffusometry measurements can be used to deduct chemically-specific information on molecular transport phenomena and diffusion behaviours [6].

Typically the catalyst pores become partially filled with liquid during the FTS reaction, however when modelling FT and its kinetics, little account is taken of this phenomenon. Also, although water is the main by-product of the reaction, because of its minimal commercial value, very little attention has been given to its role in the reaction [7]. The effect of water solubility in an organic phase or the likelihood of even forming a two-phase mixture has not been adequately explored [8].

The aim of this PhD work is to investigate and understand the multiphase hydrodynamic behaviour of FTS in a fixed-bed reactor. This is primarily done by applying PFG NMR to explore the phase behaviour and transport properties of liquid fluids confined in the pore spaces of the catalysts under industrially-relevant high temperature and pressure conditions. More specifically, the principal scientific objective of this project is to develop and establish a NMR methodology to characterise emulsion formation in porous catalysts, with a particular focus on hydrocarbon-in-water droplets forming in the presence of a water-rich, surface-wetting layer. In addition, this project focuses on the design and commissioning of the high pressure and temperature, fixed-bed tubular reactor which is placed inside a MRI magnet. This is the first *in situ* application of MRI to study the catalytic conversion of natural gas into liquid hydrocarbons. This methodology will ultimately help to elucidate FTS as a whole.

1.1.1 Phase Behaviour

During FTS, a liquid phase of reaction products prevails inside the pores of the catalysts. However, it remains uncertain whether this fluid is a single-phase liquid, a liquid-gas two-phase mixture or exists as several continuous phases. It has been hypothesised that during FT, due to capillary condensation, water vapour phase condenses and forms a separate liquid water phase [9]. In addition, many scientists in the literature have speculated about spontaneous droplets or emulsions formation in the water layer [10]. In general, numerous researchers agree that this process is poorly understood, but it has vast implications for catalyst design, model prediction and more importantly optimisation of reactor performance [11].

Simplified, hypothetical scenarios of the phase distribution of liquid water and wax in the pores can be seen in Figure 1.1. Scenario (a) is the most basic scenario in which a continuous single-phase mixture is established of water and wax. In the more complex scenarios (b) - (f), phase separation occurs between wax and water whereby in (b) and (c) either wax or water becomes the surface-wetting phase respectively. Scenario (d) proposes a situation in which different liquid pockets of alternating wax and water co-exist alongside. Some pore sections in the catalyst might have preferential bulk condensation of wax or water. Finally, emulsion formation of (e) water-in-wax or (f) wax-in-water systems are shown. A variety of scenarios might simultaneously occur depending on the catalyst, reactor or operating conditions [12].

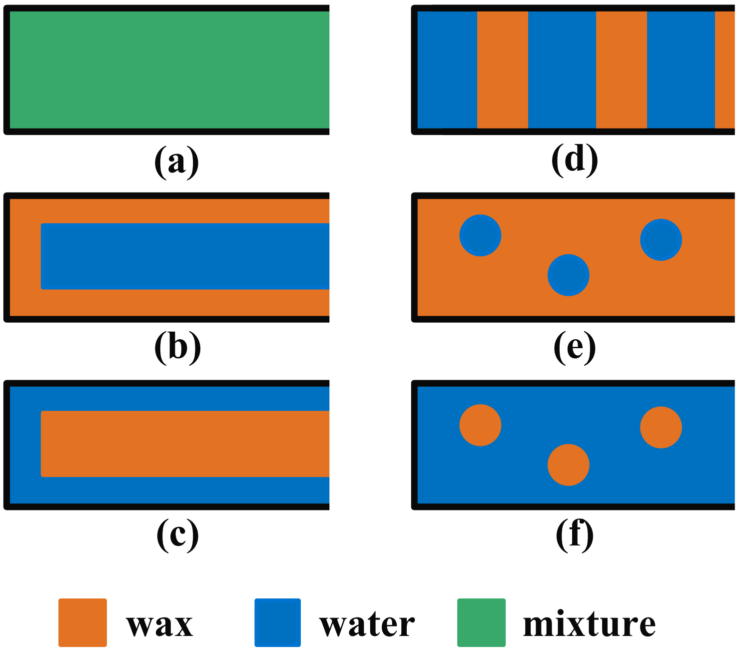

Figure 1.1 Hypothetical profiles of water-wax phases inside the catalyst pores: (a) a single-phase, continuous homogeneous mixture, (b) phase separation with wax acting as the surface-wetting species, (c) phase separation where water is wetting the pore wall, (d) phase separation with no preferred wetting, resulting in alternating phases of water and wax, (e) a water-in-wax emulsion and (f) a wax-in-water emulsion. The black line represents the pore wall with the open end of the pore on the right. Adapted from [12].

1.1.2 Scope of Thesis

FT is a commercially viable alternative to producing long-chain, linear alkanes. However, as this process remains poorly understood, there is significant scope to gain deeper understanding of the conversion and hence optimise the reaction and catalyst design. One of the major bottlenecks for this advancement is the lack of appropriate technical capabilities to study the process *in situ*. This would allow to clarify the reaction mechanisms, kinetics, catalyst properties, multiphase hydrodynamics and transport phenomena. Therefore, the aims of this PhD work are:

1. Develop and verify a PFG NMR emulsion detection technique for porous catalysts saturated with water and hydrocarbons.
2. Apply this technique in several supports and test the influence of multiple physical parameters on droplet formation and its size distribution.
3. Design and commission the world's first NMR compatible fixed-bed reactor for FT.
4. Perform FTS and study this *operando* using the novel pilot-scale reactor.
5. Characterise and investigate emulsion formation at elevated pressure and temperature post-FTS by applying the techniques developed earlier.

1.2 Outline of Thesis

Chapter 1 gives a description of the scientific motivation and importance of this project. It also contains the outline and content covered.

Chapter 2 covers the basic principles of FT, highlighting the reactions, catalysts, reactors and possible mechanisms involved. The phase behaviour and emulsion formation in porous media are discussed.

Chapter 3 provides an introduction to the fundamentals of NMR, MRI and PFG diffusion which are the MR techniques applied in this work.

Chapter 4 discusses a preliminary study of phase behaviour in θ-Al_2O_3 at ambient T and P. This Chapter presents a novel technique for emulsion detection inside saturated porous media, which is applied subsequently in the following Chapters.

Chapter 5 presents a systematic study of emulsion formation in Q-silica beads, FT TiO_2 support and 1 wt% Ru/TiO_2 catalyst particles. The influence of T, pore size, n-alcohol chain length and fatty acids on droplets and their size distribution are covered.

Chapter 6 describes the design, building and commissioning of the FT Zeton reactor. This Chapter also summarises the findings obtained during the Shell-Cambridge collaboration.

Chapter 7 reports the first ever *operando* MR study of FT catalysis, performed at industrially-relevant conditions.

Chapter 8 introduces the multiphase behaviour investigation done *in situ* at 180 and 220 °C on real FT wax and water products, where at high water partial pressures, wax-in-water emulsions are observed.

Chapter 9 summarises the main scientific achievements and presents the conclusions of this thesis. Finally, possible work directions are suggested for future research.

Chapter 2

Fischer-Tropsch Synthesis and Phase Behaviour

2.1 Introduction

FT is a highly exothermic, heterogeneous catalytic process that converts synthesis gas, containing H_2 and CO, into hydrocarbons in a temperature range between 190 and 350 °C. The fundamentals of FTS are still not well understood and there are many aspects of the (i) reactor, (ii) catalyst and (iii) reaction to be optimised.

More than ninety years ago, this syngas conversion was first performed by two German chemists, Hans Fischer and Franz Tropsch, and since then has developed to global industrial scale [13]. During World War II in Germany, oil became scarce so Germany invested in a new process to use their national coal reserves instead to generate fuel for aviation and tanks. In the 80's, as a consequence of the oil embargo against the Apartheid regime in South Africa, Sasol also developed its own capabilities to transform coal into gasoline products.

At ambient conditions, the hydrocarbon products are mostly liquid products, such as linear paraffins and α-olefins [14]. Interestingly any carbon source, ranging from non-petroleum resources like natural gas, biomass or even coal, could be used as reactant for syngas production via steam reforming, oxidation or gasification processes. The term 'liquefaction' is often used for these conversions because irrespective of the physical state of the feed resources, whether it is gas or solid, the route to a liquid hydrocarbon fuel involves a syngas intermediate [15].

Hydrocarbons derived from FT, like diesel, can be much more environmentally benign products due to their lower aromaticity, metal and heteroatom content in comparison to petroleum-based fuels. In addition, as the global reserves of conventional oil are dwindling, the need for heavy crude oil processing to meet global energy demand is increasing. Liquid fuels obtained from heavy oils are characterised by high aromatic content and high sulphur, nitrogen and heavy metal contaminants. Thus, FTS is a vital step in the sustainable pathway of converting non-petroleum based resources into high quality, green fuels and valuable chemicals [16–18]. A basic overview of how FT is commercially performed in shown in Figure 2.1 [19].

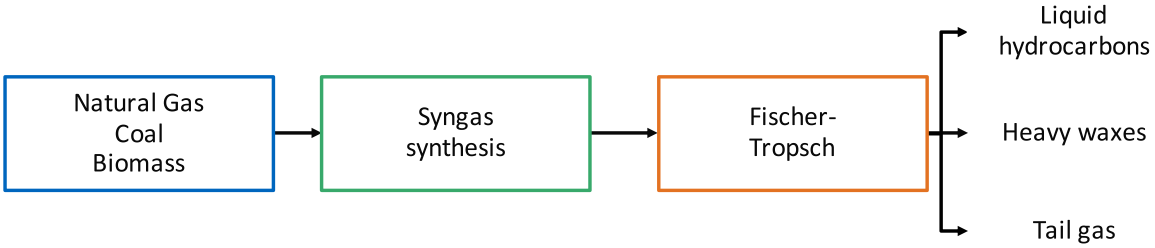

Figure 2.1 A very simplified overview of FTS.

The GTL process at Shell is known as the Shell Middle Distillate Synthesis (SMDS) process and it currently operated in two plants in the world: (i) Bintulu in Malaysia which became functional in 1993 and (ii) the Pearl GTL Shell-Qatar. Pearl is the largest GTL plant in the world producing premium base oils.

2.2 Reactions

Equations 2.1 and 2.2, respectively, show the alkane (paraffins) and alkene (olefins) reactions taking place during FTS [20]. The water molecules produced can further react with CO to CO_2 and H_2 in the water-gas shift reaction (WGSR), shown in Equation 2.3. Three undesirable reactions are the formation of methane and alcohol, Equations 2.4 and 2.5, and the Boudouard reaction, Equation 2.6 [21, 22].

$$\text{Alkane formation:} \quad (2n+1)\ H_2 + n\ CO \rightarrow C_nH_{2n+2} + n\ H_2O \tag{2.1}$$

$$\text{Alkene formation:} \quad 2n\ H_2 + n\ CO \rightarrow C_nH_{2n} + n\ H_2O \tag{2.2}$$

$$\text{Water-gas shift reaction:} \quad H_2O + CO \rightleftharpoons CO_2 + H_2 \tag{2.3}$$

$$\text{Methane formation:} \quad 3\ H_2 + CO \rightarrow CH_4 + H_2O \tag{2.4}$$

$$\text{Alcohol formation:} \quad 2n\ H_2 + n\ CO \rightarrow C_nH_{2n+2} + (n-1)\ H_2O \tag{2.5}$$

$$\text{Boudouard reaction:} \quad 2\ CO \rightarrow CO_2 + C \tag{2.6}$$

During FT, the syngas mixture is converted into a very wide product range: a multi-component mixture of primarily linear and branched hydrocarbons and a small proportion of oxygenates and methane. It comprises one of the most complex reaction networks which are still heavily debated nowadays in the literature. Methane is an undesirable product due to its low financial value and the target products are middle to long-chain hydrocarbons that can be further converted into diesel, kerosene, paraffin or even naphtha.

2.2.1 Product Distribution

The polymerisation reactions occurring in FTS are described using the Anderson-Schulz-Flory (ASF) distribution (Equation 2.7) which describes the mole fraction distribution, x_n, as a function of the number of carbon atoms, n, in a 'polymer' chain, and the chain growth probability, α [23, 24]. The parameter α, see Equation 2.8, is determined by the specific catalyst employed.

$$x_n = (1 - \alpha)\alpha^{n\text{-}1} \tag{2.7}$$

$$\text{where} \quad \alpha = \frac{R_\mathrm{p}}{R_\mathrm{p} + R_\mathrm{t}} \tag{2.8}$$

R_p and R_t in Equation 2.8 represent the chain growth rate and the chain termination rate respectively and both depend on chain length n and reaction conditions. In the ideal situation, α, is independent of the carbon chain length [25]. However, the product distributions obtained from FT are very dependent on: (i) reaction conditions, (ii) reactor configuration, (iii) conversion and (iv) catalysts and support properties. A graphical description of the FT chain growth polymerisation reaction is depicted in Figure 2.2 and a typical product distribution described by Equation 2.7 is shown in Figure 2.3.

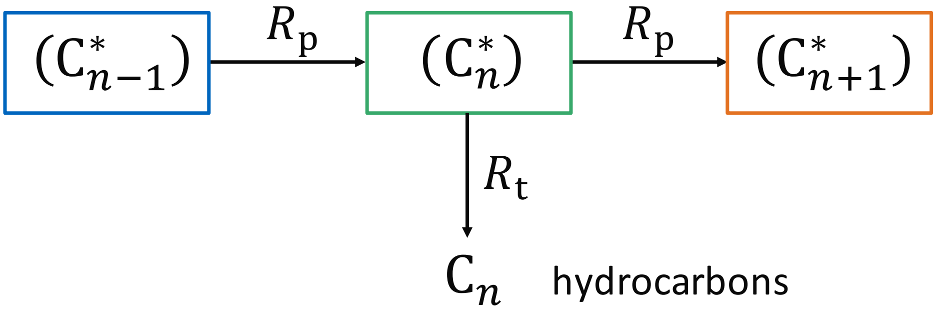

Figure 2.2 FTS chain growth with classical ASF model. Adapted from [15].

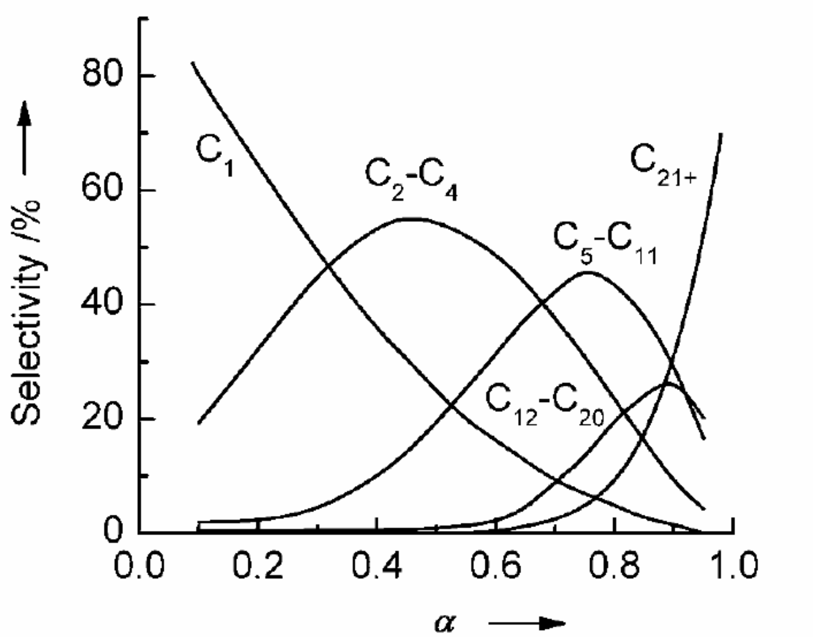

Figure 2.3 The product distribution for FTS versus the chain growth probability. Reproduced from [21].

2.2.2 Non-ASF Product Distributions

The ASF distribution is an idealised distribution function with limited applicability and the actual FTS carbon number selectivity does not fully obey this model. The distribution shown in Figure 2.3 above is a representative FT product distribution following the carbide insertion mechanism, see Section 2.6. Depending on the type of catalyst used, different deviations from the ideal ASF distribution can be observed. Although the ASF distribution predicts a fair description of the typical FTS product distribution, several significant deviations in the FT products obtained from cobalt and ruthenium catalysts can occur, see Figure 2.4. The three main types of deviations are found in [26]:

- C_1: higher yield than expected of undesired product
- C_2 and C_3: lower yield than expected
- C_{10+}: higher selectivity of desired product

Firstly, a higher molar methane (C_1) but lower C_2 and C_3 content than predicted by ASF can be observed. Also, for long-chain hydrocarbon products (C_{10+}), the α suddenly surges, which in the literature is known as a positive deviation from ASF [27, 28]. Some of these deviations in the literature are linked to non-steady state reaction conditions or non-ideal operation of the reactor. However, many more explanations are offered for these deviations.

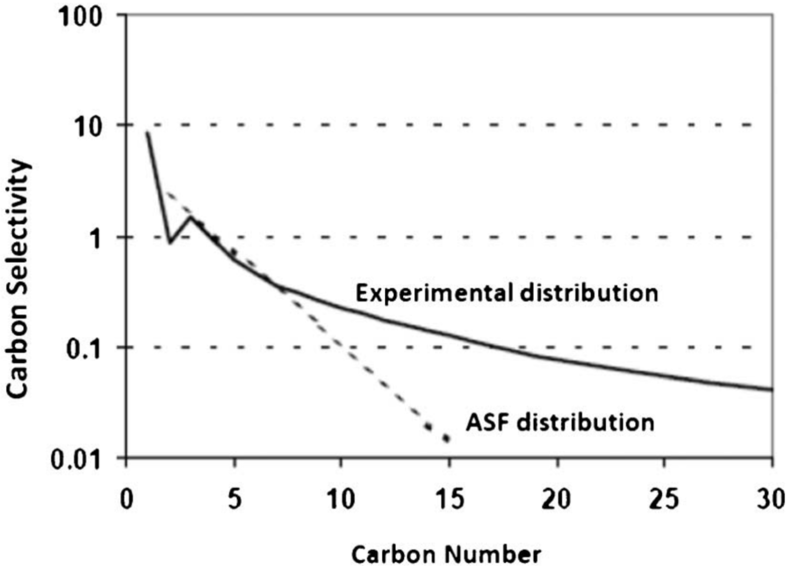

Figure 2.4 The ASF prediction compared to the experimental FT product distribution. Reproduced from [29].

The excess of methane production could be attributed to active site heterogeneity on the surface of the catalyst. It is suggested that methane might require very specific active sites, different from the sites producing other FTS products. In addition, researchers propose that certain special catalytically active sites favour methane over chain growth [30]. Alternatively, an observed increased C_1 formation can also be linked to either formation of local hot spots or even mass transfer limitations which thermodynamically would favour methane production [31].

Furthermore, in the literature ethene is generally acknowledged to be highly reactive, hence leading to a lower fraction of C_2 in the product distribution. This high reactivity would enable ethene to readsorb on the catalyst surface and subsequently further polymerise into longer hydrocarbon chains [32].

Finally, no consensus has been reported although a combination of several phenomena are generally proposed as a potential explanation for the underprediction of C_{10+} production by the ASF model. First, different chain termination reactions occurring on other sites are often suggested [33]. This deviation can be found especially for iron catalysts [34]. Researchers assume that two distinct chain growth probabilities caused by different types of catalytic sites could explain this deviation. These two α's are modelled by superimposing two independent, ideal ASF distributions and this is known as the 'double-ASF distribution'. In addition, subsequent secondary reactions of long-chain hydrocarbons affected by vapour-liquid equilibrium (VLE) effects like chain-length dependent solubility and diffusion coefficients are often suggested [35].

2.3 Process Configuration and Flowsheet

2.3.1 Syngas

Depending of the raw feed, syngas for FTS can be prepared by two different processes: (i) steam partial gasification or (ii) steam reforming. The feedstock for syngas production can vary between heavy crude oil, coal or methane, biomass or even waste. The steam partial oxidation reaction is highly endothermic, the heat required to drive the reaction is provided by combustion in the presence of oxygen. These two processes produce the syngas, which ideally has a H_2:CO ratio of approximately 2, corresponding to the stoichiometric coefficients of FTS. If during FT the H_2:CO ratio ≤ 2, the higher partial pressures of CO are known to lead to greater concentrations of surface carbon molecules, favouring longer chain products [36]. Simultaneously, a lower methane but higher alkene selectivity can be observed when the surface is more crowded with active carbon species. However, low H_2:CO ratios can also cause accelerated catalyst deactivation due to carbonaceous deposits [37].

2.3.2 Reaction Temperature and Pressure

Typically there are two operating regimes for FTS: the low-temperature Fischer-Tropsch (LT-FT) (190 - 260 °C) and high-temperature Fischer-Tropsch (HT-FT) (300 - 350 °C) with pressures ranging between 15 and 30 bar. As discussed earlier, the operating temperature will influence the types of products obtained. LT-FT is known to produce high-quality diesel, mainly consisting of linear, long-chain alkanes and waxes whereas HT-FT will result in short-to-mid range hydrocarbons (C_1-C_{15}), α-alkenes and a greater proportion of undesired branched and aromatic species [38].

2.3.3 Product Recovery

Following the FTS process, the waxes have to be upgraded to produce the highest-quality fuel. This is achieved by wax hydrocracking to selectively produce diesel, kerosene, naphtha and paraffins. In the 90's, Shell implemented the hydrocracking of their FT wax whereas Exxon typically hydroisomerised their FT wax to liquid oil.

2.3.4 Flowsheet

The process flowsheet for the production of fuels (diesel, naphtha and paraffins) and gas via FTS is depicted in Figure 2.5.

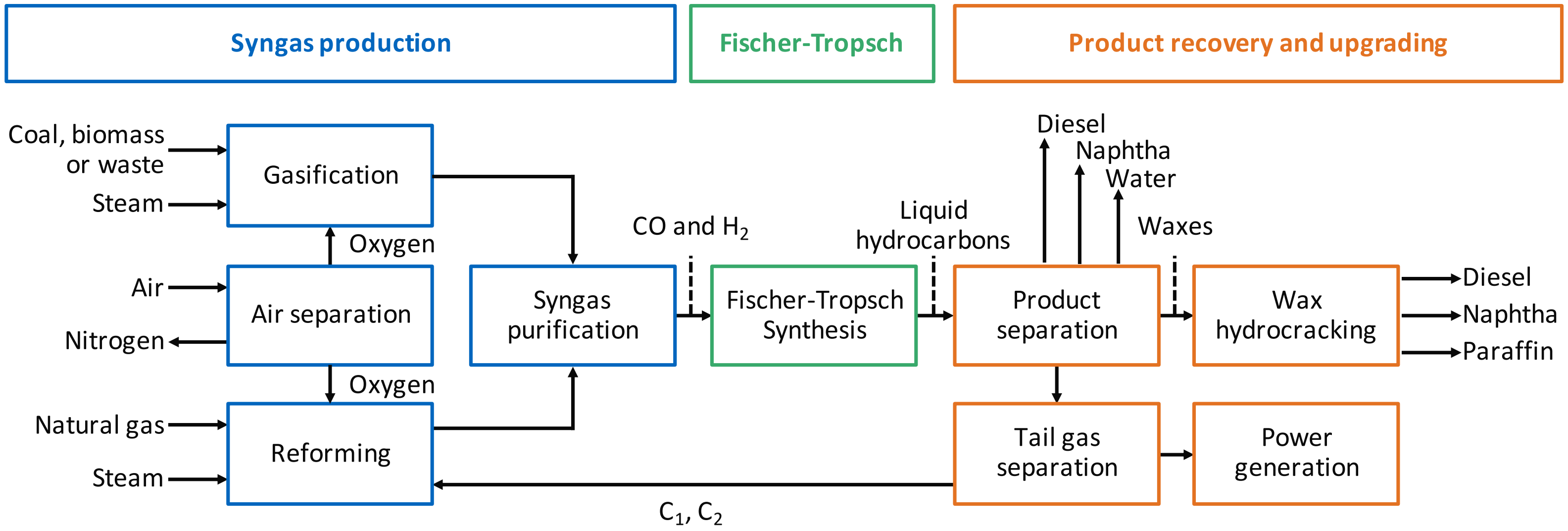

Figure 2.5 Process flowsheet for Fischer-Tropsch Synthesis.

2.4 Catalysts

FT products and waxes are produced on active sites of metal catalysts. FTS catalysts are typically group VIII metals that consist of (i) fused or precipitated iron, (ii) nickel, (iii) cobalt and (iv) ruthenium; these are reported here in order of increasing price. On a metal basis, the approximate costs of Fe:Ni:Co:Ru are 1:250:1,000:50,000. Only Fe-, Co-, Ni- and Ru-based catalysts are used as they are the only metals that have enough activity (reported in decreasing activity: Ru > Ni > Co > Fe) to be commercially viable.

Ruthenium is much more costly than iron, cobalt and nickel due to its limited reserves and thus large-scale application of Ru is uneconomic [39, 40]. Nevertheless, it is the most active catalyst for CO hydrogenation, capable of operating at temperatures below 150 °C, with high resistance to oxidation. The activity of Ru catalysts is known not to be affected by the presence of water [41]. It is reported that Ni is a very active hydrogenating catalyst since it produces significant quantities of methane. Hence, most industrial FTS catalysts have either iron or cobalt as primary catalytically active metal [42, 43].

Cobalt catalysts are also active but at an inferior rate at low reaction temperatures compared to Ru [25]. In HT-FT, cobalt has unsuitable high selectivity for C_1, hence, it is primarily used in LT-FT. Cobalt catalysts have a much longer lifetime, sometimes up to 5 years, compared to iron particles as cobalt is less susceptible to oxidation. Cobalt, due to its low selectivity for WGSR, is generally more resistant to deactivation by water and has higher selectivity towards linear long-chain hydrocarbons. Therefore cobalt has predominantly been used as a the main catalyst for the production of waxes and diesel fuels in LT-FT [44].

In comparison, fused iron catalysts are produced using alkali promoters with iron oxide to enhance their catalytic activity and selectivity. High levels of alkali are preferential to decrease methane selectivity. The lowest selectivity to CH_4 achieved using this type of catalyst is around 7% of the carbon in the hydrocarbon liquid products. As a consequence of operating at these high alkali concentrations, an increased carbon formation rate occurs in the catalyst and higher levels of organic acid are found in the liquid product. These issues can result in greater catalyst consumption rates or corrosion in the downstream operation. However, the liquid products obtained by using fused iron catalysts are highly olefinic and make this catalyst the most desirable choice for olefins production in the petrochemical industry. In general, iron catalysts are kinetically inhibited by the production of water in Equations 2.1 and 2.2 [19]. Agglomeration of iron particles due to the production of water causes deactivation kinetics to occur. Nevertheless, this feature is advantageous in the WGSR as this allows the use of mixtures of H_2-depleted or CO-rich synthetic gas, derived from coal or biomass. The typical lifetime of iron catalysts for FT is about 6 months as they deactivate more rapidly due to coke deposition. In addition, Fe-based catalysts can be operated under wider ranges of temperatures without drastic alterations in CH_4-selectivity [45].

All catalysts synthesised in the form of metal oxides have to undergo a pre-treatment stage to activate and convert the oxides to metals prior to FTS [46]. Cobalt and ruthenium catalysts are reduced under H_2 atmospheres at temperatures between 200 - 450 °C [47, 48]. Pre-treatment for iron particles is not as straightforward. The most common activations steps are either H_2 reduction, CO reduction or reduction in synthesis gas.

2.4.1 Promoters and Supports

Noble metals are often employed in FT to boost the productivity of the catalyst. These additives, also named promoters (Pt, Pd, Ru, Re and K) can be added to the active component to obtain typical chain growth probabilities between 0.7 - 0.8 [39]. These promoters can be reduced at a lower temperatures than the metal catalyst and hence promoters facilitate the overall metal reduction process. For cobalt catalysts, the addition of small quantities of noble metals allows to shift the regeneration temperatures of cobalt oxides and other related cobalt species interacting with the support to lower temperatures [49]. Iron catalysts tend to be promoted with Cu, which increases the rate of reduction, also enabling a lower reduction temperature. However, since promoters are noble metals, a significant extra cost has to be taken into account by catalyst manufacturers. Therefore it is crucial to determine a suitable loading of the promoter (< 1wt%) to maximise the availability of active cobalt surface sites [50].

In order to achieve large surface areas, the nano-scale metal particles are dispersed on a porous carrier material [51]. These pellets typically have a spherical, cylindrical or more exotic shape with a diameter of 0.1 - 3 mm, with an average pore size distribution in the range of 5 - 100 nm [52]. Typically the catalysts employed in the HT-FT process are prepared by fusing magnetite with minute amounts of metal promoters. The LT-FT catalyst can be prepared by precipitating the metal on an oxide in the presence of some alkali promoters. These supports are silica, alumina, titania, zinc oxide or combinations of these oxides. Common supported cobalt catalysts are prepared by depositing cobalt on a pre-shaped refractory oxide support.

2.4.2 Deactivation

The main causes of deactivation of LT-FT catalysts are: (i) poisoning, (ii) fouling, (iii) thermal sintering and (iv) re-oxidation in the presence of water, which are briefly discussed below and shown in Table 2.1. Figure 2.6 depicts the main types of catalyst deactivation in heterogeneous catalysis while Figure 2.7 illustrates the main processes taking place during equilibration and deactivation of Co FT catalysts.

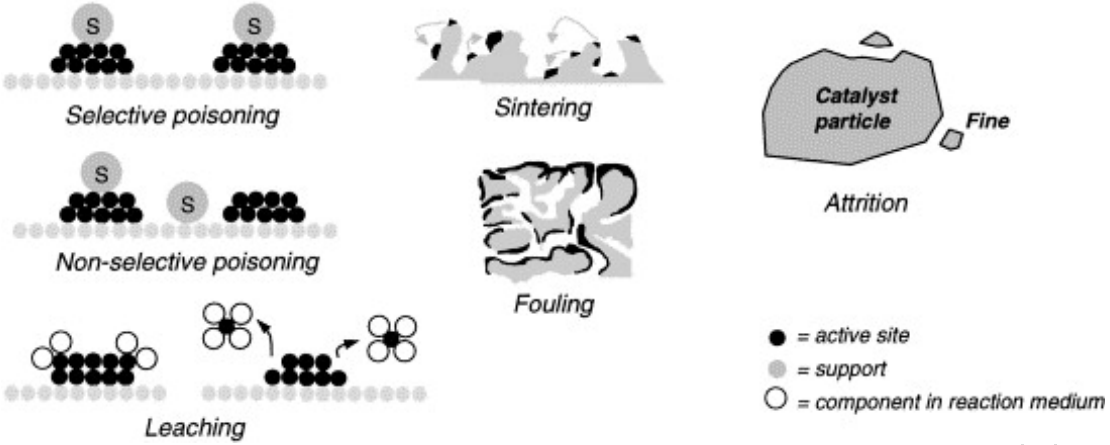

Figure 2.6 Major types of deactivation in heterogeneous catalysis. Reproduced from [53].

Table 2.1 Mechanisms of Fischer-Tropsch catalyst deactivation. Adapted from [54].

Mechanism	Type	Description
1. Poising	Chemical	Strong chemisorption of species thus blocking catalytic sites
2. Fouling	Mechanical	Physical deposition of species onto the catalytic surface and in pores
3. Sintering	Chemical	Thermally induced loss of catalytic surface area and active phase
4. Re-oxidation	Chemical	Deactivation due to oxidation of highly dispersed cobalt atoms
5. Attrition	Mechanical	Loss of catalytic material and surface area due to abrasion and crushing
6. Leaching	Mechanical	Redispersing of catalytic material due to corrosive reaction medium

Sulphur Poisoning

Sulphur poisoning is a known phenomenon that can significantly reduce the lifetime of a catalyst. Sulphur can act as a poison by adsorbing very strongly on the active sites of the catalysts and physically blocking those sites. It has been suggested that in the process, the sulphur also electronically modifies the neighbouring atoms. To prevent this from happening, in the initial synthesis gas production a purification step is added to the FT process flowsheet. This is especially important when the syngas is derived from coal or biomass [54].

Fouling

FT waxes tend to accumulate on the surface of the catalyst and are known the decrease the diffusion rates of both products and reactors, ultimately slowing down the reaction. Although the objective of FTS is to produce long-chain hydrocarbons, accumulation of waxes can further slow down a reaction which by itself is already slow. Furthermore, over time these hydrocarbons can convert to carbon or coke on the catalytic surface and in pores, blocking access to the active sites [43].

Sintering

Sintering is a common problem in catalysis engineering as it can severely reduce the surface area and active phase of the material. In addition, it is considered to be an irreversible process. Sintering is a thermally induced process whereby the crystallites agglomerate which leads to a minimisation of the surface energy, which is thermodynamically favoured. The two main sintering mechanisms are: (i) atomic migration (also termed Ostwald ripening) and (ii) crystallite migration or coalescence. It has been reported that FTS performed under high temperatures and water vapour pressures accelerate this process [55].

Re-oxidation

FT catalysed by alumina supported cobalt catalysts can encounter severe deactivation, especially in the presence of water. This deactivation can be due to re-oxidation of highly dispersed cobalt crystals and surface cobalt atoms [56].

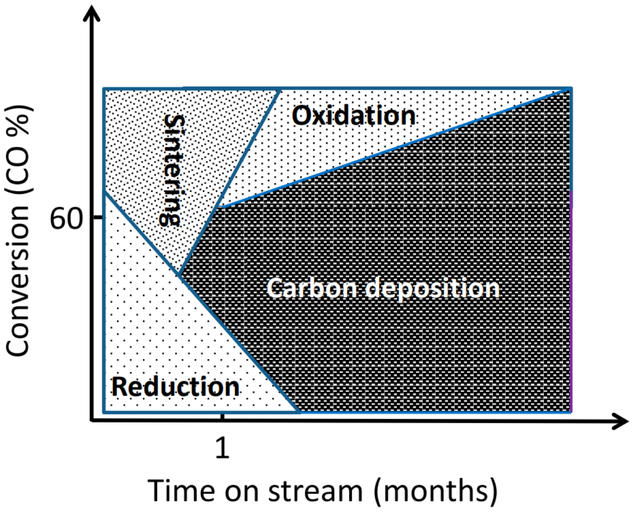

Figure 2.7 Main reactions taking place during equilibration and deactivation of Co Fischer-Tropsch catalysts. Reproduced from [56].

2.5 Reactors

This Section will cover the most important reactor designs, highlighting their main characteristics, (dis)advantages and uses. In the final Subsection 2.5.4, the two major FT reactor types used in the low-temperature regime are discussed and their production capacity and product distributions are compared.

A chemical reactor is any type of vessel that can be used to transform the reactant species into the desired products. The vessels themselves can be simple mixing tanks or complex flow reactors. See Figure 2.8 for an overview of the various chemical engineering reactors most widely used in industry and academia.

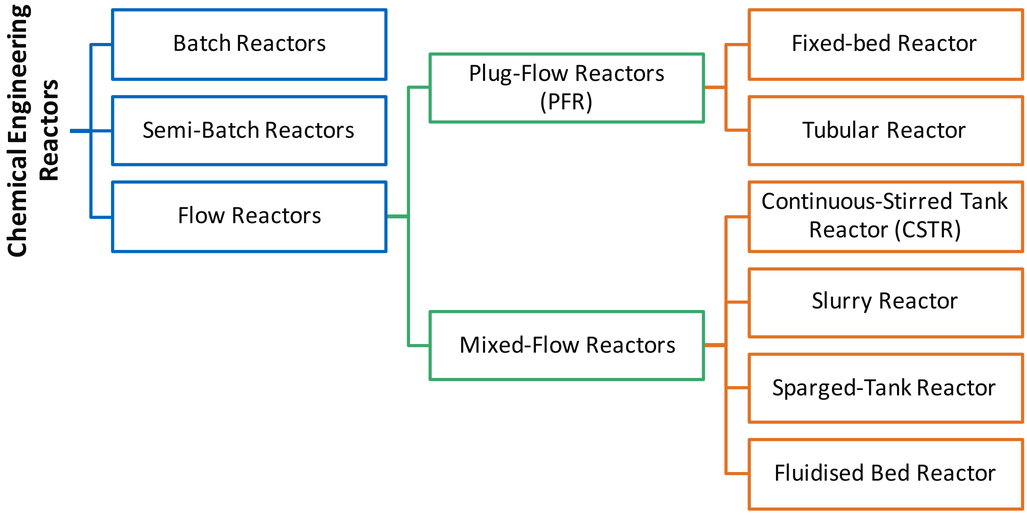

Figure 2.8 An overview of the three main types of chemical engineering reactors (blue boxes), varying from Batch Reactors, to Semi-Batch Reactors to Flow Reactors. Further examples of the Flow Reactors are given.

2.5.1 Batch

Batch reactors are typically operated by placing all of the reactant material prior to the reaction inside of the reactor. Once the reaction is completed, the reactor is emptied by removing all of the products. During the reaction process, no material is added nor withdrawn. Batch reactors are often used for laboratory work as the reactants are placed in a test-tube, flask or beaker.

The main assumptions when calculating performance behaviours for batch reactors are: (i) the reactor content is well-mixed, (ii) the reaction process only starts when the filling is completed and (iii) if the reaction is quenched, it is considered finished [57]. In a batch reactor, the initial concentrations are the greatest, resulting in high reaction and conversion rates. This can be especially advantageous for higher-order kinetic reactions. The batch reactor design is therefore very well suited for these types of reactions as most of the desired products are formed before enough time elapsed for undesired by-products to be created.

The batch reactor is flexible in production design in comparison to the flow reactor configurations. Moreover, it is very versatile, as it can be used to make many products consecutively. Temperature, filling levels and reaction time can easily be varied without affecting the product quality. Other advantages are that this reactor design is easy to clean and good to produce small amounts of products during for example testing phase [57]. On the other hand, the main disadvantages of this equipment are: (i) the high cost of labour per unit of production,

(ii) the technical complexity to maintain large scale production and (iii) the longer downtimes when cleaning is required [58].

2.5.2 Semi-batch

The semi-batch reactor combines properties from both the ordinary batch reactor as well as the continuous-stirred tank. The reactor has a batch design but combines this with a continuous inflow or outflow of material during reaction operation. For reactions taking place in a semi-batch stirred tank reactor, the following assumptions can be made when describing the reactor performance: (i) well-mixed contents of the tank and (ii) there are no inlet or outlet effects caused by the continuous stream.

In order to have better heat control over exothermic reactions, the semi-batch reactor with one feed can be advantageous. By gradually feeding cooled reactants to the reactor, a quenching effect can be simulated. Both the concentration and temperature can be kept low compared to a normal batch reactor. Similarly, a semi-batch reactor is frequently used to control the kinetics in multiple reaction sequences. This can easily be achieved by for example adding reactant A slowly, thereby keeping the concentration of reactant B higher and thus shifting the selectivity. On the product side, the semi-batch can also be used for continuous removal of the product. This has the advantage of increasing the yield in equilibrium limited reactions.

However, the temperature control is the most important drawback for the the semi-batch reactors. The batch nature and temperature conditions cause severe operational difficulties and therefore the semi-batch reactor is impractical for most reactions, even for computer-controlled systems. However, the majority of reactions considered for semi-batch are highly exothermic, often dangerous and therefore require special attention [58].

2.5.3 Continuous Flow

Continuous flow reactors form the biggest group of chemical reactor types. The two main groups of flow reactors used industrially are: (i) the continuous mixed-flow reactor, which involves a well-mixed tank with simultaneous product removal and product feeding and (ii) the plug flow reactor (PFR) which consists of a long tube where the reacting mixture moves down or up a tube resulting in a concentration gradient along the length of the reactor. See Figure 2.9 for an overview of the different types of flow reactors. In the following Sections, the main continuous flow reactors are discussed in greater detail.

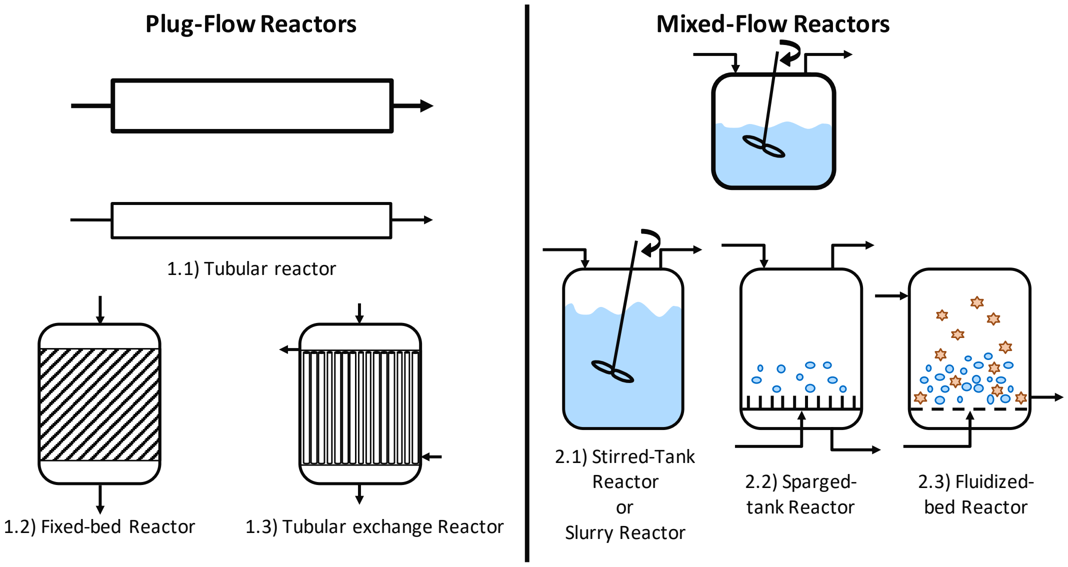

Figure 2.9 An overview of the different types of Flow Reactors, either Plug-flow or Mixed-flow reactor.

Plug-Flow Reactor

A basic PFR is a tube through which the input and output streams pass continuously. There are three main assumptions when working with PFRs. Firstly, the PFR should be modelled as a steady state operation, whereby the concentration changes when moving down the reactor. Secondly, the tube can be divided into incremental slices through which the material passes. Each of these slices experience perfect radial mixing without any forward or backward mixing between the slices. Therefore, each of the minuscule slices can be modelled as a infinitely small continuous stirred-tank reactor (CSTR). Finally, the reactor composition and conversion both vary with residence time and therefore depend on either reactor volume or reactor length [59]. Typically, the plug-flow reactor is best used for short residence time reactions. Examples of non-catalytic reactions performed in PFRs include high-pressure polymerisation of ethylene or naphtha conversion to ethylene [60].

The are many important advantages of a PFR: (i) the steady state operation mode, (ii) minimal back mixing of the product resulting in higher concentrations inside the reactor, (iii) minimum reactor volumes in comparison with a typical CSTR, (iv) infinite number of reaction operating modes possible proportional to the points that lie along the rate curve, (v) possibility to only apply heat transfer in those areas of the reactor where it is needed, allowing to create customised temperature profiles and finally, (vi) no requirement for agitation. There are two major disadvantages: (i) highly viscous reactants can lead to high-pressure drops and therefore create significant deviations from the ideal flow profile and (ii) achieving ideal operation conditions is complex.

Continuous-Stirred Tanks

The CSTR runs at steady state with continuous inflow and outflow of reactants and products. In the ideal situation, the CSTR is considered to be very well mixed thus having no dead zones or bypasses. The three main assumptions when modelling an ideal CSTR are: (i) the CSTR operates under steady state flow, (ii) the composition and temperature profiles are uniform across the tank and finally, (iii) the composition of the effluent is equal to the composition of the reactor tank.

The CSTR reactor design is frequently used for reaction mechanisms whereby low concentrations are necessary. For example, with competing reactions, selectivity towards the favoured reaction can be achieved by keeping the concentration of the other reactant low. Additionally, the CSTR also has applications for heterogeneous catalytic systems where significant mixing gives high contact time between the different phases. Nowadays, CSTRs are typically used in industry for example for the saponification of fats or for emulsion polymerisation.

The main advantages of CSTRs are: (i) continuous, steady state reaction operation, (ii) low cost and simplicity of construction, (iii) very good temperature control and (iv) the ability to back mix heat generated by exothermic reactions and therefore increase the reaction rate and overall reactor performance. However, the considerable disadvantages of CSTRs are: (i) the possibility of having by-passing or even channelling, which would harm the overall reaction performance and (ii) CSTRs have the lowest conversion per unit of volume. The latter results in having CSTRs that generally require larger reactor volumes [59].

Fluidised Bed Reactor

The final, major category of reactor types that are very regularly installed in industry are fluidised beds. The phenomena of fluidisation occurs when a fluid is passed upward through a bed of fine solids, which can either be reactants, catalyst or inert particles. At lower flow rates, the gas which is pressed up the bed can channel through the bed of solids. However, if the minimal required fluidisation flow rate is reached, the gas or liquid is able to lift the bed of solids and bubbling can be observed. The solid particles seem to be a boiling fluid. Depending on the velocity of the rising phase, it can flow as a plug or a well-mixed stream. The bubble size of the flow heavily influences the reactor efficiency and the contact area between the different phases [61, 62].

There are three significant advantages of operating in a fluidised bed reactor. Firstly, due to the small particle size used inside the beds, the high surface area per unit mass enables good heat and mass transfer. Hence, fluidised beds are known to have excellent heat distribution with minimal hotspot formation throughout the reactor [63]. Secondly, it is possible in fluidised beds to remove and replace the catalyst particles without the need to interrupt the operation. This can be a major time and money saving aspect for reactions that require frequent catalyst regeneration. Finally, fluidised beds are known to be more efficient during multiphase, catalytic reactions [64].

However, various important disadvantages are associated with fluidised bed operation: (i) the equipment vessel tends to be large, which can be very costly, (ii) if operated with too high gas velocities, a particle blow-out can occur, (iii) due to abrasion and erosion, severe deterioration of the equipment can take place, (iv) the equipment is usually expensive to construct and maintain, (v) large pressure drops can occur, (vi) catalyst pellets can break-up due to attrition, and finally, (vii) inappropriate operation with large bubble sizes can drastically reduce conversion. Fluidised beds can be used for example for catalytically cracking of petroleum. In addition, non-catalytic reactions include fluidised combustion of coal or calcination of lime [64–66].

2.5.4 Fischer-Tropsch Reactors

Typically FTS processes are subdivided into two categories according to their operating temperatures: LT-FT and HT-FT. Three main reactor designs are currently operated across the globe on a commercial scale for FTS: (i) multi-tubular fixed-bed, (ii) slurry-bubble phase and (iii) fluidised bed reactors, see Figure 2.10. The LT-FT reactor designs are illustrated in Figure 2.11. The key distinguishing features between HT-FT and LT-FT reactors are that LT-FT reactors are characterised by a three-phase operation whereas no liquid phase is present in HT-FT reactors. If this were the case, serious issues like particle agglomeration and loss of fluidisation would occur [67].

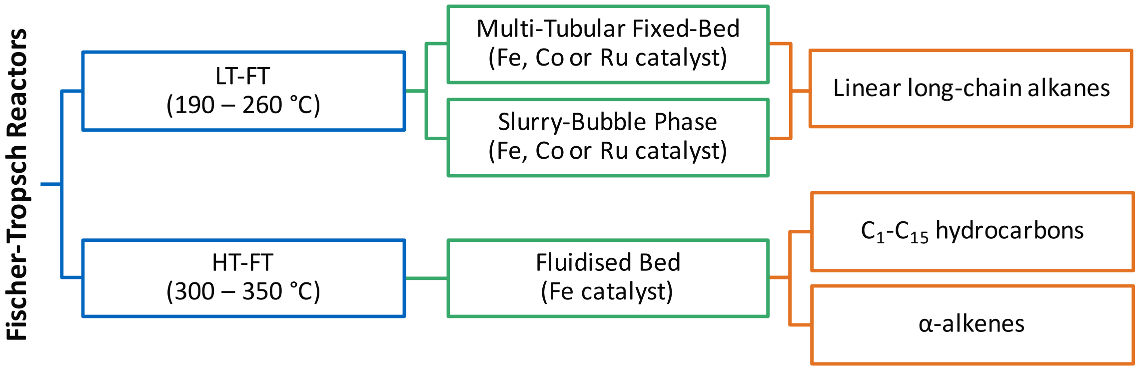

Figure 2.10 An overview of the different processes and reactors used in FTS.

Multi-Tubular Fixed-Bed Reactors VS. Slurry-Bubble Column Reactors

Shell uses fixed-bed reactors for FTS, both in Bintulu, Malaysia, and the Pearl GTL plant in Qatar, which consists of 24 parallel trains of fixed-bed reactors each with 29,000 tubes filled with catalyst, each with a daily production capacity of approximatively 6,000 barrels [68]. As FTS is a highly exothermic reaction, heat removal remains one of the main challenges when operating this reactor type. Besides, poor mixing and heat transfer can also create hotspots which can facilitate further methane formation. In addition to heat control, two other known issues with fixed-bed reactors are: (i) high pressure drop and (ii) catalyst deactivation and regeneration. As well as pressure drops, mass transfer resistance can lead to intra-particle diffusion limitations which can further hinder the reaction rate of FT. Typical catalysts have a diameter in the order of 1 - 20 mm due to pressure drop constraints. However, since the heat and mass transfer properties of the fixed-bed reactors are generally more predictable and more straightforward to model, scaling up of these reactors is easier [45].

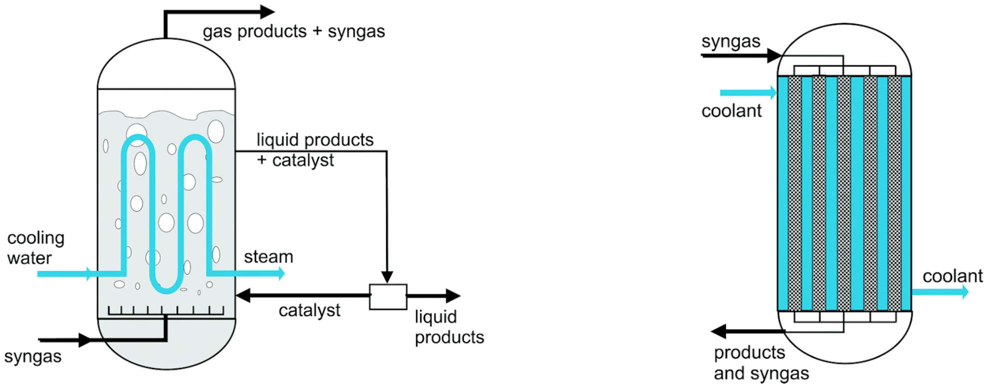

(a) Slurry-bubble column reactor *(b) Multi-tubular fixed-bed reactor.*

Figure 2.11 Commercially used industrial reactors for Low Temperature FTS: a) slurry-bubble column reactor, b) multi-tubular fixed-bed reactor. Reproduced from [69].

In comparison, slurry-phase bubble columns are another attractive alternative to fixed-bed reactors because the system is characterised by: (i) a low pressure drop, (ii) no diffusion limitations, (iii) excellent heat-transfer properties, (iv) possibility of continuous refreshments of catalyst particles and finally (v) simple and cheap to design and build [70]. Slurry reactors are essentially non-ideally stirred reactors and the residence time of the gas is very small compared to the liquid and catalyst residence times [71]. The close temperature control allows minimisation of the risk of hotspot formation thus reducing the methane production. Unlike the fixed-bed reactor, the slurry-bubble column does not experience diffusion limitations in the inter-particle space. Therefore much smaller catalyst particles can be used (1 - 300 µm range) [72]. However, the major drawbacks of operating FT in a slurry-bubble are: (i) complex catalyst and product separation especially in highly viscous phases, (ii) catalyst attrition leading to enhanced deactivation and (iii) difficult scaling-up methodologies [69].

Table 2.2 compares the LT-FT reactor types on basis of conversion, capacity per reactor and highlights some general characteristics.

Table 2.2 Properties for different reactor types for Low-Temperature FTS based on open literature and patents. Reproduced from [56].

Reactor	**Conversion per path (%)**	**Capacity per reactor (bbl day^{-1})**	**Characteristics**
Slurry-bubble column	55-65	≤25,000	Internal heat exchanger required
Tubular fixed-bed	30-35	≤6,000	≤30,000 tubes with catalysts pellets

Table 2.3 compares the products obtained either using a HT-FT fluidised bed or a LT-FT fixed-bed reactor. The HT-FT allows production of a far greater amount of short-to-mid chain products (C_5-C_{11}) but the LT-FT design is more favourable to obtain paraffins.

Table 2.3 Comparison of the products obtained with a fixed-bed reactor and a fluidised bed reactor. Reproduced from [32].

Fraction (w%)	**Fluidised Bed Reactor (310-340 °C)**	**Fixed-Bed Reactor (220-240 °C)**
C_3-C_4	7.7	5.6
C_5-C_{11} (gasoline)	72.3	33.4
Gas oil	3.4	16.6
Paraffin	3.0	40.1
Alcohol, ketones	12.6	4.3
Acids	1.0	<0.5

2.6 Reaction Mechanisms

Even though FTS has been known for almost 100 years, there is still not one single mechanism which can explain all products formed. Models which combine the overall consumption of the reactants and the product distribution are very scarce in the literature, but are extremely valuable for the understanding and prediction of the FT process. As FTS accounts for a very wide range of products, the reaction pathway is extremely complex. FT can be conducted using a variety of catalysts at various operating conditions in different reactor types, hence comparing and reconciling all the possible mechanisms is challenging. Therefore the limited discussion below is merely used as a brief summary.

Many studies aim at understanding the FT reaction mechanisms, with the main goal to improve the performance of the catalyst. However, no general FT reaction rate law exists, as the FTS kinetic expression depends on the catalyst formulation [73]. Empirical power-law kinetics for the CO and H_2 conversion rates and a simple polymerisation reaction following the ASF distribution are typically assumed [47]. Equation 2.9 describes the effects of CO and H_2 partial pressures (P_{CO} and P_{H_2} respectively) on FTS rates at both low and nearly constant water pressures in the presence of a Co and Ru catalyst:

$$-r_{CO} = r_{\text{hydrocarbon}} = \frac{\alpha P_{CO} P_{H_2}}{(1 + K_{CO} P_{CO})^2}. \tag{2.9}$$

Despite the apparent simplicity of the basic FT reaction, a lot of complex chemistry is involved. Even fundamental aspects of the surface reactions, such as the dominant CO activation pathway, have been highly controversial subjects in the field of heterogeneous catalysis for several decades [74]. It is often suggested in the literature that two or more independent mechanisms may operate simultaneously, one mechanism dominating chain growth for short chain hydrocarbons and another dominating at longer chain length [75]. Detailed mechanistic modelling of FTS is complicated owing to a number of factors: (i) the large number of reacting species, (ii) re-adsorp and conversion of primary products, (iii) difficulties in measuring surface intermediates and (iv) coverage-dependent reaction rates.

The hydrocarbon and oxygenate formation mechanisms taking place during FTS have been reviewed by several authors and the three major mechanisms found in literature are discussed below. One common feature occurring in these theories is the termination method. The different chemisorbed species during FT can be seen in Figure 2.12.

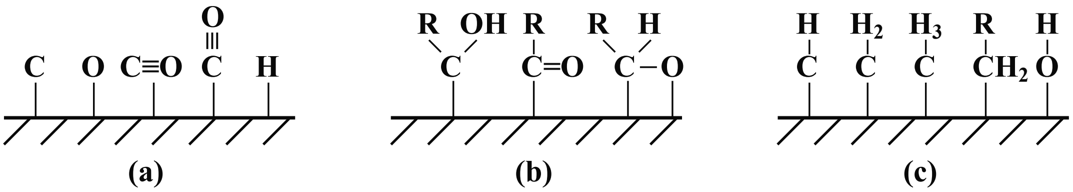

Figure 2.12 Postulated chemisorbed species during FTS, with (a) reactants, (b) oxygen-containing intermediates and (c) hydrogen-containing intermediates. Adapted from [14].

2.6.1 Carbide Mechanism

Overall, many researchers have agreed that FT is a surface polymerisation reaction involving the following steps:

1. Reactant adsorption and dissociation
2. Chain initiation
3. Chain growth and propagation
4. Chain termination and product desorption
5. Re-adsorption and any subsequent reactions

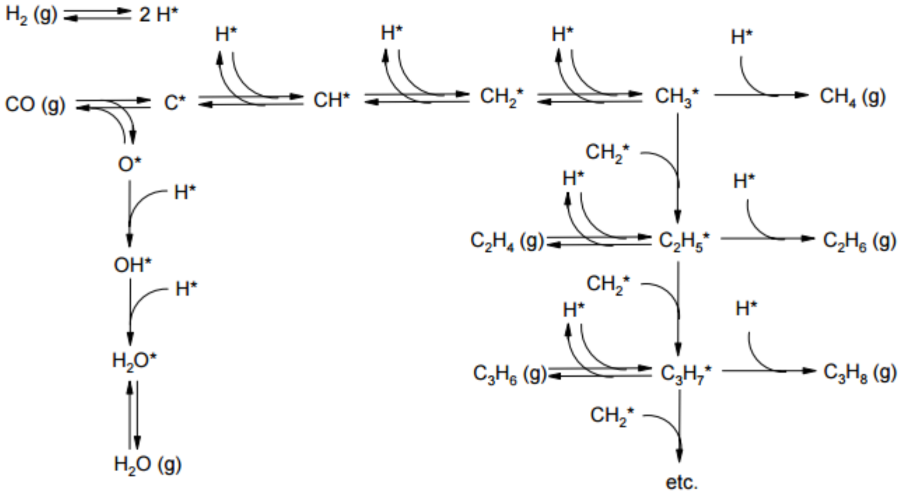

Figure 2.13 Schematic representation of the carbide mechanism. Reproduced from [76].

The carbide mechanism, first proposed by Fischer and Tropsch in 1926, assumes dissociative adsorption of both CO and H_2 on the catalyst surface. The surface carbide is hydrogenated to form a reactive $CH_2{}^*$ building block, as shown in Figure 2.13. The formation of longer hydrocarbon chains attached to the catalyst surface occurs via coupling of these methylene blocks [14]. Typical products obtained through chain termination reactions like hydrogenation, are paraffins, or hydrogen abstraction, which produces α-olefins. In addition, other products like alcohols and aldehydes can also be obtained using oxygen-containing surface species [76].

2.6.2 Enolic Mechanism

The main difference compared with the carbide mechanism is that instead of assuming methylene, $CH_2{}^*$, as a building block for the hydrocarbon chain growth, an oxygen-containing intermediate building block is involved (proposed by Anderson and Emmett *et al.*), see Figure 2.14. A further difference in this enolic mechanism is that the adsorption of CO is non-dissociative [77]. Subsequent to the adsorption, CO and H_2 react to form a HC^*COH

intermediate, acting as the main building block [78]. Chain propagation occurs when two of these building blocks are coupled in combination with H_2 to remove O_2 in the form of H_2O [76]. The termination reaction can be initiated to form products via similar types of reactions as in the carbide mechanisms [79].

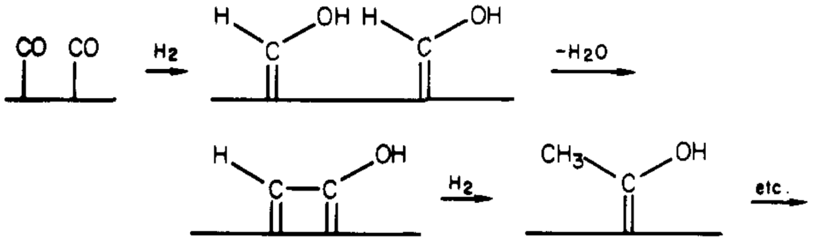

Figure 2.14 Schematic representation of the enolic mechanism. Reproduced from [78].

2.6.3 CO Insertion Mechanism

The final mechanism recurring frequently in the literature proposed by Pichler and Schultz is the CO insertion mechanism. Similar to the enolic pathway, the CO insertion theory is based on oxygen-containing intermediate building blocks, see Figure 2.15. This intermediate is formed after reaction of CO with a surface hydroxyl group and subsequent hydrogenation to CH_3C^*O, attached to the catalyst surface [80]. Succeeding reactions with CO and two H_2 molecules result in hydrocarbon chain growth. Finally, analogous to the enolic and carbide mechanisms, termination occurs via hydrogenation reactions to form paraffins or hydrogen abstraction to form α-olefins [79].

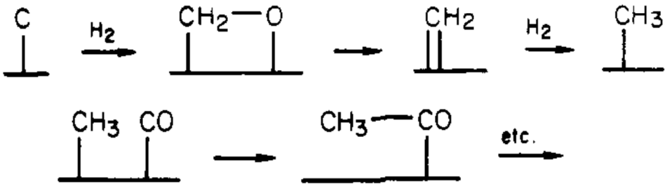

Figure 2.15 Schematic representation of the CO insertion mechanism. Reproduced from [78].

2.7 Phase Behaviour in Fischer-Tropsch Synthesis - Emulsions

Formation of Intrapore Liquids in Presence of Water

During FTS it is widely accepted that the intra-pore region of the porous catalyst support becomes completely filled with a stagnant liquid layer that is thought to be partially composed of hydrocarbons and water [28]. The presence of this stagnant liquid phase is possibly an effect of capillary condensation occurring inside the pores under close to bulk water condensation conditions [81]. In the absence of the WGSR, water is the main by-product of FTS. As water is one of the main by-products, when operating at nearly 30 bar and 250 °C, water is assumed to be in the vapour phase according to its phase diagram. However, the phase diagram for water indicates that under FTS conditions, water is very close to the VLE line. As a consequence, assuming water is immiscible with the hydrocarbon phase, a two-phase liquid layer in addition to a vapour phase water would exist in the pores of the catalysts, significantly affecting the diffusion behaviour of the reactants and products in the porous media.

It is not well reported how these different phases affect the transport mechanisms of CO, H_2 and H_2O into and respectively out of the particle. Water present in the intra-pellet region would facilitate the diffusion of CO and H_2 within the catalyst pore structure and also increase the accessibility of transport limited regions within porous pellets [82]. In that case, the gaseous components CO and H_2 initially present on the outside of the particles have to dissolve into the liquid phase layer and then diffuse to the internal pore surface to reach the active sites where the reaction actually takes place. Vice versa, the waxy, long-chain hydrocarbons and water have to detach from the metal surface and then are required to diffuse through the pores to the external surface of the particles. The discrepancy between the fast reaction rate and the slow diffusion rates could lead to concentration gradients of the reactants across the catalyst particles.

Many different explanations have been offered in the literature to explain the influence of water produced during FTS. Nijs and Jacobs *et al.* suggested a direct mechanistic involvement of water in FTS [83]. One recurring explanation is that when FT is operated at higher partial pressures of water, hydrogenation reactions were suppressed as more hydrogen sites were occupied on the surface [84]. Furthermore, the addition of water during FT catalysed over TiO_2-supported Ru particles resulted in significantly higher reaction rates and yielded lower selectivities towards methane. Also, it was concluded that the positive effect of water promoted the chain growth probabilities. Similarly, another patent also claims improved C_{5+}-selectivity, higher polymerisation rates and reduced methane selectivity during FTS with higher partial pressures of water over a Ru catalyst in a fixed-bed reactor [85]. This is also in line with other results obtained with several cobalt catalysts and a ruthenium catalyst [86]. It has even been reported that Ru catalysts are still active if suspended in liquid water, which indicates its high resistance against oxidation [87]. However, the effect of adding large amounts of water to Co catalysts could result in catalyst deactivation [88, 89]. Depending on the catalyst, this could be either a reversible or an irreversible effect [90]. The deactivation could arise due to either oxidation or the formation of inactive species from the Co and its support, that are not reducible [91, 92].

Similar conclusions have been reported by Bertole *et al.* based on a Steady-State Isotopic Transient Kinetic Analysis (SSITKA) study on Co/TiO_2. It was found that adsorbed water simultaneously accelerates the CO dissociation rate but also mediates H transfer, resulting in enhanced production rates of CH_x monomers [82]. It was reported that Co-adsorbed water interacts with CO and lowers the activation barrier for CO activation. As a consequence, this would lead to an increased coverage of surface carbon [93]. Due to the competitive nature for adsorbing species, increased concentrations of C on the surface would result in a deceased H_2 surface concentration [94, 95]. Ultimately, this would yield lower hydrogenation rates of alkanes and alkenes and a higher production of alkenes in the presence of water [82].

Numerous scientists have reported that the cobalt particle size distribution has a significant influence on the selectivity and conversion during FTS [96–99]. Researchers agree that water affects the particle size of cobalt [100]. The main concern with water is that it causes cobalt catalysts to sinter, thus influencing the size of the particles. This could lead to the complete deactivation and therefore cease the conversion. However, according to molecular dynamic (MD) Monte Carlo simulations performed by Makrodimitri *et al.* in Greece, a 10 nm layer of liquid phase water exists on the catalyst surface, i.e. in direct contact with the deposited Co particles [101–103]. The hydrocarbons would form a bulk layer in the pores.

2.8 *In Situ* Studies of Heterogeneous Catalysis

Approximately 50 years ago, researchers in heterogeneous catalysis had very limited access to atomic- and pore-scale information explaining what was actually ongoing inside the catalyst particles. Only very few techniques were readily available at the time that enabled simultaneous studies of the catalysts under real reaction condition and could provide detailed chemical and structural information on the reaction. As a consequence, the chemical reactor was regularly referred and treated as a "black box". In addition, to a large extent the catalysis research was performed "post-mortem" and the analysis on the catalysts for the kinetic deductions done *ex situ*. This degree of freedom sometimes led to (mis)-interpretations and speculations, which resulted to situations where several conflicting models were proposed for the same reaction using the same catalyst. These difficulties have been termed the "materials gap" in catalysis and significant efforts have been devoted to bridging these gaps [104].

Despite the progress obtained with *in situ* techniques, there still is a need for developing new methodologies that allow spectroscopy and other measurements to be performed under high pressure conditions [105]. Even small changes in the chemical environment may cause large changes in the catalyst surface structure. For heterogeneous catalysts, the surface reconstructions may also result in completely different morphology. In general, as the active state of a catalyst particle only exists during the catalytic reaction, this further emphasises the need for performing *operando* studies under relevant reaction conditions [106]. In order to gain fundamental understanding of the catalysis, such *operando* studies should ideally be combined with on-line measurements of catalytic activities and surface chemistry [107]. To gain those deep insights, (i) advanced characterisation methods, (ii) proper equipment and

(iii) related measurement protocols should be used [108]. The fundamental insight which can be obtained from *in situ* and *operando* studies has been important in catalyst developments since it has enabled more rational catalyst design strategies [107].

Due to the lack of direct characterisation of cobalt or ruthenium based catalysts in realistic working conditions, information found in the literature about changes occurring during the activation and deactivation steps, reaction kinetics and transport phenomena is rather contradictory [109]. Generally speaking, in order to obtain spatially- and chemically-resolved information on compositions and transport behaviour tomography techniques, such as X-ray imaging or computerised tomography (CT) scans, can be used. When adding the extra complexity of working inside a multiphase flow reactor at high pressures and temperatures, MRI remains one of the best techniques to study these complex reactor-scale systems.

Table 2.4 Strategies to obtain physicochemical properties of catalysts with their catalytic performances, both under reaction and vacuum condition. Reproduced from [110, 111].

Conditions	**Techniques**	**Information**
Reaction	1. Infrared Spectroscopy	• Surface functional groups
	2. Raman Spectroscopy	• Functional groups of adsorbates
	3. X-Ray Scattering	• Nanoparticle size distributions and size
	4. Nuclear Magnetic Resonance	• Diffusometry • Relaxometry • Liquid distribution • Composition • Correlation of protons • Imaging
	5. Electron Paramagnetic Resonance	• Molecular structure and motion
	6. Atomic Force Microscopy	• Very high-resolution probe microscopy
	7. Ultraviolet-Visible Spectroscopy	• Local environment of surface groups
	8. Mössbauer Spectroscopy	• Chemical and structural properties
	9. Temperature Programmed Desorption	• Amount of desorbed species
Vacuum	1. Ultraviolet Photoelectron Spectroscopy	• Molecular orbital energies
	2. Transmission Electron Microscopy 3. Scanning Electron Microscopy	• High-resolution microscopy

Nowadays, the choice of *in situ* methodologies is much larger, ranging from Infrared Spectroscopy (IR), Raman Spectroscopy (RS), X-Ray diffraction (XRD), Small Angle X-ray Scattering (SAXS), Mössbauer emission spectroscopy (MES), CT, Ultraviolet-Visible Spectroscopy (UV-VIS), Mass Spectroscopy (MS), electron paramagnetic resonance (EPR), MRI, NMR to finally high-resolution electron microscopy. For a detailed list of characterisation techniques available, both under reaction and vacuum conditions, see Table 2.4. Very complex systems can not only be studied theoretically by density functional theory (DFT) calculations, but more and more researchers combine such studies with *in situ* investigations to obtain atomic-scale structural and chemical insight.

Furthermore, these improved possibilities for linking the fundamental insights obtained from *operando* studies to the catalysis, also had beneficial effects on microkinetic studies. Due to this large variety of techniques available, catalyst characterisation has changed dramatically [110–112]. This illustrates how the introduction of *in situ* techniques and *operando* measurements has completely revolutionised research in heterogeneous catalysis [113, 114]. Table 2.5 highlights the most common spectroscopic characterisation techniques used to study chemical reactions, listing the main limitations as well [115].

Table 2.5 Various spectroscopic techniques available to study in situ chemical reactions, their potentials and limitations. These techniques allow to obtain information about catalysts under working conditions. Reproduced from [110, 111].

	Potentials			
Technique	**Oxidation State**	**Coordination**	**Quantitative**	**Limitations / Comments**
IR	+	+	+/-	• Vibrations of transition metals difficult to analyse
RS	+	+	+/-	• Not a sensitive process for low loadings
SAXS	+	+	-	• Average coordination numbers are obtained
EPR	+	+	+	• Only applicable to paramagnetic nuclei
UV-VIS	+	+	+	• Overlapping absorption bands complicate analysis • Quantitative measurements possible at low loadings
NMR	-	+	+	• Not applicable to all nuclei • Complicated measurements at higher T and P

Case Study on Hydrodesulfurisation Catalysts

In order to show the importance of *in situ* experiments and the positive impact they can potentially create, hydrodesulfurisation (HDS) catalysts are considered as a case study. Typical HDS catalysts are for example Co (or Ni)-promoted Mo/Al_2O_3. In the period preceding the mid 1980s, due to limited access to adequate *in situ* characterisation tools which could provide insight into the very complex structures under relevant sulfiding conditions, no universal agreement existed regarding the functionality of the promoters [116]. This is partially caused by the very complex catalytic behaviour of Co-Mo/Al_2O_3 particles and it has been reported that other catalysts with similar overall composition may exhibit very different promotional behaviours. Many models had been proposed in those times to explain such behaviours and the various effects of the promoters. However, without direct *in situ* evidence to back up, these proposals remained speculative.

Operando MES delivered the first detailed insight into the nature of the promoter atoms in the active sulfided state of the catalysts. It was concluded that typical catalysts may contain many different promoter phases. Using quantitative *in situ* MES phase analysis of several catalysts with varying activities, it was revealed that the HDS activity is dominated by the fraction of the promoter atoms present in a specific structure called Co-Mo-S. Therefore, the *in situ* insight allows the establishment of important fundamental structure-activity relationships [116].

The on-line studies into the nature of the active structures and their preparation properties leading to their formation have had a large impact on the developments of improved industrial catalysts. Before such important techniques were used, catalyst developments were achieved by trial-and-error approaches and around 1980 these catalysts were regarded by both the manufacturers and the refining industry as nearly optimised. Obviously, the opposite is true as the fundamental *in situ* information obtained has resulted in several major molecular design strategies and many improved catalysts have been introduced to the industry since. See Figure 2.16 to understand the developments during the past 70 years for HDS catalysts [117].

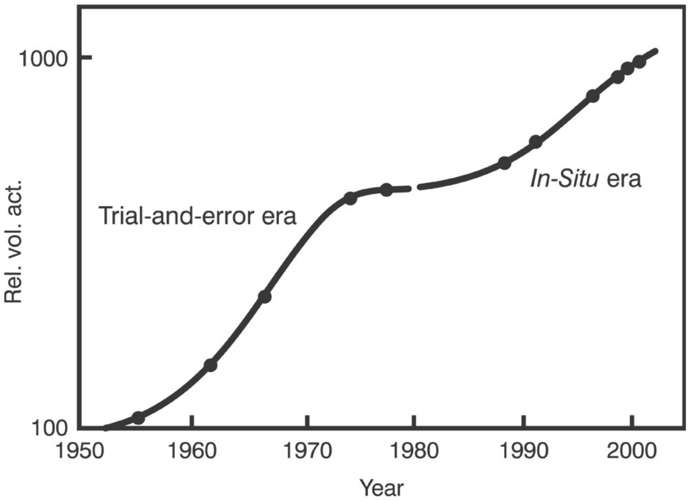

Figure 2.16 Developments in the catalytic activity of industrial HDS catalysts since 1950. The figure illustrates how in situ insights have resulted in improved catalysts based on new molecular design strategies. Reproduced from [117].

Price *et al.* reported the first imaging of conventional FT catalysts under operating conditions to gain insight on the behaviour of the Co active phase, the Ti modified support and the Re promoter. Their novel tomographic approached allowed to image Co catalysts *in situ* to study the crystalline phase and crystallite size during catalyst activation and operation, see Figure 2.17. The conditions were: the gas flow was 4 ml min^{-1} of 5% H_2/He and 2 ml min^{-1} of 5% CO/He at 200 °C and 2 bar (H_2:CO was 2:1 and 95% inerts.) Each pixel is 5 µm × 5 µm. This type of research is very scarce and this work shows the importance of *operando* microtomography to understand the evolution of chemical species [118].

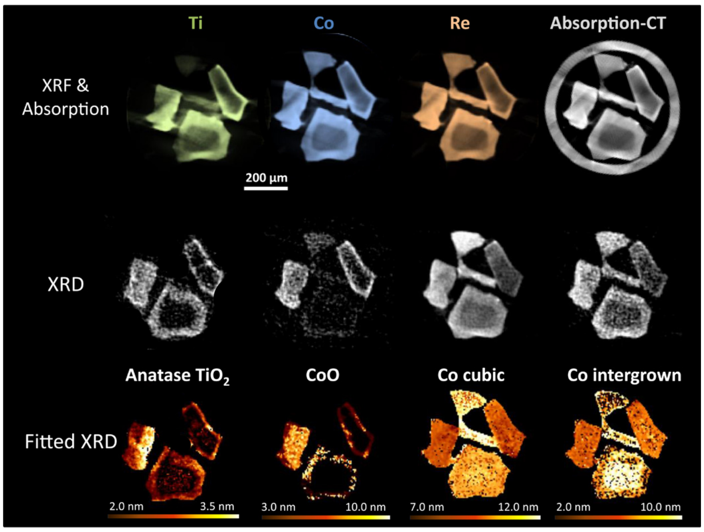

Figure 2.17 Conventional catalyst structure during FTS. (Top) XRF-CT reconstructions showing elemental distributions for the catalyst during FTS at 2 bar pressure. (Middle) XRD-CT reconstructions of the conventional catalyst revealing the phases present. (Bottom) Average crystallite size per pixel for each phase identified. Each pixel is 5 µm × 5 µm. Reproduced from [118].

2.9 Conclusions

FT is an attractive method of converting natural gas into liquid fuels in a more environmentally friendly manner. Nearly 100 years after discovering FTS, still no general consensus has been reached in the literature regarding the reaction. Also the kinetics and reaction mechanisms are generally poorly understood. Often, varied or even contradictory explanations are offered for the following phenomena: (i) role of water, (ii) complex phase behaviour affecting mass transport processes of reactants and products and (iii) effects of steps and defects on the surface of the catalysts and supports. Thus far, a systematic study dealing with the impact of water partial pressures on the steady-state activity and selectivity during FTS over Ru is not available in literature, especially not *in situ* under high temperature and pressure.

In order to be able to optimise the conversion, selectivities and catalyst design, FTS has to be further elucidated. NMR is a powerful technique that allows to study FT *operando* to shed light on the aspects mentioned above. This should be done in a purposely built reactor to characterise and quantify the FT reaction.

Chapter 3

NMR and MRI Theory

In this chapter the basic principles of NMR and MRI are introduced. In doing this, the underlying theory of NMR is discussed first using quantum mechanics followed by the vector model method. The basic theory discussions described in this chapter are covered in far more detail in works of Callaghan ([119]), Keeler ([120]), Levitt ([121]) and Gladden ([122]).

3.1 Fundamental Principles of NMR

3.1.1 Nuclear Spins

Most nuclei possess a spin, which generates a nuclear angular momentum $\boldsymbol{P}$. According to the classical picture of the atomic nucleus, assumed to be spherical, it rotates around an axis. The total angular momentum for isolated nuclei can be quantified using Planck's constant (h) and the angular momentum quantum number (I), see Equation 3.1. I is also termed the nuclear spin quantum number and is quantised in increments of $1/2$.

$$\boldsymbol{P} = \frac{h}{2\pi}\sqrt{I\,(I+1)} = \hbar\sqrt{I\,(I+1)} \tag{3.1}$$

$$\mu = \gamma \boldsymbol{P} \tag{3.2}$$

The spin angular momentum ($\boldsymbol{P}$) has associated with it a magnetic moment (μ); $\boldsymbol{P}$ and μ are proportional to each other via the gyromagnetic ratio (γ), which is a constant for each nuclide, see Equation 3.2. Nuclides with spin $I = 0$ have no nuclear magnetic moment. For most nuclides, the nuclear angular momentum vector $\boldsymbol{P}$ and the magnetic moment vector point in the same direction, i.e. they are parallel.

3.1.2 The Zeeman Splitting

If a nucleus with angular momentum $\boldsymbol{P}$ and magnetic moment μ is placed in an external, static magnetic field $\boldsymbol{B}_0$, the angular momentum takes up an orientation such that its component $\boldsymbol{P}_z$ along the direction of the field is an integral or half-integral multiple of $\hbar$, with $\hbar = h/2\pi$. This integral is m, which is the magnetic or directional quantum number and can take up any values $m = I, I\text{-}1, \ldots, \text{-}I$. There are $(2I+1)$ different number of possible orientations of the angular momentum and the magnetic moment in the magnetic field [123]. A nucleus has therefore $(2I+1)$ energy states, which are called Zeeman levels [124]. For the ^{1}H and ^{13}C nucleus, both of which have $I = \frac{1}{2}$, there are two energy values in the magnetic field corresponding to the m-values $+\frac{1}{2}$ and $-\frac{1}{2}$. The possible values I depend on the number of unpaired protons and neutrons in a nucleus. In order for a nucleus to be NMR active, $I \neq 0$.

In a macroscopic sample, nuclei distribute themselves between the different energy states in thermal equilibrium by Boltzmann statistics. In equilibrium, the populations of nuclear spins in the α- and β-state follow this Boltzmann distribution, see Equation 3.3, where N_α and N_β refer to the individual spin populations in the α- and β-energy state, and k_B and T are the Boltzmann constant (1.38×10^{-23} m^2 kg s^{-2} K^{-1}) and temperature respectively.

$$\frac{N_{\beta,-1/2}}{N_{\alpha,+1/2}} = \exp\left(\frac{-\Delta E}{k_\mathrm{B} T}\right) \tag{3.3}$$

For a hydrogen spin-½ nucleus, a Zeeman diagram is shown in Figure 3.1.

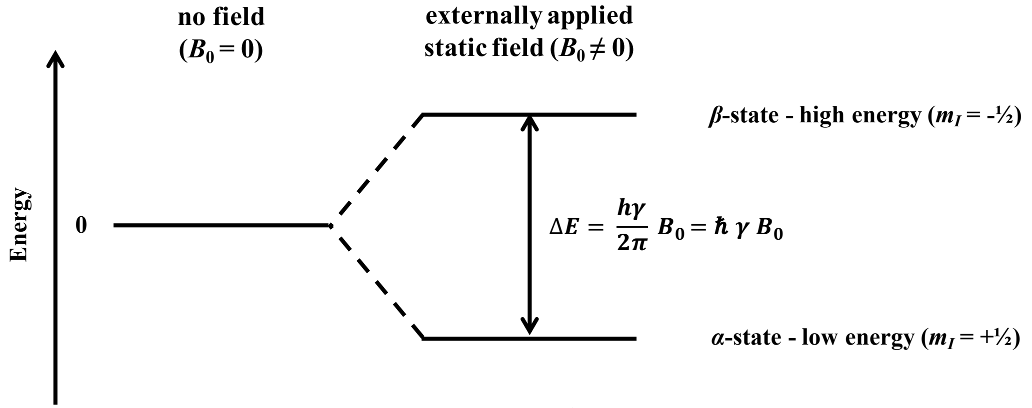

Figure 3.1 A Zeeman diagram for a nucleus with a 1/2-spin. The lower energy state has a slightly greater population than the higher energy state. Transition between both states is only possible if a photon with the appropriate associated energy is either absorbed or emitted.

According to Equation 3.3, the population in the lower energy state is slightly higher compared to the population of the higher energy state. In the absence of an external magnetic field, the magnetic moments of the individual nuclei are considered degenerate and are randomly oriented, resulting in a net moment across all nuclei ($\boldsymbol{M}_0$) of 0. If an external, static magnetic field is applied on the sample, the nuclear spins in the system will independently align along the z-direction. When all the individual spin magnetic moments are summated, a net macroscopic magnetisation is established. In addition, a net magnetisation vector $\boldsymbol{M}_0$, is created parallel to the direction of $\boldsymbol{B}_0$ by the randomly distributed spin states. The energy E of each state of a nucleus, which results from the interaction between the nuclear dipole moment and the magnetic field, is described in Equation 3.4:

$$E = -\mu \times \boldsymbol{B_0}. \tag{3.4}$$

If spins shift between the different states, the energy differences associated with these transitions are described by Equation 3.5. Equation 3.6 defines the precessional frequency of a nucleus, which is directly proportional to the field strength, in ν_0, which is the angular Larmor frequency at which the magnetisation precesses about $\boldsymbol{B}_0$ in a static magnetic field where h is Planck's constant (6.63×10^{-34} J s^{-1}) and γ is the gyromagnetic ratio (4257 Hz G^{-1} or 2.675×10^8 rad T^{-1} s^{-1} for ^{1}H).

$$\Delta E = h\nu_0 = \gamma \frac{h}{2\pi} \boldsymbol{B}_0 = \gamma \hbar \boldsymbol{B}_0 \tag{3.5}$$

$$\nu_0 = \frac{\gamma \boldsymbol{B}_0}{2\pi} \text{ [Hz] or } \omega_0 = \gamma \boldsymbol{B}_0 \text{ [rad s}^{-1}\text{]} \tag{3.6}$$

3.1.3 Bloch Vector Model

In NMR experiments, transitions are induced between different energy levels by subjecting the nuclei to irradiation of a superimposed, oscillating radio frequency (RF) field $\boldsymbol{B}_1$ of the correct quantum energy, i.e. with electromagnetic waves of the appropriate frequency ν_1 [125]. The term 'resonance' relates to the transitions, which only occurs when the frequency ν_1 of the electromagnetic radiation matches the Larmor frequency, ν_0. In a NMR experiment the evolution of $\boldsymbol{M}_0$ is followed after it is perturbed from its equilibrium by the RF pulse.

As mentioned earlier, in the Bloch model $\boldsymbol{M}_0$ is treated as a bulk magnetisation vector which results from the summation of the individual spin magnetic moments μ. This simplification allows for the motion of the magnetisation vector to be explained using classical mechanics, illustrated by Figure 3.2. In this approach, $\boldsymbol{M}_0$ can be described by μ as a vector relating to the torque $\mathbf{T}$ and $\boldsymbol{B}_0$:

$$\mathbf{T} = \mu \times \boldsymbol{B}_0. \tag{3.7}$$

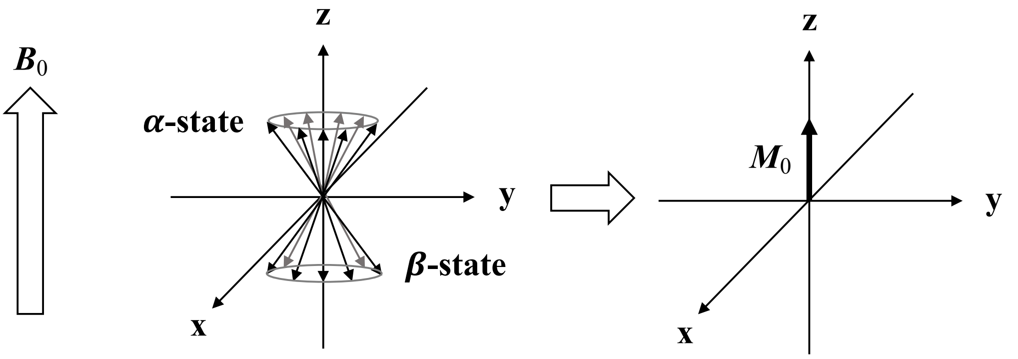

Figure 3.2 Illustration of the Bloch vector model simplification to obtain M_0.

Using the classical description method, torque can be related to the angular momentum, **L**:

$$\mathbf{T} = \frac{\mathrm{d}\mathbf{L}}{\mathrm{d}t}. \tag{3.8}$$

When including the spin angular momentum, this results in Equation 3.9:

$$\frac{\mathrm{d}\mathbf{P}}{\mathrm{d}t} = \mu \times \boldsymbol{B}_0. \tag{3.9}$$

Equation 3.10 is obtained by substituting Equation 3.2 into Equation 3.9 and taking into account the magnetic moment $\boldsymbol{M}$. It results in the same as equating the torque to the rate of the change of angular momentum in a magnetic field $\boldsymbol{B}$:

$$\frac{\mathrm{d}\boldsymbol{M}}{\mathrm{d}t} = \gamma \boldsymbol{M} \times \boldsymbol{B}. \tag{3.10}$$

For a static field $\boldsymbol{B}_0$, the solution to Equation 3.10 can be written as Equation 3.6, corresponding to the magnetisation precessing about $\boldsymbol{B}_0$ at ω_0.

3.1.4 The NMR Experiment

In order to detect signal during a NMR experiment, it is required that the spin precession contains a transverse plane component. This allows for some sort of motion of the net magnetisation vector to occur with respect to the receiver coil. By applying a magnetic field $\boldsymbol{B}_1$ in addition to the static $\boldsymbol{B}_0$ field, the spin state transitions are induced with the required ΔE. By transmitting a sinusoidal RF current through the transmitter coil, these transitions can be achieved. The net magnetisation vector of the spins precesses about both $\boldsymbol{B}_0$ and $\boldsymbol{B}_1$ when the RF pulse is applied. It is important that $\boldsymbol{B}_1$ oscillates in resonance

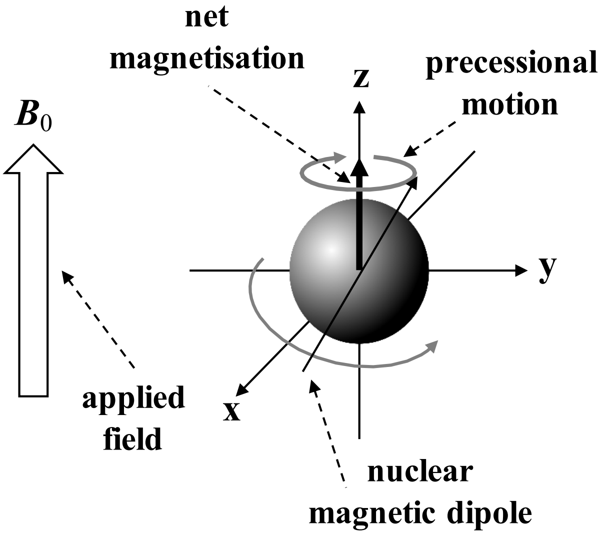

Figure 3.3 A spinning proton which has a nuclear magnetic dipole, which is not aligned but precesses about the applied magnetic field $\boldsymbol{B}_0$*.*

with the precession of the spins about $\boldsymbol{B}_0$, as this simultaneous precession about $\boldsymbol{B}_1$ can tip the magnetisation vector into the transverse plane.

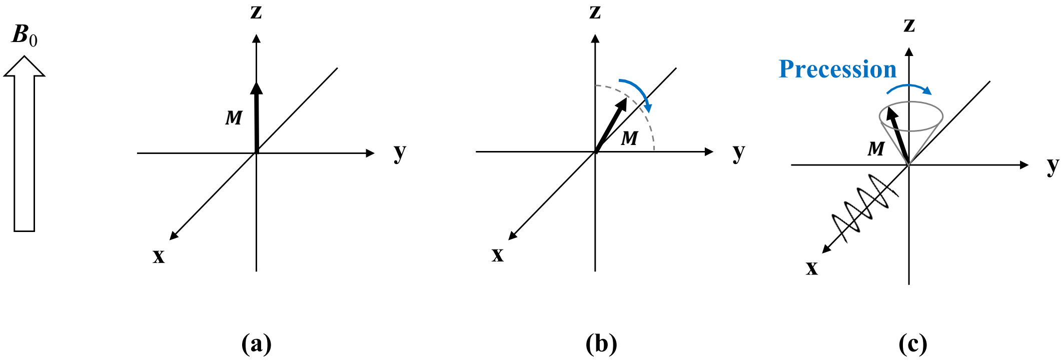

Figure 3.4 In a detection coil, which is placed around the sample, current is induced by the precessing magnetisation of the spin. This signal is amplified, recorded and termed the free induction decay.

The effective magnetic field, $\boldsymbol{B}_{\text{eff}}$, is described in Equation 3.11, which is a summation of both fields. If $\nu_1 = -\gamma \boldsymbol{B}_0$ is true, Equation 3.11 simplifies to $\boldsymbol{B}_{\text{eff}} = \boldsymbol{B}_1$, indicating that the system is on-resonance.

$$\boldsymbol{B}_{\text{eff}} = (\boldsymbol{B}_0 + \frac{\nu_1}{\gamma}) + \boldsymbol{B}_1 \tag{3.11}$$

3.1.5 Rotating Frame

When the oscillating magnetic field ($\boldsymbol{B}_1$), which rotates at the Larmor frequency (ν_0) in a perpendicular direction to the static magnetic field ($\boldsymbol{B}_0$) is applied, this results in the phenomenon called resonance. The complex behaviour described earlier whereby the net magnetisation vector of the spins precesses about both $\boldsymbol{B}_0$ at ω_0 and $\boldsymbol{B}_1$ at ω_1 is quite difficult to visualise. It can therefore by simplified by viewing it from a frame of reference rotating at the frequency ν_0 relative to the stationary laboratory frame. In that case the observer is rotated about the axis of the polarisation field at the Larmor frequency. This results in that $\boldsymbol{M}$ appears to precess only about $\boldsymbol{B}_1$ at a frequency of ν_1, illustrated by Figure 3.5. By convention, the rotating frame reference is denoted by axes: x', y' and z'.

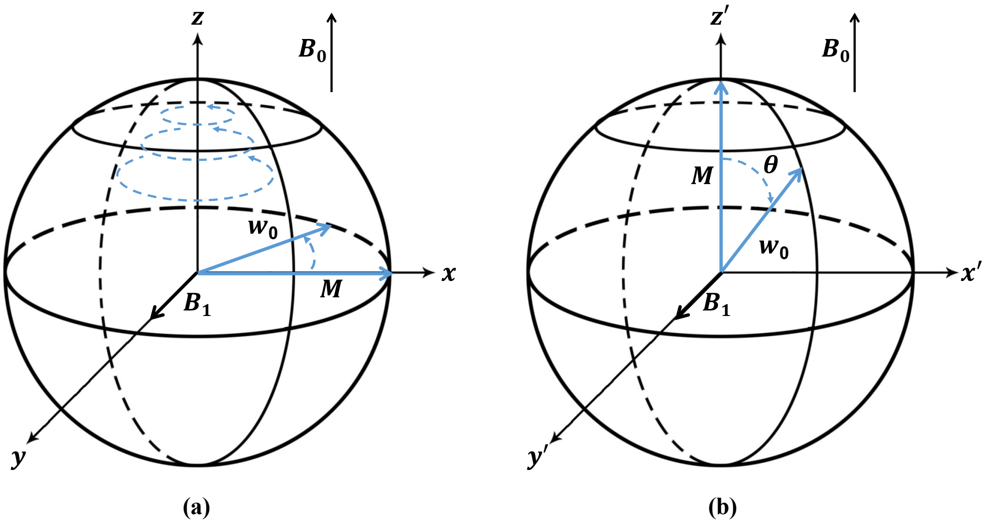

Figure 3.5 Demonstration whereby in (a) the rotation of the bulk magnetisation vector, $\boldsymbol{M}$, about $\boldsymbol{B}_0$ in the static laboratory frame of reference, after a 90° flip angle. Illustration of $\boldsymbol{M}$ in the rotating frame of reference (b) during the application of a RF pulse.

On applying $\boldsymbol{B}_1$, $\boldsymbol{M}_0$ will precess and rotate in $y'z'$ by the angle of θ, see Figure 3.5b. This depends on the duration of the RF pulse t_p and $\boldsymbol{B}_1$:

$$\theta = \omega_1 t_\mathrm{p} = \gamma \boldsymbol{B}_1 t_p. \tag{3.12}$$

3.1.6 Spin Excitation

A pulse which tips the magnetisation vector through some angle $0 < \theta < 180°$ allowing the magnetisation component to be shifted into the transverse plane, is known as an excitation pulse. A pulse that rotates the magnetisation vector by 180° is termed a refocusing pulse. These two commonly applied excitation pulses are shown in Figure 3.6.

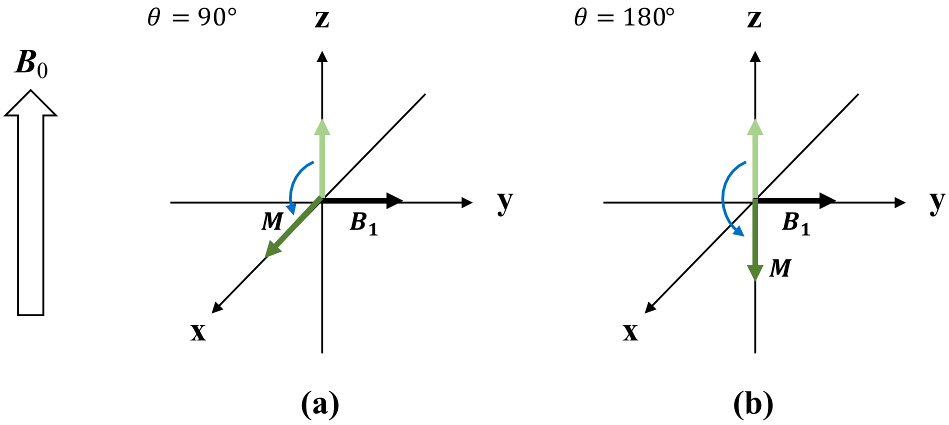

Figure 3.6 Illustration of (a) an excitation pulse of 90° and (b) a refocusing pulse of 180°.

3.1.7 NMR Signal Detection and Processing

After excitation of the spins by a RF pulse during a NMR experiment, the spins relax back to thermal equilibrium. Throughout these relaxation processes, receivers in the spectrometer detect the amplitude of the transverse magnetisation, while the longitudinal magnetisation is not measured as it does not induce any signal. This relaxation or decay process of the transverse magnetisation induces an oscillating RF current, which creates a signal registered by the coils in the receiver instrument. This signal is named the free induction decay (FID) and following Fourier transformation of this time-domain signal a frequency-based NMR spectrum is produced. By detecting and studying the changes occurring in the transverse magnetisation, information regarding the molecular environment of the various nuclei can be obtained. Being able to detect and analyse the FID is fundamental to performing any basic NMR measurement.

In the laboratory frame of reference and in the absence of relaxation effects, the precession may be described by Equation 3.13. This complex notation is used to describe the motion in a 2D plane. Equation 3.13 can also be rewritten as Equation 3.14.

$$M_{x,y}(t) = M_0 \cos(\omega_0 t) + \mathrm{i} M_0 \sin(\omega_0 t)\,. \tag{3.13}$$

$$M_{x,y}(t) = M_0 \exp(\mathrm{i}\omega_0 t) \tag{3.14}$$

As $\boldsymbol{M}$ precesses about $\boldsymbol{B}_0$, it is detected by the laboratory spectrometers by heterodyning (frequency converting) the signal using two different reference signals that are 90° out of phase with each other. This will create two orthogonal components, S_x and S_y, which are proportional to the two orthogonal magnetisation components M_x and M_y. During the processes of heterodyning, the ‘real’ and ‘imaginary’ transverse signal components are sampled separately. This process is called quadrature detection whereby only an offset frequency $\Delta\omega = \omega_0 - \omega_r$ has to be taken into account. This allows the acquired signal to be converted from the laboratory frame of reference to a rotating frame of reference. The NMR signal can therefore be given by Equation 3.15, where ϕ_r is an arbitrary receiver phase:

$$S(t) \propto M_0 \exp\left(\mathrm{i}\phi_\mathrm{r}\right) \exp\left(\mathrm{i}\Delta\omega t\right). \tag{3.15}$$

The resonant frequencies occurring in a sample can be transformed from the time-domain to the frequency-domain via a Fourier transform:

$$S(\omega) = \int_{-\infty}^{+\infty} S(t) \exp\left(\mathrm{i}2\pi\omega t\right) \mathrm{d}t. \tag{3.16}$$

During a pulse-acquire experiment, one single excitation leads to the magnetisation signal decaying exponentially. The phase corrected Fourier transform of $S(t)$ yields peaks at sample resonant frequencies which is a NMR spectrum. Figure 3.7 illustrates a schematic of a FID and its associated NMR spectrum.

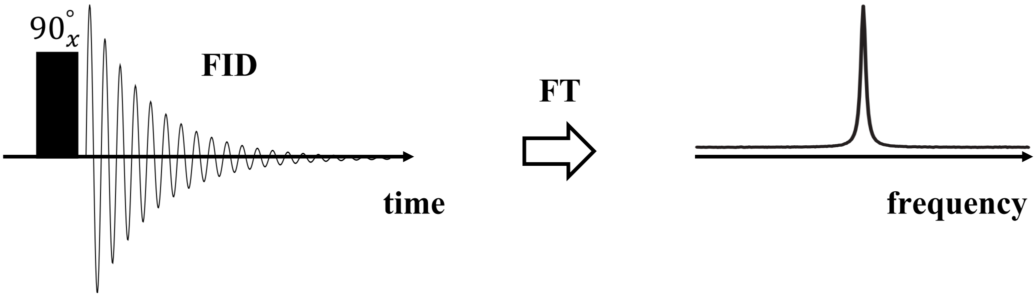

Figure 3.7 A pulse sequence diagram depicting a pulse-acquire experiment which results in the formation of a FID. Via a Fourier transformation, this signal can be transformed from the time-domain to the frequency-domain.

The real part of the Fourier transform is a Lorentzian absorption lineshape whereas the imaginary part is a Lorentzian dispersion lineshape, see Figure 3.8. The intensity of these real peaks is proportional to the number of NMR active nuclei resonating at that frequency, also termed the spin density. The lineshapes are centred around a frequency of $\frac{\Delta\omega}{2\pi}$ Hz, with a full width at half maximum (FWHM) of $\frac{1}{\pi T_2^*}$.

The dwell time (dw) is a discrete time interval at which the time domain signal is sampled and digitised. During this digitisation process, the digitiser must sample at least two points per wavelength to correctly acquire the oscillating signal, according to the Nyquist-Shannon sam-

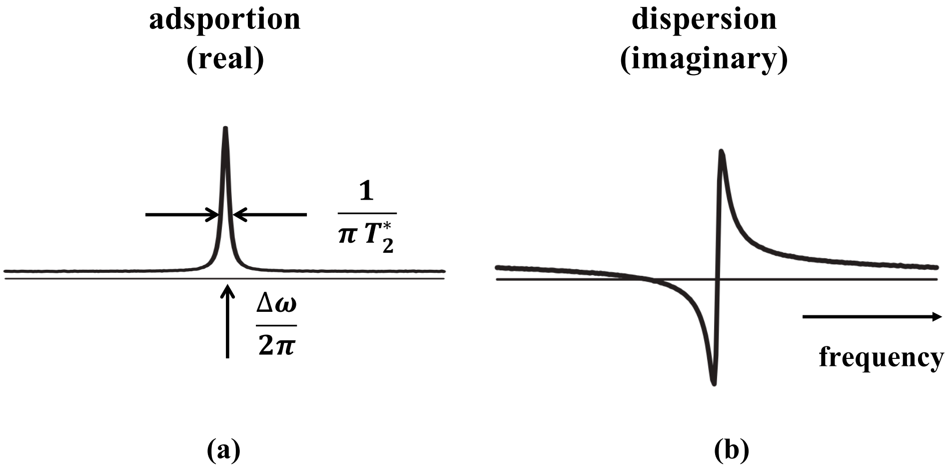

Figure 3.8 The (a) real and (b) imaginary parts of the spectrum.

pling theory [126]. The sweep width (sw) is the frequency range of the Fourier transformed spectrum which is limited by the digitisation rate:

$$sw = \frac{1}{2\ dw}. \tag{3.17}$$

Any signal with a frequency greater than the sw will be sampled incorrectly and as a consequence will appear in the NMR spectrum at a lower frequency than its actual value. This peak is ‘folded back’ or ‘aliased’ into the spectrum and this should be avoided.

3.1.8 Chemical Shift and Sensitivity

NMR is a very powerful technique for chemical analysis. The NMR spectral chemical sensitivity results from resonance frequency differences for nuclei located in different chemical environments, due to differing chemical bonds. In a molecule, the atoms probed by NMR have different chemical environments that arise due to their position and number of electrons. Neighbouring electrons ‘shield’ nuclei, altering local magnetic fields and resulting in signal oscillating at an offset frequency $\Delta\omega$. These differences lead to minor changes, in the order of parts per million (ppm), in the Larmor frequency which can be detected by NMR, especially by instruments at high field strength.

$$\delta_{\text{ppm}} = \frac{\nu - \nu_{\text{TMS}}}{\nu_{\text{TMS}}} \times 10^6 \tag{3.18}$$

Chemical shift (δ) is defined relative to a reference molecule, usually tetramethylsilane (TMS), where ν is the resonance frequency of the nucleus at interest and ν_{TMS} the TMS resonance frequency, see Equation 3.18. In this thesis, the chemical shift in ^{1}H spectra are referenced to TMS. The chemical shifts lead to different NMR spectral peaks, which form a fingerprint or unique signature for molecular structures.

3.1.9 Phase Cycling and Signal-to-Noise

Phase cycling is a technique used to reduce NMR artefact formation during acquisition. It can also suppress spurious signal that arises from irregularities in the hardware. In order to achieve phase cycling, the pulse and receiver phases are varied during multiple repeat experiments while averaging the signal. This will allow artefacts to cancel themselves out. Phase cycling is very powerful and hence is especially used in diffusometry experiments as well as in many spectroscopy and imaging measurements [127]. In a typical phase cycling experiment, 4 or 8-step phase cycles are used. However, to further explain how phase cycling can be used to correct artefact formation, only a 2-step phase cycle is discussed here. Generally speaking, an artefact appears to be a high intensity pixel or peak after Fourier transformation. This could be formed by the real and imaginary components of the signal when acquired with non-zero baselines. By using the 2-step phase cycle described in Table 3.1, the averaged signal is acquired with a 180° offset in both the pulse and receiver phases [128]. As a result, in between the two scans, the signal is added constructively whereas the baseline is cancelled out between the two acquisitions.

Table 3.1 2-step phase cycle to illustrate the removal of an artefact.

Scan	**Pulse Phase**	**Receiver Phase**
1	0°	0°
2	180°	180°

In the process of phase cycling, the acquisition of the signal is repeated several times. Moreover, by repeating this acquisition, the quality of the signal, also known as the signal to noise ratio (SNR) can be enhanced. The SNR is defined by Equation 3.19, where the mean of the actual signal (μ_{signal}) is divided by the standard deviation of the noise (σ_{noise}) [129]. During the NMR experiments, the signal is subject to several factors that can perturb it by creating noise and therefore reduce the SNR. Such factors could be (i) thermal motion effects, (ii) electrical background interference and (iii) imperfection of the electronic components.

$$\mathrm{SNR} = \frac{\mu_{\text{signal}}}{\sigma_{\text{noise}}} \tag{3.19}$$

$$\mathrm{SNR} \propto n\ T^{-1}\ \gamma_E\ \gamma_D^{\frac{3}{2}}\ B_0^{\frac{3}{2}}\ t^{\frac{1}{2}}\ NS^{\frac{1}{2}} \tag{3.20}$$

The relationship in Equation 3.20 lists the many factors that influence the SNR [130]. It is governed and proportional to the spin density (n) present in the sample, to the temperature (T), to the gyromagnetic ratios of the excited and detected species (γ_E and γ_D respectively), to the magnetic field strength ($\boldsymbol{B}_0$), to the total acquisition time (t) and to the total number of scans (NS) [131]. As discussed in Section 3.1.2, the signal intensity is proportional to the magnitude of the bulk magnetisation which itself is related to the difference in population between the energy states α and β. If the energy gap between the two states becomes larger, the population difference becomes more significant. Therefore, with a stronger $\boldsymbol{B}_0$ and a greater γ ratio, the energy gap increases hence leading to a higher SNR. However, using a higher field strength comes at the expense of higher $\boldsymbol{B}_0$ and $\boldsymbol{B}_1$ heterogeneity and capital expenditure for hardware purchase.

A higher spin density (n) could be achieved by boosting the filling factor by increasing the sample volume in the RF probe. Moreover, probing nuclei with a higher gyromagnetic ratio is an alternative but in this study only ^{1}H was studied. Finally, at a fixed $\boldsymbol{B}_0$ field strength, the SNR can be enhanced by repeating the experiment several times to increase NS. The signal scales with NS, whereas the added random noise scales with a root mean squared amplitude of $\sqrt{NS}$. However, restrictions on the experiment time usually limits the number of experiment repeats that one can achieve, especially for species with a long T_1 value. Therefore, during NMR acquisition it is crucial to optimise these parameters above to maximise signal obtained compared to noise acquired in the shortest time period.

3.2 Relaxation

Spins present in a nuclear spin system excited by a RF pulse in the $\boldsymbol{B}_1$ field, will undergo relaxation processes. During the relaxation processes, the excess energy of the spins is redistributed to the surroundings and the magnetisation returns to its equilibrium state along the $+z$-axis. The two main relaxation processes are *spin-lattice* and *spin-spin relaxation* and will be discussed in terms of the Bloch vector model in this Section. The two time constants describing both processes are characteristic for any given system, as the time constants are influenced by molecular composition, motion and structure.

3.2.1 Spin-Lattice Relaxation Time

The *spin-lattice relaxation*, also known as *longitudinal relaxation time* T_1, occurs along the direction of the applied magnetic field. The magnetisation parallel to the applied field is also termed longitudinal. During a simple NMR experiment, the equilibrium of a spin system is perturbed by a RF pulse and as a consequence the macroscopic magnetisation vector $\boldsymbol{M}_0$ (or M_z initially) can either be rotated by a 90°_x pulse into the y-axis direction, or by a 180°_x pulse into the -z direction [123]. After this perturbation, the equilibrium condition $M_z = M_0$

reasserts itself as the spin populations return to their Boltzmann distribution values. The rate at which this equilibrium is recovered, is determined by T_1. This relaxation rate is most influenced by physical properties of the sample, so therefore a study of relaxation phenomena may lead to information on these properties.

The time constant T_1 is typically in the range of milliseconds to tens of seconds for ^{1}H in the liquid phase at ambient temperatures whereas for gases the T_1 tends to be in the order of tens to hundreds of seconds. In order to decrease the recovery time of molecules that naturally relax very slowly, systems can be doped using paramagnetic ions. These ions have valence bands which have a permanent magnetic dipole. The strong interaction between the ions and the tumbling spins can strongly decrease the relaxation times. This spin-lattice relaxation is associated with a spin energy change. The energy initially absorbed by the spin system is given up to the surroundings, i.e. crystal lattice, causing its thermal energy to increase. This spin-lattice terminology dates from the early days of NMR and is misleading as it is also used for NMR in liquids and gases.

To determine the spin-lattice relaxation time T_1, an inversion recovery experiment is performed. The pulse sequence consists of a 180°_x — τ — 90°_x — FID, shown diagrammatically in Figure 3.9. The first 180°_x pulse inverts the equilibrium $\boldsymbol{M}_0$ into the -z direction, and this pulse subjects the system to the most severe disturbance from equilibrium. During the variable pulse delay, τ, the system is allowed to relax [132]. The subsequent 90°_x pulse rotates the magnetisation component M_z into the direction of the y-axis, thus giving a transverse magnetisation component M_y, which can be observed. The double-headed arrow in the sequence in Figure 3.9 indicates that the pulse sequence used in the experiment is repeated, but with increasing values of τ, described in the Variable Delay (VD) list.

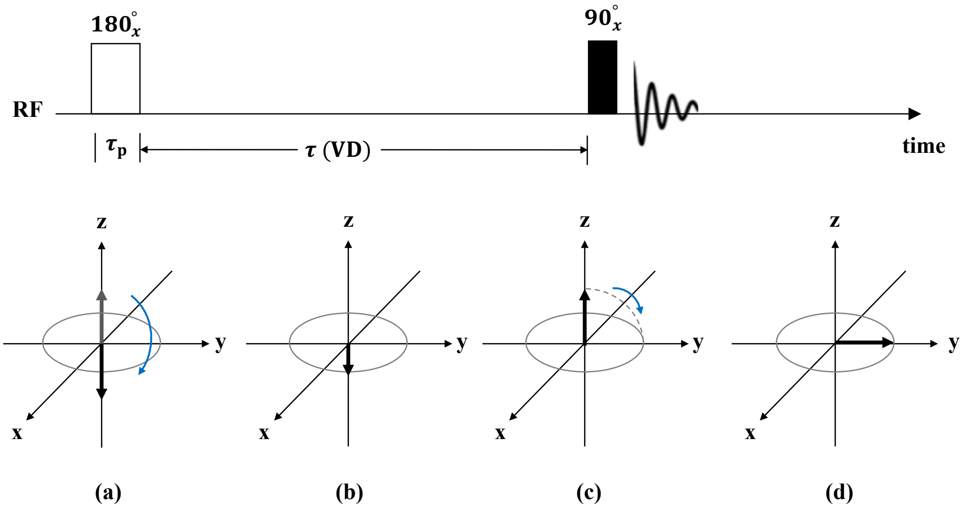

Figure 3.9 The pulse sequence for determining the ^1H NMR spin-lattice relaxation time T_1 by inversion recovery. Illustration of the spin isochromats is giving.

Bloch described the process of T_1 relaxation by the differential Equation 3.21. Integration of this equation and using the boundary condition that at $t = 0$, $M_z = -M_0$, Equation 3.22 can be derived [123]. Finally after some rearrangement, Equation 3.23 can be obtained. From Equation 3.23 it may be concluded that the shape of the plot where the z-magnetisation approaches equilibrium will have an exponential shape. A plot of M_z as a function of time t can be fitted to Equation 3.23 to give a value of T_1. Equilibrium in M_z is usually established ($\geq 99.33\%$) after $t = 5T_1$.

$$\frac{\mathrm{d}M_z}{\mathrm{d}t} = -\frac{M_z - M_0}{T_1} \tag{3.21}$$

$$M_0 - M_z = 2M_0 \exp\left(-\frac{t}{T_1}\right) \tag{3.22}$$

$$\frac{M_z(t)}{M_0} = 1 - 2\exp\left(-\frac{t}{T_1}\right) \tag{3.23}$$

3.2.2 Spin-Spin Relaxation Time

The *spin-spin relaxation* or *transverse relaxation time* T_2 gives information about the dynamics of the molecules. It describes the loss of phase coherence in the magnetisation in the transverse plane. It determines how rapidly the transverse magnetisation components M_x and M_y decay. For example after a 90°_x pulse, the z-component of the macroscopic magnetisation vector becomes equal to 0 as the M_z has been converted into a transverse magnetisation component M_y [123]. Subsequently, the precessing nuclear spins initially aligned, will start to lose their phase coherence and start precessing at slightly different frequencies. This homogeneous decay is irreversible as it cannot be recovered. The typical relaxation time T_2 for bulk liquids is in the order of magnitude of several seconds. On the contrary, the typical transverse relaxation time for large molecules in liquids or solids can range in the microseconds-milliseconds scale [121].

To measure the true T_2 of a sample, is it important to counteract the dephasing of the transverse magnetisation due to the chemical shift and $\boldsymbol{B}_0$ inhomogeneities. By running a so-called Hahn spin echo pulse, it is possible to refocus the dephased transverse magnetisation. During a spin echo, the inhomogeneous section of the signal decay is reversed allowing for the homogeneous decay constant T_2 to be measured [121]. The spin echo pulse sequence consists of a 90°_x — τ — 180°_y — FID, shown diagrammatically in Figure 3.10 and is also known as a Hahn echo.

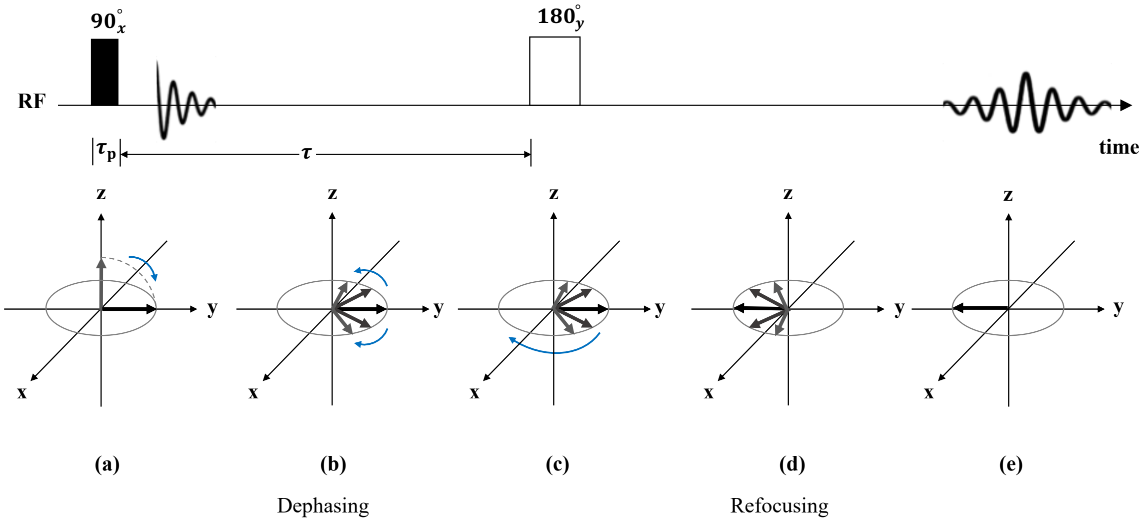

Figure 3.10 The pulse sequence for determining the ^{1}H *NMR spin-spin relaxation time* T_2 *using a spin echo experiment. This pulse sequence is also known as a Hahn echo. Illustration of the spin isochromats is giving.*

The transverse relaxation can be described using the differential Equation 3.24, part of the Bloch equations. Integration of this differential equation and solving for M_y results in Equation 3.25. Using the boundary condition that at time $t = 0$, $M_y = M_0$ and taking the logarithm, Equation 3.26 can be derived. This equation predicts that the transverse magnetisation will decay exponentially to its equilibrium value of zero. If a semi-logarithmic scale is used, this will result in a straight line if the decay is single-exponential [123].

$$\frac{\mathrm{d}M_{x,y}}{\mathrm{d}t} = -\frac{M_{x,y}}{T_2} \tag{3.24}$$

$$M_{x,y} = M_0 \exp\left(-\frac{t}{T_2}\right) \tag{3.25}$$

$$\ln\left(\frac{M_{x,y}(t)}{M_0}\right) = -\frac{t}{T_2} \tag{3.26}$$

The spin-spin relaxation is characterised by the two time constants T_2 and $T_2^{'}$. The latter represents the relaxation of transverse magnetisation components resulting from any magnetic field inhomogeneities, which are also known as background gradients. $\Delta \boldsymbol{B}_0$ represents the magnetic field variation which will lead to differences in the local Larmor frequency of $\Delta\omega = \gamma\Delta\boldsymbol{B}_0$. Spins will therefore precess at different rates with different transverse relaxation rates, which is characterised by the $T_2^{'}$. Therefore, the overall apparent ${T_2}^{*}$ decay is defined in Equation 3.27. ${T_2}^{*}$ relaxation can affect the attenuation of the FID and as a result a peak in the Fourier transformed spectrum can be broadened by ${T_2}^{*}$ relaxation. The ${T_2}^{*}$ can be obtained from the FWHM of that peak, $\Delta\nu$, see Equation 3.28.

$$\frac{1}{T_2^*} = \frac{1}{T_2} + \frac{1}{T_2'} = \frac{1}{T_2} + \gamma \Delta \boldsymbol{B}_0 \tag{3.27}$$

$$T_2^* = \frac{1}{\pi \Delta \nu} \tag{3.28}$$

Phase coherence is inherently lost for $t > 2\tau$ in a simple Hahn spin echo. In an experiment where significant diffusion takes place, the refocusing in a Hahn spin echo pulse sequence is not complete which can lead to a fast signal decay and thus a T_2 underestimation. An important modification to this sequence, made by Carr-Purcell, has become the standard sequence used in modern NMR to obtain the true T_2 of a system. This sequence is termed a Carr-Purcell-Meiboom-Gill (CPMG) sequence, see Figure 3.11.

To obtain a CPMG, the Hahn spin echo is repeated using extra 180°_y pulses to obtain several echoes [132, 133]. This sequence makes use of the fact that the ${T_2}^*$ dephasing is reversible by applying a train of 180°_y refocusing pulses. In the CPMG sequence, additional 180° RF pulses are used to: (i) avoid the cumulative effects of small turn angle errors and (ii) to obtain the full T_2 decay process. Using this method also has significant benefits in terms of signal averaging, as multiple trains lead to SNR enhancement.

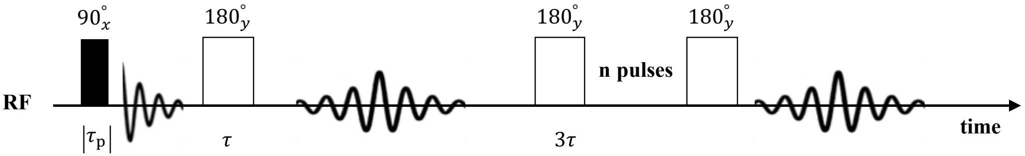

Figure 3.11 The pulse sequence for determining the ^1H NMR spin-spin relaxation time T_2 by a CPMG pulse sequence.

Stimulated Echoes

Another method to measure T_2 is by using another type of echo train: the stimulated echo (STE). The pulse sequence consists of a 90°_x — 90°_x — t_{store} — 90°_x — FID, shown diagrammatically in Figure 3.12. In addition to the first 90°_x pulse, two additional 90°_x pulse are used. After the initial 90°_x pulse, the z-component of the macroscopic magnetisation vector becomes equal to 0 as the M_z has been converted into a transverse magnetisation component M_y. From this point onwards, the spins undergo ${T_2}^*$ relaxation for a τ time period. The second 90°_x pulse projects the magnetisation in the zx plane. This enables the magnetisation to be stored in the $-z$-axis direction for a t_{store} period, where the T_2 and ${T_2}^*$ processes are 'frozen' but T_1 occurs. Finally, the third and final 90°_x pulse reverts the magnetisation back into the transverse plane, which reverses the spin phases after the second and third 90°_x pulse and allows for the stimulated echo to arise.

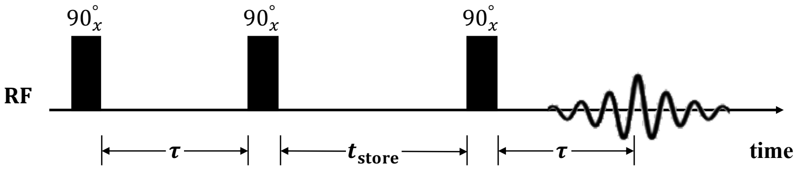

Figure 3.12 The stimulated echo pulse sequence where refocusing of the spin phases is achieved by two extra consecutive 90°pulses.

3.2.3 Relaxation Time Constants and Correlation Time

Both spin-lattice and spin-spin relaxation are caused by the variation of the local magnetic fields experienced by the spins which cause nuclei to flip between their available spin states. For the spin-lattice process, the relaxation rate is dependent on transverse local fields that oscillate at the resonance frequency ω_0 which can flip the transverse magnetisation to the z-axis and contribute to the longitudinal relaxation. For the spin-spin process, the relaxation rates are subject to the oscillating longitudinal local fields leading to the transverse relaxation. As the transverse local fields also destroy the transverse magnetisation, they cause the transverse relaxation times to shorten, hence, $T_2 \leq T_1$.

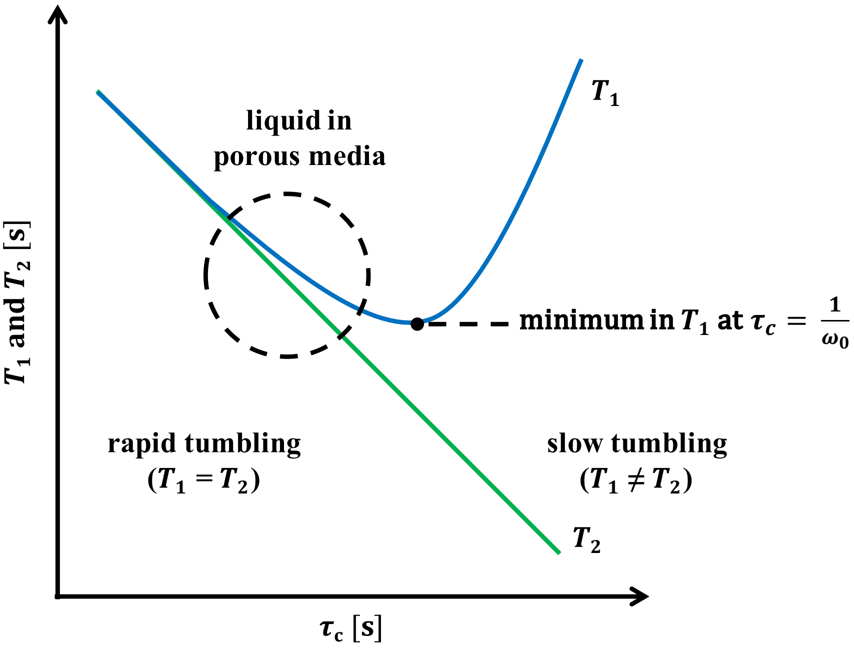

Figure 3.13 Relationship between the relaxation times T_1 and T_2 and the rotational correlation constant τ_c for fast ($T_1 \approx T_2$) and slow tumbling systems ($T_1 \neq T_2$).

For every nuclear spin in the system, the local field is different and therefore the precession frequency is slightly altered for each individual spin over time. The local field for each spin is the summation of the external field and the magnetic moment generated by other neighbouring spins. The rotational and tumbling motion of molecules affect their local field which will lead to an oscillating magnetic moment. The time characterising this motion is known as the rotational correlation time (τ_c) which corresponds to the average time needed for a molecule to achieve a rotation of one radian. Both T_1 and T_2 are dependent on τ_c, see Figure 3.13, according to the Bloembergen-Purcell-Pound (BPP) theory [134]. The T_1 dependence on τ_c shows a minimum at $\tau_c = \frac{1}{\omega_0}$ which also denotes the boundary between the rapid and slow tumbling region. This minimum arises when the transverse local fields are on resonance with the spins and also oscillate at the Larmor frequency. At this point, the energy exchange between the spins and their surrounding environment is most efficient, which results in the lowest T_1 time.

Moreover, for decreasing τ_c, the relaxation time T_2 increases. The T_2 constant increases as the dipolar interactions contribute to the local field fluctuations and hence enhances the transverse relaxation. Finally, in the rapid tumbling region, the T_1 and T_2 are approximately equal with the same dependence on τ_c. As the motion slows down and τ_c increases, the T_1 and T_2 values diverge whereby T_1 can significantly surpass T_2 at large τ_c.

3.3 Pulsed-Field Gradient NMR

A very powerful tool that can provide information about the degree of molecular mobility and motion of the species studied is PFG NMR. All NMR molecular self-diffusion measurements are based on the fact that the diffusion properties of a system can be calculated from the echo attenuation, a Gaussian function, if the amplitude and the duration of the steady magnetic field gradient are known [135]. Applying a magnetic field gradient $\mathbf{g}$ creates the Larmor frequencies of the spins to spatially vary with $\mathbf{r}$:

$$\omega(\mathbf{r}) = \gamma(\mathbf{B}_0 + \mathbf{g}\cdot\mathbf{r}). \tag{3.29}$$

In the case of the gradient $\mathbf{g}$ being applied for a duration of time δ, the phase (ϕ) of the precessing spins also varies with position according to:

$$\phi(\mathbf{r}) = \gamma\delta\mathbf{g}\cdot\mathbf{r}. \tag{3.30}$$

This associates all the spins with a specific phase and position, hence the spins become 'tagged'. After this point, the gradient is disabled and over an observation time period (Δ), the spins are allowed to diffuse. In order to measure the motion of the spins, the magnetisation is flipped by 180° and another gradient pulse with the same duration and intensity as the first one but in the opposite direction is applied. At this point, spins have either undergone motion and moved (to new position $\mathbf{r}'$) or they did not experience any motion at all (same $\mathbf{r}$). For the latter case, the second gradient pulse will rewind the phase gained by the spins during the first pulsed-field gradient, similar to the spin echo. This will result in a zero net phase shift. However, if the spins did move to position $\mathbf{r}'$, the phase unwinding will not be identical and the refocussing will be incomplete. Hence the spin will have a net phase shift equivalent to Equation 3.31.

$$\phi_{\text{net}}(\mathbf{r}) = \gamma\delta\mathbf{g}\cdot(\mathbf{r}-\mathbf{r}') \tag{3.31}$$

This net phase offset leads to the dephasing of the bulk magnetisation and hence signal attenuation is observed. Therefore, signal attenuation is related to the random motion of spins in a sample, which is illustrated in Figure 3.14. Finally, PFG NMR can be used to study both coherent (flow) and incoherent (diffusive) processes but in this work only diffusion processes were monitored.

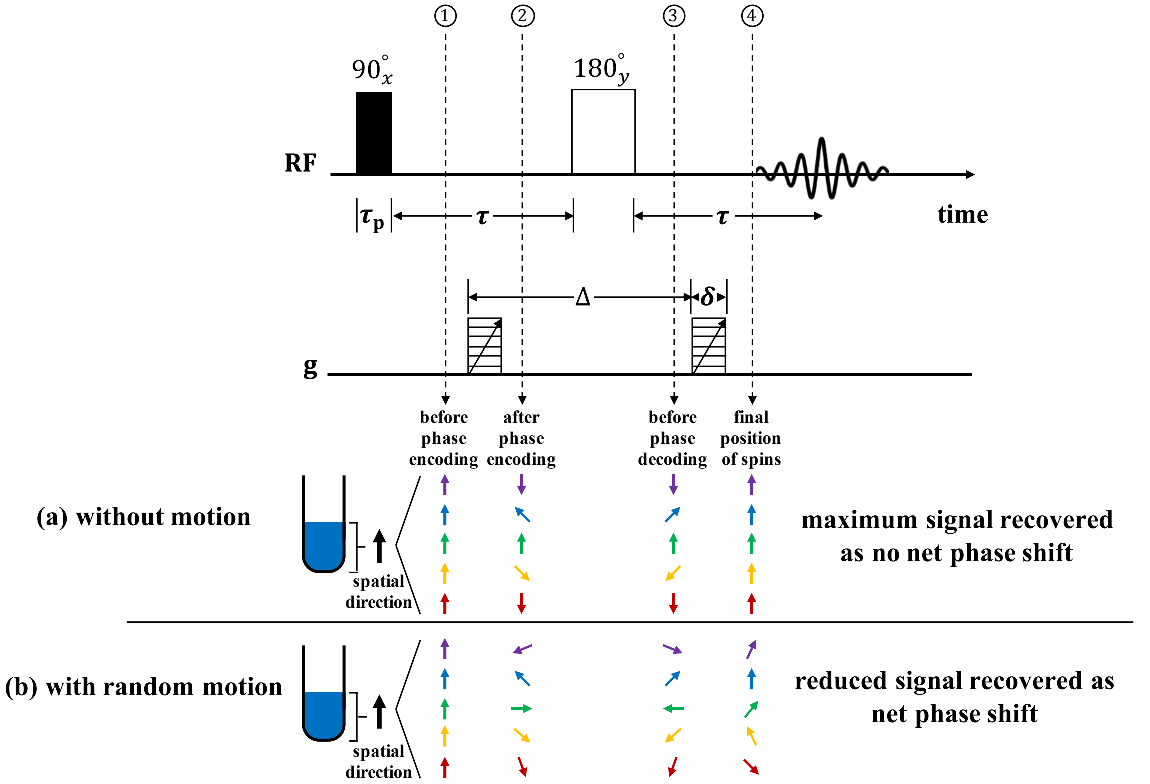

Figure 3.14 The principles of PFG NMR illustrated with (a) no motion observed and (b) when random motion is detected.

Moreover, PFG provides a direct tool to determine the molecular root mean squared displacement (RMSD) in a given time interval. Molecular, unidirectional displacement in a given gradient direction z is represented by the Einstein Equation, see Equation 3.32:

$$\mathrm{RMSD} = \sqrt{\overline{z^2(t) - z_0^2}} = \sqrt{2Dt} \tag{3.32}$$

$$\frac{S}{S_0} = \exp\left(-\gamma^2 g^2 \delta^2 (\Delta - \frac{\delta}{3}) \times D\right) = \exp\left(-b \times D\right). \tag{3.33}$$

Equation 3.33 represents the well-known Stejskal-Tanner (ST) equation for attenuation of the echo amplitude. The variables in this Equation are described in Table 5.2

Table 3.2 List of quantities with their description and unit appearing in the ST equation.

Symbol	Description	Unit
$^{S}/_{S_0}$	The echo signal intensity	[-]
γ	Nuclear gyromagnetic ratio	[rad T^{-1} s^{-1}]
g	Strength of applied magnetic field gradient	[G cm^{-1}]
δ	Gradient pulse duration	[s]
Δ	Observation time	[s]
D	Bulk self-diffusion of spins	[m^2 s^{-1}]
b	b-factor	[s m^{-2}]

In a typical set of experiments, either g or Δ is varied to acquire the diffusion-weighted spectra, while δ is kept constant. Stejskal and Tanner first demonstrated that PFG experiments can be used to determine unrestricted, self-diffusion coefficients for bulk liquids [136]. Their relationship only applies to unrestricted ordinary diffusion encountered in bulk liquid samples and does not necessarily hold for complex diffusion processes that may occur within porous media. Non-linearity behaviour of the ST plot makes interpretation of data complex as this behaviour is dependent on the physical properties of the porous medium. This non-linearity can occur for several reasons, for example when *restricted diffusion* is taking place. Such behaviour may be observed when the characteristic length scale of the porous media is smaller or on the same order of magnitude as the diffusion path length [137].

The PFG method has two major benefits: (i) the maximum possible signal is recovered in the absence of relaxation effects and (ii) chemical shifts are refocused at the echo. Finally, the important characteristic for this sequence is that the magnetisation is stored in the longitudinal form, to allow any type of motional or exchange process to take place [121].

3.3.1 PGSE

In Figure 3.15, a pulsed-gradient spin echo (PGSE) pulse sequence is shown. It involves a hard 90°_x RF pulse, rotating all of the vectors in the y-direction. The gradients are switched off during the RF and acquisition. The 180°_y pulse is to reverse the effect of the previous gradient pulse. If any motion occurred in the observation time Δ, then the nuclear spins will exhibit a net phase offset and their contribution to the spin echo will be reduced due to the incomplete refocusing of the phase-encoded spins. The gradients cause the spins, which are in different positions within the sample, to precess differently, thereby enhancing their diffusive dephasing. This will ultimately lead to various precession rates and the refocusing will be incomplete. This results in a decreased spin echo intensity.

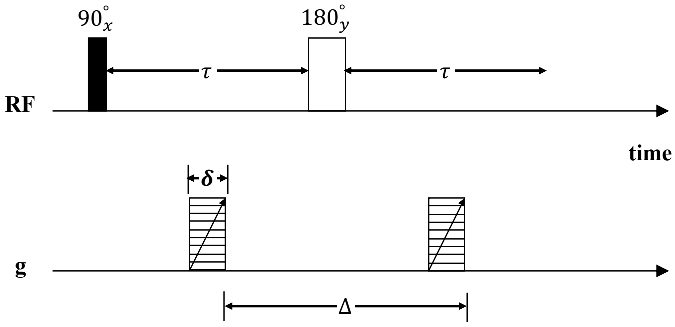

Figure 3.15 The pulse sequence for determining the diffusion coefficient by a simple PFG experiment.

The rate constant determining the signal decay can be used as an estimation for the diffusion constant. The signal attenuation decays as a function of the interval between the gradient pulses. If the experiments are performed and repeated with gradient pulses in the three different directions, this gives the possibility to estimate D_x, D_y and D_z.

3.3.2 PGSTE

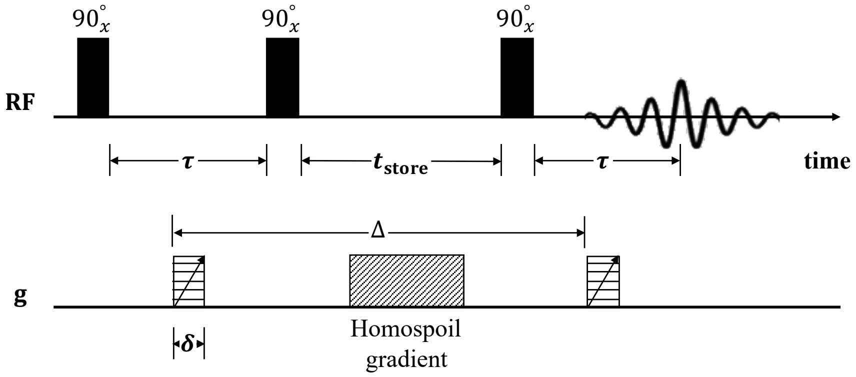

Figure 3.16 The pulse sequence used during PGSTE experiments.

The PGSE pulse sequence discussed previously can suffer from signal attenuation and reduced SNR due to T_2 relaxation. If a sample has a short T_2 value, it is more common to use a pulsed-gradient stimulated echo (PGSTE) sequence, see Figure 3.16 [138, 139]. With the PGSTE sequence, the $\mathbf{180^\circ_y}$ pulse is replaced by two additional $\mathbf{90^\circ_x}$ pulses. The system undergoes T_1 relaxation in the z-direction during the storage time t_{store} where the signal attenuation due to relaxation is less significant and longer observation times are possible.

An additional advantage of this type of experiment is that the magnetisation undergoes less precessional dephasing caused by residual gradients. The homospoil gradient is applied to destroy any residual magnetisation in the transverse plane.

3.3.3 APGSTE

In Figure 3.17, the alternating pulsed-gradient stimulated echo (APGSTE) pulse sequence is shown [140]. This sequence is very valuable when studying highly heterogeneous systems, as the magnetic susceptibility of the sample can produce local magnetic field gradients. This sequence is therefore often used for systems where $T_2 \ll T_1$, which is common in porous media. The APGSTE sequence substantially reduces the effect of background gradient, as well as the systematic errors in the diffusion measurements. If this sequence is used, the b-factor described in the ST Equation 3.33 changes, and becomes $b = \gamma^2 g^2 \delta^2 (\Delta - {}^{t_g}/_2 - {}^{\delta}/_{12})$, with t_g representing the time between opposite gradient pulses.

The APGSTE sequence consists of a pair of alternating gradients prior to and after a hard 180°_y RF pulse. This pulse tags the refocussed spins with a gradient of the opposite sign. During the observation time Δ, the magnetisation is stored in the z-direction while the spins in the system are allowed to diffuse. The final, hard 90°_x pulse reverts the magnetisation vector back to the transverse plane. Subsequently the spins are decoded and rephased with another pair of alternating gradients around the 180°_y pulse.

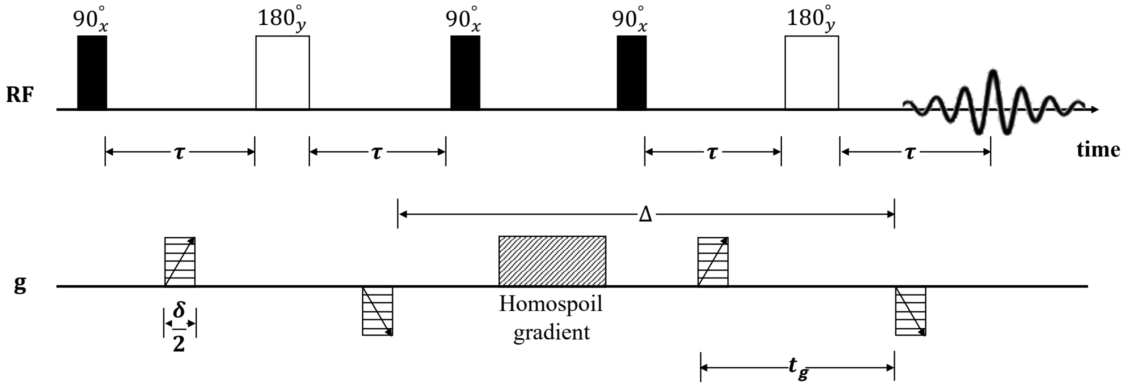

Figure 3.17 The pulse sequence for determining the diffusion coefficient by an APGSTE experiment.

3.4 Fundamental Principles of MRI

Using NMR in addition to magnetic field gradients forms the basis of MRI. During the production of images with NMR, spatial resolution in experiments is obtained by spatially varying the applied magnetic field gradient ($\mathbf{G}$) linearly across a sample ($\mathbf{r}$) according to Equation 3.34 [141, 142]:

$$\mathbf{G} = \frac{\partial \mathbf{B}}{\partial \mathbf{r}} = \frac{\partial \mathbf{B}}{\partial x} + \frac{\partial \mathbf{B}}{\partial y} + \frac{\partial \mathbf{B}}{\partial z}. \tag{3.34}$$

When applying a magnetic field gradient on a sample, the spins will obtain a precession frequency which is spatially dependent. The received signal can be Fourier transformed which will result in a frequency distribution that gives a spatial distribution of the spins. In the case a constant gradient is used, the precession frequency ω becomes:

$$\omega(\mathbf{r}) = \gamma\left(B_0 + (\mathbf{G}\cdot\mathbf{r})\right), \tag{3.35}$$

where $\mathbf{G} = \nabla\mathbf{B}$ is the applied field gradient. By applying a gradient in the z-direction, spatial resolution can be obtain in that specific direction. Application of an additional field gradient in the x- and y-directions enables images in three dimensions to be obtained. Figure 3.18 illustrates this phenomenon, whereby for two tubes with water, depending on the gradients and the directions they are used in, 2D and 3D images can be obtained [128].

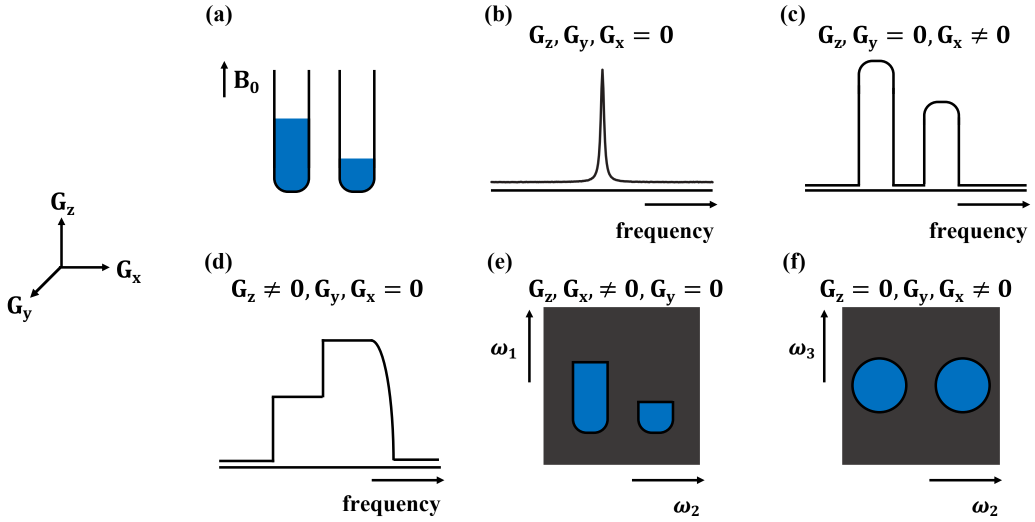

Figure 3.18 The fundamental principle of MRI is illustrated here: (a) two cylindrical tubes with different amount of water. (b) If no magnetic field gradients are activated, only a distribution of frequencies from the protons in the water about the Larmor frequency can be detected. If the magnetic field gradient in the (c) x-axis or (d) z-axis is applied, the $\boldsymbol{B}_0$ field homogeneity is disturbed, resulting in a 1D projection of the sample. Finally, if two field gradient are simultaneously applied, (e) on the x- and z-axis or (f) on the x- and y-axis, this yields 2D images.

For a sample with spin density $\rho(\mathbf{r})$ and volume dV at position $\mathbf{r}$ in a static field B_0, the signal detected dS is equal to Equation 3.36, where t is the time in which relaxation effects are neglected:

$$\mathrm{d}S(\mathbf{G},t) \propto \rho(\mathbf{r})\mathrm{d}V \exp(\mathrm{i}\omega(\mathbf{r})t). \tag{3.36}$$

Combining Equations 3.35 and 3.36, and not taking the proportionality constant into account, yields:

$$\mathrm{d}S(\mathbf{G},t) \propto \rho(\mathbf{r})\mathrm{d}V \exp\left(\mathrm{i}\gamma(\mathbf{G}\cdot\mathbf{r})t\right). \tag{3.37}$$

Equation 3.37 can be integrated over the entire 3D volume dV with respect to the spin position, to yield:

$$S(\mathbf{G},t) = \int\int\int \rho(\mathbf{r}) \exp\left(\mathrm{i}\gamma\mathbf{G}\cdot\mathbf{r}t\right)\mathrm{d}\mathbf{r}. \tag{3.38}$$

Mansfield *et al.* recognised Equation 3.38 was a form of a Fourier transform [143]. Subsequently, the concept of **k**-space was introduced, which simplified the relationship in Equation 3.38 [144, 145]. **k**-space has become a standardised protocol in NMR imaging and the reciprocal space vector **k** (units of m^{-1}) is defined by Equation 3.39:

$$\mathbf{k} = \frac{\gamma\mathbf{G}t}{2\pi}. \tag{3.39}$$

In order to sample the **k**-space vector, one can vary either the gradient magnitude **G** (phase encoding) or the time t (frequency encoding). When Equation 3.39 is substituted into Equation 3.38, this results in Equation 3.40, which is the Fourier relationship between the time domain signal and the spatial spin density.

$$S(\mathbf{k}) = \int\int\int \rho(\mathbf{r}) \exp(\mathrm{i}2\pi\mathbf{k}\cdot\mathbf{r})\,\mathrm{d}\mathbf{r} \tag{3.40}$$

The equivalent Fourier conjugate is obtained by inverting Equation 3.40 yielding Equation 3.41, which shows that the NMR signal can be used to produce the spin density in the real space, $\rho(\mathbf{r})$.

$$\rho(\mathbf{r}) = \int\int\int S(\mathbf{k}) \exp(-\mathrm{i}2\pi\mathbf{k}\cdot\mathbf{r})\,\mathrm{d}\mathbf{k} \tag{3.41}$$

By sampling signal points in **k**-space, a map of the spin density is obtained, which is also termed a NMR image.

3.4.1 Spin Density and k-Space

In order to reconstruct an image by Fourier transformation with a certain number of pixels, the same number of points have to be sampled in **k**-space, which is the mathematical domain in which the MRI signal is acquired. These pixels are usually called voxels, which is equivalent to a 3D volume element. The number of points acquired is typically obtained in a rectilinear raster of the size $2^N \times 2^M$. The field of view (FOV) of the N^{th} dimension of an image is determined by the space between two adjacent points in **k**-space: FOV = $\frac{1}{\Delta \mathbf{k}}$. The spatial resolution of an image is inversely proportional to the extent of **k**-space.

Figure 3.19 illustrates how frequency and phase encoding are related to **k**-space and show how the magnetic field gradients $\mathbf{G}_{\mathrm{read}}$ and $\mathbf{G}_{\mathrm{phase}}$ can be interpreted.

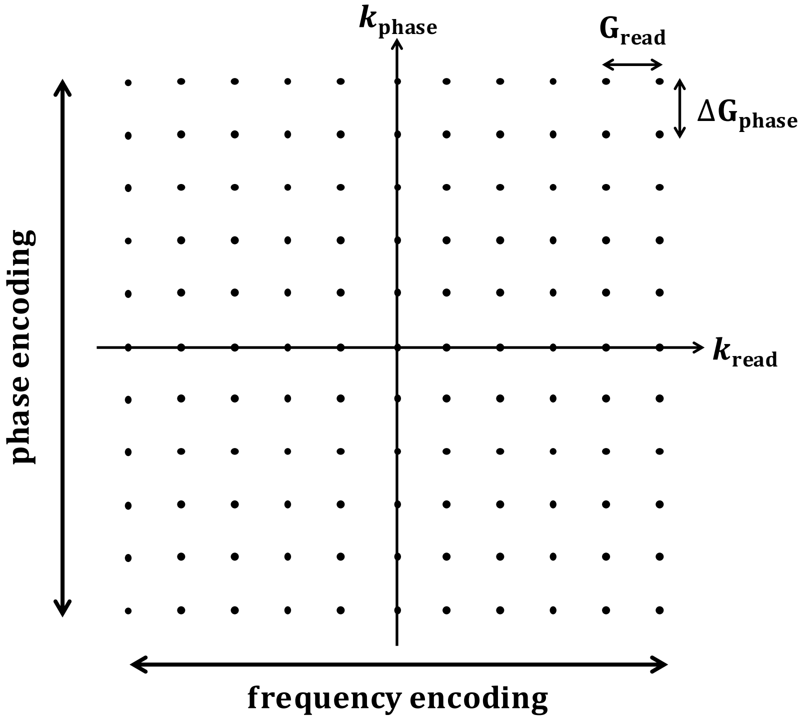

Figure 3.19 An illustration of a ***k****-space grid with the read and phase directions.*

3.4.2 Frequency Encoding

As mentioned earlier, the frequency encoding technique allows to traverse **k**-space. It can linearly be sampled by applying a constant field gradient, $\mathbf{G}_{\mathrm{read}}$, the read gradient, while at time interval t_d the **k**-space points are acquired. This method allows to continuously sample a straight line in **k**-space during the application of the encoding gradient, whereby the spatial-dependency of the Larmor frequency is measured in that direction.

The FOV during a frequency encoded experiment is shown in Equation 3.42, where $\mathbf{G}_{\text{read}}$ is the gradient strength used in the read direction and t_d is the frequency encoding dwell time.

$$\text{FOV}_{\text{read}} = \frac{1}{\Delta\mathbf{k}} = \frac{2\pi}{\gamma\mathbf{G}_{\text{read}}\,t_d} \tag{3.42}$$

In reality, a more commonly applied sampling strategy is where the dwell time is fixed and the strength of $\mathbf{G}_{\text{read}}$ is adjusted to achieve the desired FOV.

3.4.3 Phase Encoding

Phase encoding is another method to traverse **k**-space. During this process, a varying field gradient, $\mathbf{G}_{\text{phase}}$, is applied for a fixed time t_p. During phase encoding, the NMR signal in **k**-space is acquired following an initial phase encode which dephases the magnetisation vectors in **k**-space proportional to their position in the direction of the applied gradient. This enables to encode a spatial dependency to the phase of the magnetisation. The FOV during a phase encoded experiment is shown in Equation 3.43, where $\mathbf{G}_{\text{phase}}$ is the increment in gradient strength used in the phase direction and t_p is phase encoding time.

$$\text{FOV}_{\text{phase}} = \frac{1}{\Delta\mathbf{k}} = \frac{2\pi}{\gamma\mathbf{G}_{\text{phase}}\,t_p} \tag{3.43}$$

3.4.4 Slice Selection

The bandwidth of a RF pulse is representative of the range of frequencies of spins that can be excited. This bandwidth, $\Delta\omega_{\text{s}}$, is inversely proportional to the duration of the RF pulse. So far in this work, RF pulses were high-power, ‘hard’ pulses, denoted by the rectangular shapes in the pulse sequences. Hard pulses typically have a short duration with a high intensity and therefore affect a large range of spins uniformly with their large bandwidth.

In MRI, often ‘soft’ pulses are used, which have a much narrower bandwidth range compared to ‘hard’ pulses. The soft pulses are characterised by their longer duration with lower intensity which enables to only selectively excite a slice in the sample. This process is called slice selection. This is achieved by applying a magnetic field gradient, the slice gradient G_{slice}, resulting in the spins gaining a range of resonance frequencies depending on their position along the gradient direction. The thickness of the excited slice (Δz) is given by:

$$\Delta z = \frac{\Delta\omega_{\text{s}}}{\gamma\mathbf{G}_{\text{slice}}}. \tag{3.44}$$

The applied magnetic gradient, $\mathbf{G}_{\text{slice}}$, dephases the transverse magnetisation which subsequently must be rephased following the slice selective pulse. For the 90° soft pulse, it is assumed that the magnetisation vector is tipped in the transverse plane halfway through the pulse. This change in $\mathbf{k}$ is balanced by applying another slice refocusing gradient of equal, opposite intensity but half duration, $-\mathbf{G}_{\text{slice}}$, see Figure 3.20. For the 180° soft pulse, this additional refocusing slice gradient is not required as the dephasing taking place in the first half of the pulse is automatically compensated for by the refocussing of the 180° inversion.

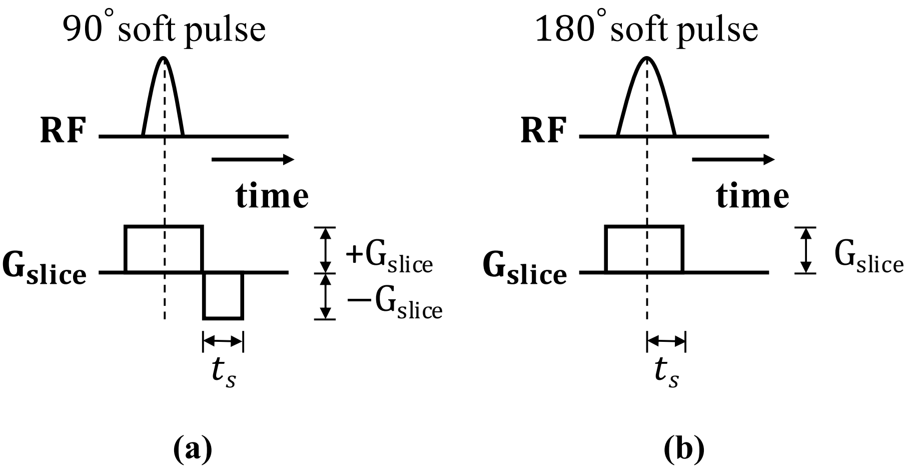

Figure 3.20 The (a) 90° and (b) 180° soft pulses and refocusing gradient pulses used during the slice selection procedures.

3.4.5 Magnetic Susceptibility

Susceptibilities are local distortions of the magnetic field $\boldsymbol{B}_0$ that typically occur at the interface between different phases. These susceptibilities acts as unintentional gradients that cause the $\boldsymbol{B}_0$ field to become less homogeneous. If the strength of the magnetic field increases, the effect of changes in the magnetic susceptibility also becomes more pronounced. Hence, a trade-off takes place between obtaining better sensitivity by operating at higher field strengths but having greater sensitivity to the imperfections caused by the magnetic susceptibilities.

Differences in the local magnetic susceptibility negatively affect the SNR of experiments as these susceptibilities affect spins in all environments of the sample. Not only can it cause reduced SNR, the susceptibilities can also lead to spectral peak broadening. In this work good spectral resolution is crucial for data interpretation when studying water and wax transport behaviour in porous media inside a reactor. MRI images can also become distorted due to the local magnetic susceptibilities.

3.4.6 RARE Imaging

The Rapid Acquisition with Relaxation Enhancement (RARE) imaging pulse program is based on the spin-echo sequence and allows to rapidly sample multiple lines of **k**-space per single excitation. An example of this is the RARE imaging sequence, presented in Figure 3.21. The initial 90°_x soft pulse excitation transfers the magnetisation into the transverse plane and subsequently the dephasing, frequency encoding, read gradient is applied. This brings the **k** value to the right edge of the 2D **k**-space grid, with coordinates of ($\mathbf{k}_{\text{read, max}}$, 0). Then, a 180°_y refocusing soft pulse inverts the phase to the left edge of the **k**-space grid (-$\mathbf{k}_{\text{read, max}}$, 0). Next, the first phase encoding gradient $\mathbf{G}_{\text{phase}}$ is applied which shifts the magnetisation to the upper-left corner of the **k**-space raster (-$\mathbf{k}_{\text{read, max}}$,$\mathbf{k}_{\text{phase, max}}$). A frequency encoding gradient is simultaneously applied which samples the signal and acquires a complete line in **k**-space which brings the magnetisation to ($\mathbf{k}_{\text{read, max}}$,$\mathbf{k}_{\text{phase, max}}$). A second phase encoding gradient, with equal magnitude but inverse direction to the first, brings the magnetisation back to its initial position at ($\mathbf{k}_{\text{read, max}}$, 0).

In the RARE acquisition, the 180°_y and RF pulse are looped for n times while incrementing the phase encoding gradient. The number of repeats is known as the RARE factor that determines how many lines of **k**-space are sampled per initial excitation, usually $1 \leq n \leq 64$ [146, 147]. For experiments with higher n, the signal obtained is weighted by the T_2 relaxation effect. In 3D RARE experiments, a second phase-encoding gradient is used instead of slice gradients [148, 149].

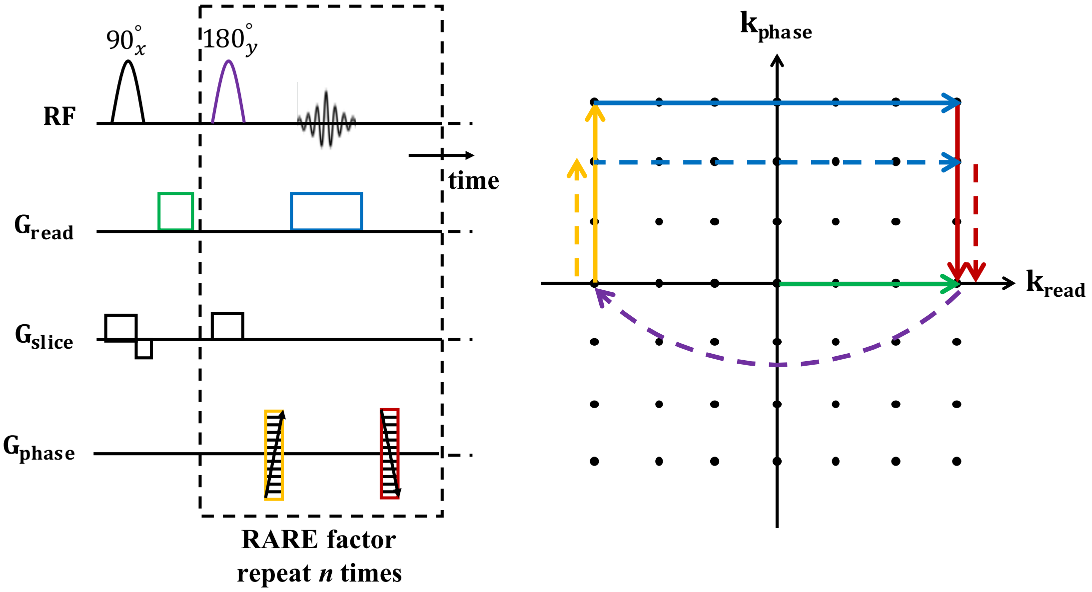

*Figure 3.21 The pulse sequence used for 2D RARE imaging and the movements through the **k**-space raster.*

3.5 The Impact of NMR during *Operando* Measurements

MRI is a very powerful instrument used extensively in a medical environment because of its ability to non-invasively and non-destructively look inside a human body. Furthermore, within the world of chemical engineering and reactors, MRI is a very sophisticated and versatile toolkit able to provide spatially-resolved information about the internal characteristics of a reactor, including heat and mass transport processes, composition, liquid distributions, surface chemistry and chemical transformations [150–153]. While a living body is different from a catalyst body or a reactor, the *in situ* and *operando* studies in catalysis clearly benefit from the use of this non-destructive toolkit as a very powerful complement to other available spectroscopic tools [154–156]. The work presented in this thesis in Chapters 7 and 8 reports the first NMR and MRI study of multiphase transport phenomena in porous catalysts at industrially relevant conditions.

Of all the various *in situ* characterisation techniques, MRI is the only methodology that can provide both chemically- and spatially-resolved information directly without the need of any tracer materials or isotopic labels. In addition, MRI is widely used to obtain images of hydrodynamics inside fixed-bed reactors. For example, NMR and MRI techniques enable to distinguish intra- and inter-particle liquid based on the differences in their relaxation times [157]. In addition, they also allow to evaluate the internal and external wetting efficiency of catalysts and the liquid hold-up in the catalyst bed under real-life operating conditions [158].

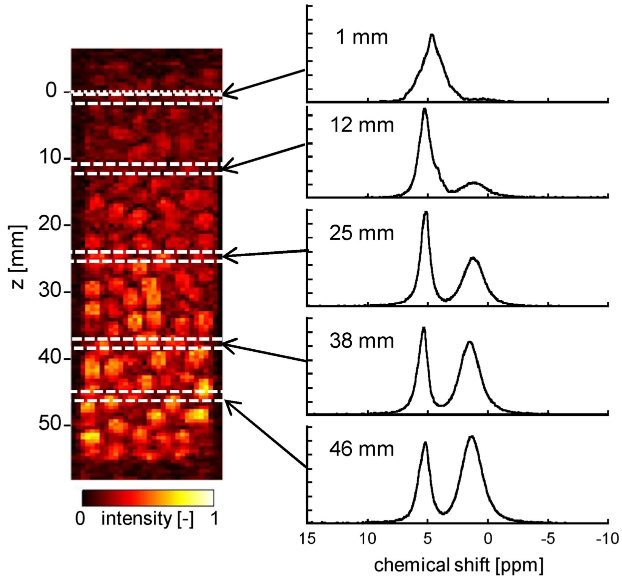

Figure 3.22 The longitudinal-plane (z-x) 2D MRI image and associated spectra acquired during the ethene oligomerisation reaction. Reproduced from [159].

The first example discussed in this Section showcases the ability of NMR to track catalytic studies is the 2D ^{1}H MRI and spatially-resolved ^{1}H MR spectroscopy and diffusion measurements. These were recorded as a function of time-on-stream (TOS) within a fixed-bed reactor providing direct measurements of the progress of the heterogeneous catalytic oligomerisation of ethene occurring over a 1wt% Ni-Al_2O_3-SiO_2 catalyst, see Figure 3.22. Experiments were conducted at a temperature and pressure of 110 °C and 29 bara. It was reported that oligomers of carbon number C_{20+} are produced within the pores of the catalyst pellets which eventually block the pore space, thereby deactivating the catalyst over time [159].

A second example of an on-line measurement performed at the MRRC is the NMR study of the (i) intra-pellet compositions and (ii) liquid-solid mass transfer coefficients during the hydrogenation and isomerisation reactions of 1-octene, see Figure 3.23. This was the first time that the local intra-pellet compositions along the axial direction (z-axis) of the pilot-scale reactor were measured using NMR [160]. All experiments were performed at 21 °C and 1 atm.

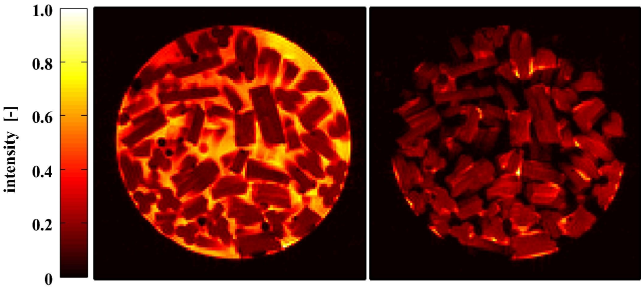

Figure 3.23 2D ^{1}H MRI data from which bed porosity, liquid holdup and wetting efficiency were calculated. Reproduced from [160].

The third example illustrates the impact of NMR to study processes taking place on a larger length scale inside a pilot scale reactor. Hydrogenation of olefins was analysed in an almost regular packing of 1% Pd/γ-Al_2O_3 catalyst beads. The beads were 4 mm in diameter which made it possible to observe liquid distribution both within the entire bed as well as in each individual bead at the same time, see Figure 3.24 [154].

In addition, a fast imaging sequence was implemented only taking 20 - 30 s to obtain 3D images of the entire bed or several 2D cross-sectional slice images of the bed in 2 - 3 s. With these MRI images, it becomes possible to distinguish intra- and inter-particle liquid based on the differences in their relaxation times [161].

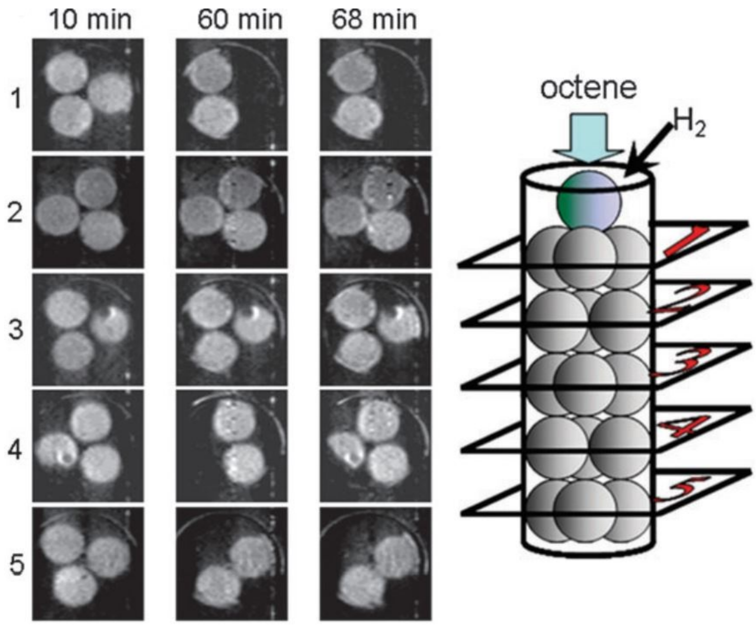

Figure 3.24 2D ^1H MR images of the liquid phase distribution in a regularly packed bed of spherical catalyst beads (Pd/Al_2O_3) detected during hydrogenation of 1-octene. Rows 1 - 5 correspond to the respective layers of the catalyst beads. Reproduced from [154].

Finally, this is the fourth example and most recent advancement of *in situ* MRI of reactors with gases. MRI of reactors containing gases are less advanced than experiments performed on liquids in reactors because the spin density of the gas phase is roughly 3 orders of magnitude lower compared to the condensed phase. This significantly limits the use of MRI to study gas phase reactions [162].

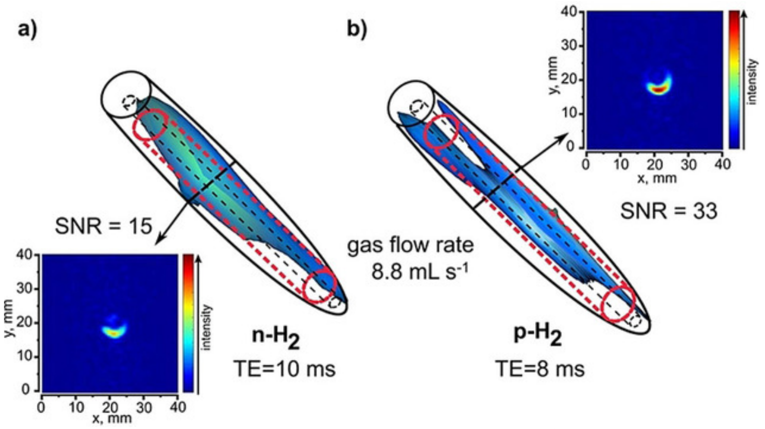

Figure 3.25 3D model of the gas flow containing a mixture of a) propene:n-H_2 and b) propene:pH_2 at 1 : 3.5 ratio. The black solid line represents the edges of the NMR tube while the red dashed line indicates the reactor glass tube. Reproduced from [163].

In addition, MRI studies of heterogeneous catalytic reactions are particularly challenging because of the magnetic field inhomogeneity caused by the presence of a solid catalyst inside. Recently, a new model type for catalytic reactors using MRI that allows the characterisation at room temperature of heterogeneous hydrogenation reactions is presented in Figure 3.25, which is suitable for (non)-polarised gases [163].

In the literature, several FTS studies attempting to characterise FTS were performed using model compounds under simplified reaction conditions. Due to the experimental hardware and chemical complexities of FT, model systems are common to approximate the GTL conversion. As has been highlighted thus far, NMR is a very powerful, non-destructive technique very well suited to study FTS *in situ* under high pressure and temperature. The *operando* NMR reactor described in this thesis is specifically built to study this reaction and it will be able to overcome the challenges highlighted above.

3.6 The NMR Spectrometer

NMR spectrometers have four major components: (i) the transmitter, (ii) the magnet, (iii) the receiver and (iv) the computer with a console. The transmitter is responsible for delivering both the high-power, short pulses and the low-power, longer slice excitation pulses to the RF coil. The transmitter also comprises the gradient control and amplifier. During a NMR experiment, the probe houses the RF coil which produces the excitation pulses for the nuclei and detects their decaying NMR signal. The probe is located inside the magnet. Moreover, the receiver combines, amplifies and converts the NMR signal before it is sent to the computer. The magnet is controlled by the console, which transmits the pulses, receives the signals and where the experiments are set up on TopSpin and Paravision. Finally, shimming coils are used to fine-tune extra magnetic fields to the $\boldsymbol{B}_0$ field, to produce a magnetic field which is as homogeneous as possible.

Chapter 4

Detection of Emulsions - Preliminary Study in Al_2O_3 at Ambient $\boldsymbol{T}$ and $\boldsymbol{P}$

4.1 Introduction

The aim of this chapter is to understand the behaviour of liquid mixtures inside porous media, relevant to a FT reaction. In this study, generic catalyst supports were used while liquid water and dodecane were co-fed at ambient conditions. This allowed intrapore liquid formation to be studied. Deionised water and dodecane act as model compounds for the liquid FT reaction products, that are thought to be mainly composed of hydrocarbons and water [82]. The experiments consisted of relaxation and diffusion measurements on these pure, bulk liquids and liquids imbibed in θ-Al_2O_3.

Understanding phase behaviour has significant implications for catalyst design, reactor performance and more importantly GTL as a whole. If during reaction emulsions spontaneously form in catalysts, this could severely affect diffusion behaviours and transport phenomena. Therefore getting a better understanding of what is happening inside commercially relevant catalysts during FTS is pivotal. In June 2015, the Shell CEO Ben van Beurden said his company has changed from "oil-and-gas company to a gas-and-oil company" [164]. Hence, any improvements or optimisation made within FTS are crucial for their business.

Finally, relaxometry and pulsed field gradient PFG NMR measurements were performed at ambient conditions on bulk liquids of deionised water and dodecane, on those bulk liquids imbibed in θ-Al_2O_3 and on binary mixtures imbibed in the same porous media. These systems were used to get a better understanding of the behaviour of the liquids during FTS. The relaxation parameters strongly suggest that water is the surface wetting phase, while dodecane is isolated from the surface. In the binary mixture, the dodecane experiences restrictive diffusion, indicating the formation of a dodecane-in-water emulsion or droplets.

4.2 Emulsions

Emulsions are two-phase, colloidal systems typically consisting of discrete dispersions of droplets of one liquid phase within another continuous liquid phase; the two phases are thus immiscible.

These droplets are thermodynamically unstable and their size can have a broad distribution and thus are generally difficult to characterise due to huge variability. Being able to measure the size distribution of droplets in an emulsion is an important characterisation technique. The size determines greatly the viscosity and stability of the emulsion [165–169]. NMR can provide a non-invasive ability to measure the emulsion DSD by studying the restricted molecular self-diffusion of emulsions. When this diffusion within the discrete droplet phase is restricted by the boundaries of the droplet, this can be interpreted and modelled to obtain the emulsion droplet size [170–175]. The sizing of emulsion droplets is a comparatively well developed application of NMR, in particular of PFG, techniques. Also, in the oil-and-gas industry the investigation and characterisation of emulsions are highly valuable during pipeline transport of recovered crude oils and the creaming processes present in oil-in-water emulsions [176].

PFG spin-echo NMR experiments can be used to study and characterise emulsions. The mean displacement during the measurement time of the liquid molecules inside the droplets is on the same order of magnitude or larger than the diameter of the droplet. In an ideal case, the diffusion time covers a broad range of times enabling the typical diffusing molecules to encounter restricting barriers [168]. Investigators have studied multiple systems and it was pointed out that the experimental data could be insensitive to (i) the assumed geometry and (ii) the nature of any distribution of sizes of the restrictive volumes [168, 172, 177–179]. Generally, the emulsion droplets are spherical as this is the shape that minimises the surface for a given volume and thereby the surface energy [166]. The diffusion inside the droplet will differ from the bulk diffusion behaviour if the RMSD of the molecules during the measuring time significantly exceeds the droplet size. In that case the diffusion will be restricted by the droplet walls.

4.3 NMR Methods and Interpretation of Data

4.3.1 PFG Pulse Sequence

The NMR PFG pulse sequence first described by Stejskal and Tanner used to measure molecule self diffusion is depicted in Figure 4.1. Stejskal and Tanner monitored the self diffusion in restricted environments and also studied diffusion in emulsion droplets (spherical cavities). The molecules in the cavities will undergo multiple collisions with the enclosing droplet walls. This will lead to an expression for the diffusion which is independent of Δ. The space-labelling PFG pulses will cause phase shifts in the nuclear precessional motion, whose magnitudes depend upon the position of each specific nuclei in the gradient field. If no diffusion occurred, after having applied the 180° RF pulse, the second field gradient pulse should completely revert the destructive effect of the first. However, if the nuclei diffused to new positions in the gradient direction during the observation time Δ, this second field gradient pulse will only partially reverse the effect. By fitting a model to the resulting NMR signal attenuation, it is possible to find a DSD for the emulsion [171].

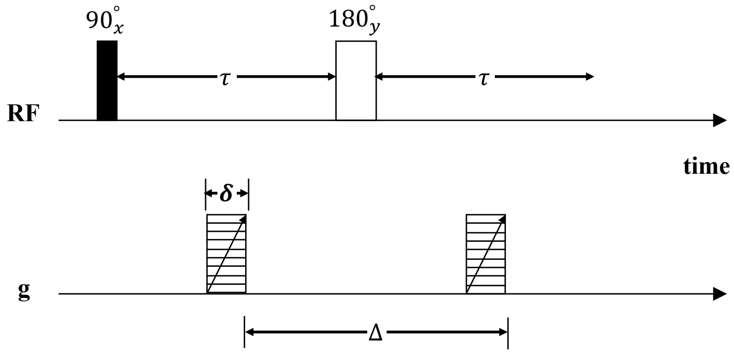

Figure 4.1 The pulse sequence for determining the diffusion coefficient by a simple PFG experiment.

The signal attenuation caused by diffusion also occurs due to a distribution of velocities within a sample, which thus results in a phase shift distribution in the NMR signal. As a consequence, conventional NMR droplet sizing cannot be applied to a practical flowing emulsion system [165]. Hence, no flow was applied in this preliminary study. Stejskal and Tanner first demonstrated that PFG methods could be applied to measure free, unrestricted self-diffusion of liquid molecules. The signal loss relies on the random motion of the molecules between two imposed magnetic field gradients [165]. The signal attenuation, Equation 4.1 is described by [180]:

$$\frac{S}{S_0} = \exp\left[-\gamma^2 g^2 \delta^2 (\Delta - \frac{\delta}{3}) \times D\right] = \exp[-b \times D]. \tag{4.1}$$

Diffusion behaviour of a liquid can be studied by varying the values of the observation time. The effects of the cavity wall on the diffusion can be observed by studying the RMSD of the spins. In the work reported here, the model that was used to fit the NMR data is described in Equation 4.1. The curvature in the signal attenuation can suggest non-ideal behaviour, which could be potentially due to restricted diffusion. To investigate this further, the signal attenuation can be independently plotted of observation time. If the signal decay behaves independently of Δ, this could suggest the molecules are present in the form of droplets, as no matter how long the diffusion is monitored, the distance travelled and thus the signal attenuation is limited by the droplet walls.

As a consequence the molecules undergo restricted diffusion. The bulk, continuous fluid renders standard diffusion coefficients, however these can be slightly reduced due to obstruction effects of the emulsion droplets [166]. These methods assume that the diffusion of the droplets themselves, due to Brownian motion, is negligible. For emulsion droplets larger than approximatively 0.1 µm, the effect of droplet diffusion is minimal [181].

4.3.2 Restricted Diffusion

In a PFG experiment, the first gradient pulse is used to mark the starting position of the diffusing species while the second gradient pulse, at a later Δ time, to probe its final position with respect to the gradient direction. In Figure 4.2, this is schematically represented to understand the process to measure the diffusion coefficient when it is either undergoing free or restricted diffusion in a sphere of radius R. The RMSD is depicted by the length of the arrow $\mathbf{R}$ which denotes the measured displacement [182]. The dimensionless variable $\xi = D\Delta / R^2$ is useful in characterising restricted diffusion as will be discussed below.

If particles diffuse freely, the diffusion coefficient obtained will be independent of Δ and the displacement measured in the z-direction will be reflective of the true diffusion coefficient, since the mean square displacement (MSD) scales linearly with time. However, for the particle confined to a sphere, the situation is entirely different. Three relevant time scales are considered during this measurement to understand the effects of restricted diffusion.

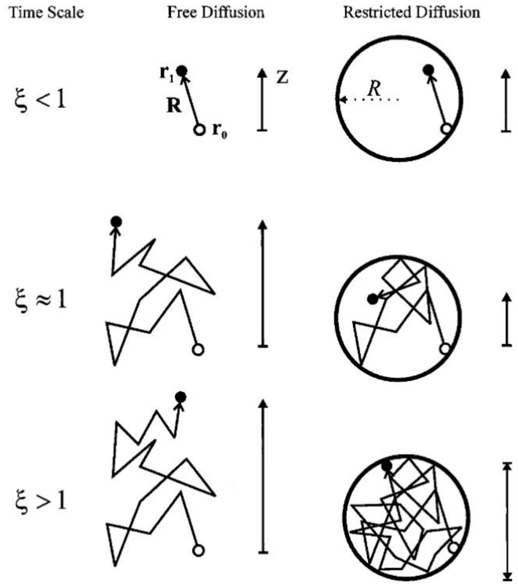

Figure 4.2 Schematic representation of PFG experiments during free and restricted diffusion regimes. Reproduced from [182].

1. $\xi < 1$: In the region, the particle does not diffuse far enough to feel the effects of restrictive boundary. To calculate the real D, the measurement should be performed in this time scale as the measured diffusion coefficient will be the same as that observed for the freely diffusing species.
2. As Δ becomes finite ($\xi \approx 1$), a certain proportion of the species will feel the effects of the boundary and the MSD along the z-axis will not scale linearly with Δ. Therefore, the measured diffusion coefficient (D_{app}) will appear to be time dependent.
3. At very long Δ ($\xi > 1$) the maximum distance that the confined particle can travel is limited by the boundaries of the sphere, and thus the measured MSD and diffusion coefficient becomes independent of Δ.

In summary, for short values of Δ, the measured displacement of a particle in a restricting geometry observed via the signal attenuation in the PFG experiment is sensitive to the diffusion of the particle. At long Δ, the signal attenuation becomes sensitive to the shape and dimensions of the restricting geometry [182].

Figure 4.3 illustrates the effects of restriction on diffusion as simulated data was plotted for free diffusion and diffusion within a sphere as a function of Δ. In the case of free diffusion, the MSD scales with time, and as a result a straight line is obtained. However, in the case of diffusion within a sphere, at very small values of Δ the results of the simulation agree with that for free diffusion. As Δ increases, there is a transition from free diffusion to surface effects as the boundaries significantly affect the motion of the diffusing species, and thus the

MSD no longer scales linearly with time. At large Δ values, the motion becomes completely restricted, the displacement becomes time independent and the attenuation curve plateaus.

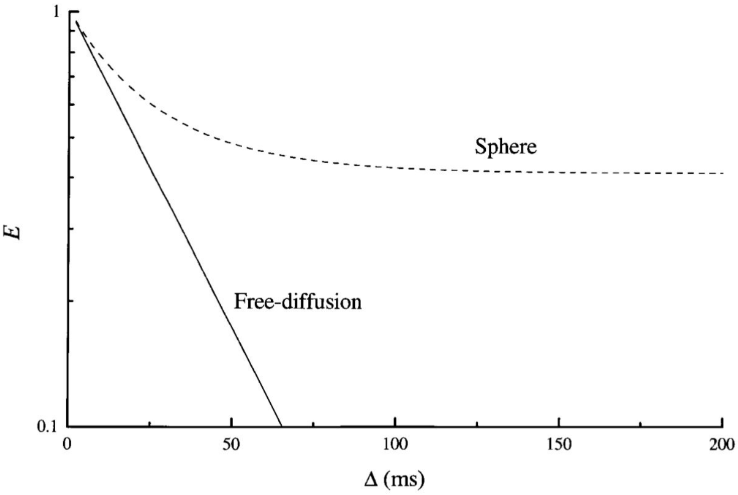

Figure 4.3 A plot of simulated echo attenuation in the case of free diffusion (——) and diffusion in a sphere (- -) versus Δ*. Reproduced from [182].*

4.3.3 Tortuosity

In porous media, the pore connectivity is defined by the tortuosity and is characterised by the reduction in apparent diffusion coefficient of any species as a result of the tortuous path it has to travel through [183]. Equation 4.2 relates the diffusion coefficient as measured by PFG, $D_{\text{eff}\,(\infty)}$, of a liquid inside a medium to the self diffusion coefficient, D_0, of a pure liquid to the tortuosity of a porous support. In general the tortuosity can also be considered to be a mobility factor of the liquid drained in porous media:

$$\text{tortuosity} = \frac{D_0}{D_{\text{eff}\,(\infty)}}. \tag{4.2}$$

4.4 Experimental

The catalyst supports used in this study are 2.5 mm θ-Al_2O_3 HTC^{TM} trilobes obtained from Johnson Matthey. N_2 porosimetry measurements of this material are shown in Figure 4.4. The pore size was determined to be 16 nm according to Barrett-Joyner-Halenda (BJH), the Brunauer-Emmett-Teller (BET) surface area to be 102 m^2 g^{-1} and the pore volume to be 0.44 cm^3 g^{-1}. Deionised water was obtained at the MRRC by using a laboratory purification unit (Purelab Option DV 25, ELGA Process Water) and dodecane ($>$ 99%, pure) was obtained from Acros Organics. Hereafter deionised water will only be referred to as water.

In Table 5.5, all materials for this work are summarised.

Table 4.1 List of components and materials used in this experimental study.

Component	**Description**	**Supplier**
H_2O	deionised water	MRRC
Dodecane	> 99% pure	Acros Organics
θ-alumina	bare, HTC^{TM} supports	Johnson-Matthey
Nickel catalyst pellets	1 wt% Ni/SiO_2(70%)·Al_2O_3(30%)	Johnson-Matthey
N_2	gas 99.998%	BOC

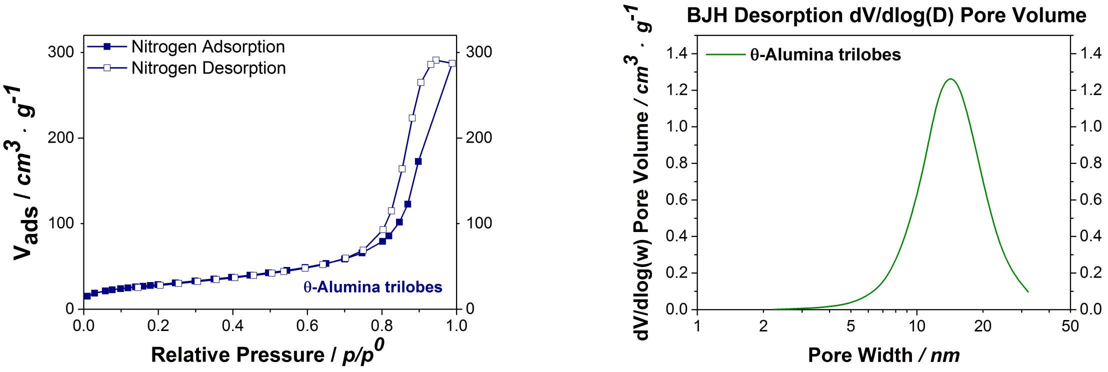

(a) The N_2 physisorption measurements. *(b) The pore width distribution.*

Figure 4.4 The N_2 physisorption for porosimetry experiments.

4.4.1 Sample Preparation

Prior to any measurements, all the trilobes were dried overnight for approximately 8 hours at 105 °C, to ensure any physisorbed water would be removed as much as possible from the pores [184]. Subsequently, the supports were soaked in either water or dodecane, according to the measurements, for 24 hours at ambient conditions, to achieve complete saturation of the pores [185]. To obtain binary mixtures in the pellets, the trilobes were first saturated with dodecane and 60 minutes before the measurement, dodecane was replaced with water. Finally, 20 trilobes were removed from the bulk liquid and dried using a pre-soaked tissue of the same liquid to make sure that any residual bulk, interparticle fluid on the surface of the trilobes was removed as much as possible. Thereafter those 20 trilobes were placed in a 10 mm NMR tube with a solvent-soaked paper in the cap. This was done to minimise the evaporation from the pellets and to obtain a saturated vapour inside the tube. All of the NMR measurements were performed on a Bruker DMX 300 MHz vertical bore superconducting magnet controlled with an Avance console, operating with Topspin V1.5 software.

Figure 4.5 The samples used during this project.

The samples prepared for the intrapore liquid formation study are shown in Figure 4.5. The samples are **a.** bulk water and dodecane; **b.** the same bulk liquids imbibed in the θ-Al_2O_3 trilobes; **c.** the binary mixture of water/dodecane imbibed in the trilobes; and **d.** finally the bare θ-Al_2O_3 trilobes.

4.4.2 NMR Experimental

The inversion recovery pulse sequence, see Section 3.2.1, was used to measure T_1, while the CPMG pulse sequence, see Section 3.2.2, was implemented to obtain T_2. Diffusion measurements were performed using the APGSTE pulse sequence, see Figure 3.17 on Page 52, to minimise the effect of background radiation and internal gradients due to the porous system. A micro-imaging probe probe with a 10 mm coil was used, with a gradient set reaching a maximum magnetic field gradient of 120 G cm^{-1} in the z-direction. Diffusion measurements were carried out varying g and Δ, while holding δ constant at 1 ms, with a gradient ramp time of 0.12 ms and with a gradient stabilisation time of 0.5 ms. A homospoil gradient of 100 G cm^{-1} with a duration of 5 ms, to destroy any remaining transverse magnetisation, was applied.

The maximum magnetic field gradient varied between 50 and 120 G cm^{-1}. In addition, Δ was varied between 20 and 100 ms for pure, bulk liquids, while for bulk liquids and binary mixtures imbibed in porous media, Δ ranged between 50 and 200 ms. Finally, the experiments were averaged over 32 scans to increase the SNR ratio and to accommodate the complete phase cycle of the sequence. The average experimental times for acquisitions for PFG NMR experiments were approximatively 45 minutes. Typical pulse parameters for the diffusion measurements on the binary mixtures are listed in Table 4.2.

Table 4.2 Pulse parameters and delays used in the diffusion experiments on the binary mixtures.

Variable	**Description**	**Unit**	**Value**
AQ	Acquisition time	[s]	0.10
D1	Delay 1	[s]	3
DW	Dwell time	[µs]	25
DE	Pre-scan-delay	[µs]	35.71
FW	Filter width	[Hz]	125K
SW	Spectral width	[Hz]	20k
O1	Offset	[Hz]	-1885
P1	90° high power pulse	[µs]	20.5
PL1	Power level	[dB]	6
RG	Receiver gain	[-]	512
	Gradient ramp time	[ms]	0.12
	Gradient pulse stabilisation time	[ms]	0.5
	Repetition time	[ms]	3000
Δ	Observation time	[ms]	120
δ	Gradient pulse duration	[ms]	1
NS	Number of scans	[-]	32
TD	Time domain size	[-]	4096
	Homospoil gradient strength	[G cm^{-1}]	100
	Homospoil duration	[ms]	5
$\boldsymbol{G}_{\mathrm{max}}$	Max. field gradient strength	[G cm^{-1}]	120

4.5 Results

4.5.1 Pure Liquids

Relaxometry Experiments

This section presents the results obtained by using ^{1}H NMR relaxometry and diffusometry experiments to study the pure, bulk liquids and the binary mixtures imbibed in porous media. Table 4.3 summarises all the values for the relaxation parameters, T_1 and T_2, and the diffusion coefficients, D, separately obtained for both the bulk water and bulk dodecane. The errors reported in the table below represent the standard deviation of three repeated measurements on the same sample. No error estimations of fits have been reported. However, the values retrieved from the fits are always reported with 95% confidence bounds.

Table 4.3 ^{1}H NMR relaxation and diffusion parameters for water and dodecane in bulk conditions and when imbibed in alumina. The D in the table represents the D_0 for bulk liquids or the $D_{eff(\infty)}$ for liquids imbibed in alumina.

Component	D [× 10^{-10} m^2 s^{-1}]	T_1 [s]	T_2 [s]
Water	21.0 ± 0.1	2.8 ± 0.1	2.00 ± 0.04
Water/θ-Al_2O_3	12.0 ± 0.1	0.26 ± 0.04	0.005 ± 0.001 (91%) 0.10 ± 0.01 (9%)
Dodecane	8.5 ± 0.3	1.3 ± 0.1	0.02 ± 0.01 (29%) 0.49 ± 0.03 (71%)
Dodecane/θ-Al_2O_3	4.3 ± 0.1	0.65 ± 0.01	0.091 ± 0.001 (16%) 0.226 ± 0.005 (84%)

Bulk Water The relaxation, T_1 and T_2, and self-diffusion, D_0, values of pure, bulk water are shown in Figure 4.6. The observed behaviour is single exponential.

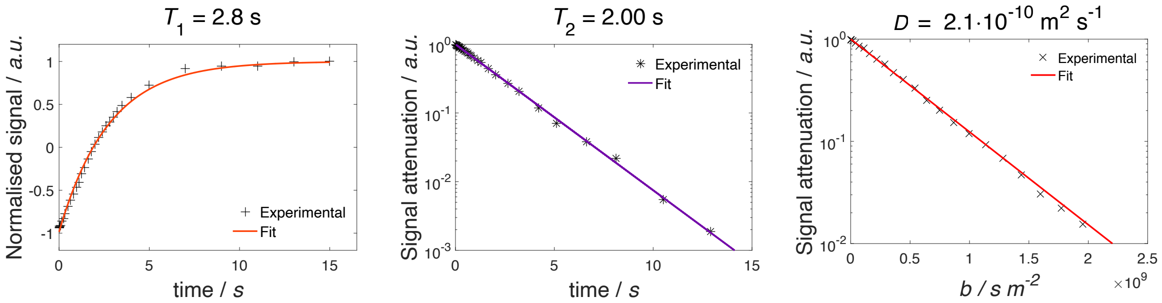

(a) The line is the fit of Equation 3.23 to the T_1.

(b) The line is the fit of Equation 3.26 to the T_2.

(c) The line is the fit of Equation 3.33 to the D data.

Figure 4.6 Bulk water behaviour.

Water in θ-Al_2O_3 The relaxation, T_1 and T_2, and diffusion, $D_{\mathrm{eff}\,(\infty)}$, values of pure water imbibed in θ-alumina are shown in Figure 4.7. The fraction of the population of the sample with a T_2 value of 0.005 s ± 0.001 is approximatively 91%. The remaining 9% have a T_2 relaxation rate of 0.10 s ± 0.01.

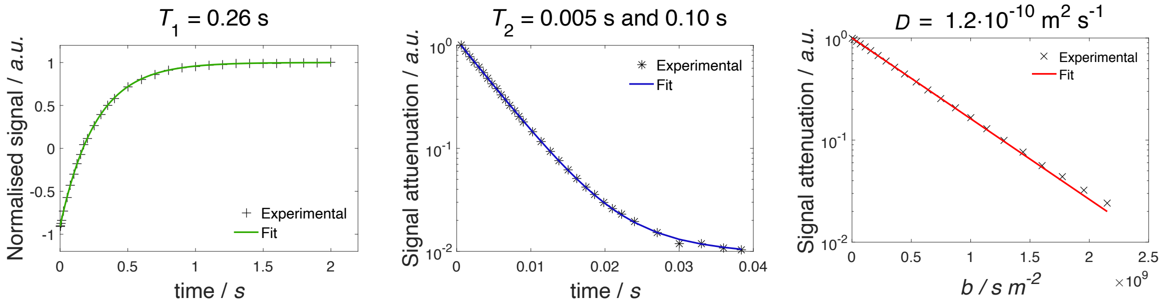

(a) The line is the fit of Equation 3.23 to the T_1. *(b) The line is the fit of Equation 3.26 to the T_2.* *(c) The line is the fit of Equation 3.33 to the D data.*

Figure 4.7 The behaviour of water imbibed in θ-alumina.

Bulk Dodecane The relaxation, T_1 and T_2, and self-diffusion, D_0, values of bulk dodecane are shown in Figure 4.8. The observed behaviour is bi-exponential for the T_2 attenuation, which could be explained by the existence of J-coupling. The fraction of the population of the sample with a T_2 value of 0.49 s ± 0.03 is approximatively 71%. The remaining 29% has a T_2 relaxation rate of 0.02 s ± 0.01.

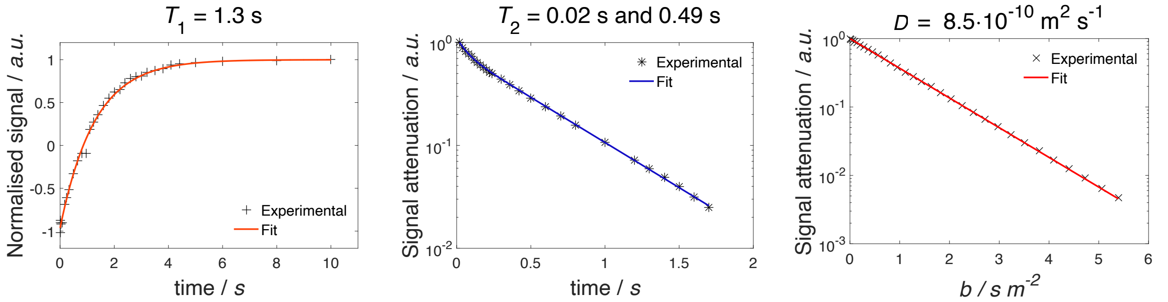

(a) The line is the fit of Equation 3.23 to the T_1. *(b) The line is the fit of Equation 3.26 to the T_2.* *(c) The line is the fit of Equation 3.33 to the D data.*

Figure 4.8 The behaviour of bulk dodecane.

Dodecane in θ-Al_2O_3 The relaxation, T_1 and T_2, and diffusion, $D_{\mathrm{eff}\,(\infty)}$, values of bulk dodecane imbibed in θ-alumina are shown in Figure 4.9. The observed behaviour is bi-exponential for the T_2 attenuation. The fraction of the population of the sample with a T_2 value of 0.226 s ± 0.005 is approximatively 84%. The remaining 16% have a T_2 relaxation rate of 0.091 s ± 0.001.

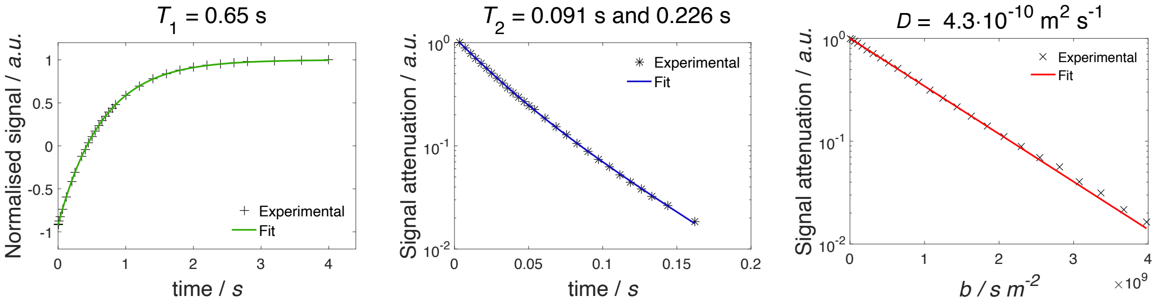

(a) The line is the fit of Equation 3.23 to the T_1. *(b) The line is the fit of Equation 3.26 to the T_2.* *(c) The line is the fit of Equation 3.33 to the D data.*

Figure 4.9 The behaviour of dodecane imbibed in θ-alumina.

PFG NMR

The experimental values reported in the literature for the self-diffusion coefficients at 25 °C for bulk water and dodecane are 23×10^{-10} m^2 s^{-1} and 8.1×10^{-10} m^2 s^{-1} respectively [186]. These compare well to the self-diffusion coefficients obtained for water and dodecane of 21×10^{-10} m^2 s^{-1} and 8.5×10^{-10} m^2 s^{-1} respectively, reported in Table 4.3. Figures 4.7 c. and 4.9 c. show the expected straight line on a semi-log scale, characteristic of free diffusion of the pure, bulk liquids, not encountering any tortuosity from the porous medium. From these D_0 values, Equation 4.2 can be used to calculate the tortuosities that the liquids experience. The tortuosity of the trilobes calculated for water is 1.8 ± 0.1, while the tortuosity based on the diffusivities for dodecane is 2.0 ± 0.1. The slightly lower water tortuosity could be a result of the disruption of the hydrogen bonding network, which reflects the effect of physical interactions within the porous material in addition to the pore space structure [187].

The tortuosity of the porous alumina is similar for both liquids, within the range of uncertainty. This strongly suggests that both water and dodecane can fill up all the pore system and thus are not excluded from the tortuous pore geometry. When the liquids are adsorbed in porous media, their diffusion behaviour is decreased due to the diffusion restriction that the pore geometry and surface structure impose. For both liquids, the diffusivity decreased by a factor 2 with respect to the bulk conditions in both cases due to the confinements effects.

2-component fits are applied for the curve fitting of water imbibed in alumina, dodecane imbibed in alumina and for the bulk dodecane sample. The need for a 2-component fit can arise by the potential presence of liquid on the outer surface of the trilobes, if the drying procedure with the pre-soaked tissue was not done thoroughly enough. This could result in having interpore and intrapore liquids, justifying the two components. This interpore liquid was clearly visible in tiny amounts in one of the NMR test tube. In addition, a distribution of pore sizes in the α-alumina trilobes could lead to 2-components.

In Figure 4.10, the ST plots for pure water and dodecane imbibed in alumina are shown, acquired with varying Δ, namely 50 and 90 ms for water and 50 - 150 ms for dodecane. For both liquids, if the Δ is varied, the data acquired for the signal attenuation aligns neatly onto the same line and provides a value for the $D_{\mathrm{eff}\,(\infty)}$.

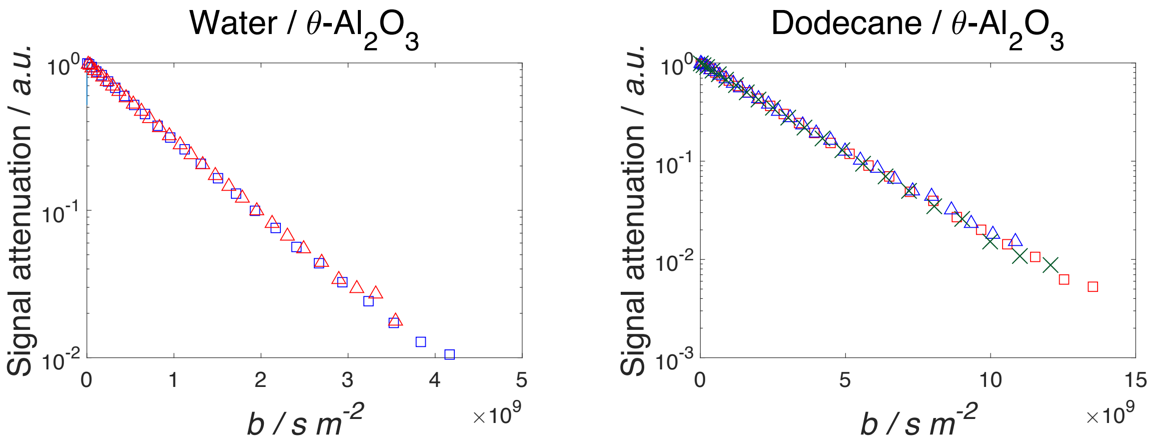

(a) ST plot for water imbibed in θ-Al$_2$O$_3$, with Δ = 50 ms (△) or Δ = 90 ms (□). The δ = 1 ms.

(b) ST plot for dodecane imbibed in θ-Al$_2$O$_3$, with Δ = 50 ms (△), Δ = 100 ms (□) or Δ 150 ms (×) and δ = 1 ms.

Figure 4.10 ST plots for bulk water or dodecane imbibed in θ-Al$_2$O$_3$, with δ = 1 ms.

4.5.2 Water/Dodecane Mixture Imbibed in θ-Al$_2$O$_3$

Relaxometry Experiments

In Table 4.4, the relaxation parameters for the water/dodecane binary mixture are tabulated.

Table 4.4 Relaxation parameters for a water/dodecane mixture imbibed in θ-Al$_2$O$_3$.

Component	T_1 [s]	T_2 [s]	T_1/T_2
Water	0.18 ± 0.01	0.0033 ± 0.0005	60 ± 5
Dodecane	1.25 ± 0.02	0.25 ± 0.06	5.0 ± 0.4

Dodecane - T_1 and T_2

For dodecane, the values in the binary mixture are lower than bulk dodecane, however they are higher than bulk dodecane imbibed in the porous trilobes. The T_1 of dodecane in alumina in the mixture of 1.25 s ± 0.02 is very comparable to the relaxation time of dodecane in the bulk phase, 1.3 s ± 0.03. However, this value decreased to 0.65 s ± 0.01 for the pure liquid in alumina.

On the other hand, the T_2 values are not as similar for dodecane in the binary system (0.25 s ± 0.06) and the bulk liquid (0.49 s ± 0.03 and 0.02 s ± 0.01). The T_2 values of bulk dodecane in alumina are 0.091 s ± 0.001 and 0.226 s ± 0.005. This difference in trend behaviour between the T_1 and T_2 of dodecane in binary phase and bulk dodecane might be attributed to internal gradient effects in such heterogeneous systems, and as a consequence, the T_2 measurements might have some inconsistencies.

Water - T_1 and T_2

As can be seen, in comparison with the values in Table 4.3, the relaxation times of water in this binary system are quite similar to bulk water imbibed in θ-alumina, but much shorter compared to pure, bulk water. The T_1 for water in the binary system is 0.180 s ± 0.01, in comparison with 0.260 s ± 0.04 for the bulk imbibed system and 2.8 s ± 0.01 in the bulk, non-porous phase.

The initial T_2 value of bulk water of 2 s ± 0.04, decreased to 0.005 s ± 0.001 and 0.01 s ± 0.01 in the porous, bulk medium, and was reduced even further to 0.0033 s ± 0.0005 in the binary mixture in alumina.

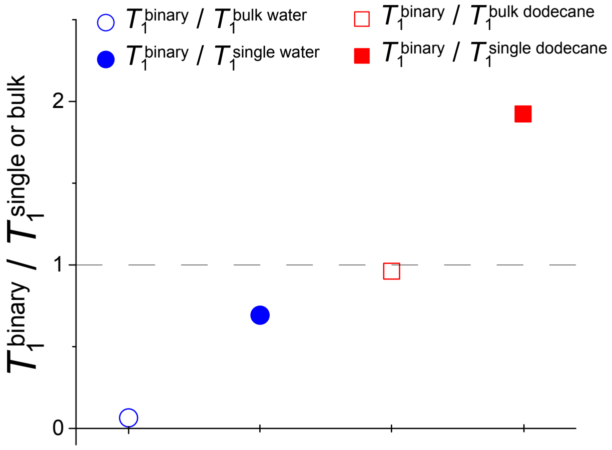

Figure 4.11 Plot for comparison of normalised T_1 values for water (● and ○) and dodecane (■ and □). The numerator consists of the T_1 value for the respective liquid in the binary mixture. The denominator is either the T_1 of the liquid in the bulk phase or the single phase liquid imbibed in the θ-Al_2O_3.

Figure 4.11 summarises all the normalised T_1 values for water and dodecane in their binary mixture confined in θ-$\mathrm{Al_2O_3}$, to get a better understanding of how the molecular surroundings affect the relaxation rates of the individual species. The ratios are either normalised to the T_1 value of the respective bulk liquids (empty symbols) or normalised to the single-phase liquid imbibed in the θ-$\mathrm{Al_2O_3}$ (full symbols). T_1 ratios < 1 indicate enhanced relaxation, i.e. stronger molecular interaction, while the opposite is true for ratios > 1. Ratios $= 1$ (see dashed line as reference) indicate no relative T_1 variation. It is clear that the latter condition is verified for dodecane in the binary mixture compared to bulk dodecane (□). This suggests that dodecane in the binary mixture is not much affected by the confinement nor by the the presence of water. On the other hand, the ratio of T_1 of dodecane in the binary mixture over that for the single phase dodecane, both imbibed in alumina (■), is about 2. This indicates that the interaction of dodecane with the surface of the alumina in the binary mixture is much weaker than in the single-phase. This value shows that in the binary mixture the presence of water partially shields the interaction of dodecane with the pore walls.

In contrast to the results for dodecane, water exhibits much faster relaxation, by a factor of 20, in the confined, binary mixture (○) than in the bulk. In good agreement with the dodecane behaviour, this seems to indicate that water acts as a surface-wetting specy while dodecane would be in the bulk phase, more isolated from the surface, forming a pool in the centre of the pores. This indicates the formation of emulsions in pores. In addition, the hydroxyl groups present on the surface of the alumina supports are hydrophilic, supporting the statement that water is interacting strongly with the surface. On the contrary, the hydrophobic dodecane would not interact strongly with the alumina surface. This is also reflected by the T_1/T_2 parameter, indicative of the surface interaction strength, shown in Table 4.4: indeed water has a T_1/T_2 coefficient of 60 while dodecane has a T_1/T_2 of only 5.

PFG NMR

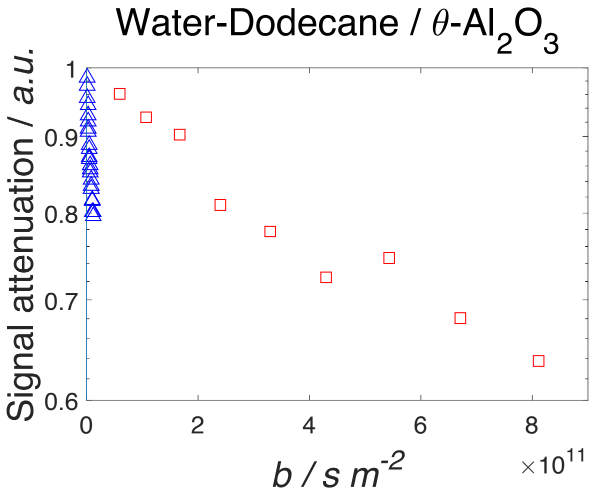

Figure 4.12 ST plot for dodecane (□) and water (△) in the binary mixtures imbibed in θ-Al_2O_3.

The diffusion data acquired using an APGSTE pulse sequence to obtain the two ST plots for both components in the mixture of water and dodecane in θ-$\mathrm{Al_2O_3}$ are shown in Figure 4.12. In comparison with previous ST plots, the signal attenuation is remarkably lower in the binary mixtures. If both attenuations are plotted in the same figure with the same axis, the water signal decays significantly faster. The very fast T_2 relaxation of water might cause this phenomenon to occur, as the relaxation is taking place during the phase encoding interval of the APGSTE pulse sequence. However, water has a diffusion coefficient $D_{\mathrm{eff}\,(\infty)}$ of approximately 7 $\times 10^{-10}$ m^2 s^{-1}, which is slightly lower than the coefficient measured for pure water in θ-Al$_2$O$_3$.

On the other hand, dodecane has a $D_{\mathrm{eff}\,(\infty)}$ in the order of 10^{-13} m^2 s^{-1} and 10^{-14} m^2 s^{-1}, which is nearly three orders of magnitude lower than for bulk or imbibed dodecane. It has been reported that in similar systems, significant signal of dodecane still survives at g = 1000 G cm^{-1} [11]. The ST plot for dodecane in Figure 4.12 clearly indicates a non-ideal diffusion regime. In addition, the b-values needed to obtain the decay are at least two orders of magnitude different (~ 10^{-11} s m^{-2} versus ~ 10^{-9} s m^{-2} in Figure 4.10). Figure 4.12 was obtained by superimposing two attenuations, acquired separately for water (△) and dodecane (□). This is permitted as water signal decays significantly faster.

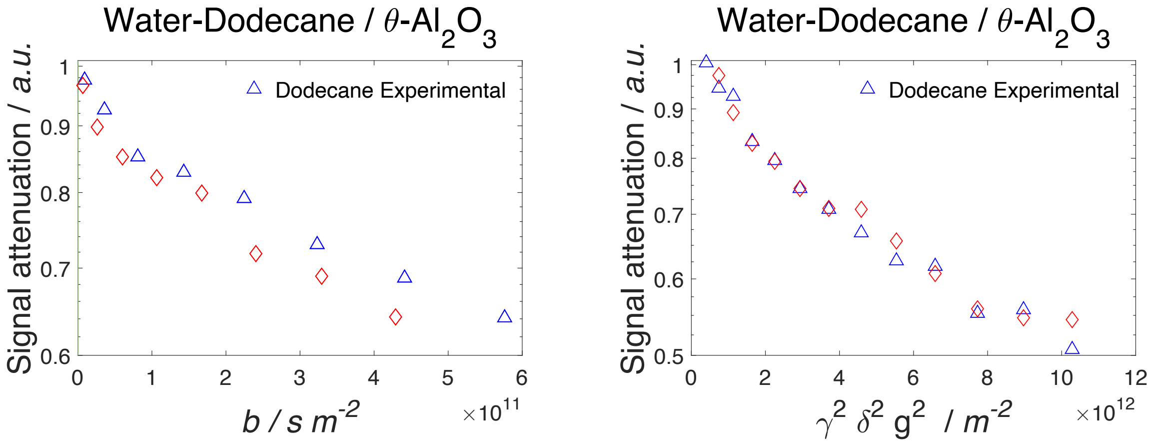

(a) ST plot for dodecane in the binary system imbibed in alumina, with Δ = *150 ms* (◇) *or* Δ = *200 ms* (△).

(b) The same data set plotted in Figure (a) as a function of $\gamma^2\delta^2 g^2$*, with* Δ = *150 ms* (◇) *or* Δ = *200 ms* (△).

Figure 4.13 APGSTE data acquired for water-dodecane imbibed in θ-*Al*$_2$*O*$_3$*, comparing (a) a ST signal decay to (b) the same data plotted independent of observation time* Δ.

The ST plots obtained by APGSTE measurements at varying Δ for dodecane in the water-dodecane mixture in θ-alumina are shown in Figure 4.13a. The diffusivity of dodecane in this binary mixture is particularly slow, especially in comparison to the bulk dodecane and dodecane in θ-Al$_2$O$_3$. The non-linearity of the ST plot for dodecane could be caused by non-ideal diffusion behaviour attributed to potential restricted diffusion phenomena. By plotting the signal attenuation versus the b-factor, in Figure 4.13a, for two different Δ values, it can be observed that the PFG NMR response does not overlay on the same curve. In addition, for longer observation times, the diffusion measured by this experiment seems to decrease as Δ increases. This trend could be indicative of restricted diffusion behaviour of dodecane, as discussed with Figure 4.3. This restrictive effect did not occur for water or dodecane in alumina, as the values for varying Δ aligned neatly in Figure 4.10. The co-existence of water in combination with dodecane causes this feature to occur.

To further examine this restrictive diffusion, Figure 4.13a is plotted independently of Δ in Figure 4.13b, this is achieved by replacing the b-factor with the so-called q-factor, namely $\gamma^2\delta^2 g^2$, with the dimensions of m^{-2}. The two datasets in Figure 4.13b behave very similarly. From this figure it can be concluded that the dodecane signal decays independently of the observation time Δ. This would suggest that dodecane is present in the form of droplets in the pores, as no matter how long the diffusion is observed, the distance travelled by the dodecane molecules and thus the signal attenuation obtained by PFG NMR is constant. This is strongly indicating that dodecane is confined in an emulsion state within the alumina pores.

4.6 Discussion

Emulsions can be thermodynamically unstable liquid-liquid dispersions of two immiscible fluids that can be further stabilised by the addition of surfactants or solid particles [188]. However, emulsions may also form spontaneously when the immiscible liquids in non-equilibrium conditions are brought in contact. The phenomenon of spontaneous emulsification was first discovered in 1879 by Johannes Gad [189].

Hydrocarbon-in-water emulsion phenomena are very common in petroleum engineering [190, 191]. Especially in porous media, it is of great importance for reservoir engineers to understand how emulsions affect flow and pressure drop [192]. Emulsions are ubiquitous to oil production operations when crude oil-in-water emulsions are injected into rock cores as a method to increase oil recovery. Moradi *et al.* identified that such emulsions are an effective technique to extract more heavy crude oil from sandstone [193]. These emulsions are formed due to oil-water interactions whereby the oil migrates through rock cores or quartz sandpacks in the form of dispersed droplets [194]. However, more detailed studies at the pore-scale are required in order to obtain more reliable models describing emulsion formation and flow through porous media [195].

To gain a better understanding on the fluid mechanics within the pores, emulsion formation has often been simplified by using a two-phase model system in a transparent capillary tube. An important obstacle when studying fluids in porous media is the ability to reproduce the pore geometry and the surface forces of porous materials on lab-scale experiments [188]. Similar to this study, NMR diffusometry has allowed Tehrani-Bagha *et al.* to gain insights into spontaneous emulsification in a ternary system of water/ethanol/toluene. It was reported that a bimodal distribution of droplets was established: large, micrometer-scale droplets and small droplets in the 100 - 400 nm range [196]. Tehrani-Bagha *et al.* observed from the diffusometry data of the NMR signal corresponding to dissolved toluene that it was strictly mono-exponential, which is typical for molecularly dissolved substances. However, in the presence of emulsions, the signal decay of toluene was distinctly bi-exponential and the two droplet sizes were calculated.

In line with this work, in most hydrophilic rock cores the surface is water-wetting and the oil phase exists in the form of globules in the middle of the pores. A thin film of water separates the rock surface from the oil phase [197]. Similar phenomena have been reported by Payatakes *et al.*, when oil ganglia formed in the presence of a pair of wetting and non-wetting phases in water-wet porous media [198].

4.7 Conclusions

Finally, relaxometry and PFG NMR measurements were performed at ambient conditions on pure, bulk liquids of water and dodecane, on the same pure bulk liquids imbibed in θ-alumina and on binary mixtures imbibed in the same porous media. These techniques were used to probe the mixtures to get a deeper understanding of the behaviour of liquids formed during FTS. Obtaining this knowledge is crucial for future developments in the GTL industry. The relaxation parameters strongly suggests that water is the surface wetting phase, while dodecane is isolated from the surface. In the binary mixture, the dodecane experiences restrictive diffusion, indicating the formation of a dodecane-in-water emulsion.

This Chapter lays the foundation for Chapter 5, investigating in greater detail the effects of various parameters on droplet formation in a systematic approach.

Chapter 5

Detection of Emulsions - Effect of T, Pore Size, n-Alcohols and Fatty Acids

5.1 Introduction

Chapter 5 presents the outcome of a study on emulsion formation in Q-silica spherical beads and FT Ru/TiO_2 catalyst pellets. This builds onto the findings of Chapter 4, where the formation of emulsions was qualitatively identified and in this Chapter the associated DSDs are quantitatively determined. This is a systematic study on the phase behaviour of water and dodecane in pores. Initially this investigates the effect of pore size (either 15 or 50 nm) and temperature (20, 40 or 60 °C) on droplet formation and the relevant DSDs. In addition, as during FT various oxygenates are produced, the effect of adding n-alcohols is studied on emulsion formation. The objective is to understand the stabilising effect the aliphatic tail would have on emulsion formation. Also, following up on Shell's interest, the surface of these hydrophobic samples was modified with a fatty acid. Subsequently, the effect of adding stearic acid on the droplet formation was analysed.

The work described in this Chapter is thus far, to the author's knowledge, novel as nobody published work on exploring spontaneous oil-in-water emulsion formation inside porous media with PFG NMR. Furthermore, the effect of stearic acid on preventing the droplet formation inside Q-silica spheres observed with NMR is new.

The aim of this systematic study is to (i) develop a technique to detect emulsion formation within porous catalyst and (ii) to study the emulsion DSD. By understanding the effect of the various parameters, a deeper understanding of the diffusion behaviour of liquid mixtures inside porous media can be obtained. By using industrially relevant catalysts and supports, by feeding liquid water and dodecane at ambient conditions, the intrapore liquid formation is studied. Deionised water and dodecane act as model compounds for the stagnant liquid layers produced during FTS, that are thought to be partially composed of hydrocarbons and water.

5.2 Emulsions and Oxygenates Effect on Phase Behaviour

5.2.1 Emulsions

Emulsions are two-phase, colloidal systems typically consisting of discrete dispersions of droplets of one liquid phase within another continuous liquid phase; the two phases are thus immiscible. In the literature, the continuous phase is also referred to as the external phase, dispersion medium or suspending medium. Emulsions can also be mixed with a third component: an emulsifying agent. This emulsifier has two principal functions: (i) decrease the interfacial tension between the dispersed and continuous phase, thereby facilitating the emulsion formation and (ii) reduce the coalescence rate of the dispersed phase [199].

In order to create emulsions, the following three elements are usually mixed:

1. Two immiscible liquids, such as oil and water
2. An emulsifying agent
3. Sufficient turbulence or mixing energy to disperse one liquid into another

There are four different types of emulsions:

1. Water-oil (W/O)
2. Oil-water (O/W)
3. Water-oil-water (W/O/W)
4. Oil-water-oil (O/W/O)

W/O emulsions are formed when the water droplets are dispersed throughout the oil continuous phase. O/W emulsions are formed when the oil emulsions are dispersed throughout the water continuous phase, see Figure 5.1. Multiple emulsion is a complex system, whereby W/O or O/W emulsions are dispersed in an additional immiscible phase. Multiple emulsion includes water-oil-water (W/O/W) emulsions and oil-water-oil (O/W/O) emulsions [200].

IUPAC defines micro-emulsions as dispersions made of water, oil and surfactant(s). Micro-emulsions tend to be both kinetically and thermodynamically stable, whereas nano-emulsions are only kinetically stable [201]. They are transparent, isotropic, thermodynamically stable systems with diameters varying approximately between 10 - 50 nm. Nano-emulsions are typically transparent systems, mostly covering the size range between 50 - 200 nm. The droplets of emulsions usually exceed 0.5 µm in diameter so that they are visible under the optical microscope. Nano-emulsions and micro-emulsions are very alike. However, nano-emulsions are obtained by mechanical force unlike to micro-emulsions which form spontaneously.

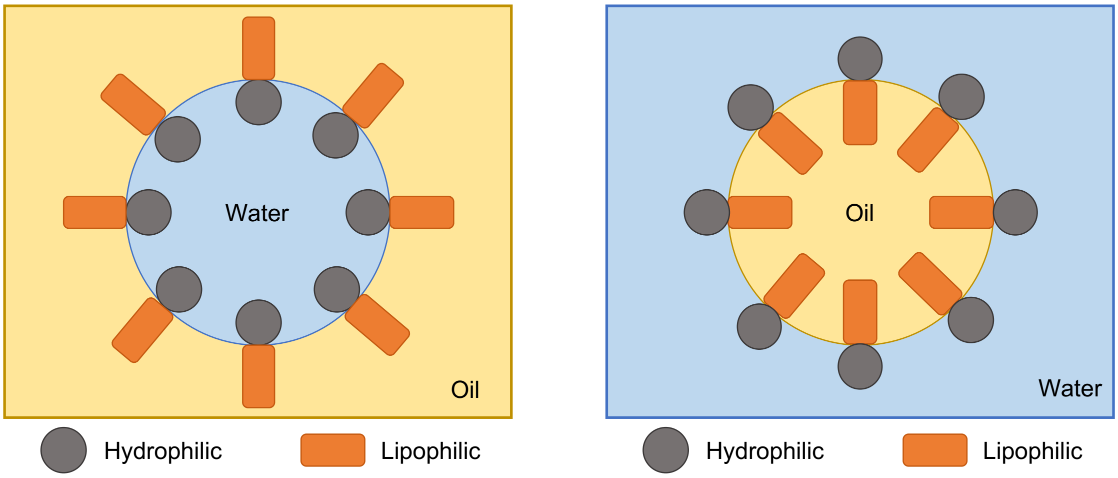

(a) W/O emulsion. *(b) O/W emulsion.*

Figure 5.1 Different type of emulsion. Adapted from [200].

There are several methods to enable emulsification: (i) low agitation energy, (ii) static mixers, (iii) general stirrers, (iv) high speed mixers, (v) colloid mills, (vi) high pressure homogenisers and (vii) ultra-sound generators. Emulsions can be prepared in a continuous or batch-wise method.

An important parameter that describes the rate of droplet deformation is the Weber number, W_e. This parameter represents the ratio of the external stress $G\eta$ over the Laplace pressure. G is the velocity gradient and η is the viscosity, see Equation 5.1. The droplet deformation increases if the Weber number increases. In order to produce small droplets, one requires high rates of stress and shear. Therefore, to produce nano-emulsions more energy is required than to produce macro-emulsions [202].

$$W_e = \frac{G\eta r}{2\gamma} \tag{5.1}$$

An overview of the key characteristics of emulsions, micro-emulsions and nano-emulsions is provided in Table 5.1.

Table 5.1 Overview of key parameters when describing emulsions. Adapted from [203].

Parameters	Emulsion	Micro-emulsion	Nano-emulsion
1. Particle Size	>500nm	1 - 200 nm	1 - 200 nm
2. Formation	Mechanical shear	Self assembly	Mechanical shear
3. Thermodynamic stability	Unstable	Stable	Unstable
4. Kinetic stability	Stable	Stable	Stable
5. Phases	Biphasic	Monophasic	Monophasic
6. Viscosity	High	Low	Low
7. Preparation cost	High	Low	High
8. Interfacial tension	High	Ultra low	Ultra low
9. Formation methods	Gum method	Titration	High Energy

5.2.2 Effect of Surfactants on Emulsion Formation

An emulsion consists of an oil-soluble portion and a water-soluble fraction. Due to its special structure, a surfactant is a substance that reduces the surface or interfacial tension of the fluid in which it is dissolved by enabling an easier formation of an extended interface. The interfacial tension σ_{ab} between pure water and an oil is about 50 mN m^{-1}. The addition of an amphiphile leads to a strong decrease of σ_{ab}. This surfactant has to have an amphipathic structure possessing both hydrophilic and lipophilic properties, a monolayer orientation at fluid interfaces and it should adsorb at interfaces. A surfactant molecule is made up of two main groups, a hydrophilic head and a lipophilic carbon chain [204]. The balance of the head group and carbon chain tail determines which phase the surfactant molecule will dissolve into more easily. If the head group is dominating, the surfactant as a whole will be more water soluble, or vice versa. This balance is called the hydrophilic-lipophilic balance (HLB). When the emulsifier is a surfactant, the HLB number can be used to determine its ability to stabilise water-in-oil (low HLB, more hydrophobic) or oil-in-water (high HLB, more hydrophilic) [205, 206].

If two immiscible liquids such as oil and water are mixed together and subsequently mechanically shaken, they tend to form two distinct layers. However, if a surfactant is added to this mixture to lower the interfacial tension between the oil and water layers, this will result in one of the liquids being dispersed in the other, thus producing an emulsion, see Figure 5.2. The formation of emulsions can be explained via two different theories: (i) *thermodynamics* or (ii) *solubility mechanisms*. Firstly, thermodynamically, the formation of emulsions is mainly governed by interfacial surface forces. The Gibbs free energy of the system during droplet formation from a bulk liquid, ΔG, can be described according to ΔA, γ_{12}, T and TΔS. These are described in Table 5.2 below.

$$\Delta G = \Delta A \gamma_{12} - T \Delta S \tag{5.2}$$

$$n\,\mathrm{S} \rightleftharpoons \mathrm{S}_n \tag{5.3}$$

Usually, emulsion formation is a non-spontaneous process whereby $\Delta G > 0$ indicating that $\Delta A\gamma_{12} \gg T\Delta S$, see Equation 5.2. However, the energy required for emulsification tends to be orders of magnitudes larger than the thermodynamic energy ($\Delta A\gamma_{12}$) for creating a new surface [204]. This requirement can be lowered by the addition of a surfactant.

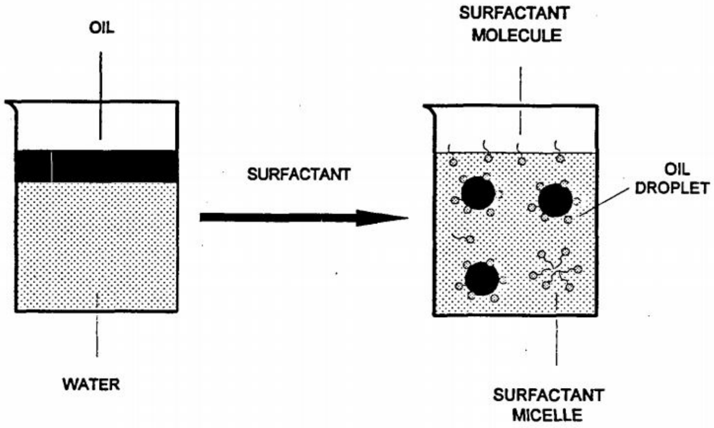

Figure 5.2 Formation of an emulsion in the presence of a surfactant. Reproduced from [204].

Secondly, the formation of emulsions can also be understood using solubility mechanisms. Solute molecules can aggregate to form clusters, also known as micelles which are also seen in Figure 5.2. If the number of amphipathic species is represented by S, this aggregation process can be described by Equation 5.3 where S_n are the micelles with n degrees of aggregation. Clusters tend to form spontaneously if the surfactant concentration is equal or above the threshold surfactant concentration, also known as the critical micelle concentration (CMC). Solutes that would normally be insoluble or only slightly soluble in water dissolve extensively in surfactant solutions if the surfactant concentration is above this CMC.

Table 5.2 List of quantities with their description and unit appearing in the thermodynamic formation of emulsions.

Symbol	**Description**	**Unit**
ΔA	increase in interfacial area due to the formation of droplets	[m^2]
γ_{12}	interfacial tension between the two liquids	[$kg\ s^{-2}\ m^{-1}$]
T	temperature	[K]
$T\Delta S$	entropy contribution resulting from formation of droplets	[$kg\ m^2\ s^{-2}$]
S	number of amphipathic species	[-]
n	degrees of aggregation for amphipathic species	[-]

5.2.3 Droplet Sizes

Droplet sizes of emulsions depend on a number of factors such as (i) the type of oil, (ii) interfacial properties of the oil-water system, (iii) surface-active agents present (added or naturally occurring) and (iv) nature of the porous material. Emulsion DSDs can be changed by varying the concentration of a surfactant added to the oil, as shown in Figure 5.3 [207, 208]. Similar results were obtained for colloidal metallic systems that were stabilised using different surfactants such as organic thiols, carboxylates, poly(acrylic acid), oleic acid, phosphonates, and trioctylphosphine [209].

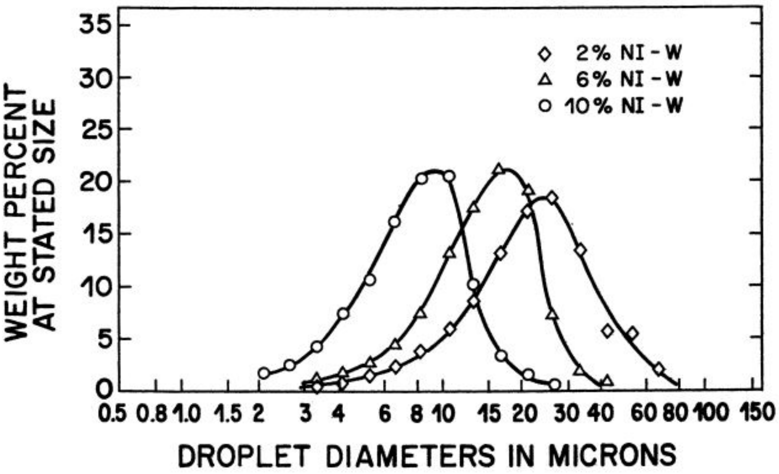

Figure 5.3 Size distribution of emulsions prepared from Richfield-Kraemer crude oil, water and dispersant NI-W containing NaOH. Oil content of emulsion was 60%. Reproduced from [207].

5.2.4 Oil

According to Strassner approximately 67% of world's crude oil is produced in an emulsion state. The viscosity and interfacial tension play very important roles in the *in situ* formation of emulsions in porous materials [210, 211]. The concentration and type of emulsifier greatly determines the amount of reduction of interfacial tension. Peake and Hodgson reported that oil soluble organics acids such as fatty acids contribute to emulsification [212, 213]. Soo and Radke have studied the flow mechanisms of dilute, stable emulsions with a mean DSD ranging from 1 to 10 µm in fine grained porous sandpacks of Berea sandstone [214]. They observed oil-in-water emulsions in porous media when mixing refined mineral oil with sodium oleate and oleic acid for stabilisation.

A method predicting the spontaneous formation of emulsions in partially miscible ternary system phases is described by Ruschak and Miller [215, 216]. Three toluene-water systems mixed with either ethanol, propanol or propionic acid were investigated. Ethanol was present in higher concentration in the aqueous phase. Propanol was present in higher concentration in the toluene-rich phase. And finally propionic acid was present in about equal concentration in the two phases.

Rang and Miller investigated the phase behaviour and spontaneous emulsification of *n*-hexadecane/oleyl alcohol/$C_{12}E_6$ mixtures at 30 °C [217]. One main feature of this experiment was that the presence of an alcohol of intermediate chain length with a high enough solubility in water. This alcohol was transferred from the oil phase to water at a fast rate and thus resulted in the oil phase continuously becoming more hydrophobic and eventually being supersaturated in oil. This would allow the nucleation of oil drops to occur [217]. In practice the process is termed *self-emulsification*. Rang and Miller also established that their emulsification process only yielded small oil droplets when the initial oil phase was completely converted to a micro-emulsion that had become supersaturated in oil. However, for the particular system investigated these conditions occurred when the alcohol-to-oil ratio was close to the excess oil phase in equilibrium with a micro-emulsion and when surfactant concentration was high enough. It was found that small oil droplets had diameters in the order of 1 µm.

Fukuda *et al.* studied micro-emulsion formation of hydrocarbon and water solutions mixed with an alkyl polyglucosides and alkyl glycerol ether. In addition, the NMR self-diffusion was investigated [218]. However, for some daily commercial applications it is required to produce emulsions with very small drops without intensive stirring or mixing. One possible method to achieve this is to select initial compositions of oil and water phases such that small drops form spontaneously when the phases are brought into contact with no externally applied agitation.

5.2.5 Phase Behaviour of Ternary Mixtures of Water, Oil and a Surfactant

Micro-emulsions are generally thermodynamically stable, transparent and have a low viscosity. In addition, they are isotropic dispersions consisting of oil and water stabilised by an interfacial film of surfactant molecules [219]. Micro-emulsions have a very small droplet size because of their ultra-low interfacial tension between the oil and water phases. This is due to the presence of surfactant molecules which intercalate between the surfactant molecules at the oil-water interface [220].

It appears that spontaneous emulsification in ternary mixtures can be produced by three different mechanisms. Two of these involve mechanical breakup of the interface but can be attributed to two different reason: (i) a result of an intense interfacial turbulence or (ii) the existence of negative values of interfacial tension. The third mechanism is called "diffusion and stranding" and is completely different as it involves a chemical instead of a mechanical instability. In this final mechanism, local supersaturation regions occur that can be produced by the diffusion process. As phase transformation occurs between these regions, emulsion droplets are therefore formed [221], see Figure 5.4.

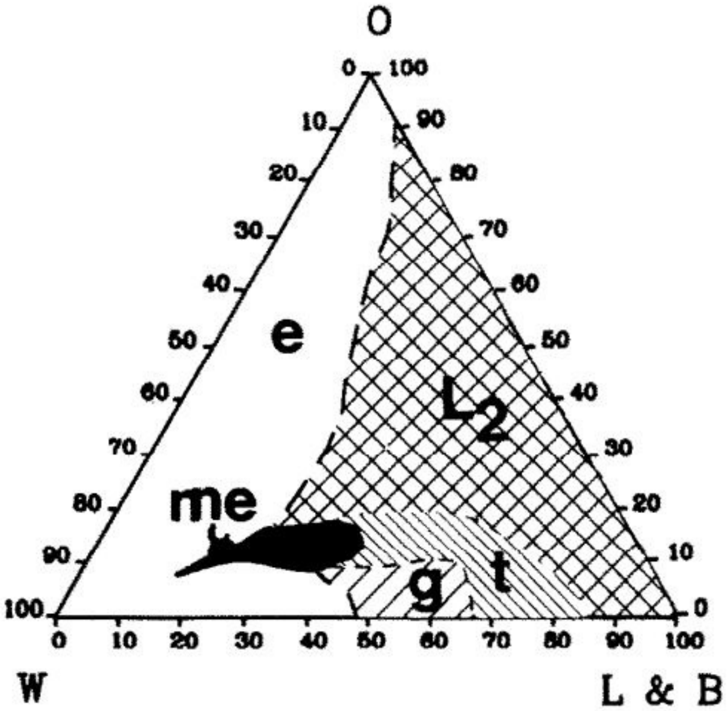

Figure 5.4 Partial phase diagrams of the system butanol / IPM / water showing stable oil-in-water micro-emulsion (me), gel (g), monophasic turbid (t), unstable emulsion (e) and isotropic (L_2) regions. Reproduced from [220].

5.2.6 Effect of the Silica Surface Chemistry

Emulsions which in the presence of solid particles can be stabilised are named after S. Pickering. He discovered that coalescence of droplets is suppressed when solid particles are adsorbed at the oil-water interface. It is widely accepted that this suppression in coalescence is a kinetic effect caused by a two properties: (i) the formation of a rigid interfacial film and (ii) the increase in viscosity of the continuous phase [222, 223]. As shown by Shen and Resasco, they produced emulsions of water and various organic phases which were stabilised by carbon nanotube-silica particles. They modified the type of emulsion from w/o to o/w, so different types of liquid biphasic reactions could be carried out. By depositing different catalysts on either side of the interface, they could selectively convert functional groups of molecules that are water-soluble or oil soluble at the same time in a selective manner.

This phase selectivity might allow one to work with complex mixtures and selectively hydrogenate water-soluble molecules in the aqueous phase in the presence of oil-soluble molecules that one does not want to hydrogenate. Working with emulsions, one can have the added benefit of catalytically converting at the interface molecules that are soluble in one phase so they become insoluble products in that phase and migrate to the other phase for easy separation [223, 224].

Aggregation of particle-stabilised droplets may occur due to interactions between particles adsorbed on different drops or where adsorbed particles act as bridges between droplets. Assuming that the extent of surfactant adsorption is lower on the larger silica particles, which would reduce the extent of particle adsorption onto the drop surfaces, it is possible that the larger particles bridge the droplets to stabilise the oil-water interface created during emulsification [225].

Nanoparticles can be used as emulsifiers for the stabilisation of Pickering emulsions. Nanoparticles are dispersed in the water or oil phase in the same way as an emulsifier is dissolved in one of the phases. These nanoparticles are one type of additive which can be used to populate the liquid-liquid interface formed during homogenisation. Although the interfacial tension is probably unaffected by particle adsorption, the area of the bare oil-water interface is reduced, which lowers the amount of energy required to form the interface.

The free-energy change associated with the transfer of an isolated, spherical particle from a bulk water or oil phase to a planar oil-water interface is at a maximum for a particle which is wet to an intermediate extent by both liquid phases. Such particles are effectively irreversibly adsorbed at the liquid-liquid interface and, if the drops are covered sufficiently, are responsible for sterically hindering drop coalescence, thus stabilising the emulsion. The type of drops formed (oil or water) is primarily determined by the wettability of the particles [225]. Many researchers have been focussing on investigating the formation of solid-stabilised emulsions of oil and water [226].

Figure 5.5 presents the DSDs of a water continuous emulsion for different oil volume fractions. As the oil volume fraction increases, the drop population shifts towards the larger diameters. Since the particle concentration in the system falls progressively, it seems that the addition of extra oil increases the interfacial area which may not be sufficiently covered by the available particles. Thus, the droplet size increases as the drops coalesce [227–231].

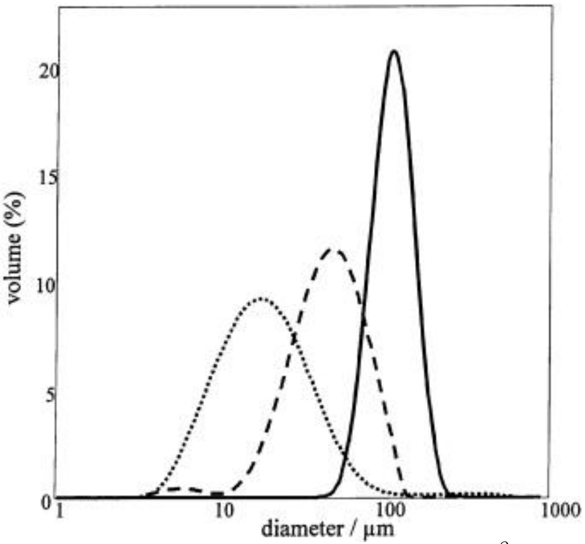

Figure 5.5 Drop size distributions for emulsions of PDMS and 10^{-2} *M NaCl stabilised by 0.7 wt% hydrophobic silica in the aqueous phase formed as the oil volume fraction was increased continuously between 0.1 (o/w, dotted line), 0.4 (o/w, dashed line), and 0.6 (w/o/w, full line). In the emulsion, the size of the oil globules was measured. Notice the narrowing of the distribution with increasing oil content. Reproduced from [222].*

5.2.7 Oxygenates Derived from FT

Oxygenates are organic oxygen compounds or common oxygenated hydrocarbon derivatives. The main oxygenate classes are alcohols, carbonyls and carboxylic acids. During FTS, synthesis gas (H_2 and CO) is converted into a mixture of (i) hydrocarbons, (ii) oxygenates, (iii) water and (iv) carbon dioxide. During LT-FT, *n*-paraffins and *n*-olefins are the main products of the LT-FT synthesis but side-products like oxygenates and branched compounds can also be obtained [232]. The combined amount of oxygenates produced during FTS varies between 0 to 15%, depending on the type of catalyst used and other process conditions [233]. The hydrocarbon and oxygenate fraction is commonly referred to as the *synthetic crude oil* or *syncrude*. This syncrude, just like conventional crude oil, has to be further processed and refined in order to produce useful products, such as transportation fuels and chemicals. It has been reported that oxygenates do not have a great effect on the conversion during FTS but can be more problematic during the subsequent processing of FT waxes.

5.2.8 Further Treatment of FT Wax Containing Oxygenates

During further processing of FT waxes, metallic catalysts are generally used. During this transformation, the oxygenates tend to have a higher polarity and thus interact stronger with most refining metal catalysts. The presence of oxygenates in the FT effluent can significantly alter the catalytic properties of such bifunctional catalysts. The oxygenates can for example change the balance between the acidic and the hydrogenation/dehydrogenation function and may thus lead to catalyst inhibition [47].

Furthermore, oxygenates are reactive molecules and they may also cause unwanted side-reactions. For example, during hydrocracking of FT wax, 1-decanol can easily be decomposed into water and C_{10} alkanes. It has been argued that the main effect of 1-decanol (or even water) is to adsorb on the acidic sites of the silica-alumina while competing with the alkenes intermediates. This would in turn reduce the number of acidic sites available for the hydrocracking reaction and therefore decrease the activity of the catalyst [232].

Oxygenates formed as by-products of FT syntheses can be transformed into other FT derived oxygenates instead of treating them as unwanted chemicals. One-step direct synthesis of ethyl acetate from ethanol is feasible with the use of some heterogeneous catalysts through various hydrogenation reactions [234]. For FT, syncrude refining performed with oxygenate-free feed materials, the catalyst life cycle can extend up to 1 year. But with oxygenates present in the feed, that lifetime is reduced to a mere 1 - 2 months. The main cause of catalyst deactivation is the formation of carbonaceous deposits, or also known as coke. The production rate of coke is higher at more elevated operating temperatures. The presence of oxygenates requires the operating temperatures to be higher and therefore the coke production is even more pronounced [235, 236].

5.2.9 FT Performed in an Emulsion System

Investigating the flow of water-oil mixtures through rocks is important to better understand the flow behaviour. It has been reported that long-chain hydrocarbons such as wax formed during FTS reaction generally contain water and trace amounts of oxygenates which are conducive to the formation of macro-emulsions of wax products. A novel reaction system for FTS was designed by D. Resasco *et al.* in which metal-doped carbon nanotubes simultaneously (i) stabilise emulsions due to their amphiphilic nature and (ii) catalytic reactions at the water/oil interface [237]. In this process, an emulsion acts as the reaction system to perform FT with a Ru catalyst while water and decalin are present as the reaction medium.

The nanohybrid particles at the water/oil interface facilitated and stabilised the formation of a water-in-oil emulsion, giving rise to an oil emulsion/water trilayer liquid structure. FTS which occurred in the emulsion phase had a much higher conversion rate than FTS performed in oil single-phase reactions, still yielding products with an ASF distribution. Hydrocarbons enriched in alkanes migrate to the top oil phase, while short alcohols remain in the bottom water phase.

Performing FT in an emulsion system provides important advantages, such as (i) increased liquid/liquid interfacial area that consequently means (ii) faster mass transfer rates of molecules between the two phases, (iii) effective separation of products from the reaction mixture by differences in the water-oil solubility, and (iv) significant changes in product selectivity that can be adjusted by modifying the emulsion characteristics [238, 239]. Very similar results were observed by Zapata *et al.* when studying the condensation and hydrogenation of biomass-derived oxygenates in water-in-oil emulsions stabilised by hybrid catalysts. The possibility of maximising the selective conversion of molecules present in each of the phases (phase-selectivity), and the direct partitioning and separation of molecules based on differences in relative solubilities were observed [240].

5.3 Experimental

5.3.1 Experimental Plan and Systems Studied

In the first part of this systematic study, the goal is to identify oil-in-water droplets and study the effects of temperature and average pore size of the support. To understand these effects on an oil-in-water emulsion formation, the following systems were studied, see Table 5.3. Firstly, porous CARiACT Q-silica spheres with an average pore size of 15 and 50 nm were imbibed in (i) water, (ii) dodecane and (iii) water/dodecane to study emulsion formation at 3 different temperatures (20, 40 and 60 °C) and analysed using PFG NMR diffusion experiments.

Table 5.3 The various systems studied during the experiments: (i) bulk liquids, (ii) bulk liquids in silica spheres and (iii) binary mixtures in the same spheres.

System		**Q-15 silica**			**Q-50 silica**			**No support**	
		W	D	W-D	W	D	W-D	Water (W)	Dodecane (D)
T [°C]	20	✓	✓	✓	✓	✓	✓	✓	✓
	40	✓	✓	✓	✓	✓	✓	✓	✓
	60	✓	✓	✓	✓	✓	✓	✓	✓

In the second section of this project, Q-silica supports were also submerged in various mixtures of water-dodecane with an *n*-alcohol (ranging between ethanol, butanol and heptanol). Furthermore, stearic acid was used to chemically modify the surface. In Table 5.4, a summary is provided of all systems studied: (i) single component liquids, (ii) binary mixtures of water and dodecane, (iii) ternary mixtures of water-dodecane with an *n*-alcohol, (iv) ternary mixtures of water-dodecane with stearic acid and finally (v) Ru/TiO_2 FTS catalyst pellets. These porous media studied for these systems were either Q-silica beads or the real FT catalysts. Initially, the Q-silica supports were chosen as they have very distinct pore size distributions. Subsequently, the same mixtures were studied in the Ru/TiO_2 pellets to ensure that under FTS, same behaviours could be examined.

All systems where emulsions were detected are marked with a **V** and the opposite is true for those marked with a **X**. From this table it is clear that water and an alkane are needed together in a hydrophilic environment to provide emulsions. In single component mixtures or supports with a hydrophobic environment, due to addition of stearic acid acting as a fatty acid, no emulsions were observed.

Table 5.4 The complete overview of various systems studied during the experiments: (i) ***V*** *indicate systems where emulsions were observed and (ii)* ***X*** *refers to mixtures without emulsion detection. OH and FA refer to n-alcohol and fatty acid respectively.*

System	Water (W)	Dodecane (D)	W-D	W-D-OH	W-D-FA	W-D-OH-FA
1. Q-15 or Q-50 Silica	**X**	**X**	**V**	**V**	**X**	**X**
2. TiO_2 and Ru/TiO_2	**X**	**X**	**V**			

5.3.2 Materials and Chemicals

The spherical Q-15 and Q-50 beads are catalyst supports supplied by Fuji Silysia Chemical, Ltd. These bare supports have a very precise pore size distribution, of 15 and 50 nm respectively, and particle size, ranging between 0.7 - 4.0 mm. Both the bare TiO_2 and Ru/TiO_2 were supplied by Shell and have a pore size of 28.9 nm. Deionised water was produced at the MRRC by using a laboratory purification unit (Purelab Option DV 25, ELGA Process Water) and dodecane (> 99%, pure) was obtained from Acros Organics. All other chemicals (*n*-alcohols and stearic acid) were obtained from Alfa Aesar. In Table 5.5 all materials for this projects are summarised.

Table 5.5 List of components and materials used in this experimental study.

Component	Description	Supplier
deionised water	Purelab Option DV 25	MRRC
dodecane	> 99%, pure	Acros Organics
1-methanol	> 99%, pure	Alfa Aesar
1-ethanol	> 99%, pure	Alfa Aesar
1-butanol	> 90%, pure	Alfa Aesar
1-heptanol	> 90%, pure	Alfa Aesar
stearic acid	> 98%, pure	Alfa Aesar
Q-15 silica CARiACT	spherical beads support	Fuji Silysia, Ltd.
Q-50 silica CARiACT	spherical beads support	Fuji Silysia, Ltd.
TiO_2	bare FT support	Shell Global Solutions
Ru/TiO_2	1 wt% Ru FT catalyst	Shell Global Solutions

5.3.3 Sample Preparation

Prior to any measurements, all the spherical beads were dried overnight for approximately 8 hours at 105 °C, to make sure any physisorbed water would be removed as much as possible from the pores [184]. Subsequently, the supports were soaked in either water or dodecane, according to the measurements, for 24 hours at ambient conditions, to achieve complete saturation of the pores [185]. To obtain binary mixtures in the pellets, the beads were first saturated in a beaker with dodecane. 60 minutes before the measurement, the pellets were removed from the dodecane and in a separate beaker, the pellets were submerged in water.

Ternary mixtures of dodecane with water and n-alcohols were prepared by submerging the dodecane pre-saturated pellets in a mixture of water (20vol%) and surfactant (80vol%). This could either be n-ethanol, n-butanol or n-heptanol. These alcohols were chosen for their different solubilities in water. Ethanol is known to be infinitely soluble, whereas butanol and heptanol have a solubility of 9 and 0.2g/100g of water respectively [241]. Unfortunately the range of water soluble n-alcohols is limited. Finally, the beads were removed from the bulk liquid and dried using a pre-soaked tissue to ensure that any residual bulk, interparticle fluid on the surface of the beads was removed as much as possible.

To chemically modify the surface of the Q-silica beads, the porous pellets were immersed for 2 hours in a mixture of n-octane and stearic acid (mass ratio 9:1) at 90 °C in a sealed container. Subsequently, for 12 hours the, n-octane was allowed to evaporate at room temperature in an open container. Finally, just as in the binary mixtures procedure, the pellets were then soaked in dodecane first followed by water to obtain dodecane and water imbibition. This procedure is based on the recommendation of the collaborators from Shell who suggested to use n-octane to solubilise stearic acid.

Thereafter those beads were placed in a 5 mm NMR tube with a minuscule solvent-soaked paper in the cap. This was done to ensure minimum evaporation from the pellets and to obtain a saturated vapour inside the tube. All of the NMR measurements were performed on a Bruker DMX 300 MHz vertical bore superconducting magnet controlled with an Avance console. For the temperature control of the PFG probe, a 800 L/h air flow rate was used. Equation 5.4 is obtained empirically and used to obtain the set point (SP) of the temperature control system for the experimental temperatures of 20, 40 and 60 °C.

$$\text{set point [K]} = \frac{\text{true temp [K]} - 22.007}{0.9278} \tag{5.4}$$

An overview of the whole imbibition procedure for the various systems is shown in Figure 5.6.

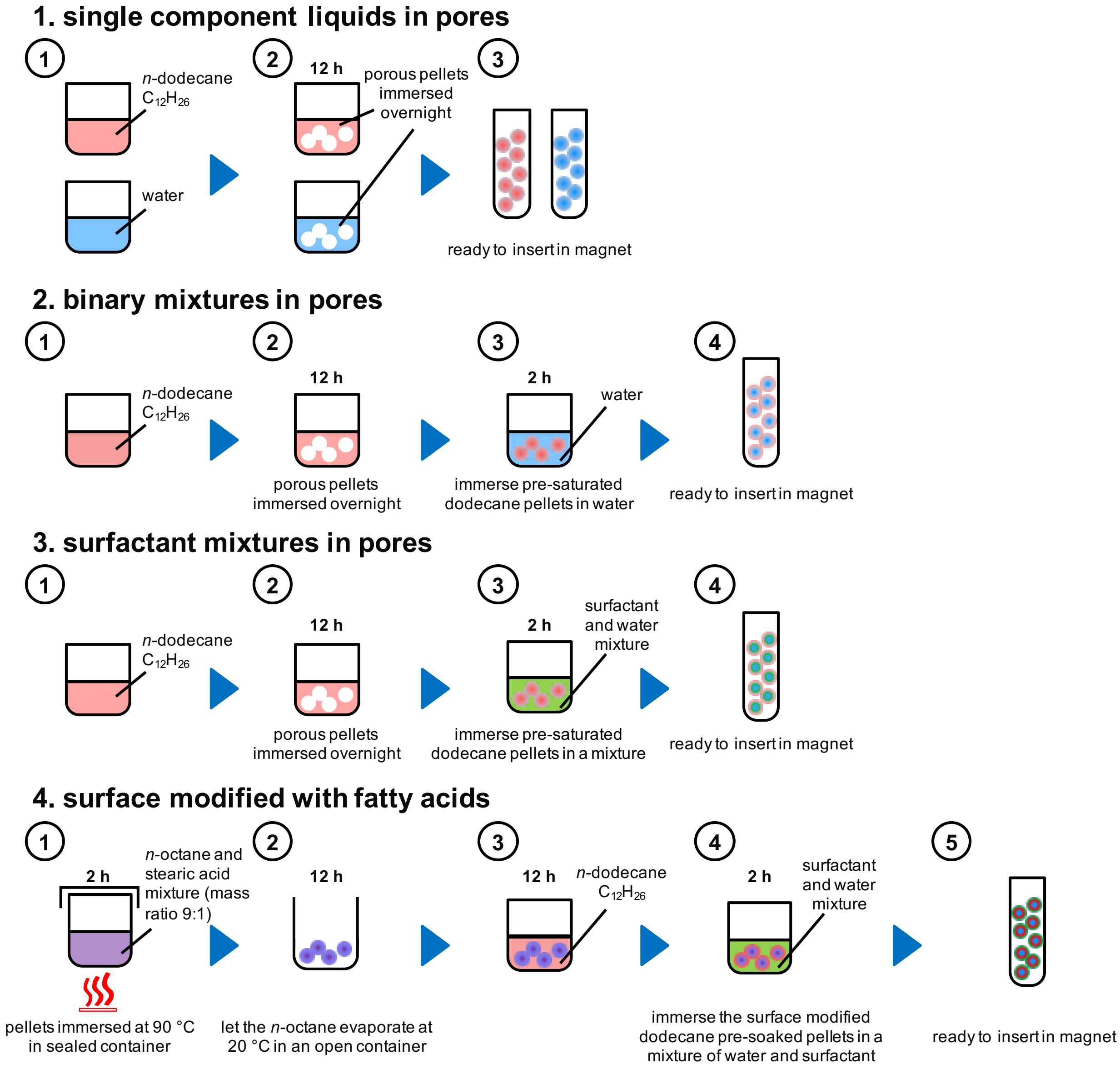

Figure 5.6 The sample preparation method per system: single component, binary, ternary and chemically modified samples.

5.3.4 NMR

The inversion recovery pulse sequence was used to measure T_1, while the CPMG pulse sequence was implemented to obtain T_2. Diffusion measurements were performed using the APGSTE pulse sequence to minimise the effect of background radiation and internal gradients in the porous system. The diffusion probe with a 10 mm coil was used as this also gives temperature control, with a gradient set reaching a maximum magnetic field gradient of 1000 G cm^{-1} in the z-direction. Diffusion measurements were carried out by varying δ or Δ with a gradient ramp time of 0.15 ms and with a gradient stabilisation time of 0.5 ms.

A homospoil gradient of 100 G cm^{-1} with a duration of 5 ms, to destroy any remaining transverse magnetisation, was applied. The maximum magnetic field gradient varied was usually extended between 200 and 1000 G cm^{-1}. In addition, Δ was 50 ms for pure, bulk liquids, while for bulk liquids and binary mixtures imbibed in porous media, Δ ranged between 50 and 500 ms. Finally, the experiments were averaged over 8 scans to increase the SNR ratio and to accommodate the complete phase cycle of the sequence. It is important to note that all standard errors are quoted using a 95% confidence interval for each relaxation or diffusion value. Typical pulse parameters for the diffusion measurements on the binary mixtures are listed in Table 5.6.

Table 5.6 Pulse parameters and delays used in the diffusion experiments on the mixtures.

Variable	**Description**	**Unit**	**Value**
D1	Delay 1	[s]	5
P1	90° high power pulse	[µs]	11.5
PL1	Power level	[dB]	6
RG	Receiver gain	[-]	8
	Gradient ramp time	[ms]	0.15
	Gradient pulse stabilisation time	[ms]	0.5
	Repetition time	[ms]	3000
Δ	Observation time	[ms]	5-500
δ	Gradient pulse duration	[ms]	1-5
NS	Number of scans	[-]	8
TD	Time domain size	[-]	4096
	Homospoil gradient strength	[G cm^{-1}]	100
	Homospoil duration	[ms]	5
$\boldsymbol{G}_{\max}$	Max. field gradient strength	[G cm^{-1}]	200-1000

5.4 Data Analysis

5.4.1 Sensitivity Analysis: Effect of Integration Methods

This section discusses how the data is analysed in MATLAB® R2015b using a personalised script to perform the following steps:

1. Automatic phase correction for each individual spectrum
2. Perform a baseline correction to each individual spectrum
3. Plot the processed, non-deconvoluted peaks of both water and dodecane together
4. If chosen, deconvolute peak 1 (*water*) and peak 2 (*dodecane*)
5. If chosen, perform curve-fitting to peak 1 and peak 2
6. Integrate area: the normal spectrum (**Step 3**) or deconvoluted peak (**Step 4**)
7. Calculate maximum intensity and normalise this value
8. Plot the diffusion data
9. Fit the diffusion data to ST equation
10. Extract the fitting coefficients and obtain self-diffusion coefficient

In this Section, three different analysis methods of the water signal are discussed. The three different methods differ only in Steps 3 and 6 from above. All the other steps are kept similar throughout the different methods. It should be mentioned that the water and dodecane peak have a peak separation of approximately 3.4 ppm relative to the ^{1}H resonance of TMS and therefore are arguable well enough separated not to require any peak deconvolution. The water and dodecane peak overlap minimally, and therefore their respective influence is negligible.

In order to assess the quality of the different ways of analysing the PFG NMR data, the data is processed using the three methods. The ST results of the water signal in the binary system of water-dodecane imbibed in Q-15 silica at 20 °C are obtained for a signal attenuation to 0.1% of the original signal and the self-diffusion coefficients of water are calculated.

The three analysis methods are listed below. Only the water signal is analysed and discussed here. However, the same method is applied to the dodecane signal and very similar results are obtained. The same conclusion applies for both signals and therefore only 1 water signal case is discussed.

1. Integrate the area underneath the deconvoluted peak and use a normal baseline correction for both peaks. This correction is performed by averaging the baseline and subtracting it from the processed spectrum.
2. Integrate the area underneath the deconvoluted peak but apply a baseline correction only applicable for the water peak. The deconvoluted fitted peak will match the water peak much better using this method, see Figure 5.8a.
3. Integrate the area underneath the normally processed, non-deconvoluted peak assuming the 3.4 ppm peak separation is sufficient.

In Figure 5.7a one can observe that the deconvoluted peak of water (—) does not fit 100% well but on the contrary the dodecane (—) does. The deconvoluted water peak is fitted and used to integrate the water signal. Figure 5.7b shows the signal attenuation and the fit to the diffusion data accordingly. A nearly perfect fit is obtained resulting in a $D_{\mathrm{eff}\,(\infty)} = 1.35 \pm 0.1 \times 10^{-9}$ m^2 s^{-1}.

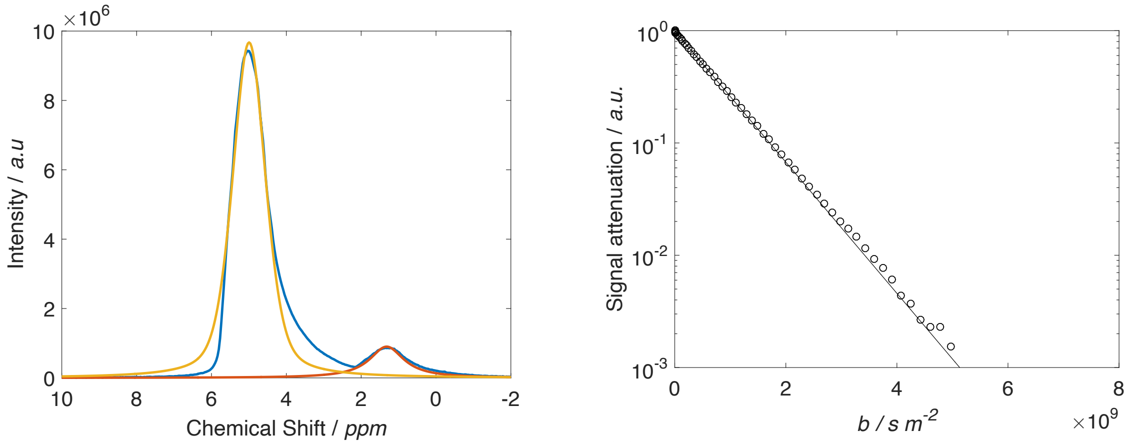

(a) ^{1}NMR spectra of the binary system of water and dodecane. The normal spectra (—), the deconvoluted peaks of water (—) and dodecane (—).

(b) ST plot for water signal in the binary system of water-dodecane imbibed in Q-15 silica at 20 °C, resulting in $D_{\mathrm{eff}\,(\infty)} = 1.35 \pm 0.1 \times 10^{-9}$ m^2 s^{-1}.

Figure 5.7 Results of method 1 for analysis of spectra of binary mixture of water-dodecane / Q-15 with δ = 1 ms and Δ = 100 ms.

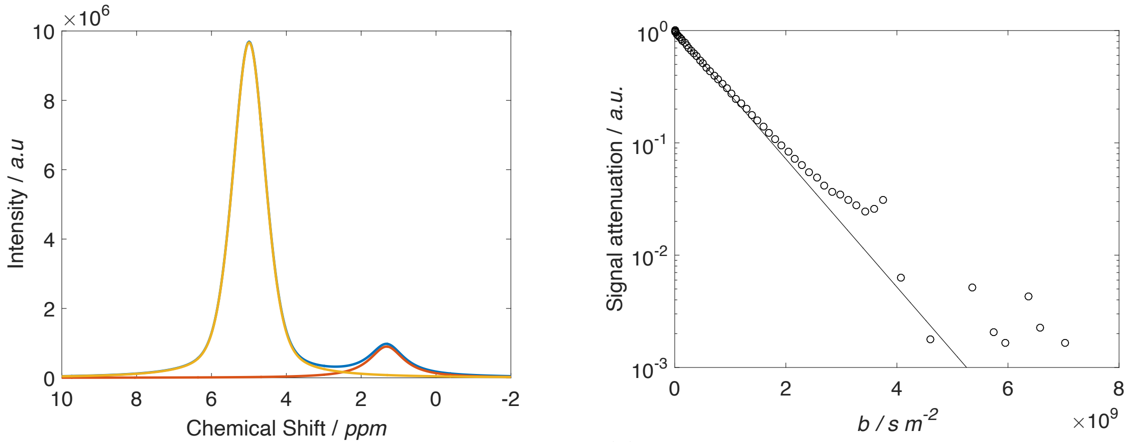

(a) ^{1}NMR spectra of the binary system of water and dodecane. The normal spectra (—), the deconvoluted peaks of water (—) and dodecane (—).

(b) ST plot for water signal in the binary system of water-dodecane imbibed in Q-15 silica at 20 °C, resulting in $D_{\mathrm{eff}\,(\infty)} = 1.30 \pm 0.1 \times 10^{-9}$ m^2 s^{-1}.

Figure 5.8 Results of method 2 for analysis of spectra of binary mixture of water-dodecane / Q-15 with δ = 1 ms and Δ = 100 ms.

In Figure 5.8a it can be seen that the deconvoluted peak of water (——) does fit very well to the original water peak (——). This is logical as only the water peak was used for the baseline correction and phasing, neglecting the dodecane peak. As a consequence, the dodecane peak (——) does not match the original peak well. In this method the new deconvoluted water peak is used to integrate the water signal. Figure 5.8b shows the signal attenuation and the fit to the diffusion data accordingly. For the second analysis method the data points in the very low SNR region fluctuate greatly and deviate from the fit. The $D_{\mathsf{eff}\,(\infty)}$ obtained for this fit equals 1.30 ± 0.1 × 10^{-9} m^2 s^{-1}.

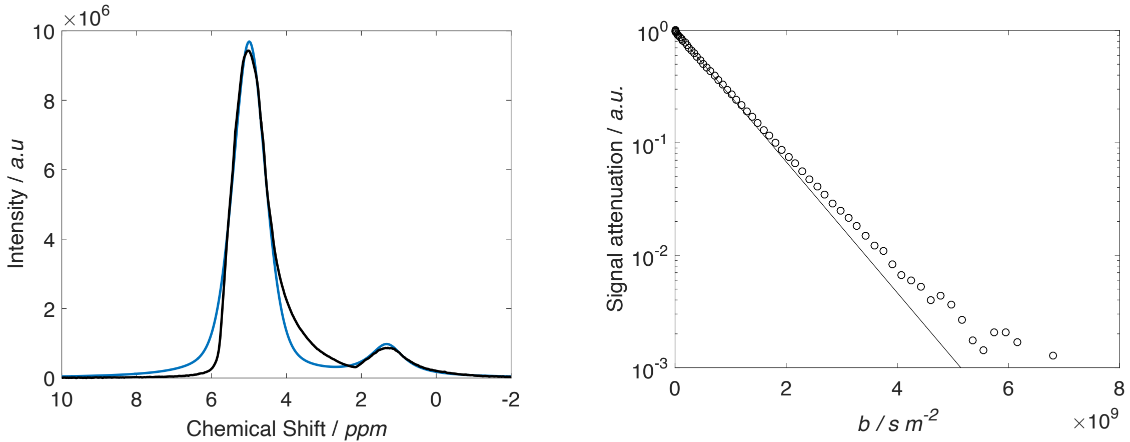

(a) ^{1}NMR spectra of the binary mixture of water and dodecane. The normal spectra (——) and the sum of deconvoluted water and dodecane peaks (——).

(b) ST plot for water signal in the binary system of water-dodecane imbibed in Q-15 silica at 20 °C, resulting in $D_{eff\,(\infty)}$ = 1.33 ± 0.1 × 10^{-9} m^2 s^{-1}.

Figure 5.9 Results of method 3 for analysis of spectra of binary mixture of water-dodecane / Q-15 with δ = 1 ms and Δ = 100 ms.

Figure 5.9a is the same as Figure 5.7a, except the sum of the deconvoluted peaks are shown (——) in comparison to the original peaks of water and dodecane (——). This analysis method does not integrate the area underneath the deconvoluted water peak, but only integrates underneath the original water peak (——) on the left hand side. Figure 5.9b shows the signal attenuation and the fit to the diffusion data accordingly. Using this third analysis method there is a slight deviation from the fit starting halfway through the gradient steps. The $D_{\mathsf{eff}\,(\infty)}$ obtained for this fit equals 1.33 ± 0.1 × 10^{-9} m^2 s^{-1}.

As can be seen from all the fits to the diffusion data, method 1 clearly has the best fit. In addition, the variation in self-diffusion coefficient obtained vary between 1.30 and 1.35 × 10^{-9} m^2 s^{-1}, which is only a 3 % difference. It can therefore be concluded that the three methods give very similar diffusion coefficients. For all future diffusion data processing, method 1 is chosen.

5.4.2 General NMR Restricted Diffusion Methods

There are two general approaches to interpret the signal loss for the case of restricted molecular diffusion in a spherical emulsion droplet to extract droplet size radius a. They are presented below.

1. Gaussian Phase Distribution Model (GPDM) This was formulated by Murday and Cotts, [242], and assumes that the NMR signal phase distribution of the signal can be described using a Gaussian shape. This is the most commonly used model of restricted diffusion within emulsion droplets to enable droplet sizing. An emulsion consists of droplets with a distribution of radii. The NMR signal attenuation observed is a volume-weighted average of the attenuations due to the range of droplet sizes [243]. The NMR attenuation due to the diffusion of protons in a sphere with diameter $2a$ can be calculated as:

$$\begin{gathered}\left(\ln \frac{S}{S_0}\right) = R(\Delta, \delta, a, g) = -2\gamma^2 g^2 \sum_{m=1}^{\infty} \frac{1}{\alpha_{\mathrm{m}}^2(\alpha_{\mathrm{m}}^2 a^2 - 2)} \times \\ \left(\frac{2\delta}{\alpha_{\mathrm{m}}^2 \mathrm{D}} - \frac{2 + e^{-\mathrm{D}(\Delta-\delta)\alpha_{\mathrm{m}}^2} - 2e^{-\mathrm{D}\Delta\alpha_{\mathrm{m}}^2} - 2e^{\mathrm{D}\delta\alpha_{\mathrm{m}}^2} + e^{-\mathrm{D}(\Delta+\delta)\alpha_{\mathrm{m}}^2}}{(\alpha_{\mathrm{m}}^2 \mathrm{D})^2}\right).\end{gathered} \tag{5.5}$$

The α_{m}^2 is given by the positive roots of the following expression, where J_n is an nth order Bessel function [244]:

$$J_{\frac{3}{2}}(\alpha a) = \alpha a J_{\frac{5}{2}}(\alpha a). \tag{5.6}$$

2. Short Gradient Pulse Method (SGPM) This model is also commonly used in NMR droplet size measurements and assumes that the duration of the applied field gradient, δ, tends to zero [244]. Balinov *et al.* considered the relative accuracy of the SGPM to size emulsion droplets by comparing their predictions against numerical random walk simulations of diffusion restricted to a spherical cavity. Their conclusion was that for this methodology the error in the predicted droplet size was consistently less than 6% [245].

$$\begin{gathered}\frac{S}{S_0} = \frac{9(qa\cos(qa) - \sin(qa)^2)}{(qa)^6} - 6(qa)^2 \times \sum_{n=0}^{\infty} \left[J_n'(qa)\right]^2 \\ \times \sum_m \frac{(2n+1)\alpha_{nm}^2}{\alpha_{nm}^2 - n^2 - n} \times \left(\exp\left\{-\frac{\alpha_{nm}^2 D_0 \Delta}{a^2}\right\}\right) \frac{1}{\left[\alpha_{nm}^2 - (qa)^2\right]^2}.\end{gathered} \tag{5.7}$$

This equation can be reduced for the case of an infinite Δ to:

$$\frac{S}{S_0} = \frac{9(qa\cos(qa) - \sin(qa)^2)}{(qa)^6} \tag{5.8}$$

The only free parameter is the radius droplet, a, and all the other variables are determined by the experiment execution. q is equal to $g\gamma\delta$ and α_{nm} is the mth root of the equation $J_n'(\alpha) = 0$.

The experimentally observed NMR attenuation $< R(\Delta,\delta) >$ can be expressed in terms of the calculated attenuation of individual droplets R from Equation 5.5 through the relation:

$$< R(\Delta,\delta) >= \frac{\int_0^\infty a^3 P(a) R(\Delta,\delta,a) da}{\int_0^\infty a^3 P(a) da} \tag{5.9}$$

where $P(a)$ is the DSD and the factor a^3 reflects that the NMR intensity is proportional to the number of protons. The functional form of $P(a)$ is not unique. Packer and Rees adopted a log-normal function [168, 246]:

$$P(a) = \frac{1}{2a\sigma(2\pi)^{0.5}} \exp\left\{-\frac{(\ln 2a - \ln\xi)^2}{2\sigma^2}\right\}. \tag{5.10}$$

By fitting the NMR data, Packer and Rees were able to extract the parameters ξ and σ and hence obtain the size distribution of the water droplets in their emulsion samples [246].

5.4.3 Alternative Methods for Droplet Size Distributions

1) Emulsion droplet sizing via PFG NMR is conventionally a time consuming measurement, with typical acquisition times ranging from 5 - 120 minutes. A much faster variant of the stimulated echo pulse sequence is the Difftrain. This relies on a train of signal acquisitions following one single excitation in which Δ is gradually increased. The total acquisition time can be about 4 s [247].

2) Another method of using NMR for emulsion droplet sizing is based on T_2 relaxation of the dispersed droplet phase molecules. The value of T_2 for the dispersed phase can be related to the droplet size by Equation 5.11 using ρ for the surface relativity:

$$\frac{1}{T_2} = \frac{1}{T_{2,bulk}} + \rho\frac{S}{V} = \frac{1}{T_{2,bulk}} + \rho\frac{3}{a}. \tag{5.11}$$

If this condition is met, a distribution of droplet sizes will result in a distribution of T_2.

5.4.4 Droplet Size Distribution Regularisation Method

As Equation 5.9 is not known as an analytical function, but rather as a discrete set of measurements contaminated with experimental error, it is not possible to extract directly $P(a)$. However, it is possible to solve Equation 5.9 without using prior knowledge about the functional form of $P(a)$ by employing Tikhonov regularisation techniques, see [170].

The denominator in Equation 5.9 is a constant for a given emulsion and hence neglecting it, the integral in the numerator can be rewritten as:

$$b_i = \sum_{j=1}^{m} R(g_i, a_j) P(a_j) \delta_j, \tag{5.12}$$

where b_i is the i th attenuation reading corresponding to a gradient field strength of g_i. The matrix R represents the value of the attenuation for discrete values of g and a, multiplied by a^3. Equation 5.12 can thus also be rewritten in matrix algebra as:

$$\mathbf{b} = \mathbf{RP}. \tag{5.13}$$

Such linear algebra systems can be solved by finding $\mathbf{P}$ such that a certain quantity, H, is minimised:

$$H = \min \|\mathbf{RP} - \mathbf{b}\|^2. \tag{5.14}$$

Two general issues with this regularisation method are that (i) noise in $\mathbf{b}$ could cause large fluctuations in the solution $\mathbf{P}$ and (ii) that $\mathbf{P}$ could become very oscillatory. To overcome both issues, a penalty function to increase the smoothness is added to Equation 5.14:

$$H = \min \left\{ \|\mathbf{RP} - \mathbf{b}\|^2 + \lambda^2 \|\mathbf{LP}\|^2 \right\}. \tag{5.15}$$

This Equation 5.15 can be divided into two terms; the first ($\|\mathbf{RP} - \mathbf{b}\|^2$) known as the *residual norm* indicates how close $\mathbf{P}$ is to the true solution. The second term ($\|\mathbf{LP}\|^2$) determines the value of the *penalty function* and therefore represents the smoothness of the function. λ is a regularisation parameter used to control the extend of smoothing the solution. Finally, $\mathbf{L}$ is the operator which is used to regulate the smoothness criterion and is based on the second derivative of $\mathbf{P}$. A high value of λ will result in a very smooth solution, while on the contrary low λ values will create more exact solutions to the analytical problem. Finally, the DSD obtained using this Tikhonov regularisation method is not only expected to be smooth and continuous but all the points should also be positive according to this solution [244].

In this work, the Tikhonov regularisation was initially used but replaced by the regularisation method described below. The Tikhonov is not used as it can only be used reliably if one has prior knowledge that H will give a smooth solution [248].

The regularisation method used in this work to process diffusion data to obtain DSD is termed the Modified Total Generalized Variation (MTGV) regularisation, further described by Reci *et al.* [248]. To estimate the distribution $\underline{F}$, one needs Equation 5.16. All terms appearing in this Equation are tabulated below in Table 5.7

$$(\underline{F}, \underline{W}) = \arg\ \min_{\underline{F}\geqslant 0, \underline{W}} \left(\frac{\alpha}{2}\|\underline{K}\underline{F} - \underline{S}\|_2^2 + \|\underline{F} - \underline{W}\|_1 + \beta\|\underline{D}_2\underline{W}\|_1^*\right). \tag{5.16}$$

In this minimisation problem, α and β are regularisation parameters, $\underline{W}$ represents an auxiliary vector and $\underline{D}_2$ is a matrix that acts like a second derivative of the vector it is applied on. The second and final term in the MTGV regularisation form the penalty term. The reason it is composed of two parts is to balance the discrete and smooth features. The parameter β controls the weighting that enforces any of these two features.

Table 5.7 List of parameters of Equation 5.16 with their description.

Symbol	**Description**
α	regularisation parameter
β	regularisation parameter
$\underline{F}$	distribution functions
$\underline{W}$	auxiliary vector
$\underline{K}$	kernel matrix
$\underline{S}$	discretised vector of signal
$\underline{D}_2$	matrix that acts like a second derivative

5.5 Results and Discussion

5.5.1 Pure Liquids

The relaxometry and diffusometry results for these pure, bulk liquids are summarised in Table 5.8. The T_1, T_2 and D_0 values are reported for both liquids, and the literature values for the self-diffusion coefficients are tabulated as well, according to Holz *et al.* [249]. There is in very good agreement with the diffusion coefficients at 20 and 40 °C, however at 60 °C the literature values are slightly higher [249]. In addition, the temperature dependence on the relaxometry and diffusometry results can be observed; as temperature increases, all values rise accordingly.

Table 5.8 ^{1}H NMR relaxation and diffusion parameters for water and dodecane in bulk conditions. The D in the table represents the D_0 (× 10^{-9} m^2 s^{-1}) for free, bulk water and the D_{lit} (× 10^{-9} m^2 s^{-1}) for similar systems described in literature.

	Water			**Dodecane**		
	20 °C	40 °C	60 °C	20 °C	40 °C	60 °C
$\boldsymbol{T_1}$ [s]	2.80 ± 0.05	3.37 ± 0.06	3.50 ± 0.06	1.07 ± 0.04	1.47 ± 0.04	1.89 ± 0.04
$\boldsymbol{T_2}$ [s]	2.10 ± 0.01	3.47 ± 0.02	4.70 ± 0.03	1.34 ± 0.01	1.51 ± 0.01	1.73 ± 0.02
$\boldsymbol{D_0}$ [m^2 s^{-1}]	2.10 ± 0.08	3.10 ± 0.11	4.50 ± 0.12	0.76 ± 0.07	1.10 ± 0.08	1.40 ± 0.09
$\boldsymbol{D_{lit}}$ [m^2 s^{-1}]	2.02	3.25	4.77	0.81	1.20	1.60

The ST plots for pure water and dodecane at $\delta = 1$ ms and $\Delta = 50$ ms are shown in Figure 5.10 at 20, 40 and 60 °C. The data points align well on a straight line on a semi-log scale, indicating the free self-diffusion of those molecules. The signal attenuates below 1% for both cases. In Figure 5.10, the slopes of the diffusion decays are proportional to the MSD of the molecules at different observation times Δ. For longer observation times, the slope becomes steeper as the molecules are allowed to travel a further distance thus the MSD increases.

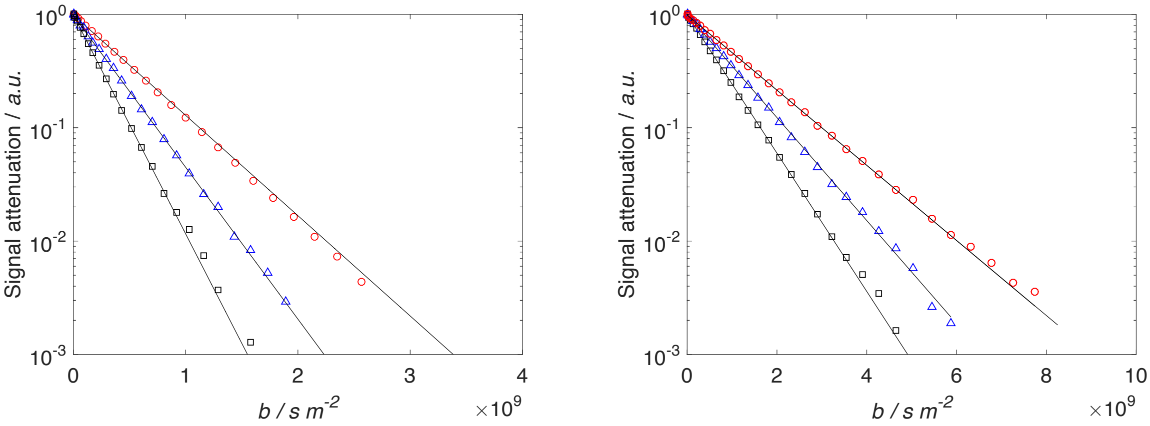

(a) ST plot for bulk water at 20 °C (○), 40 °C (△) and 60 °C (□).

(b) ST plot for bulk dodecane at 20 °C (○), 40 °C (△) and 60 °C (□).

Figure 5.10 ST plots for bulk, pure water (a) or dodecane (b), with δ = 1 ms and Δ = 50 ms at various temperatures.

5.5.2 Pure Liquids in Q-silica

Tables 5.9 and 5.10 summarise all the relaxometry and diffusometry results for the pure, bulk liquids imbibed in either Q-15 or Q-50 silica beads. As expected the T_1 and T_2 results for the imbibed liquids are one or two orders of magnitude lower than the pure, bulk liquids, reported in Table 5.8. Again, all the values follow an increasing trend according to a temperature rise.

Table 5.9 ^{1}*H NMR relaxation and diffusion parameters for water imbibed in Q-15 or Q-50 silica. The D in the table represents the* D_0 *(×* 10^{-9} m^2 s^{-1}*) for free, bulk water and the* $D_{\mathrm{eff}\,(\infty)}$ *(×* 10^{-9} m^2 s^{-1}*) for water imbibed in Q-silica beads.*

	Water / Q-15			**Water / Q-50**		
	20 °C	40 °C	60 °C	20 °C	40 °C	60 °C
T_1 [s]	0.68 ± 0.05	0.93 ± 0.06	1.25 ± 0.07	0.74 ± 0.05	1.04 ± 0.04	1.45 ± 0.03
T_2 [s]	0.05 ± 0.01	0.07 ± 0.01	0.10 ± 0.01	0.12 ± 0.01	0.17 ± 0.01	0.23 ± 0.01
D_0 [m^2 s^{-1}]	2.10 ± 0.08	3.10 ± 0.11	4.50 ± 0.12	2.10 ± 0.08	3.10 ± 0.11	4.50 ± 0.12
$D_{\mathrm{eff}\,(\infty)}$ [m^2 s^{-1}]	1.36 ± 0.08	2.07 ± 0.11	2.94 ± 0.16	1.30 ± 0.04	2.07 ± 0.09	2.90 ± 0.10
Tortuosity [-]	1.5 ± 0.1	1.5 ± 0.1	1.5 ± 0.1	1.6 ± 0.1	1.5 ± 0.1	1.6 ± 0.1

The diffusion parameters are obtained from the ST fits, shown in Figure 5.11. By comparing the D_0 and the $D_{\mathrm{eff}\,(\infty)}$ values, which are representing the free self-diffusion and the diffusivity of the imbibed liquids, Equation 4.2 can be used to determine the tortuosity of the Q-silica catalyst supports. It is important to note that this is the apparent tortuosity experienced by a particular liquid. The calculated tortuosities for all systems are very similar, varying around 1.5 with the necessary 95% confidence interval. This strongly suggests that both water and dodecane can fill up all the pore system independently and thus are not excluded due to any pore confinements effects. When the liquids are adsorbed in porous media, their diffusivity decreases due to the diffusion restriction that the pore geometry and surface structure impose.

Table 5.10 ^{1}*H NMR relaxation and diffusion parameters for dodecane imbibed in Q-15 or Q-50 silica. The D in the table represents the* D_0 *(×* 10^{-9} m^2 s^{-1}*) for free, bulk dodecane and the* $D_{\mathrm{eff}\,(\infty)}$ *(×* 10^{-10} m^2 s^{-1}*) for dodecane imbibed in Q-silica beads.*

	Dodecane / Q-15			**Dodecane / Q-50**		
	20 °C	40 °C	60 °C	20 °C	40 °C	60 °C
T_1 [s]	0.94 ± 0.05	1.06 ± 0.03	1.34 ± 0.08	0.93 ± 0.05	1.20 ± 0.07	1.53 ± 0.09
T_2 [s]	0.45 ± 0.02	0.69 ± 0.03	0.93 ± 0.04	0.58 ± 0.02	0.78 ± 0.01	0.97 ± 0.02
D_0 [m^2 s^{-1}]	0.76 ± 0.07	1.10 ± 0.08	1.40 ± 0.09	0.76 ± 0.07	1.10 ± 0.08	1.40 ± 0.09
$D_{\mathrm{eff}\,(\infty)}$ [m^2 s^{-1}]	4.23 ± 0.13	6.23 ± 0.15	8.38 ± 0.13	5.16 ± 0.08	7.20 ± 0.11	9.90 ± 0.15
Tortuosity [-]	1.8 ± 0.1	1.8 ± 0.1	1.7 ± 0.1	1.5 ± 0.1	1.5 ± 0.1	1.4 ± 0.1

One interesting result is that the tortuosity of the dodecane imbibed in Q-15 system is approximately 1.8, thus slightly higher than the 1.5 of the other systems. The bulky, long hydrocarbon has somewhat more difficulty in filling up the complete pore network of the smaller Q-silica bead. This could be caused by a chain confinement effect when the pore size becomes too small for dodecane that it be could excluded from the smaller pores in the support. This effect is not seen for the dodecane in Q-50, where the tortuosity is again 1.5. On the contrary, water is (i) not excluded from the smaller pore regions and (ii) does not have a sufficiently strong surface interaction strength to hinder its mobility through the pore confinements.

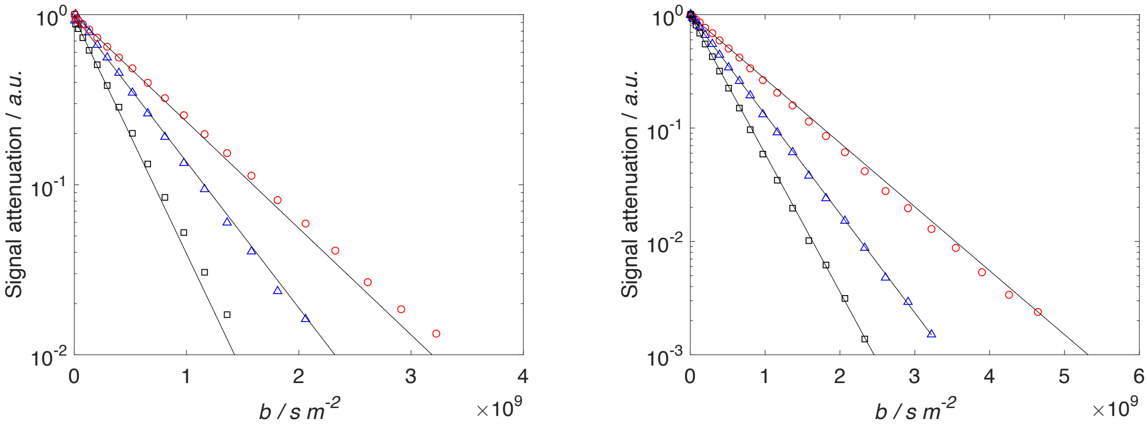

(a) ST plot for water in Q-15 silica at 20 °C (○), 40 °C (△) and 60 °C (□).

(b) ST plot for water in Q-50 silica at 20 °C (○), 40 °C (△) and 60 °C (□).

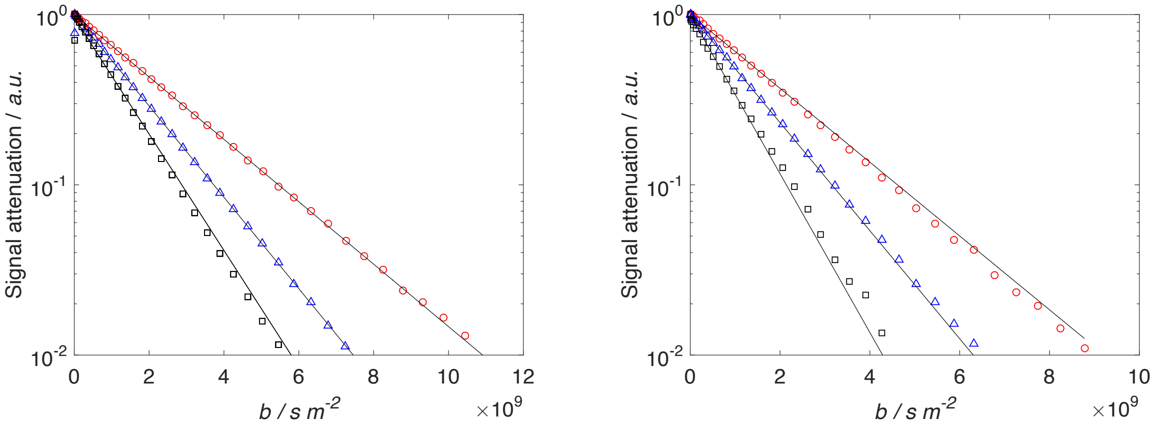

(c) ST plot for dodecane in Q-15 silica at 20 °C (○), 40 °C (△) and 60 °C (□).

(d) ST plot for dodecane in Q-50 silica at 20 °C (○), 40 °C (△) and 60 °C (□).

Figure 5.11 ST plots for bulk water or dodecane imbibed in either Q-15 or Q-50 silica spherical beads with δ = 1 ms and Δ = 50 ms at various temperatures.

5.5.3 Water/Dodecane Binary Mixtures

Relaxometry and Spectroscopy Results

Table 5.11 summarises all the relaxometry values for the binary mixture of water-dodecane imbibed in either Q-15 or Q-50 silica beads. As can be seen, in comparison with the values in Tables 5.8 and 5.9, the relaxation times of water in this binary system are quite similar to pure water imbibed in Q-silica, but much shorter compared to pure, bulk water. The T_1 for water in the binary system in Q-15 silica at 20 °C is 0.58 s ± 0.02, in comparison with 0.68 s ± 0.05 for the bulk imbibed system and 2.8 s ± 0.05 in the bulk, non-porous phase. The relaxometry behaviour of water in Q-50 silica is very similar. The T_2 value of bulk water in Q-15 silica at 20 °C of 2.10 s ± 0.01, decreased to 0.05 s ± 0.01 in the porous, bulk medium, and it was reduced even further to 0.03 s ± 0.01 in the binary mixture in silica.

Table 5.11 ^{1}H NMR relaxation parameters for water and dodecane in the binary mixture of water/dodecane imbibed in Q-15 or Q-50 silica.

		Water-dodecane / Q-15			**Water-dodecane / Q-50**		
		20 °C	40 °C	60 °C	20 °C	40 °C	60 °C
Water	T_1 [s]	0.58 ± 0.02	0.77 ± 0.02	1.06 ± 0.04	0.66 ± 0.06	0.97 ± 0.02	1.29 ± 0.03
	T_2 [s]	0.03 ± 0.01	0.05 ± 0.01	0.07 ± 0.01	0.11 ± 0.01	0.16 ± 0.02	0.18 ± 0.02
	T_1/T_2	19	15	15	6.0	6.0	7.1
Dodecane	T_1 [s]	1.06 ± 0.02	1.34 ± 0.02	1.64 ± 0.04	1.04 ± 0.06	1.31 ± 0.02	1.57 ± 0.03
	T_2 [s]	0.42 ± 0.01	0.47 ± 0.01	0.79 ± 0.03	0.22 ± 0.01	0.32 ± 0.02	0.34 ± 0.02
	T_1/T_2	2.5	2.8	2.0	4.7	4.1	4.6

For dodecane imbibed in Q-15 silica at 20 °C, the T_1 values in the binary mixture are lower than the bulk dodecane phase, however they are slightly higher than the bulk dodecane imbibed in the porous silica spheres. The T_1 of dodecane in Q-15 silica in the binary mixture of 1.06 s ± 0.02 is very comparable to the relaxation time of dodecane in the bulk phase, 1.07 s ± 0.04. However, this value decreased to 0.94 s ± 0.05 for pure dodecane in silica.

On the other hand, the T_2 values are not as similar for dodecane in the binary system (0.42 s ± 0.01) and the bulk liquid (1.34 s ± 0.01). The T_2 value of bulk dodecane in silica is 0.45 s ± 0.02. This difference in trend behaviour between the T_1 and T_2 of dodecane in the binary phase and bulk dodecane might be attributed to internal gradient effects in such heterogeneous systems.

The observed relaxation of water and dodecane suggest that water in the binary system experiences a stronger interaction with the surface of the supports and therefore causes an increase in its relaxation rate. This can be seen from the T_1/T_2 ratios in Table 5.11, indicative of the surface interaction strength, as water has a significantly higher ratio for all systems than dodecane [187]. On the other hand, dodecane behaves more like a bulk liquid, without great interaction with any surface. Therefore, it can be concluded that water is the surface-wetting phase and dodecane tends to be isolated from the surface walls.

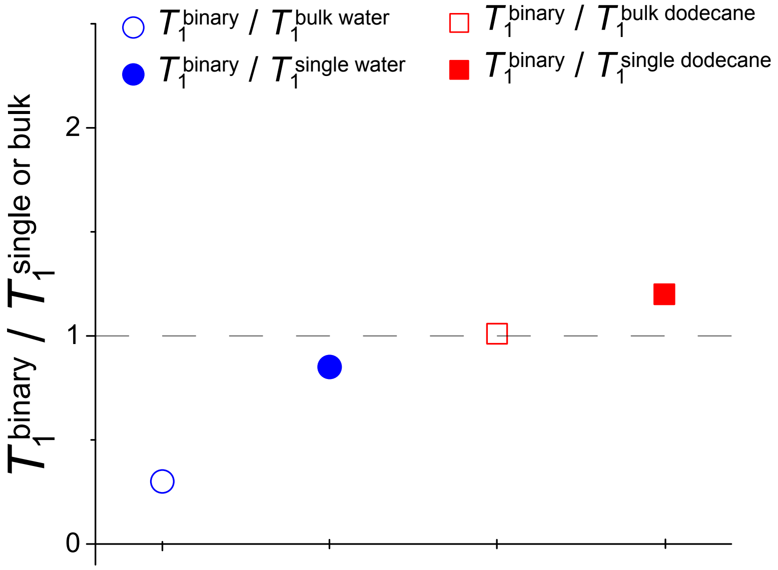

Figure 5.12 Plot for comparison of normalised T_1 values for water (● and ○) and dodecane (■ and □). The numerator consists of the T_1 value for the respective liquid in the binary mixture. The denominator is either the T_1 of the liquid in the bulk phase or the single phase liquid imbibed in the Q-15 silica at 20 °C.

Figure 5.12 summarises all the normalised T_1 values for water and dodecane in their binary mixture confined in Q-15 silica at 20 °C, to get a better understanding of how the molecular surroundings affect the relaxation rates of the individual species. The ratios are either normalised to the T_1 value of the respective bulk liquids (empty symbols) or normalised to the single-phase liquid imbibed in the Q-15 silica (full symbols). T_1 ratios < 1 indicate enhanced relaxation, i.e. stronger molecular interaction, while the opposite is true for ratios > 1.

Ratios $= 1$ (see dashed line as reference) indicate no relative T_1 variation. It is clearly seen that the latter condition is verified for dodecane in the binary mixture as to bulk dodecane (□). This suggests that dodecane in the binary mixture is not much affected by the confinement. On the other hand, the ratio of T_1 of dodecane in the binary mixture over that for the single phase dodecane both imbibed in Q-15 silica (■), is about 1.13. This indicates that the interaction of dodecane with the surface of the alumina in the binary mixture is weaker than in the single-phase. This value indicates that in the binary mixture the presence of water partially shields the interaction of dodecane with the pore walls.

In contrast, water exhibits much faster relaxation, by a factor of 5, in the confined, binary mixture (○) than in the bulk. In good agreement with the dodecane behaviour, this seems to indicate that water acts as a surface-wetting component while dodecane would be in the bulk phase, more isolated from the surface, forming a pool in the centre of the pores. For water, the T_1/T_2 parameter, indicative of the surface interaction strength has a T_1/T_2 coefficient of 20 ± 5 while dodecane has a T_1/T_2 of only 2.5 ± 0.5 for the Q-15 silica temperature range. Very similar behaviours are found for the systems at 40 and 60 °C.

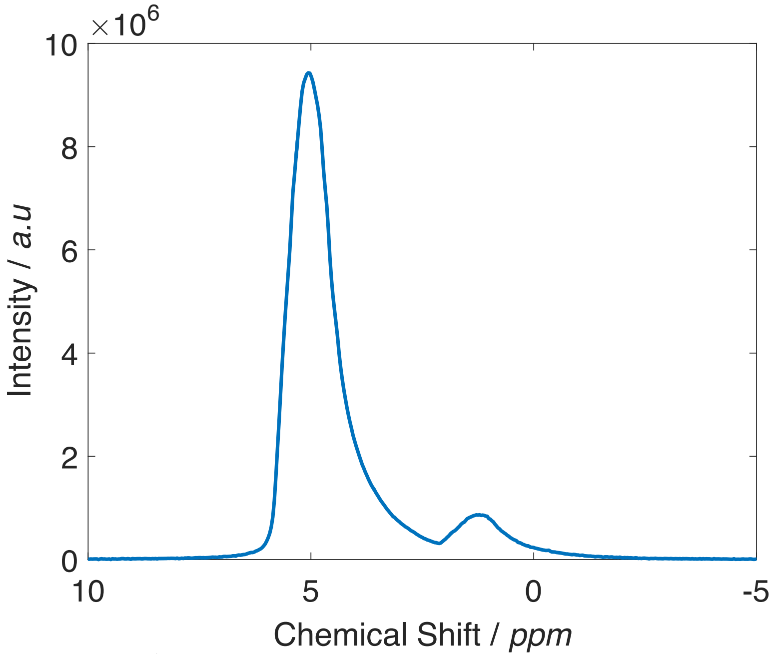

Figure 5.13 ^{1}H NMR spectra of water-dodecane imbibed in Q-15.

Using the spectra shown in Figure 5.13, the composition of the intrapellet liquid in Q-15 silica beads can be determined by integrating the ^{1}H NMR spectrum to obtain the signal contribution of each component. The composition inside the Q-15 pellets is found to be around 90± 4 vol% of water and the remainder being dodecane. The spectrum for the binary mixture imbibed in Q-50 pellets is nearly identical to the spectrum in Figure 5.13.

Diffusometry Results of Water / Q-silica

Table 5.12 summarises all diffusion values for the binary mixture of water-dodecane imbibed in either Q-15 or Q-50 silica beads. These parameters are based on the water signal, as the ST theory is only valid for non-restricted self-diffusion components. Therefore extracting an apparent diffusion coefficient for dodecane is not applicable in this situation. Again, the tortuosity can be calculated using Equation 4.2 for water in this case. Very similar values are obtained of around 1.8. However these values are logically a fraction higher than the 1.5 for pure water in Q-silica as both water and dodecane are competing to enter the porous system, therefore increasing the tortuosity.

Table 5.12 ^1H NMR diffusion parameters for water in the binary mixture of water/dodecane imbibed in Q-15 or Q-50 silica. The D in the table represents the D_0 (× 10^{-9} m^2 s^{-1}) for free, bulk water and the $D_{\mathrm{eff}(\infty)}$ (× 10^{-9} m^2 s^{-1}) the water signal in the binary mixture imbibed in Q-silica beads.

Water signal	**Water-dodecane / Q-15**			**Water-dodecane / Q-50**		
	20 °C	40 °C	60 °C	20 °C	40 °C	60 °C
$\boldsymbol{D_0}$ [m^2 s^{-1}]	2.10 ± 0.08	3.10 ± 0.11	4.50 ± 0.12	2.10 ± 0.08	3.10 ± 0.011	4.50 ± 0.08
$\boldsymbol{D_{\mathrm{eff}\,(\infty)}}$ [m^2 s^{-1}]	1.20 ± 0.02	1.81 ± 0.03	2.65 ± 0.04	1.26 ± 0.06	1.90 ± 0.02	2.70 ± 0.09
Tortuosity [-]	1.8 ± 0.1	1.7 ± 0.1	1.7 ± 0.1	1.7 ± 0.1	1.6 ± 0.1	1.7 ± 0.1

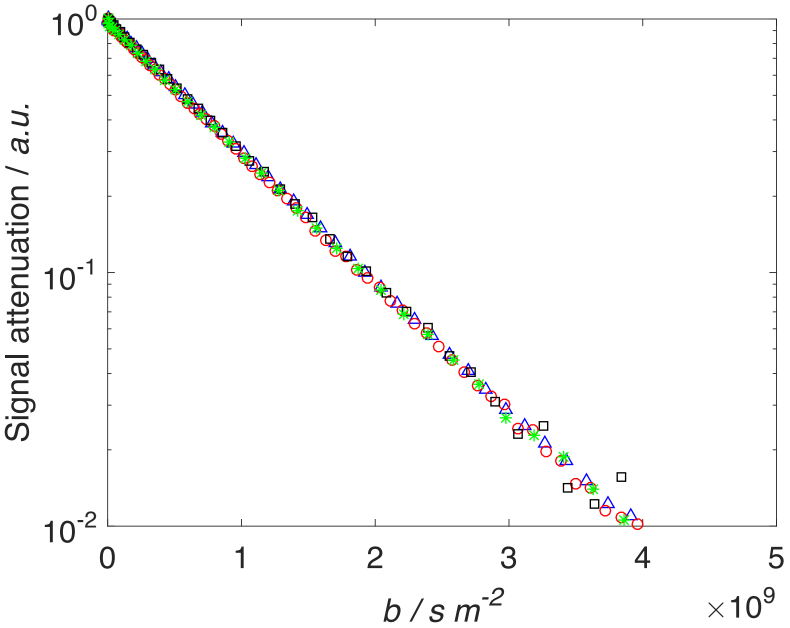

Figure 5.14 ST plot for water signal in water-dodecane imbibed in Q-15 silica, with Δ = 50 (∗), 150 (○), 300 (△) and 500 (□) ms at 20 °C.

To understand why water is the continuous phase and therefore does not encounter any restrictive diffusion behaviour, Figure 5.14 is important. It shows the signal attenuation of water in the binary mixture at 20 °C at increasing observation times Δ, ranging from 50 to 500 ms. All experimental data points overlap very well on the straight line, therefore showing that the PFG NMR response of water in the binary mixture follows the ST theory. Combining this finding with the conclusion from its relaxometry, it can be concluded that the water is the continuous phase. In all future plots, the water signal attenuation will be plotted for one single observation time of 50 ms only.

When comparing the $D_{\mathsf{eff}\,(\infty)}$ for water in the binary phase to diffusion for the single component reported in Table 5.9, it is revealed that the water diffusivity is only decreased by 12%. Thus the water behaviour is relatively unaffected by the presence of dodecane. From Figure 5.14 one can conclude that water still diffuses rather freely, but encounters a slightly more tortuous environment, due to the presence of dodecane. Figure 5.15 shows the ST plots for water in the binary system imbibed in Q-15 and Q-50 silica at various temperatures. These measurements were obtained with a δ of 1 ms and Δ of 50 ms. The water diffusivity increases as temperature rises. The effect of pore size is minimal, as the larger pore size distribution of 50 nm only allows for marginally higher diffusion rates.

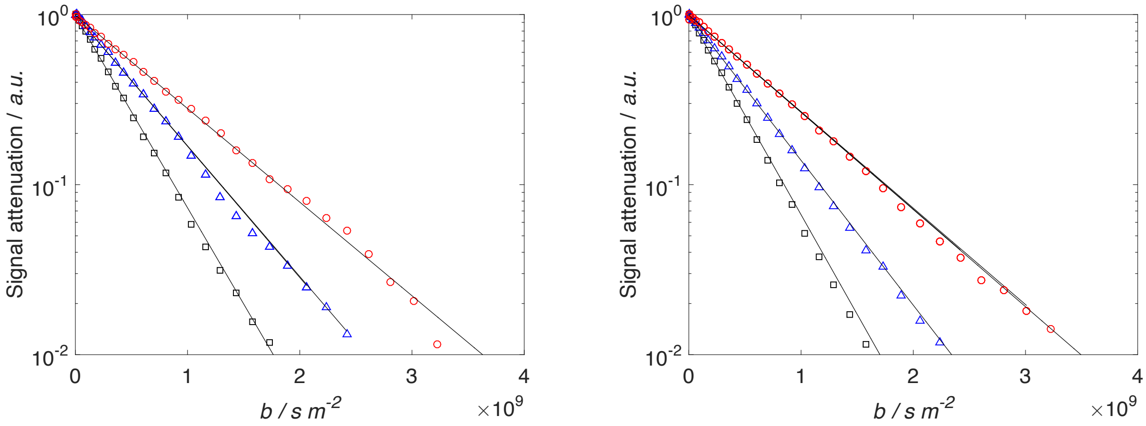

(a) ST plot for water signal in the binary system of water-dodecane imbibed in Q-15 silica at 20 °C (○), 40 °C (△) and 60 °C (□).

(b) ST plot for water signal in the binary system of water-dodecane imbibed in Q-50 silica at 20 °C (○), 40 °C (△) and 60 °C (□).

Figure 5.15 ST plots for water in binary mixture of water-dodecane imbibed in Q-silica, with δ = 1 ms and Δ = 50 ms at various temperatures.

Diffusometry Results of Dodecane / Q-15 silica

In order to better understand the diffusion behaviour of dodecane in the binary mixture, it is necessary to look at the plots in Figure 5.16. Firstly, one can observe that the attenuation of the dodecane signal has a very different curvature than water. Moreover, even at gradients strengths of 1000 G cm^{-1}, roughly 10% of the dodecane signal remains. The approximate diffusion coefficient for dodecane would be in the order of $D_{\mathsf{eff}(\infty)} \times 10^{-14}$ m^2 s^{-1}. Additionally, it can be observed that the diffusion data points do not lie along the same, straight line, as was the case for water in the binary systems. The curvature for the dodecane signal attenuation indicates clearly non-ideal diffusion behaviour, as a result of restricted dodecane molecules.

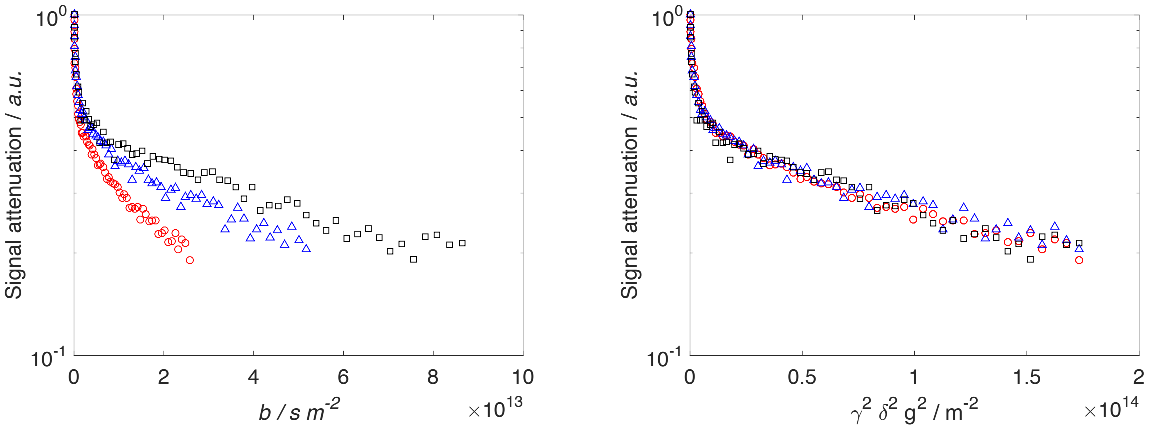

(a) ST plot for dodecane in water-dodecane imbibed in Q-15 silica, with $\Delta = 150$ *(○), 300 (△) and 500 (□) ms at 20 °C.*

(b) The same data plotted as in Figure (a) but as function of $\gamma^2\delta^2 g^2$*, with* $\Delta = 150$ *(○), 300 (△) and 500 (□) ms at 20 °C.*

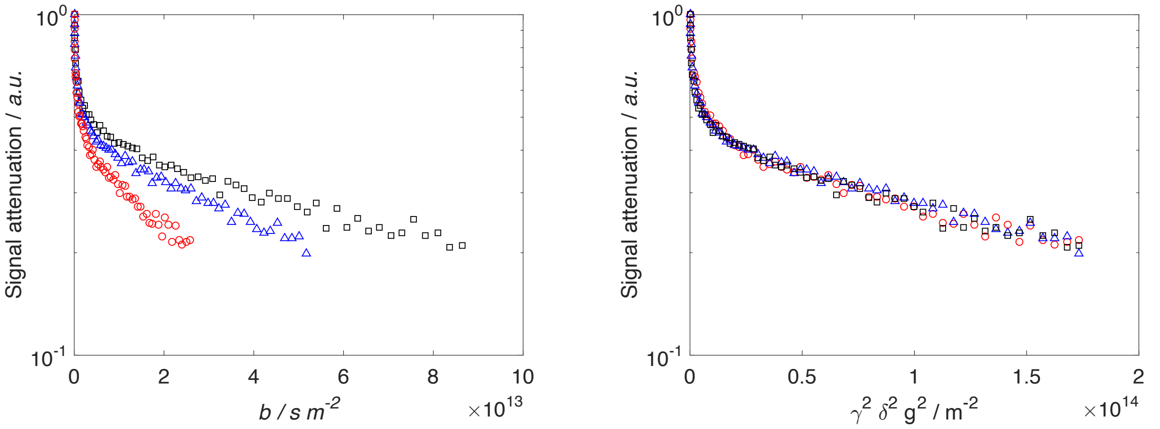

(c) ST plot for dodecane in water-dodecane imbibed in Q-15 silica, with $\Delta = 150$ *(○), 300 (△) and 500 (□) ms at 40 °C.*

(d) The same data plotted as in Figure (f) but as function of $\gamma^2\delta^2 g^2$*, with* $\Delta = 150$ *(○), 300 (△) and 500 (□) ms at 40 °C.*

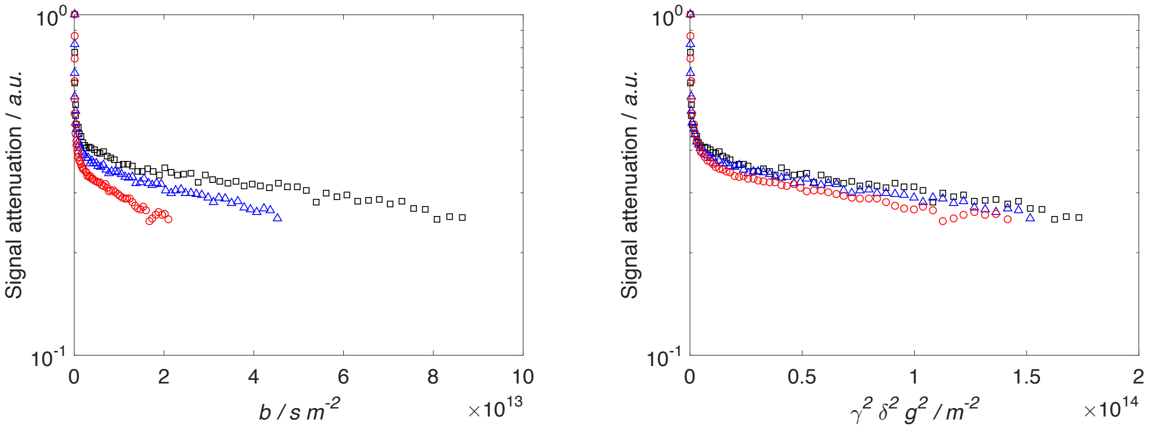

(e) ST plot for dodecane in water-dodecane imbibed in Q-15 silica, with $\Delta = 150$ *(○), 300 (△) and 500 (□) ms at 60 °C.*

(f) The same data plotted as in Figure (e) but as function of $\gamma^2\delta^2 g^2$*, with* $\Delta = 150$ *(○), 300 (△) and 500 (□) ms at 60 °C.*

Figure 5.16 APGSTE data acquired for water-dodecane imbibed in Q-15 silica beads at various temperatures, comparing the ST signal decay to the same data plotted independent of observation time Δ*.*

To reveal this restricting diffusion behaviour of dodecane, the ST plots for dodecane in the binary mixture are shown in Figures 5.16a, 5.16c and 5.16e at increasing observation times Δ, ranging from 150 to 500 ms. The same was done for the water signal and it was concluded that the data points overlapped neatly for varying Δ. For dodecane, the PFG NMR diffusion data points do certainly not overlap with increasing Δ. Bulk dodecane in Q-silica did not show the same behaviour and therefore it can be concluded that the restrictive diffusion of dodecane is caused by the presence of water in the pore system.

To further investigate the dodecane diffusion behaviour, the PFG NMR diffusion data is plotted independently of the observation time Δ, as can be seen in Figures 5.16b, 5.16d and 5.16f. One can observe that the dodecane diffuses independently from the chosen observation time. This is the key test for any characteristic restrictive diffusion behaviour, where the dodecane is trapped in pockets and thus present in droplets. The distance travelled by the dodecane molecules, which causes the PFG signal to decay, is limited by the droplet size.

Diffusometry Results of Dodecane / Q-50 silica

Figure 5.17 shows very similar trends for the diffusion of dodecane imbibed in Q-50 silica beads, as discussed above. It can be concluded from this Figure that the dodecane signal attenuates again very slowly; at very high gradients strengths, roughly 9% of the dodecane signal survives. The approximate diffusion coefficient for dodecane is in the order of $D_{\text{eff}(\infty)} \times 10^{-14}$ m^2 s^{-1}. The curvature for the dodecane signal attenuation clearly indicates restrictive, non-ideal diffusion behaviour. At increasing observations times, the diffusion data of dodecane does not overlap neatly in the ST plots in Figures 5.17a, 5.17c and 5.17e. Bulk dodecane in Q-50 silica did not show this behaviour and therefore it can be concluded that the restrictive diffusion of dodecane is caused by the presence of water in the pore system. Also the PFG NMR diffusion data is plotted independently of observation time Δ, as can be seen in Figures 5.17b, 5.17d and 5.17f. One can observe again that the dodecane diffuses independently from the chosen observation time. Therefore the dodecane is confined into droplets surrounded by the water phase.

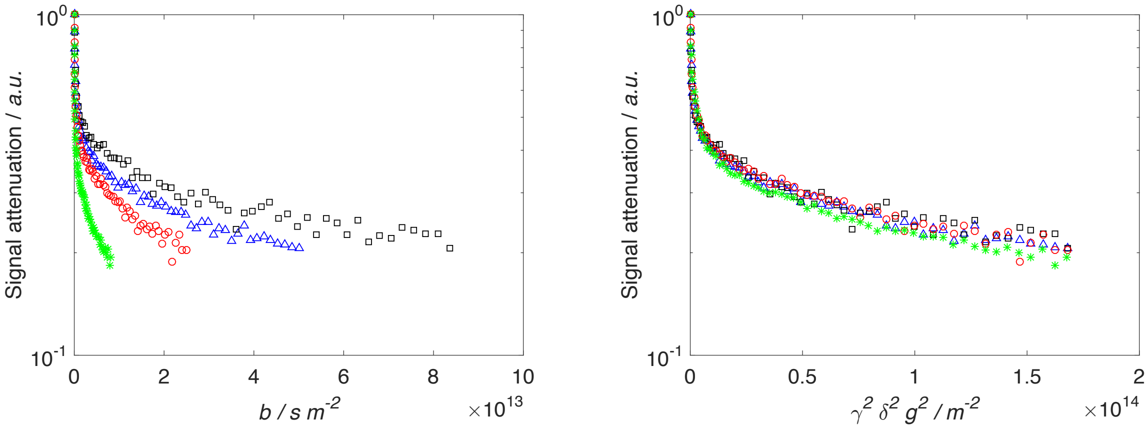

(a) ST plot for dodecane in water-dodecane imbibed in Q-50 silica, with Δ *= 50 (∗), 150 (○), 300 (△) and 500 (□) ms at 20 °C.*

(b) The same data plotted as in Figure (a) but as function of $\gamma^2\delta^2 g^2$*, with* Δ *= 50 (∗), 150 (○), 300 (△) and 500 (□) ms at 20 °C.*

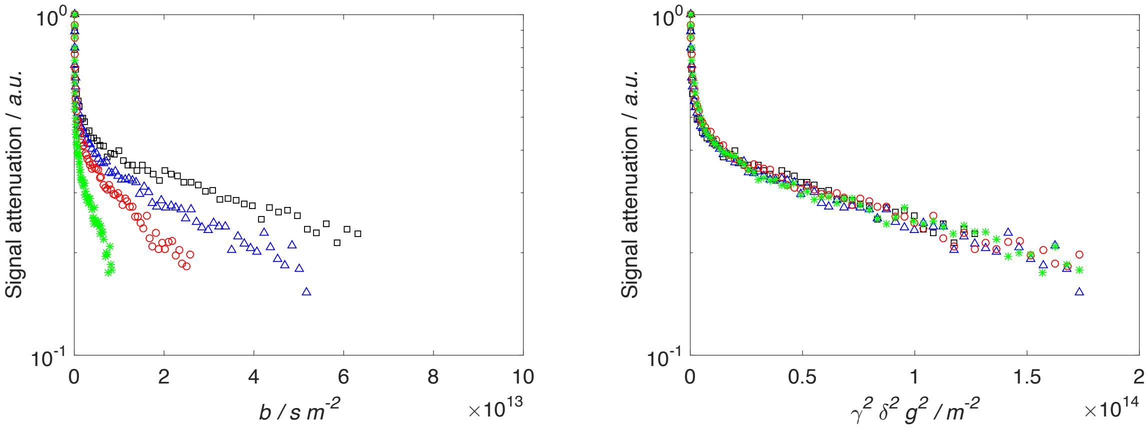

(c) ST plot for dodecane in water-dodecane imbibed in Q-50 silica, with Δ *= 50 (∗), 150 (○), 300 (△) and 500 (□) ms at 40 °C.*

(d) The same data plotted as in Figure (c) but as function of $\gamma^2\delta^2 g^2$*, with* Δ *= 50 (∗), 150 (○), 300 (△) and 500 (□) ms at 40 °C.*

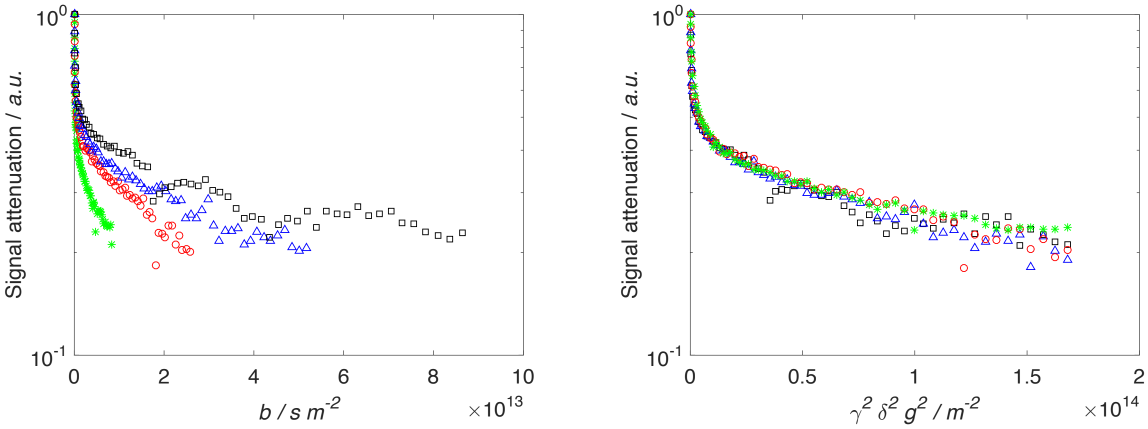

(e) ST plot for dodecane in water-dodecane imbibed in Q-50 silica, with Δ *= 50 (∗), 150 (○), 300 (△) and 500 (□) ms at 60 °C.*

(f) The same data plotted as in Figure (e) but as function of $\gamma^2\delta^2 g^2$*, with* Δ *= 50 (∗), 150 (○), 300 (△) and 500 (□) ms at 60 °C.*

Figure 5.17 APGSTE data acquired for water-dodecane imbibed in Q-15 silica beads at various temperatures, comparing the dodecane ST signal decay to the same data plotted independent of observation time Δ*.*

5.5.4 Effect of Temperature and Pore Size of Support

Figure 5.18 summarises all the variations on the self-diffusion coefficients plotted against temperature. Firstly, the main trend that can be concluded from this Figure is that with increasing temperatures, the diffusion tends to become more accelerated. Pure, bulk water has the sharpest increase from all systems, but water imbibed in silica is also more affected by temperature increases than dodecane. In molecular diffusion, molecules are self-propelled by the presence of thermal energy. As dodecane is a larger molecule than water, it requires more thermal energy to diffuse than water. Thus it is reasonable to believe that temperature variation does not seem to influence dodecane to the same extent.

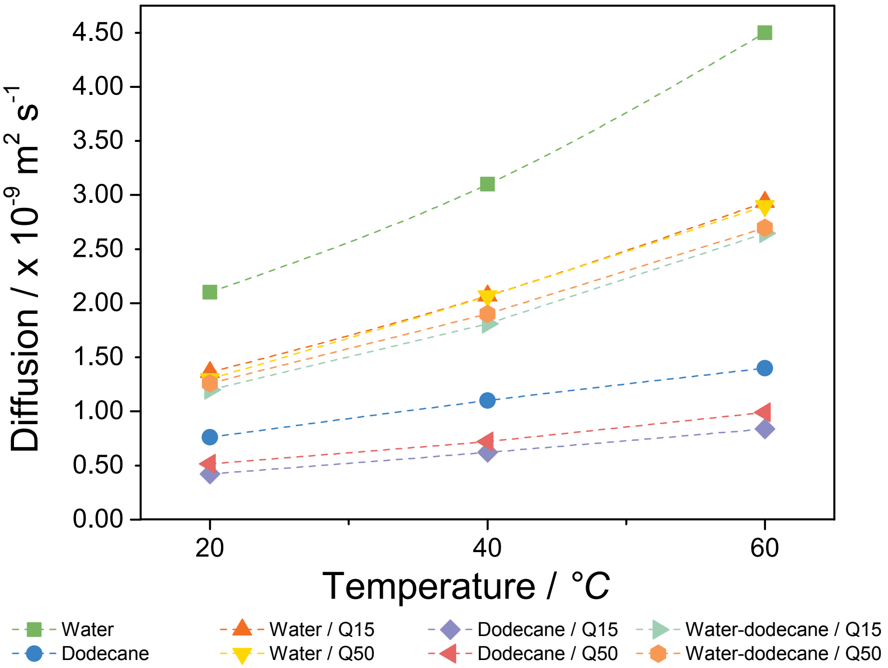

Figure 5.18 Comparison of all the self-diffusion coefficients for the systems studied in this project. The temperature and pore size distribution effects can be observed from these plots.

Furthermore, it can also be concluded that water in the binary system has a very similar diffusion behaviour to the pure water imbibed in Q-silica. However, the imbibition decreases the diffusion of water to a much higher degree than for dodecane, as pure dodecane diffuses only slightly faster than dodecane / Q-silica. Also, the self-diffusion coefficients for bulk water in the silica beads compared to water in the binary phase has to be slightly higher, due to the presence of dodecane. This is accentuated at 60 °C as we have seen for the fractionally higher tortuosity factors for the binary systems. The pore size has a marginal effect for the diffusion behaviour of water as the water / Q-15 and water / Q-50 behave very similarly. Additionally, as expected for dodecane, the diffusion behaviour has fractionally dropped when comparing the large Q-50 to the smaller pore systems Q-15. It was previously concluded that the tortuosity for dodecane / Q-15 of 1.8 decreased to 1.5 for dodecane / Q-50 due to the pore confinement restrictions.

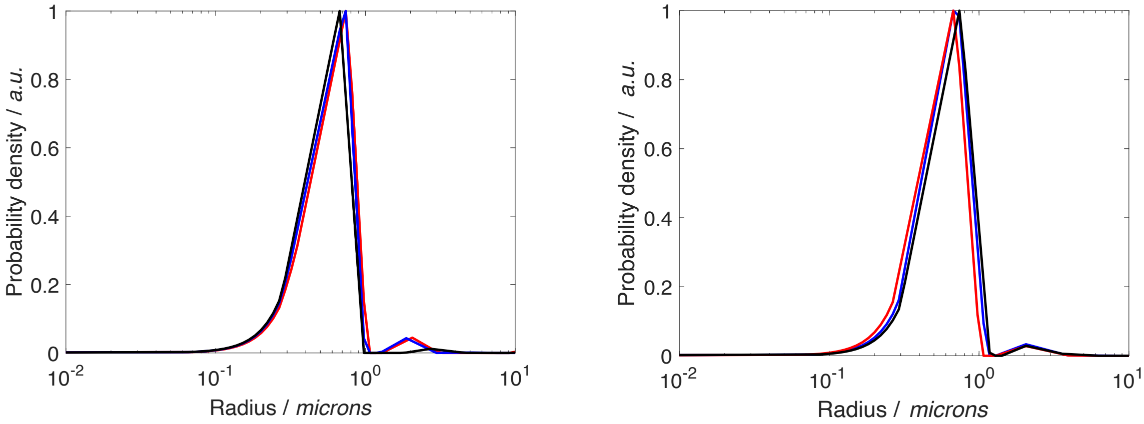

(a) Droplet size distribution of dodecane in water-dodecane system imbibed in Q-15 silica, calculated from APGSTE data acquired with 20 (—), 40 (—) and 60 (—) °C.

(b) Droplet size distribution of dodecane in water-dodecane system imbibed in Q-50 silica, calculated from APGSTE data acquired with 20 (—), 40 (—) and 60 (—) °C.

Figure 5.19 Droplet size distributions of dodecane in the binary mixture of water-dodecane in Q-15 silica in Figure (a) and in Q-50 silica in Figure (b) at increasing temperatures ranging from 20 to 60 °C. Temperature and pore size have little influence on emulsion droplet size for ranges investigated.

Figure 5.19 indicates that there is little influence of temperature on the emulsion droplet size for the temperature range investigated. In addition, the droplet size does not significantly depend on the pore size studied as the DSD in the Q-15 or Q-50 system does not vary greatly. The droplets are in the order of a micron in diameter which is many times larger than the pore size studied of the silica.

5.5.5 Ternary Systems with n-Alcohols

Ternary systems were obtained by combining either methanol, ethanol, butanol or heptanol with water and dodecane. These solutions were imbibed in Q-50 silica spherical beads at room temperature. Ternary systems were studied to better understand the effect of adding a surfactant to a system which, as previously shown, enabled spontaneous droplet formation. As discussed in Section 5.2.2, surfactants reduce the surface tension of the emulsion fluid, thereby favouring droplet formation. By varying the carbon chain length of the alcohol, the effect of the lipophilic property of the surfactant was tested. The objective was to see whether changes in the DSD could be observed. As depicted in Figure 5.20a, the ST diffusion decay for the water signal is shown at increasing observation time ranging between 50 and 200 ms. It is evident that the addition of methanol did not change the diffusion behaviour of water, as we can still observe the straight line which is characteristic for free diffusion. In Figure 5.20b, the same diffusion data is plotted while removing the time-dependence. As none of the data points overlap for increasing Δ, one can conclude that water in ternary systems is not restricted.

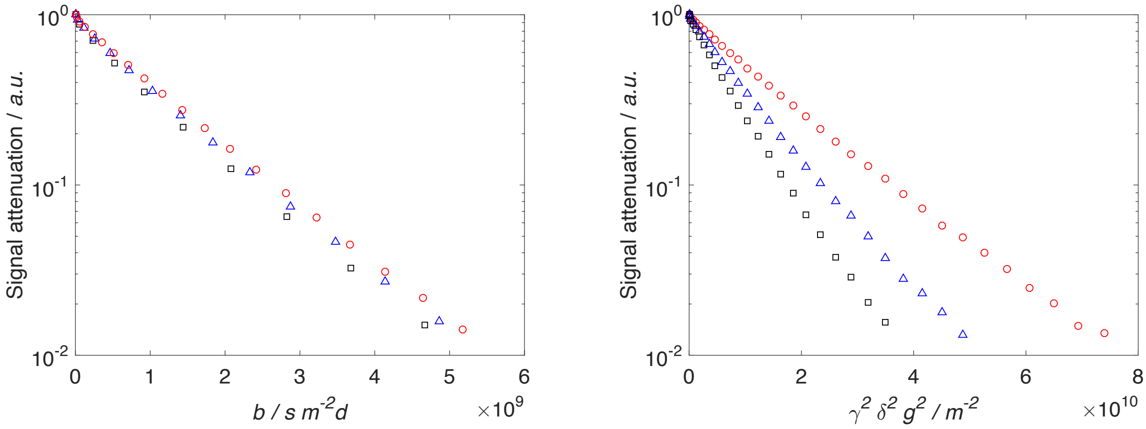

(a) ST plot for water signal in water-dodecane-methanol imbibed in Q-50 silica, with Δ = 100 (○), 150 (△) and 200 (□) ms at 20 °C.

(b) The same data plotted as in Figure (a) but as function of $\gamma^2\delta^2g^2$, with Δ = 100 (○), 150 (△) and 200 (□) ms at 20 °C.

Figure 5.20 ST plots for water in ternary system of water-dodecane-methanol imbibed in Q-50 spherical silica beads, with δ = 1 ms and Δ varying between 100 and 200 ms.

The opposite diffusion behaviour can be observed when studying the dodecane diffusion obtained by analysing the dodecane signal in the ternary system. Four major conclusions can be drawn when comparing the diffusion plots shown in Figure 5.21. Firstly, in Figure 5.21a, one can see that the ST plots are not straight lines any more, but consist of a “hockey-stick” like curvature, with regions of fast-diffusing dodecane molecules and a vast region of very slow diffusing molecules.

Secondly, this curvature is associated with restricted diffusion behaviour, similarly as has been shown in Section 5.5.3 for simple binary systems. Thirdly, when comparing Figures 5.21a and 5.21b and the remaining other figures in pairs, one can see that by removing the time dependency from the x-axis units, all diffusion data points overlap. This trend is very consistent with what was observed thus far for dodecane emulsions in any binary system. No matter how long the diffusion is observed for, the diffusion pattern is very similar. Regardless of the observation time, whether it is 150 or even 500 ms, the diffusion is almost identical. This trend is seen across the three alcohols. Finally, when analysing Figures 5.21a, 5.21c and 5.21e, the amount of fast diffusing dodecane, represented by the section of the curve with the very steep curvature, tends to decrease. This will have an effect on the DSD, which is discussed below.

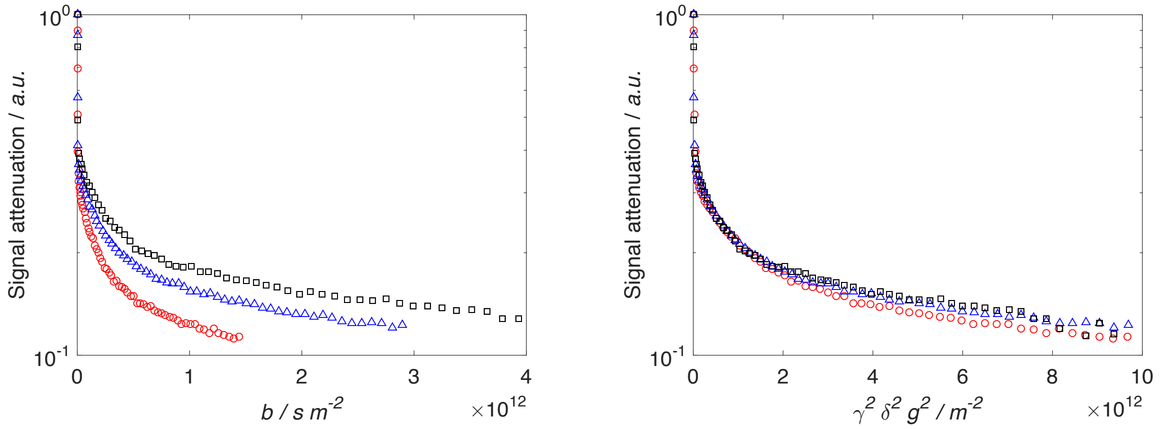

(a) ST plot for dodecane signal in water-dodecane-ethanol imbibed in Q-50 silica, with Δ *= 150 (○), 300 (△) and 500 (□) ms at 20 °C.*

(b) The same data plotted as in Figure (a) but as function of $\gamma^2\delta^2g^2$*, with* Δ *= 150 (○), 300 (△) and 500 (□) ms at 20 °C.*

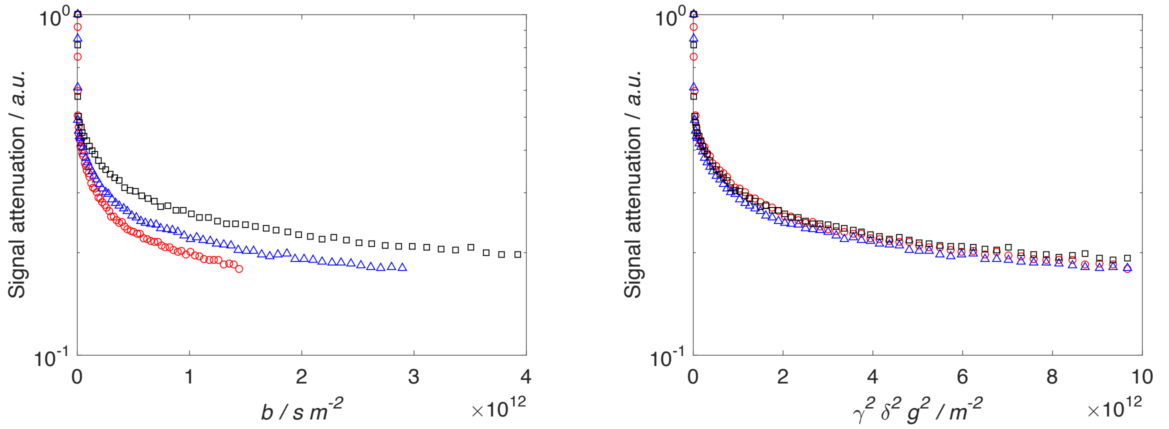

(c) ST plot for dodecane signal in water-dodecane-butanol imbibed in Q-50 silica, with Δ *= 150 (○), 300 (△) and 500 (□) ms at 20 °C.*

(d) The same data plotted as in Figure (c) but as function of $\gamma^2\delta^2g^2$*, with* Δ *= 150 (○), 300 (△) and 500 (□) ms at 20 °C.*

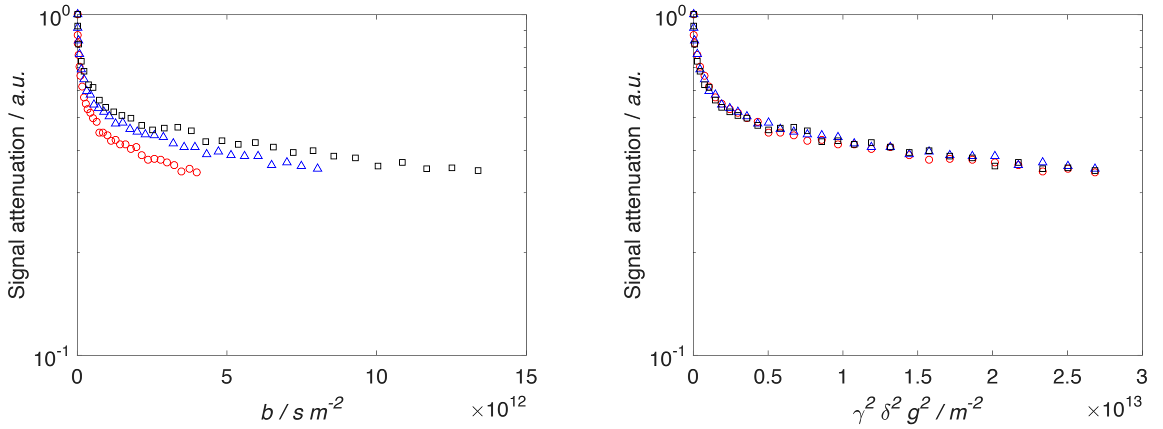

(e) ST plot for dodecane signal in water-dodecane-hepthanol imbibed in Q-50 silica, with Δ *= 150 (○), 300 (△) and 500 (□) ms at 20 °C.*

(f) The same data plotted as in Figure (e) but as function of $\gamma^2\delta^2g^2$*, with* Δ *= 150 (○), 300 (△) and 500 (□) ms at 20 °C.*

Figure 5.21 APGSTE data acquired for water-dodecane mixed with various n-alcohols imbibed in Q-50 silica beads, comparing the dodecane ST signal decay to the same data plotted independent of observation time Δ*.*

The x-axis plotted in Figure 5.21e extends until approximately 15 × 10^{12} s m^{-2}, whereas those in Figures 5.21a and 5.21c are plotted until 4 × 10^{12} s m^{-2}. In Figure 5.21e, the gradient strength was set at 1000 G cm^{-1}, versus 600 G cm^{-1} for Figures 5.21a and 5.21c. Even if the data in Figure 5.21e extends much further into q-space, the diffusion behaviours and trends are still valid to be compared and thus has no effect on the conclusions.

The DSD of the ternary systems prepared in Q-50 silica spherical beads at 20°C are shown in Figure 5.22a for three different systems with either n-ethanol, n-butanol or n-heptanol. The overall maximum of the all DSD is around 0.9 µm in all systems. When comparing the three DSD, starting with the water-dodecane-n-heptanol, the distribution is very similar to the previous results of the water-dodecane binary mixtures, seen on Page 116. Due to the very low solubility of n-heptanol in water, the surfactant effect of heptanol is negligible and therefore the DSD is nearly identical to the binary system. As solubility in water increases for n-butanol and n-ethanol respectively, the amount of surfactant increases [241]. In Figure 5.22a, one can notice that the DSD widens as the surfactant content grows. Thus a longer alcohol chain length can lead to a small increase in droplet size. Similar results can be found in the literature, where ternary systems are made of water/$C_{12}E_4$/hexadecane. T. Tadros *et al.* have reported that by increasing the weight content of their surfactant, the droplet radius decreases significantly, as can be seen in Figure 5.22b. This is the expected behaviour since the amount of surfactant determines the total interfacial area and thus the average size of the emulsion droplets [202, 250]. This is in line with the trend reported in Figure 5.22a.

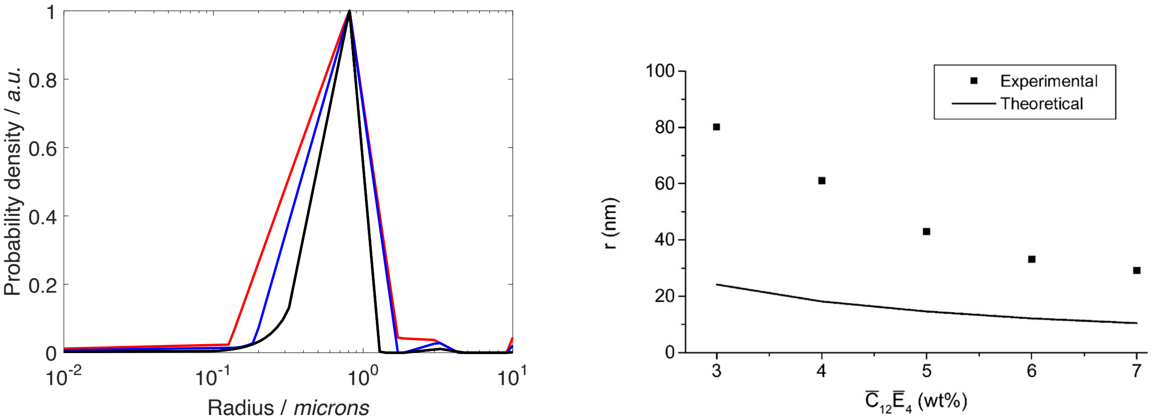

(a) Droplet size distribution of dodecane in water-dodecane-surfactant systems in Q-50 silica, calculated from APGSTE data acquired with ethanol (—), butanol (—) and heptanol (—).

(b) Nano-emulsion droplet radius (r) at 25° C as a function of $C_{12}E_4$ concentration in the ternary system containing water/$C_{12}E_4$/hexadecane. Reproduced from [202].

Figure 5.22 The effect of adding a surfactant on the droplet size distribution (a) or droplet radius (b) for ternary systems consisting of water-dodecane and a surfactant with a long aliphatic tail.

5.5.6 Surface Modification using Stearic Acid

The work discussed in this section is presented to better understand what would happen when the carrier surface was made hydrophobic using fatty acids. This was particularly important for Shell's internal research purposes. In this case stearic acid was used to make the surface of the catalyst less hydrophilic, thus lowering the amount of water present inside pores. This eventually led to no emulsions formation and this can be concluded from Figure 5.23. As in Figure 5.23a the data points overlap, in line with all the water signals in the binary mixtures, the dodecane is no longer present in the form of droplets in water. In Figure 5.23b, where the diffusion data is plotted independently of time, for every observation time the dodecane has a different MSD. Therefore no dodecane emulsions are formed.

The data presented in Figure 5.23 is from the system where both n-ethanol and stearic are combined with water-dodecane. The effect of adding a surfactant does not enable emulsion formation but the fatty acid effect is dominant. For similar samples consisting of only water-dodecane-stearic acid, nearly identical results are obtained. The non-linear diffusion decay for dodecane could be attributed to different regions in the pores. This results in a distribution of diffusion behaviours, where some dodecane molecules diffuse faster than others.

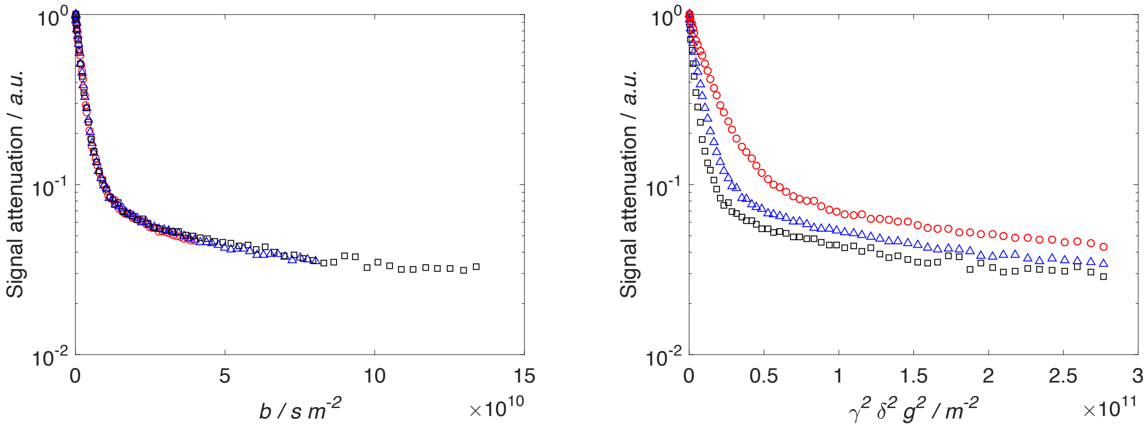

(a) ST plot for dodecane signal in water-dodecane-ethanol-stearic acid imbibed in Q-50 silica, with Δ *= 150 (○), 300 (△) and 500 (□) ms at 20 °C.*

(b) The same data as shown in Figure (a) but plotted as function of $\gamma^2\delta^2g^2$ *to remove time dependence, with* Δ *= 150 (○), 300 (△) and 500 (□) ms at 20 °C.*

Figure 5.23 The effect of adding a fatty acid, stearic acid and ethanol, on the APGSTE data acquired for water-dodecane mixed with stearic acid imbibed in Q-50 silica beads. Comparing the dodecane ST signal decay to the same data plotted independent of observation time Δ*.*

Very similar results were obtained by Chen *et al.* [251]. Oil-in-water droplets flowed in a capillary from right-to-left, first encountering the hydrophilic section before entering the hydrophobic part. As soon as the droplets entered the hydrophobic surface, the oil-in-water emulsion was broken. This process is illustrated by the time sequence of images as shown in Figure 5.24.

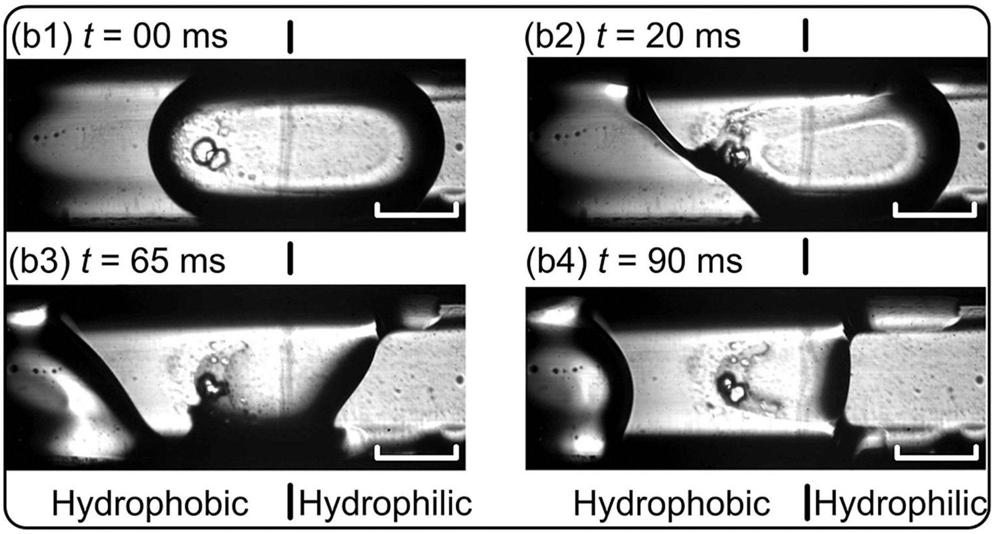

Figure 5.24 Observation of a droplet breaking inside a capillary which has modified wettability: hydrophilic region on the right whereas hydrophobic region on the left. The oil-in-water droplets flow from the hydrophilic section into the hydrophobic section of the capillary. At t = 65 ms, the emulsion broke. Reproduced from [251].

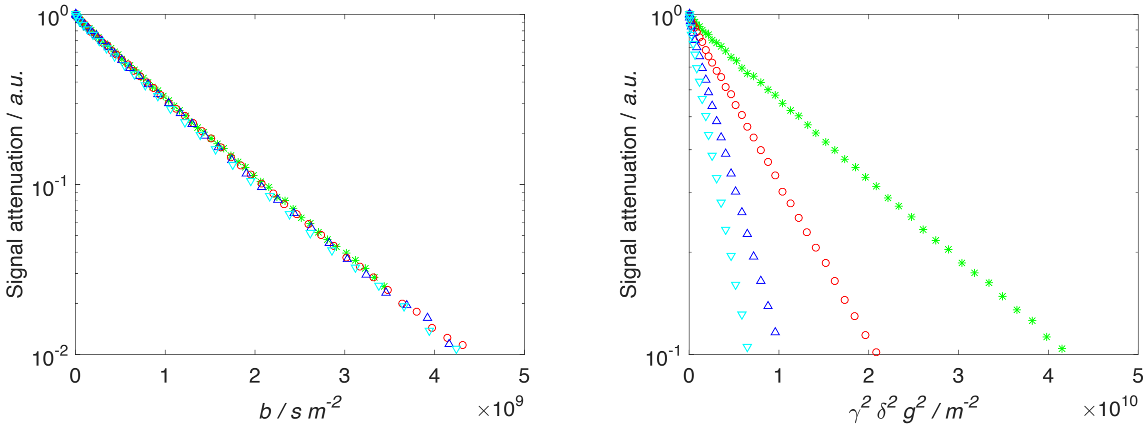

(a) ST plot for water signal in water-dodecane-stearic acid imbibed in Q-50 silica, with Δ *= 50 (*), 100 (○), 150 (△), 200 (□) and 300 (▽) ms.*

(b) The same data as shown in Figure (a) but plotted as function of $\gamma^2\delta^2g^2$ *to remove time dependence, with* Δ *= 50 (*), 100 (○), 150 (△), 200 (□) and 300 (▽) ms.*

Figure 5.25 The effect of adding a fatty acid, stearic acid, on the APGSTE data acquired for water-dodecane mixed with stearic acid imbibed in Q-50 silica beads. Comparing the water ST signal decay to the same data plotted independent of observation time Δ*.*

In Figure 5.25, the diffusion decay data for the water signal in the ternary system of water-dodecane-stearic acid is shown. Again, the straight line is observed for increasing observation times, indicating that water is undergoing unrestricted self-diffusion. When the same data is plotted without the time dependence in Figure 5.25b, the experiments at varying observation times have different slopes thus other MSDs. This proves that even with stearic acid in a hydrophobic environment, the water molecules do not appear as water-in-dodecane droplets. Not enough water is present in the pores of the support as the surface was chemically modified.

5.5.7 TiO_2 and Ru/TiO_2 Fischer-Tropsch Pellets

Diffusometry results of bulk liquids

In this final Section, the results are reported for (i) the bare FT catalyst support TiO_2 and (ii) catalyst Ru/TiO_2 pellets when they are submerged in the water-dodecane system. The objective is compare the emulsion formation within this support to the previous behaviours taking place inside Q-50 silica spherical beads.

In Chapter 8, emulsions in Ru/TiO_2 catalysts under real FT reaction conditions are studied, one has to ensure that the systems behave comparably and similar trends are observed. In order to do so, again bulk liquids of either water and dodecane were imbibed into the two different pellets. Subsequently, also the binary systems were studied, using the emulsion detection technique to observe any emulsion formation.

In Figure 5.26, the ST diffusion decays are plotted for either bulk water or dodecane in either TiO_2 or Ru/TiO_2. All decays at varying observation times Δ have nearly identical free self-diffusion decays. For these bulk liquids, no other behaviour is expected and it follows the same trends seen thus far in this Chapter for bulk liquids.

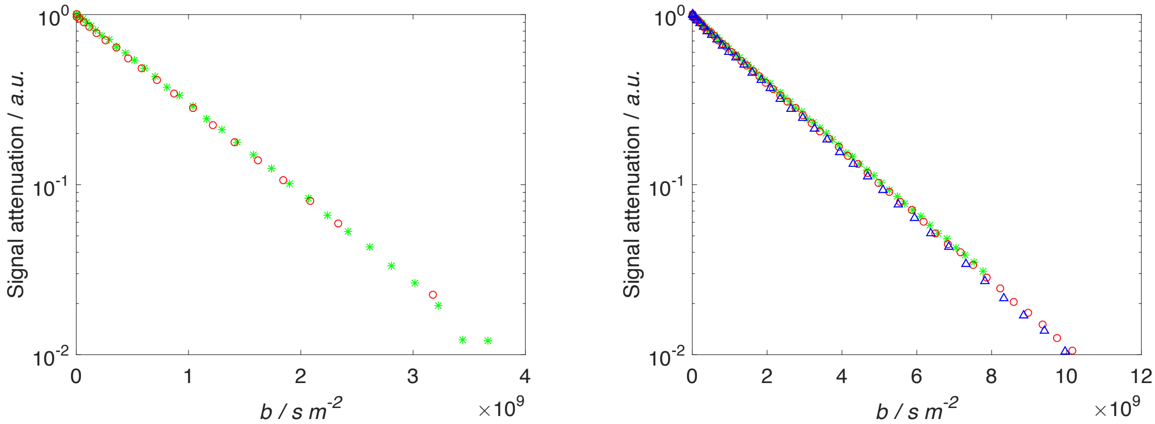

(a) ST plot for water imbibed in TiO_2, with Δ = 50 (*) and 100 (○) ms at 20 °C.

(b) ST plot for dodecane imbibed in TiO_2, with Δ = 50 (*), 100 (○) and 150 (△) ms at 20 °C.

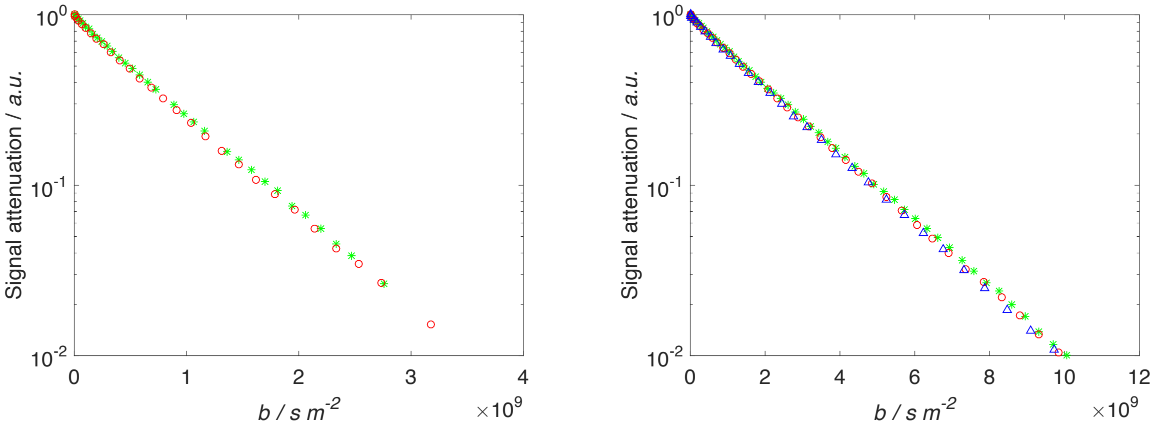

(c) ST plot for water imbibed in Ru/TiO$_2$ pellets, with Δ = 50 (∗) and 100 (○) ms at 20 °C.

(d) ST plot for dodecane signal imbibed in Ru/TiO$_2$ pellets, with Δ = 50 (∗), 100 (○) and 150 (△) ms at 20 °C.

Figure 5.26 ST plots for bulk water or dodecane imbibed in either Ti/O$_2$ or Ru/TiO$_2$ pellets, with δ = 1 ms.

Diffusometry Results of Binary Mixtures

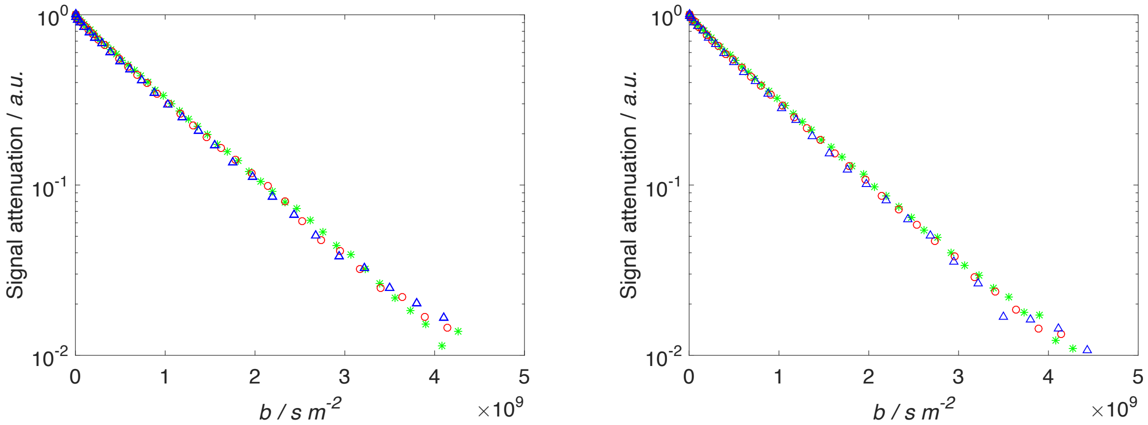

(a) ST plot for water signal in water-dodecane imbibed in TiO$_2$ pellets, with Δ = 50 (∗), 100 (○) and 150 (△) ms at 20 °C.

(b) ST plot for water signal in water-dodecane imbibed in Ru/TiO$_2$ pellets, with Δ = 50 (∗), 100 (○) and 150 (△) ms at 20 °C.

Figure 5.27 ST plots for water in water-dodecane imbibed in either Ti/O$_2$ or Ru/TiO$_2$ pellets, with δ = 1 ms.

In Figure 5.27, one can observe that in both environments water is again the continuous phase and therefore does not encounter any restrictive diffusion behaviour. It shows the signal attenuation of water in the binary mixture at 20 °C at increasing observation times Δ, ranging from 50 to 150 ms. As both Figures 5.27a and 5.27b show very similar diffusion behaviours for the water molecules, it becomes apparent that the metal loading of 1 wt% is negligible and does not affect the diffusion. In addition, the shape of the distribution exhibits the same characteristic shape as observed before.

From Figure 5.28, one can conclude that dodecane diffuses very slowly in both supports. Once again, the diffusion behaviour plotted without time dependency indicates that dodecane forms droplets inside the aqueous layer. This is valid for both systems.

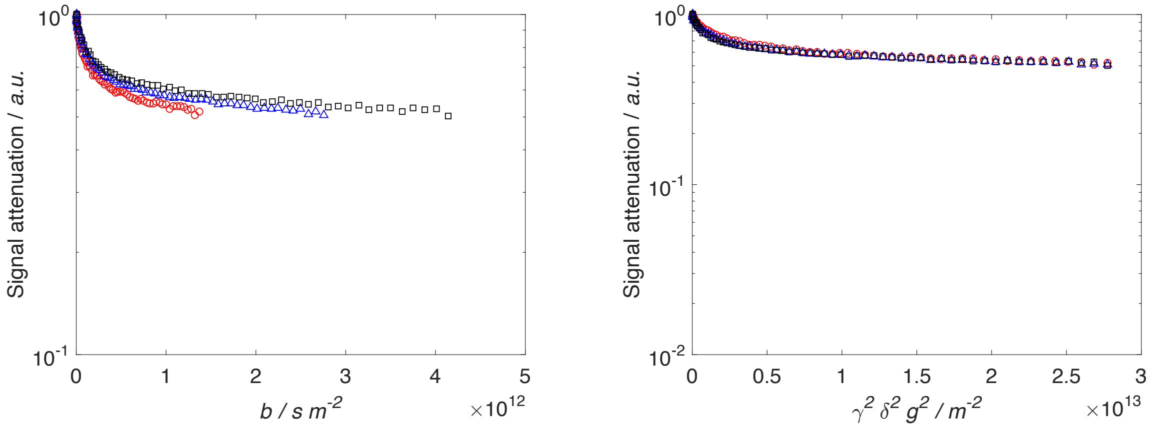

(a) ST plot for dodecane signal in water-dodecane imbibed in TiO_2*, with* $\Delta = 150$ *(○), 300 (△) and 500 (□) ms at 20 °C.*

(b) ST plot for dodecane signal in water-dodecane imbibed in TiO_2*, with* $\Delta = 150$ *(○), 300 (△) and 500 (□) ms at 20 °C.*

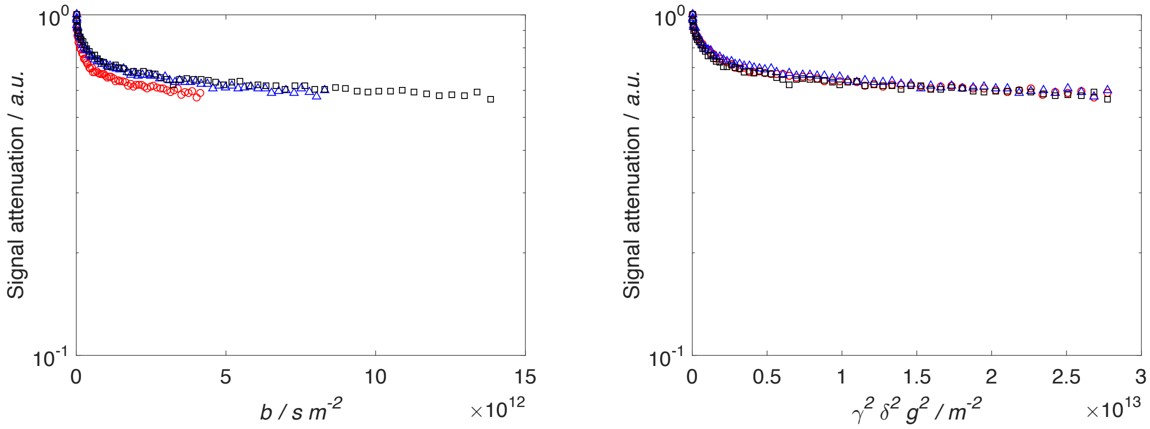

(c) ST plot for dodecane signal in water-dodecane imbibed in Ru/TiO_2*, with* $\Delta = 150$ *(○), 300 (△) and 500 (□) ms at 20 °C.*

(d) ST plot for dodecane signal in water-dodecane imbibed in Ru/TiO_2*, with* $\Delta = 150$ *(○), 300 (△) and 500 (□) ms at 20 °C.*

Figure 5.28 ST plots for dodecane in binary mixture imbibed in either TiO_2 *or* Ru/TiO_2*, with* $\delta = 2$ *ms.*

Figure 5.29 depicts the DSD for dodecane in the binary system in either TiO_2 or Ru/TiO_2. The distributions are very similar and this reconfirms that the systems encounter very little effect from the metal loading. However, the droplet sizes for emulsions in TiO_2 and Ru/TiO_2 are different; the droplet size and distributions are smaller in TiO_2, with a maximum at roughly 0.5 µm versus the 0.8 µm in Ru/TiO_2. This is partly due to the smaller pore size of the TiO_2 support (29 nm) compared to Ru/TiO_2 (50 nm) but can also indicate an effect of the support.

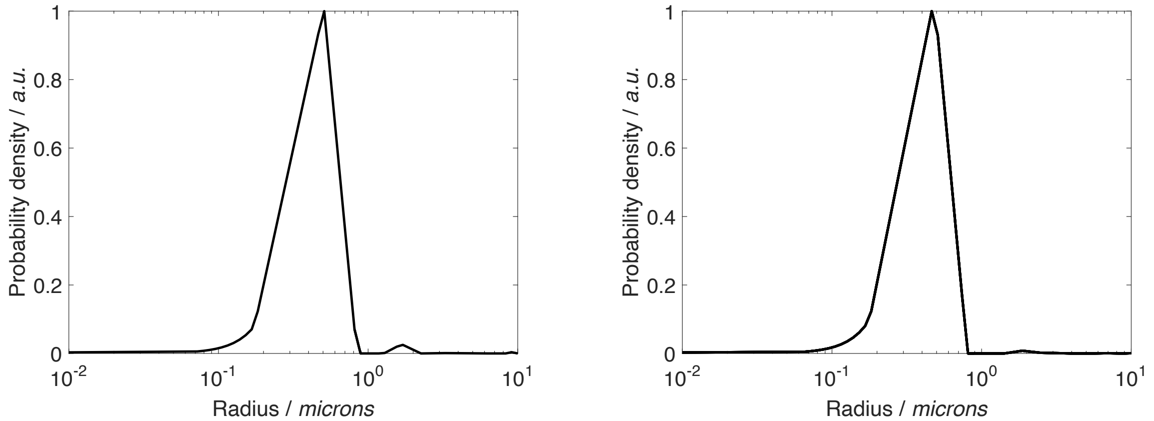

(a) Droplet size distribution of dodecane in water-dodecane imbibed in TiO_2, calculated from APGSTE data acquired at 2 ms δ and 150 ms Δ observation time (——).

(b) Droplet size distribution of dodecane in water-dodecane imbibed in Ru/TiO_2, calculated from APGSTE data acquired at 2 ms δ and 150 ms Δ observation time (——).

Figure 5.29 DSD for dodecane in water-dodecane imbibed in either TiO_2 or Ru/TiO_2.

5.6 Conclusions

PFG NMR is used at ambient pressure to study emulsions of oil-in-water in porous media. A technique has been developed to study the formation of liquid pockets of dodecane and obtain their DSD. These systems were chosen to mimic realistic FT conditions where both main products in a hydrocarbon/aqueous mixture coexist in a porous catalyst support. *In situ* multi-component intrapore liquid was studied and characterised, at various temperatures and pore size distributions of the spherical Q-silica beads. At ambient pressure and temperature and in bulk conditions, dodecane and water do not form any emulsions. However, when imbibed in the porous network, an emulsion system is formed. In the macropores of the support, liquid pockets of dodecane are formed, stretching over several pore lengths.

The intraporous water-dodecane / Q-silica systems can be described as oil-in-water emulsions, with water acting as the continuous, surface wetting phase and dodecane present in the form of restricted pockets. This can be concluded from the relaxometry and diffusometry experiments. Water in the binary phase has relaxation times that are heavily reduced but diffusion behaviours that are relatively unaffected by the presence of dodecane.

On the other hand, (i) the diffusion behaviour of dodecane is heavily decreased and (ii) the relaxation rates are similar to bulk dodecane, which is consistent with the dodecane present in large emulsions, isolated from the pore walls. These droplets and their size distribution, with a maximum of around 0.8 µm, are suggested to be present in the shape of ganglia regardless of the temperature, extending over several pore lengths. In the literature, it has been reported that spontaneous emulsification can lead to micrometer size droplets [189]. Hydrocarbon ganglia form which tend to be bigger than the pore size of the material [252]. This is in agreement with results reported by Perazzo *et al.* in the case of an oil-in-water emulsion numerical simulation [188].

When heating up the binary mixtures, the diffusion coefficients of all system increase linearly; water is most affected by this temperature rise. There is little influence of temperature on the emulsion droplet size for the temperature range investigated up to 60 °C. In addition, the droplet size does not significantly depend on the pore size studied as the DSD in the Q-15 or Q-50 system does not vary greatly. When adding surfactant to the water-dodecane systems, the DSD widens as the surfactant content increases. Higher surfactant concentration can lead to a small increase in ganglia size. Very similar effects have been concluded after the addition of long-chain, aliphatic surfactants [253].

In the case stearic acid was added to the systems to make the surface less hydrophilic, thus lowering the amount of water present inside pores, this eventually led to no emulsion formation. When a surfactant was added with the stearic acid, again no emulsions were formed as the fatty acid effect is dominant. Even with the stearic acid in a hydrophobic environment, the water molecules do not appear as water-in-dodecane drops. A very similar behaviour was published by Chen *et al.* who studied droplet adhesion in a microfluidic device. Oil-in-water emulsion droplets were generated and transported from a hydrophilic section in the device to a downstream hydrophobic section in a capillary [251]. The oil droplets adhered on the hydrophobic surface and hence the oil-in-water emulsion was broken.

Finally, when comparing the PFG NMR results from the water-dodecane systems in TiO_2 or Ru/TiO_2, it can be concluded that the metal loading of 1 wt% is negligible and does not affect the diffusion behaviour. In this Chapter, various effects were analysed on spontaneous droplet formation in different sizes and types of supports. Also, this method proves to be an effective technique to quantify the droplet sizes of oil-in-water systems.

Chapter 6

Reactor Design and Commissioning

6.1 Introduction

This Chapter summarises (i) the design, commissioning and testing work done on the FT rig and (ii) other related catalysis studies performed at STCA. This Chapter will cover the design of the Zeton B.V. FT rig and more specifically how the STCA and the MRRC collaboration helped in designing an inherently safe apparatus.

A period of two months was spent at STCA to learn about reactor handling, the catalyst preparation and gas chromatography analyses. Experience was acquired using their SSITKA machine to study the effect of changing the gas feed composition on a FT cobalt catalyst [254, 255]. Finally, due to the new skills obtained, the commissioning work and modifications implemented on the FT rig, to further improve the operation and the gaseous product analysis, are discussed.

6.2 Design and Description of Zeton Fischer-Tropsch Reactor

6.2.1 Overview

The FT reactor has been designed and constructed in partnership with Zeton B.V., a company based in Enschede, the Netherlands, and in collaboration with researchers from STCA. Zeton is a company specialised in designing and building customised, chemical engineering reactor plants. Zeton B.V. was contracted to manage procurement, design and construction of the *in situ* NMR reactor. Taking into consideration all of the design requirements set out below, the FT reactor, made of non-magnetic ceramic material Si_3N_4, is purposely built for this application only and has a unique design to be accommodated in a superconducting super-wide-bore (SWB) Bruker magnet.

The maximum operating conditions are set at 250 °C and 50 bar. Running the reactor within these conditions guarantees safe operation as the design limits of the reactor are $T_{max} = 300$ °C and $P_{max} = 60$ barg. Essential to delivering this project, is the close collaboration with STCA to ensure that both the safety aspects and operation conditions could be achieved at the MRRC in Cambridge. Three key elements of operating the FTS experiment safely are the need to prevent: (i) exposure to CO and H_2, (ii) the formation of hotspots inside the catalyst bed and (iii) the solidification of the heavy, waxy products that have the potential to clog up the rig and thus create a hazardous pressure build-up. To prevent these three situations from taking place, very good reactor control is needed. In the design, many safety measures and precautions have been taken into account to ensure safe operation.

Figure 6.1 The FT reactor.

In the following Sections, the operation and design of the reactor will be explained, while highlighting all of its main customised features. All units and components with their tag numbers discussed in these Sections, can be found on the technical P&ID drawings, found in Appendix A on Page 224. In addition, all the FT reactor components discussed in this Chapter are labelled and described in Table 6.2. In Figure 6.1 the reactor during its final building stage at Zeton B.V. can be seen. All the main elements of the rig are listed in Table 6.1. This set up is the only pilot-scale, fixed-bed reactor in the world that enables *in situ* NMR measurements of FTS under real operating conditions.

Table 6.1 The legend for Figure 6.1 describing the FT reactor.

Number	Description
1	Reactor
2	Gas/Liquid separator
3	Heavy hydrocarbons storage
4	HPLC pump and liquid storage
5	Electrical cabinet
6	Short hydrocarbons and water storage
7	Water cooler
8	Wet-gas flow-meter (WGFM)
9	Feed flow valves and readings
10	Pressure gauge and relieve valve

Figure 6.2 depicts a photograph of the actual Zeton B.V. FT reactor in the MRRC laboratory in Cambridge. On the left in the forefront is the SWB magnet embodying the fixed-bed reactor. On the right-side, the main section of the rig can be seen, with the electrical cabinet, the feed lines and flow meters, product collection vessels and extraction caps. The gas chromatograph (GC) can be seen in the back, in the middle between both sections of the rig.

Figure 6.2 The FT reactor in the MRRC laboratory, after full commissioning in operation.

Table 6.2 The FT reactor components discussed in this Chapter, including label number and description.

Tag with labelling number	**Description**
CK-010 - CK-040 / CK-060	Check valves for H_2, CO, spare, N_2 and liquid feed
E-250 / HE-250	Refrigerator and heat exchanger
F-010 - F-040 / F-060	Filters for H_2, CO, spare, N_2 and liquid feed
FTC-010 - FTC-040 / FTC-060	Flow controllers for H_2, CO, spare, N_2 and liquid feed
FQI-250	Wet-gas flow-meter
HV-010 - HV-040 / HV-060	Ball valves for H_2, CO, spare, N_2 and liquid feed
HV-200 / HV-250	Ball valves for product shut-off
JE-060 / JE-106	Electrical tracing for mixing inlet and outlet heaters
JE-100 / JE-102	Electrical tracing for reactor top and bottom heaters
JE-200 / JE-202	Electrical tracing for product collection vessels heaters
LVK-600	Leak detector
MX-060	Evaporative mixer
P-060	High pressure liquid feed pump
PCV-250	Dome Loaded Back-Pressure Regulator
PI-010 - PI-040 / PI-060	Pressure gauges for H_2, CO, spare, N_2 and liquid feed
PI-100	Pressure gauge for the reactor
PSV-010 - PSV-040 / PSV-060	Pressure safety valves for H_2, CO, spare, N_2 and liquid feed
PSV-100	Pressure safety valve for reactor
R-100	Ceratec main reactor body
TE-060 / TE-106 & TSE-060 / TSE-106	Thermocouples and safety switches for inlet and outlet
TE-100 / TE-102 & TSE-100 / TSE-102	Thermocouples and safety switches for reactor
TE-104 / TE-105 & TSE-104 / TSE-105	Thermocouples and safety switches for inside of reactor
TE-200 / TE-202 & TSE-200 / TSE-202	Thermocouples and safety switches for product vessels
V-060	Liquid feed vessel
V-200	Gas/Liquid separator
V-201 / V-202 / V-250 / V-251	Product collection vessels
XV-010 - XV-040	Actuated ball valves for H_2, CO, spare, and N_2 feed
XV-200 / XV-250	Actuated ball valves for product collection valves

6.2.2 Gas Feed lines

The three main feed gases (H_2, CO and N_2) are fed separately and their flow is regulated by thermal mass flow controller (MFC) (FTC-010, FTC-020 and FTC-040 respectively). These are calibrated to measure flow rates between 0.5 - 30 NL h^{-1} and each MFC is calibrated for its own dedicated gas. A conversion factor, C, for other non-calibrated gases can be calculated and this is related to the specific heat capacity, c_{p_N}, and the density, ρ_N, see Equation 6.1. The c_{p_1} and ρ_1 refer to the properties of the gas used for initial calibration, whereas c_{p_2} and ρ_2 are for the non-calibrated gas.

$$C = \frac{c_{p_1}\ \rho_1}{c_{p_2}\ \rho_2} \tag{6.1}$$

Analogue pressure gauges (PI-010 - PI-040) are installed on the rig which indicate the incoming gas cylinder pressures to the operator. However, this data is not logged but is checked regularly to ensure the maximum reactor pressure of 50 barg is not surpassed. A bypass feed line (HV-011) is placed over the main H_2 feed line, if rapid pressurising of the system by bypassing the MFC is required. A fourth, spare inlet is available (FTC-040) if any other reactant should be co-fed. An example when this extra feed could be used would be to co-feed sulphur in order to examine the catalyst stability in the presence of sulphur impurities. In addition, inert N_2 is fed to the rig, mainly for (i) pressure regulation, (ii) reactor purging, (iii) reactor cooling or even (iv) reaction quenching.

As the gas MFC controllers are very sensitive to moisture, liquids and solids, Swagelok filters (stainless steel 7 µm mesh size) are placed on all gas feed lines (F-010 - F-040). These remove any remaining solid particles from the gas cylinder or any liquid that was present as vapour in the cylinder to avoid damage to the flow controllers. All feed lines have a double valve system. The first is operated manually and is controlled via the panel on the main body of the rig. These two-way hand-valves are denoted HV-010 - HV-040 for H_2, CO, N_2 and spare gas 4 respectively.

In addition, the rig has a secondary system using air-actuated, automatic solenoidal shut-off valves (XV-010 - XV-040) only controlled electronically via the LabVIEW control system. Using pressurised air, the valves are connected to the laboratory gas detection system which can detect dangerous levels of CO, H_2 and O_2. In the event of leaks, the valves can open/close automatically to prevent a greater gas leak or an unwanted pressurising of the rig. Downstream of the pneumatic valves, check valves (CK-010 - CK-040) are installed after as an extra safety barrier, further protecting the MFCs from any back-pressure or liquid.

6.2.3 Liquid Feed lines

Water, or any other fluid, can be fed from a glass Schott Duran pressure bottle (V-060), 1000 mL capacity, by using a high-performance liquid chromatography (HPLC) pump (P-060). There is no blanketing mechanism present on this bottle but the storage bottle is equipped with a pressure equaliser preventing vacuum or vaporisation of the fluids to occur. The feed pump is specially designed to be able to precisely pump minute amounts of fluid, ranging from 0.001 - 5 mL min^{-1}. A coriolis meter measures the pump's outlet pressure and subsequently controls the flow rate of the liquid. A pressure relief valve system is placed at the outlet of the pump to protect against over-pressure.

All feed lines (both gas and liquid) are mixed in a 3-way valve and enter the controlled evaporative mixer (CEM) unit (MX-060), which evaporates all components at any temperature up to 200 °C. The feed gases act as a carrier gas while the liquid is vaporised. Ideally, the flow rates of the liquid and gas should be in the same order of magnitude to ensure the best performance of the CEM unit. If not, pulsating flow may be observed. Downstream of the CEM, all lines have trace heating (JE-060 - JE-106), to ensure (i) optimal pre-heating of the feed, (ii) prevent condensation of the fluids or (iii) prevent solidification of the waxy products could occur.

6.2.4 Reactor

Following the CEM, the reactants enter the fixed-bed reactor (R-100), which itself is placed inside the spectrometer. The ceramic reactor body, made from silicon nitride (Si_3N_4) can be operated in down-flow mode only. The top and bottom of the reactor body are constructed from SS-316 stainless steel. However, as silicon nitride is non-magnetic and has excellent thermal conductivity, it was chosen as primary building material for this rig. Si_3N_4 has a thermal conductivity of 43 W m^{-1} K^{-1} at 20 °C compared to only 15 W m^{-1} K^{-1} at 23 °C for SS-316 stainless steel. However, in general ceramic materials can be very brittle so special care should be taken when handling the reactor.

To connect the main reactor body to the rig process lines, the three parts that make up the stainless steel outer ends of the reactor are combined. Two half nuts are clamped over a groove and tightened together using a custom built spanner supplied by Zeton B.V. This fixes the nuts safely to the ceramic part. See Figure 6.3 for a schematic of the ceramic reactor, where the green and red units represent the two half nuts with the clamp. Figure 6.4 shows the reactor dimensions.

The reactor head and bottom coupling pieces are hardened by Kolsterising®. In this preventative process, a very thin layer of carbon is diffused and applied on the outer layer of the SS-316 stainless steel to prevent galling. In addition, the reactor body is equipped with a pressure transmitter and pressure gauge (PI-100). To protect the rig against any overpressure, a pressure relieve valve (PSV-100) was installed.

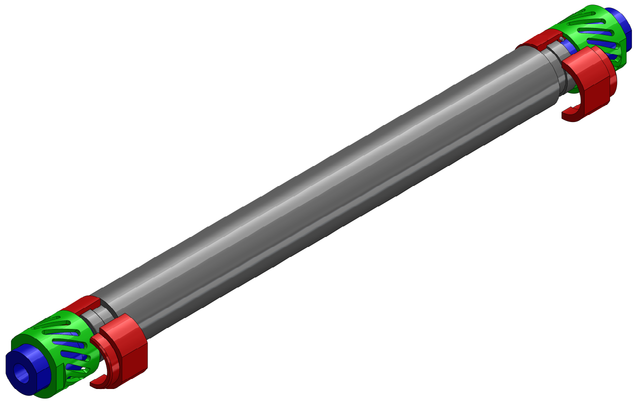

Figure 6.3 A schematic of the stainless steel reactor built by Ceratec. The green and red parts at both ends comprise the clamping unit to connect the reactor to the rig process lines.

The top and bottom of the reactor body are connected to the rig and sealed using Swagelok VCR® gaskets. These fittings limit the wear of the actual Swagelok connections. The gaskets are disposed and replaced every time to ensure minimal leak risk. All wetted soft goods in the reactor are made from either Viton® or Kalrez®. These fluorocarbon rubbers both have great temperature (long-term exposure to temperatures between -21 °C and +327 °C) and chemical resistance (can withstand attack from more than 1,800 chemicals, solvents and plasmas) and hence are used in the O-rings [256].

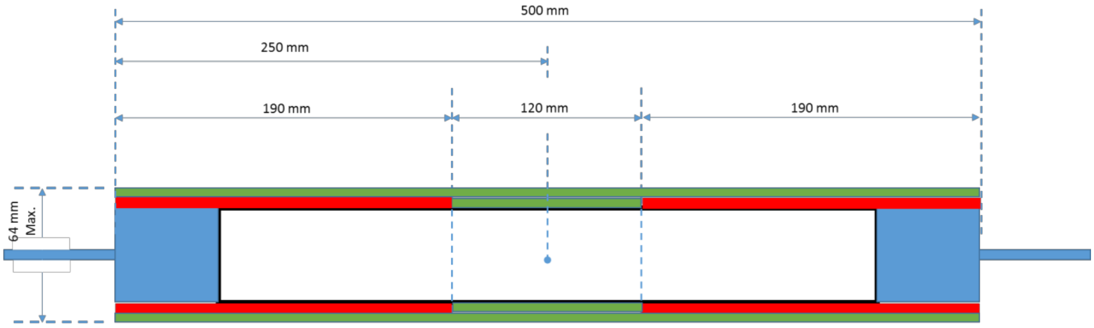

Figure 6.4 Diagram showing the dimensions of FT reactor, provided by Zeton B.V. The red lines indicate the reactor trace heating. The central region of the reactor body, which extends over the FOV of the magnet, does not have any trace heating.

The reactor has two separate trace heating loops that cover either the top or bottom section. The centre of the rig which is placed inside the FOV has no trace heating as this can influence the acquisition of the NMR signal. However, the central region of the reactor body is well insulated to prevent significant heat losses. Insulation is provided to cover the trace heating lines in the form of a fibreglass woven fabric that is secured in place with temperature resistant glass tape, see Figures 6.5b and 6.5c.

(a) The Ceratec main reactor body reactor.

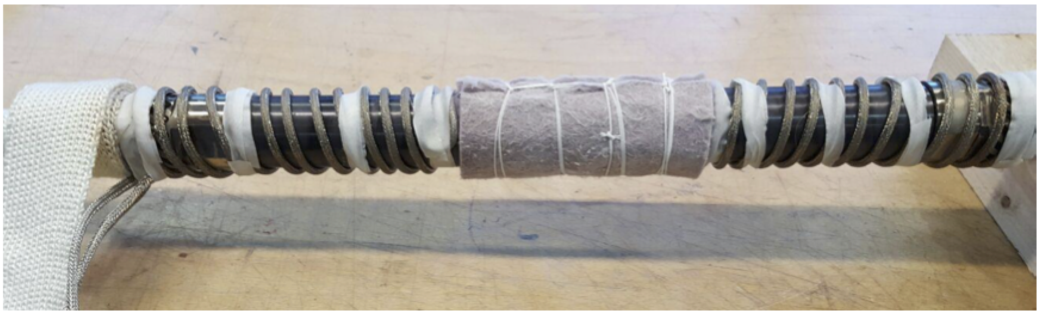

(b) Reactor traced with the first layer of thermal insulation.

(c) The fully insulated reactor, ready to be inserted in the magnet.

Figure 6.5 The Ceratec main reactor body reactor, with trace heating and insulation wrapped around.

All electrical trace heating (JE) consists of a pair of two thermocouples (TE and TSE). The miniature thermocouples are made of stainless steel with a titanium shielding, are rated up to 900 °C and have an accuracy of ±1.5 °C [257]. The TE-thermocouple feeds back into the control system which sets the heating power output. The TSE-thermcouples is connected to a separate display screen on the control cabinet of the reactor. Both thermocouple readings operate independently but the TSE-thermocouples act as a safety switch in case the primary thermocouples TE fail. If in the event of overheating the TE-thermocouples are not switched off automatically, the TSE-thermocouples can turn off the heating mechanism independently.

Using six sets of two thermocouples, the temperature around the catalyst bed and reactor is closely regulated and monitored. These thermocouples are only made of non-magnetic materials and are never placed inside the FOV of the spectrometer. Two long titanium shielded thermocouples (TE-105 and TE-106) measure the temperature at the top- and bottom-end of the reactor. Two frits are placed at both outer ends of the central imaging area, which have a large hole through which the two thermocouples fit.

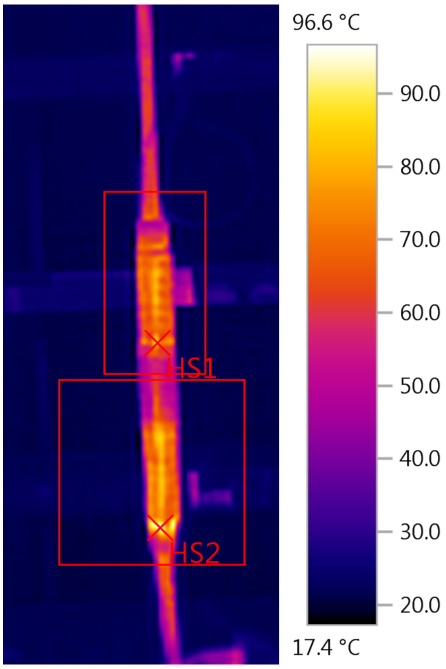

Figure 6.6 Infrared thermal imaging of the reactor, heated up to 250 °C, clearly indicating the effect of the insulation. Image supplied by Zeton B.V.

During the Factory Acceptance Testing (FAT) performed at Zeton B.V., the efficiency of the reactor insulation was tested. The results can be seen in Figure 6.6 where an infrared thermal image of the reactor, heated up to 250 °C, is shown. The middle section of the reactor, which covers the FOV of the magnet, is best insulated with outer temperatures reaching only 50 °C. This section has an additional insulation layer, as was shown in Figure 6.5b. The top and bottom of the reactor reach temperatures of around 85 °C.

6.2.5 Product Collection Vessels

Downstream of the reactor, the separation section comprises several product collection vessels which are all heat traced. Using gravity, the waxes, liquid and gas products exit the reactor and enter a gas-liquid separator. The waxy products and longer hydrocarbons (C_{6+}) condense and are contained in the first collection vessel (V-201), while the gaseous products and shorter carbon chains flow further to the condensation section. The wax collection vessel V-201 is a

500 mL bottle that has its own trace heating loop. To prevent solidification of the products that can clog up the system, it is always necessary to operate the product lines at elevated temperatures (>150 °C). The second separation stage contains both a refrigerator (E-250), which maintains the cooling water at 3 °C, and a heat exchanger (HE-250) where the gaseous $C_{1\text{-}5}$ products are condensed. This collection vessel is a jacketed cooling vessel where a tube-in-tube cooler cools downs the species in the line. The water and $C_{1\text{-}5}$ carbon chains are collected in the second product collection vessel (V-250).

After the cooling unit, all remaining gaseous products that did not condense, leave the system via a gas outlet at the top of the cooling vessel. The outlet gases are first passed through the dome loaded back-pressure regulator (DLBPR) (PCV-250) and subsequently through the water-gas flow-meter (WGFM) (FQI-250). This meter measures the product gas flow leaving the reactor. Finally, the outlet gas is fed to the GC analysis system. The results obtained from the GC are used for conversion and selectivity analysis.

Both product containers (V-202 and V-251) can be emptied in two removable product collection vessels using a small 1.5 mL sample holder connected to a 3-way valve. The bottom of both collection vessels has an automated, air-actuated 3-way valve (XV-200 or XV-250) and a needle valve (HV-200 or HV-250). The 3-way valve is regulated via the main control system, and has a set time interval for opening and closing. A Start/Stop button on the rig enables this 3-way valve to operate. To protect the glass collection bottles from shattering, they are positioned in a polycarbonate box.

6.2.6 Pressure Control

The pressure of the entire rig is controlled by a unit termed a DLBPR, see Figure 6.7. The operating principle of DLBPR provided by Equilibar®, is that the desired system pressure is also the dome pressure of the regulator. To create and regulate the pressure on the dome, a Bronkhorst pressure controller is installed in the dome feed line using N_2. The Equilibar® DLBPR uses a flexible membrane diaphragm to sense the pressure applied and to provide a direct seal against the orifice unit. The pilot port is pressurised with N_2 to the desired operating pressure. While the pressure on the inlet port is below the pilot pressure, no flow towards the reactor occurs. This inlet pressure is equal to the pressure that is applied to the diaphragm of the regulator. The diaphragm pressure is applied via the pilot port located on top of the back-pressure regulator.

Once the inlet- and pilot pressures are equal, the diaphragm opens and this allows flow towards the reactor for pressurising. Normally under steady condition, an equilibrium is achieved and the diaphragm modulates into a position where just enough flow is allowed out of the regulator in order to maintain a steady pressure on the inlet port. During reaction, the inlet of reactants or a temperature rise in the reactor can lead to an increase in reactor pressure. Even with fluctuating inlet pressures, the diaphragm can enable a stable reactor pressure. The diaphragm can compensate by closing, thereby maintaining the outlet pressure and thus keeping a constant reactor pressure. Obviously this is only valid if the pilot pressure is maintained. The electronic flow control system can regulate the inlet flow rates of the dome to obtain a stable pressure in case of over-pressure.

Two capillaries are installed in the DLBPR unit, but are not depicted in Figure 6.7a. To keep the optimal pressure control, the dome line vents some of the supplied gas via the capillary. This constant bleeding creates a dynamic response behaviour for the pressure control of the system. By giving the controller a set-point, the flow control valve will open until the set-point pressure is reached. A second capillary, which is usually closed, is placed downstream of the automated ball valve and is only used in case of an emergency system shut-down. If this occurs, the ball valve opens and the dome pressure is released, thereby depressurising the whole reactor slowly. This is done to prevent sudden depressurisation in order to protect the on-line equipment such as the WGFM and the HPLC pump.

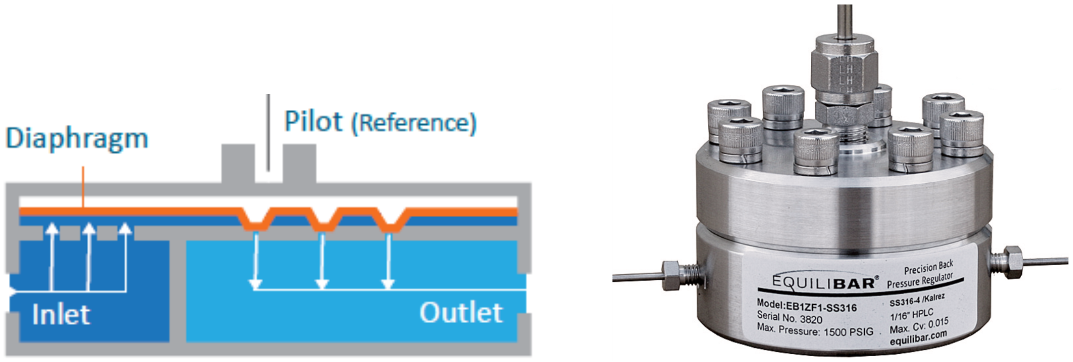

(a) Cross section schematic of the dome loaded back-pressure regulator. Supplied by Zeton B.V.

(b) An Equilibar® dome loaded back-pressure regulator.

Figure 6.7 A schematic showing the flow directions used in an Equilibar® dome loaded back-pressure regulator.

6.2.7 Customised Operational Control Additions

Several customised solutions were implemented to improve the operation of the FT rig.

Turning Off Reactor Heaters with a 5 V Signal

First, during the acquisition of most NMR experiments, the reactor heaters (TIC-100 and TIC-102) can be switched off automatically. These heaters can create temperature fluctuations which induce variations to the measured NMR signal. The magnetic susceptibilities can lead to local distortions of the signal thereby affecting the measurement. To prevent this, pulse sequences were modified to implement the heaters shut-down for several milliseconds. By sending a 5 V signal from the rig to the control system during the signal acquisition, the heaters are turned off by setting their output to 0%. The heaters are turned on automatically when a 0 V signal is received. This timing was optimised to prevent significant temperature fluctuations in the reactor.

SMS Alarms

Second, as a typical FT experiment involves testing the life-time of catalysts and study the evolution of the products, the reactor is required to run safely overnight for an extended period of time. To make sure a 24/7 monitoring of the rig can be achieved, the rig was programmed to send automatic SMS text messages to the operators. In case of any alarms, deviations or trips, the operators were informed and could act accordingly.

Leak Detector

Third, in collaboration with the scientists from STCA, a leak detection (LVK-600) system was implemented. All gas lines (from the feed section, the CEM and the back pressure regulator) are connected to a vessel containing transparent oil. In the case any fitting, valve or tube is leaking, the gas will follow the route with the least pressure resistance and this will result in minute bubble formation in this leak detector. This Shell in-house design permits visual detection of small leaks ($\geq$ 0.1 mL min^{-1}).

6.2.8 Power Supply

The main AC power (400 VAC) circuit is a 5-wire connection (3 phases, 1 neutral and 1 ground). The 3-phase and neutral lines are all connected to the main switch of the main distribution board (SE-1). The secondary power circuit is the 230 VAC control power circuit which is a three wire connection (phase, neutral and ground). The control cabinet is the primary communication port between the reactor and its operators. This circuit powers the power supplies, control system and instrumentation on the rig.

6.2.9 P&ID Drawing

In Figure 6.8, a technical, simplified flow sheet is shown of the reactor. A real P&ID drawing supplied by Zeton B.V. can be found in the Appendix A on Page 224.

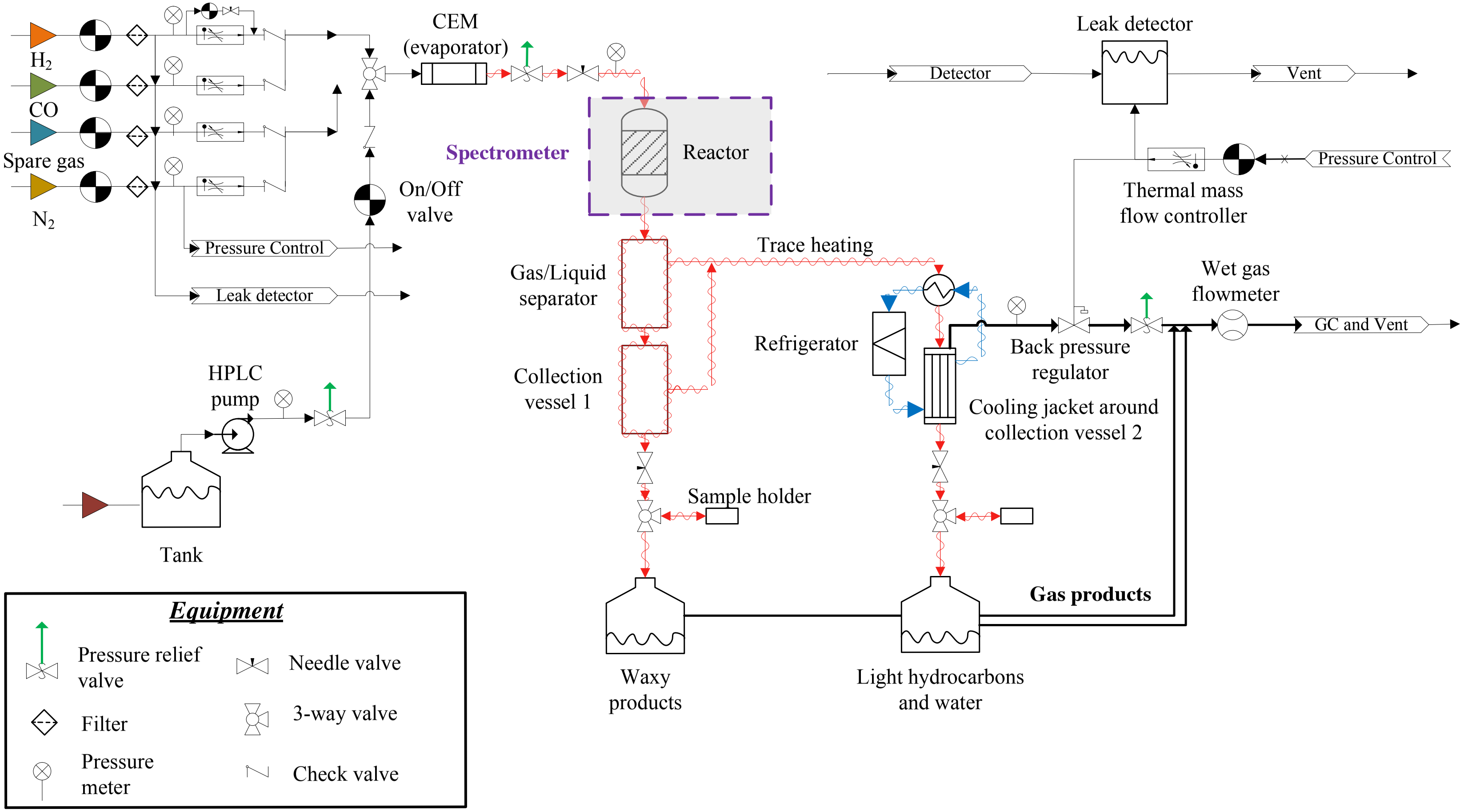

Figure 6.8 A technical diagram of the FT reactor.

6.3 Safety Aspects

6.3.1 Causes and Effect Matrix

In order to create an additional layer of safety and to manage any potential hardware or software failures on the FT rig, the C&E (Causes & Effects) matrix was designed, in collaboration with STCA, Zeton and MRRC. The C&E diagram is a comprehensive matrix which can be divided into two main sections. The first shows all the trips, alarms or failures of the various components that could occur on the rig. This section details the time delays and set-point deviations required before a trip is triggered. The second section shows what actions (or effects) take place when a specific trip is reached. These are pre-programmed, automatic sequences that for example turn off heaters, shut-off valves or depressurise the reactor. The C&E system is used to ensure maximum safety during operation and enable safety mechanisms to be triggered while the rig is left unattended.

Figures 6.9 and 6.10 give an overview of the different triggers and effects that are programmed for both hardware and software units on the Zeton B.V. FT reactor. The blue boxes are the several situations that could take place on the rig, varying from pressing the emergency button, to having a computer failure, power cut or temperatures rises for specific trace heating areas. In orange, all effects are listed that are triggered when a trip takes place.

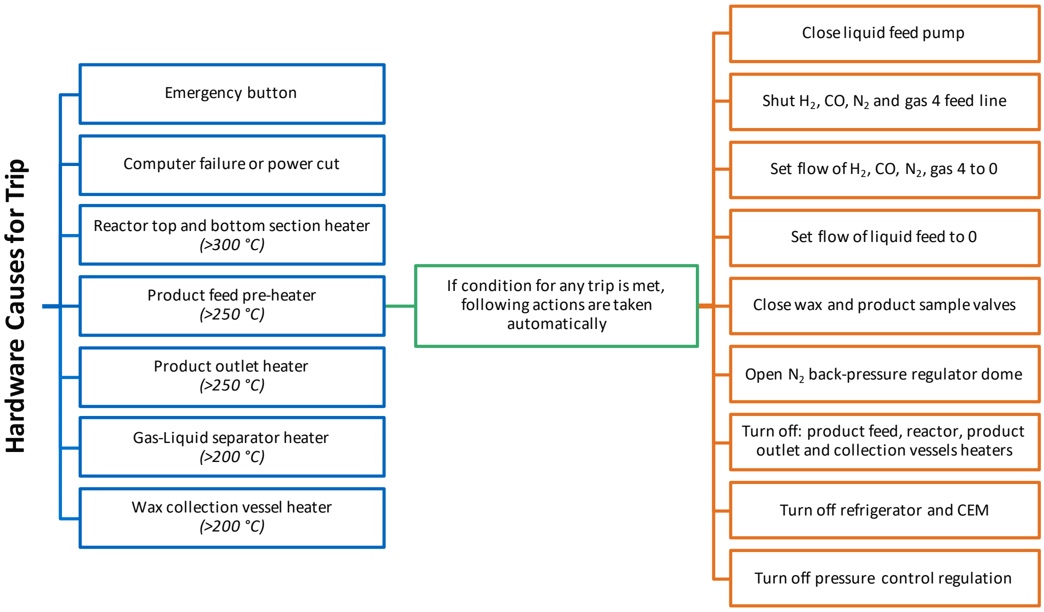

Figure 6.9 First part of the Cause and Effect Matrix. In case of any accident (possible Causes in blue boxes), the necessary precautions (Effects in orange boxes) for hardware are taken. Adapted from matrix supplied by Zeton B.V.

For the possible hardware failures or over-heating issues (see required temperature limit in blue boxes), the effects listed in the orange boxes in Figure 6.9 are automatically enabled: (i) the gas and liquid feeds are set to 0 and their valves are shut, (ii) the reactor is depressurised, (iii) all heater power outputs are set to 0 and turned off and finally, (iv) the CEM and refrigerator are switched off. This is similar to simply shutting down the whole reactor and stopping all activities. In case of a hardware failure, any ongoing reaction is simply interrupted and the reactor is brought to a shut-down mode.

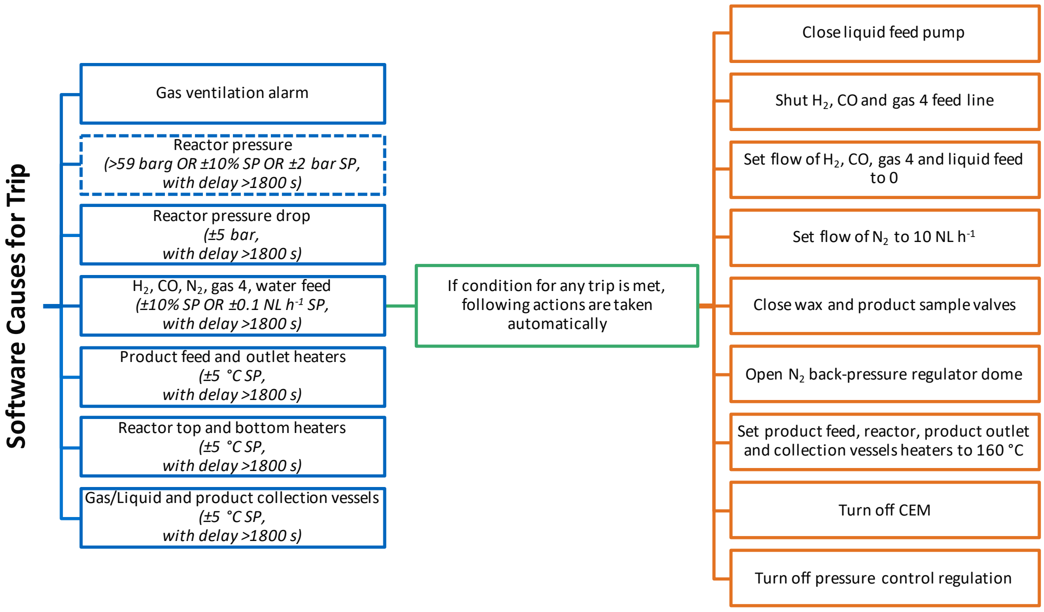

Figure 6.10 Second part of the Cause and Effect Matrix. In case of any accident (possible Causes in blue boxes), the necessary precautions (Effects in orange boxes) for software are taken. Any trip is only triggered when a deviation from the set-point for at least 1800 s occurs. In addition, a deviation counts when either ±10% or ±2 bar from the reactor pressure set-point, ±10% from the flow rate set-point or ±5 °C from the heater set-point is registered. Adapted from matrix supplied by Zeton B.V.

The trips and consequences are slightly different when a software issue occurs, as can be seen in Figure 6.10. Firstly, for the software trips (in the blue boxes) to be triggered, a deviation from the set-point for at least 1800 s is required before any safety mechanisms are enabled. A deviation is classified as either ±10% or ±2 bar from the reactor pressure set-point, ±10% from the flow rate set-point or ±5 °C from the heater set-point.

The different triggers for a software trip can vary from: (i) CO detection above its safety levels, (ii) over-pressurising or a pressure drop across the reactor, (iii) deviation from the gas or liquid feed flow rate set-points or finally (iv) deviation from the trace heating set-points. Any of these causes lead to a limited shut-down of the reactor while it is kept warm and safe under low N_2 flow. This is done to prevent any products from solidifying and causing a potential blockage with the risk of over-pressurising while any CO or H_2 remains can be purged. The effects triggered by the automatic safety mechanism are: (i) the gas feed (CO, H_2 and gas 4) and liquid feed are set to 0 and their valves shut, (ii) the reactor is depressurised and finally (iii) the CEM is switched off. The main difference compared to a hardware issue shut-down is that N_2 is kept flowing at 10 NL h^{-1} and the heaters are kept at 160 °C.

One exception is marked by the dotted-line box around the reactor pressure as this is the only cause that will enable a different effect mechanism. If the reactor pressure has not reached the set-point yet, one very likely cause is that the set-point pressurising rate was set too high and the reactor has not had enough time yet to reach the desired pressure with the used gas flow rate. Another likely possibility is that the N_2 cylinder is not pressurised enough to reach the required reactor pressure. In those situations, only (i) the gas feed (CO, H_2 and gas 4) and liquid feed are set to 0 and their valves shut and (ii) the CEM and refrigerator are switched off. The reactor heaters are left on, the N_2 feed is kept open and the reactor pressure control is not switched off.

Figure 6.11 is called the Range, Alarm & Trip Settings List. For every component on the reactor with its associated tag number and description, this list tabulates the control range in which the unit can safely be operated in. In addition, in the last four columns, the LowLow (LL), Low (L), High (H) and HighHigh (HH) alarm trip settings are shown. Depending on how significant the deviation from the set-point is, either a L, LL, H or HH alarm is triggered. This has different consequences in terms of what alarms are sent out in the text messages.

6.3.2 Standard Operating Procedures

In order to ensure the best operating practices using the highest standards for safety, a Standard Operating Procedures (SOP) was designed, in collaboration with the specialists at Zeton and scientists at STCA. Hence, our FT SOP is based on the operating guidelines from STCA. The instructions below are a summary and can be used as a reactor manual. The SOP can be divided into 7 main categories:

1. The gas feed and cylinders
    (a) All cylinders, regulators and hand valves have to be opened safely and pressurised.
    (b) Instrument air is turned on to operate the pneumatic valves.
    (c) N_2 is opened to allow reactor pressure control and GC is turned on.
2. LabVIEW initiation
    (a) LabVIEW control system is activated and main switch on the rig is turned on.
    (b) Any start-up alarms are acknowledged.
3. Start-up procedure: heating and pressurising with H_2 and N_2
    (a) All trace heating and thermocouples are connected appropriately.

Range, Alarm & Trip Settings List

Hardwired

					Installed span				Control							
Tag number	Tag Hexagon	P&ID	Location	Description	Low	-	High	Unit	Low	-	High	Unit	LL	L	H	HH
TSE-061	TSE - 061	1		Mix inlet heater TSS	0	-	400	°C	0	-	400	°C				250
TSE-101A	TSE - 101A	2		Reactor top section heater TSS	0	-	400	°C	0	-	400	°C				300
TSE-101B	TSE - 101B	2		Reactor top section heater TSS	0	-	400	°C	0	-	400	°C				300
TSE-103A	TSE - 103A	2		Reactor bottom section heater TSS	0	-	400	°C	0	-	400	°C				300
TSE-103B	TSE - 103B	2		Reactor bottom section heater TSS	0	-	400	°C	0	-	400	°C				300
TSE-107	TSE - 107	2		Reactor product outlet heater TSS	0	-	400	°C	0	-	400	°C				250
TSE-201	TSE - 201	2		Wax separator heater TSS	0	-	400	°C	0	-	400	°C				250
TSE-203	TSE - 203	2		Product storage heater TSS	0	-	400	°C	0	-	400	°C				200

Labview

					Installed span				Control							
Tag number	Tag Hexagon	P&ID	Location	Description	Low	-	High	Unit	Low	-	High	Unit	LL	L	H	HH
FTC-010	FIC - 010	1		Hydrogen feed	0	-	30	Nl/h	0	-	30	Nl/h				
FTC-020	FIC - 020	1		Carbon monoxide feed	0	-	30	Nl/h	0	-	30	Nl/h				
FTC-030	FIC - 030	1		Gas 3 feed	0	-	30	Nl/h	0	-	30	Nl/h				
FTC-040	FIC - 040	1		Nitrogen feed	0	-	30	Nl/h	0	-	30	Nl/h				
FTC-060	FIC - 060	1		Liquid feed	0	-	5	g/h	0	-	5	g/h				
FQIT-250	FQI - 250	2		Gas outlet meter	0	-	120	l/h	0	-	120	l/h			110	120
MX-060	MX - 060	1		Evaporator mixer	0	-	200	°C	0	-	200	°C				
PT-100	PI - 100	2		Reactor pressure	0	-	60	barg	0	-	60	barg			55	60
PT-200	PI - 200	2		High pressure separator outlet pressure	0	-	60	barg	0	-	60	barg			55	60
PTC-300	PIC - 300	2		Pressure control PCV-250	0	-	60	barg	0	-	60	barg				
TE-104A	TI - 104A	2		Reaction zone top TE	0	-	400	°C	0	-	400	°C			260	280
TE-104B	TI - 104B	2		Reaction zone top TE	0	-	400	°C	0	-	400	°C			260	280
TE-105A	TI - 105A	2		Reaction zone bottom TE	0	-	400	°C	0	-	400	°C			260	280
TE-105B	TI - 105B	2		Reaction zone bottom TE	0	-	400	°C	0	-	400	°C			260	280
TE-060	TIC - 060	1		Mix inlet heater TE	0	-	400	°C	0	-	400	°C			230	240
TE-100A	TIC - 100A	2		Reactor top section heater TE	0	-	400	°C	0	-	400	°C			260	280
TE-100B	TIC - 100B	2		Reactor top section heater TE	0	-	400	°C	0	-	400	°C			260	280
TE-102A	TIC - 102A	2		Reactor bottom section heater TE	0	-	400	°C	0	-	400	°C			260	280
TE-102B	TIC - 102B	2		Reactor bottom section heater TE	0	-	400	°C	0	-	400	°C			260	280
TE-106	TIC - 106	2		Reactor product outlet heater TE	0	-	400	°C	0	-	400	°C		140	230	240

Figure 6.11 The Range, Alarm & Trip Settings List. This tabulates all the ranges that each component can safely operate in and at what levels the various alarms are triggered. Matrix supplied by Zeton B.V.

   (b) Refrigerator and CEM switched on.
   (c) All trace heaters set to desired temperature.
   (d) Pressure test with N_2 and aim for stable pressure for pressure-tight system.
   (e) If leaks occur, depressurise system and find the leak.
4. Reaction
   (a) Set desired temperature, gas flow rates and other reaction conditions.
   (b) If necessary, open CO cylinder and start flowing synthesis gas.
   (c) Track reaction in LabVIEW. Check temperature and pressure to spot deviations.
   (d) Start NMR experiments.
5. Product sampling
   (a) Open HV-250 or HV-200.
   (b) Press green Start buttons on the rig.
   (c) Disable sequence when product collection vessels are emptied by pressing on Stop.
6. Depressurising system and shutdown
   (a) Change temperatures and pressure set-points. Cool-down and depressurise slowly.
   (b) If stripping of intra-particle product is required, purge overnight using H_2 and N_2.
   (c) Close hand valves and cylinders as required.
7. Reactor removal with catalyst replacement
   (a) Disconnect the trace heating and thermocouples and unscrew the VCR® gaskets.
   (b) Carefully lift the reactor while supporting it to prevent it from falling or sliding.
   (c) Open the reactor using the purpose-built spanners supplied by Zeton B.V.
   (d) Replace the catalyst bed supported by the tripods and replace Kalrez® O-rings.

6.3.3 Risk Assessments

In order to comply with the safety rules and regulations of the Department of Chemical Engineering and Biotechnology, it was required to conduct a risk assessment of FTS. In addition, the FT rig is a one-off, experimental set-up, working with toxic and flammable gases. Hence, both the Head of Department and the University Safety Officer had to approve the safety design of this rig. In total, 12 different Risk Assessments forms had to filled in. The three main types of forms are described below:

- **Form 1 - General Risk Assessment:**
  describing the general experiments and associated risks.
- **Form 2 - Hazardous Substance Risk Assessment:**
  fulfilling the requirements of the Control of Substances Hazardous to Health (COSHH) and Dangerous Substances and Explosive Atmospheres Regulations (DSEAR) Regulations relating to FTS working with (i) CO, (ii) H_2, (iii) SiC, (iv) Ru/TiO_2 and (v) linear hydrocarbons.

- **Form 7 - Rig Risk Assessment:**
  outlining the apparatus and rig used which compromise a pressurised vessel.

6.3.4 LabVIEW control system

The control of the FT reactor is done through the National Instruments LabVIEW application. This program gives full control via a graphical user interface. The main, custom built LabVIEW instrument control panels are shown in Figure 6.12 (feed section) and Figure 6.13 (reactor section). This software also allows to view historical data. The reaction process can be monitored and temperature, pressure and flow rates can be set. Moreover, the operator entries are logged and the alarm conditions can also be reported. This allows one to understand how the reactor behaved in case of an alarm trip. The LabVIEW control system enables the operator to:

1. Monitor the process (pressure, temperature, flow) and change set-points.
2. View real-time and historical data.
3. Log operator entries and alarm trips.

Figures 6.12 and 6.13 have the same layout as the P&ID drawings. In Figure 6.12, the four gas feed lines can be seen in addition to the liquid feed pump. These are mixed and heated up by the CEM. Four options in the bottom right corner of Figure 6.12 can be seen: (i) GC Communication, (ii) Seq. Trigger, (iii) Gas and Ventilation and (iv) NMR Communication. Only options (iii) and (iv) are in use: option (iii) is enabled by default indicating that the gas safety detectors (CO, H_2 and O_2) in the lab are active. Option (iv) disables the reactor heaters TIC-100 and TIC-102 for a few milliseconds during certain NMR acquisitions, as discussed previously.

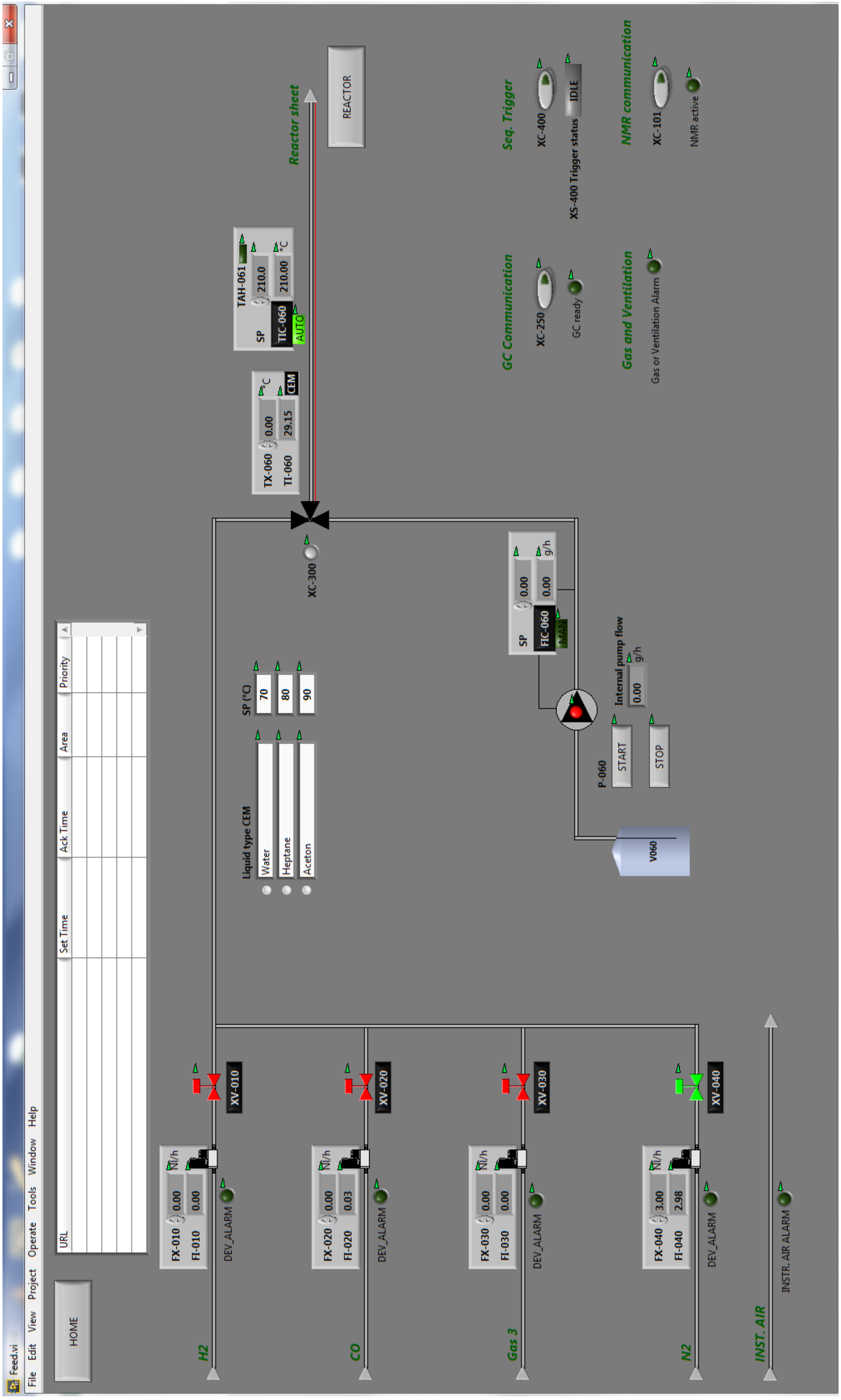

Figure 6.12 Overview of the LabVIEW Feed control screen giving access to the feed system of the reactor, including temperature and flow.

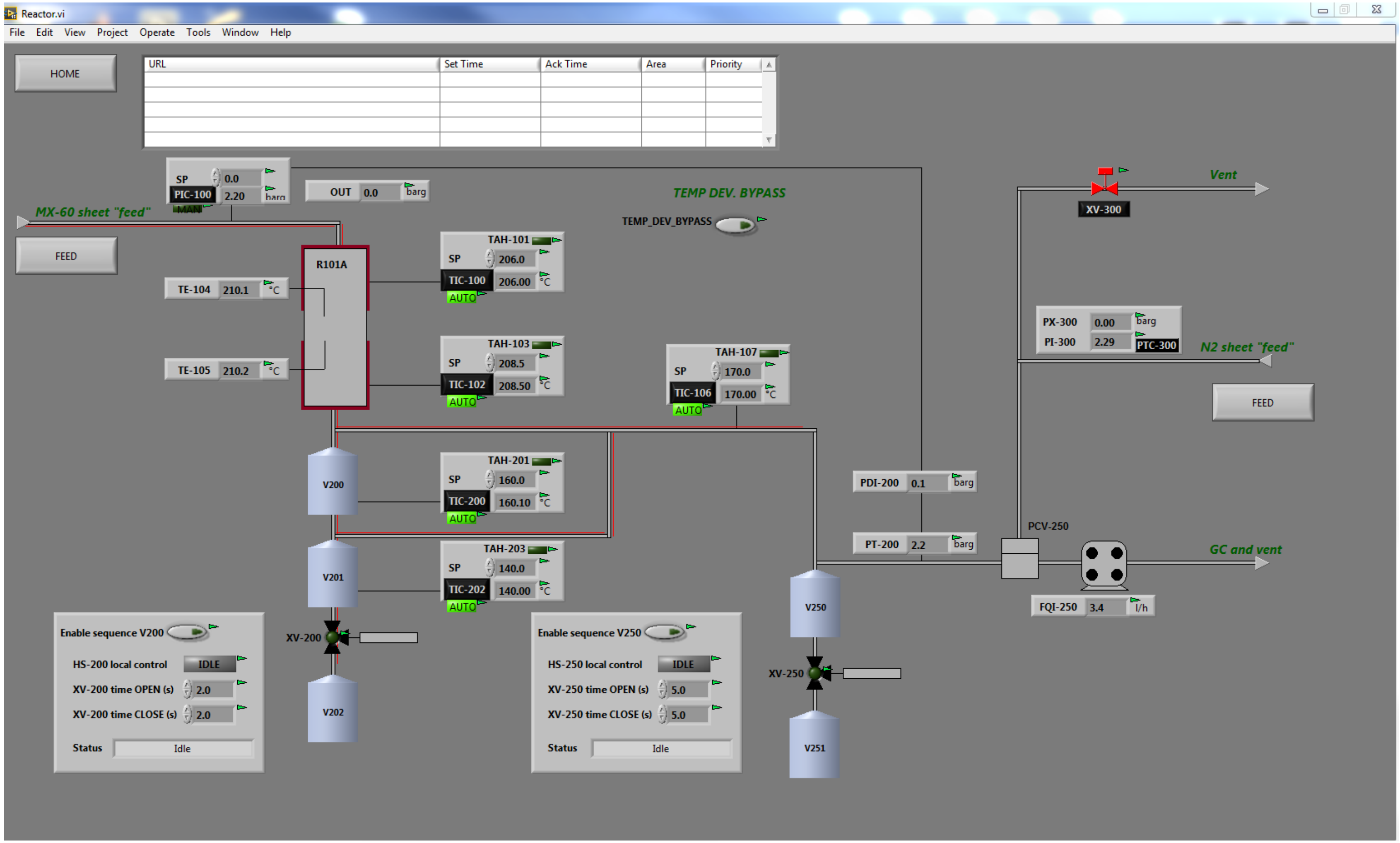

Enable sequence V200
HS-200 local control IDLE
XV-200 time OPEN (s) 2.0
XV-200 time CLOSE (s) 2.0
Status Idle

Enable sequence V250
HS-250 local control IDLE
XV-250 time OPEN (s) 5.0
XV-250 time CLOSE (s) 5.0
Status Idle

Figure 6.13 Overview of the LabVIEW Reactor control screen giving access to the reactor, product collection vessels, temperature and pressure.

6.4 The Agilent Gas Chromatogram

The model and make of the Agilent GC, shown in Figure 6.14, is a: SP1 7890-0378 Three Channel Fast Refinery Gas Analyser (RGA) with no C_{6+} back-flush. In collaboration with Agilent, this equipment was custom built for the FT research objectives on the rig. It operates on the OpenLab EZChrome chromatography system, same software as used at STCA. It is specifically designed and calibrated to study short-chain, linear hydrocarbons.

The GC has eight columns (e.g. made from Al_2O_3 with dimensions of 50 m × 0.53 mm) and consists of three detectors for compound separation: (i) a thermal conductivity detector (TCD) channel which can measure H_2 using N_2 as carrier gas, (ii) a second TCD channel detecting permanent gases (O_2, N_2, CO_2 and CO) using He as carrier gas and (iii) a flame ionisation detector (F-I-D) hydrocarbon channel detecting C_1-C_6 molecules with H_2 as carrier gas. The lower detection limit is 100 ppm for permanent gases and 5 ppm for the hydrocarbons. See Appendix B for a complete system overview.

Figure 6.14 The Agilent GC: 7890-0378 - Three Channel Fast Refinery Gas Analyser.

The key features of this equipment are:

1. Three parallel channels with simultaneous detection for complete refinery gas analysis within eight minutes. This allows up to six analysis runs per hour.
2. A Sample Stop/Divert Valve. Significantly improves repeatability and precision by allowing sample injection loops to equilibrate to atmospheric pressure before injection.
3. Moisture and hydrocarbon filters to maintain hydrocarbon sensitivity and stable operation.

Figure 6.15 depicts the chromatograms obtained from the three detectors during FT. The peaks can be correlated to molecular concentrations which are needed to calculate selectivity and conversion.

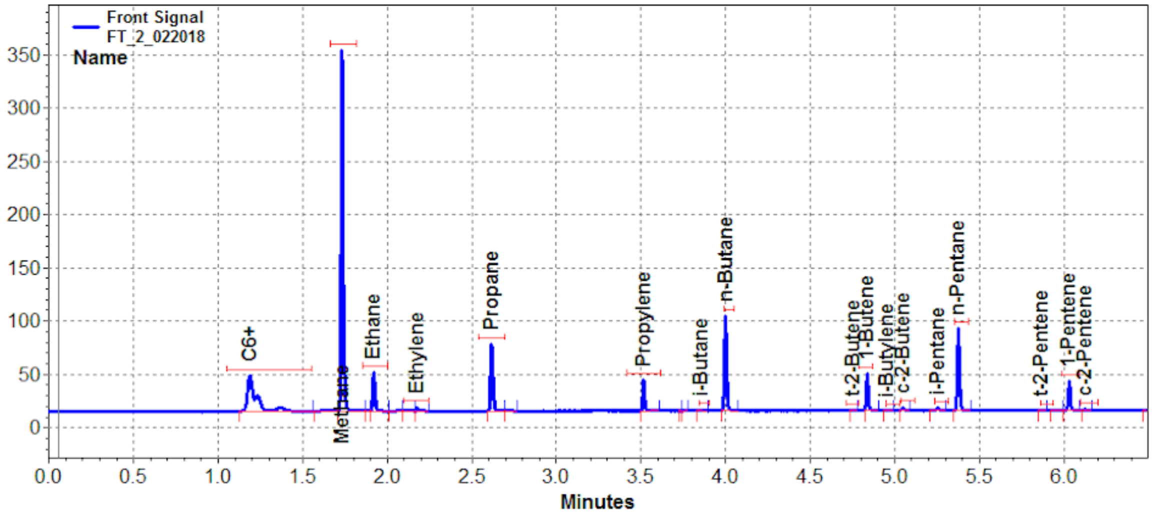

(a) The front F-I-D hydrocarbon channel detecting C_1-C_6 species.

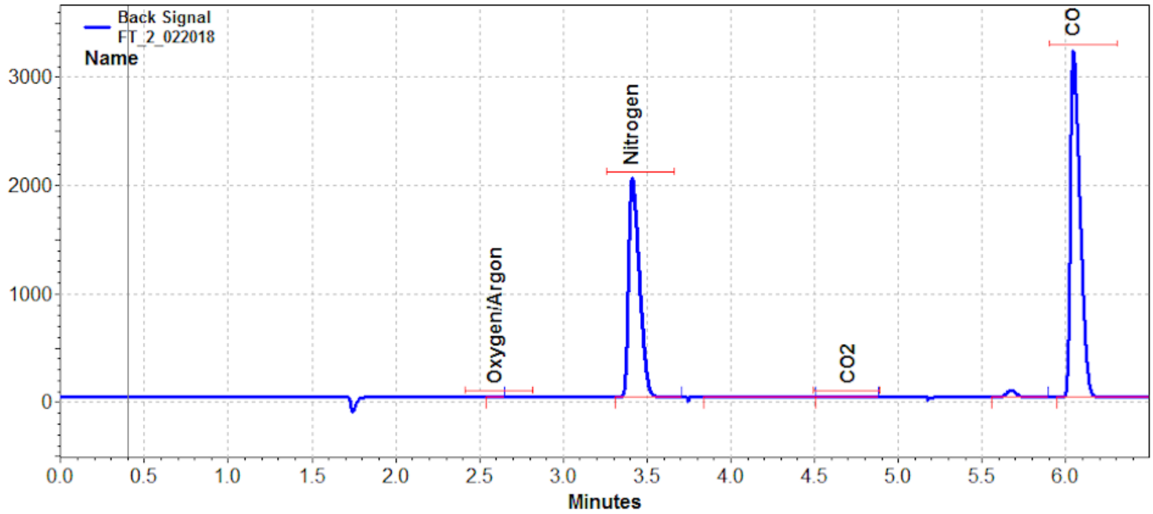

(b) The back TCD channel detecting permanent gases (He, O_2, N_2, CO_2 and CO).

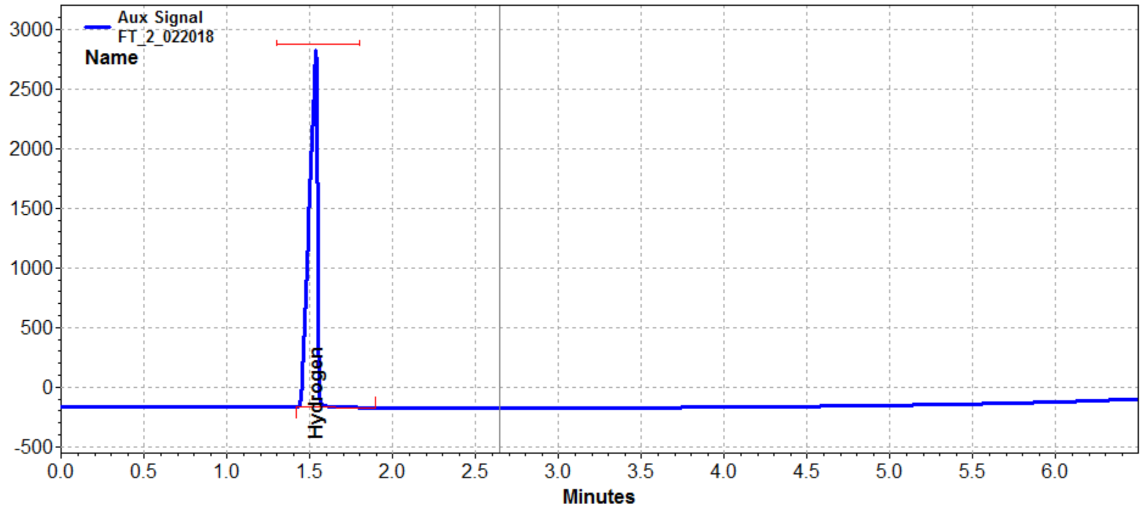

(c) The auxiliary TCD channel detecting H_2.

Figure 6.15 Examples of chromatograms obtained from the three detectors during FT experiments. These are used to calculate selectivities and conversions of the FT reaction.

6.4.1 Calibration

The GC was calibrated in two stages. The manufacturer Agilent supplied a standardised Refinery Gas mixture to perform the initial calibration. This is a mixture of various gas streams typically produced during a refinery process. This sample could be a fuel gas, a final product or even a feedstock for further processing [258]. In order to calibrate the GC for individual components, known concentrations have to be injected to calculate the Response Factor, which is the reciprocal of the slope of the calibration line [259], see Equation 6.2.

$$\text{Response Factor} = \frac{\text{Area}}{\text{Concentration}} \tag{6.2}$$

Figure 6.16 depicts the three final calibration lines for N_2, H_2 and CO which are needed to calculate the conversion of the FT reaction. Using the initial Refinery Gas mixture, only the red points (○) on the calibration line could be obtained. For N_2 this covered the range between 0 - 63 mol%, for H_2 between 0 - 13 mol% and for CO only between 0 - 3 mol%. However, as the concentrations during steady state FT for N_2, H_2 and CO are approximately 26, 43 and 28 mol% (see - - -) respectively, the initial calibration mixture did not suffice. Hence, the GC was further calibrated with various mixtures with different concentrations of CO, N_2 and H_2 to cover the necessary FT operating range, see black points (○). Using these extra calibration points, the full calibration line (—) was determined.

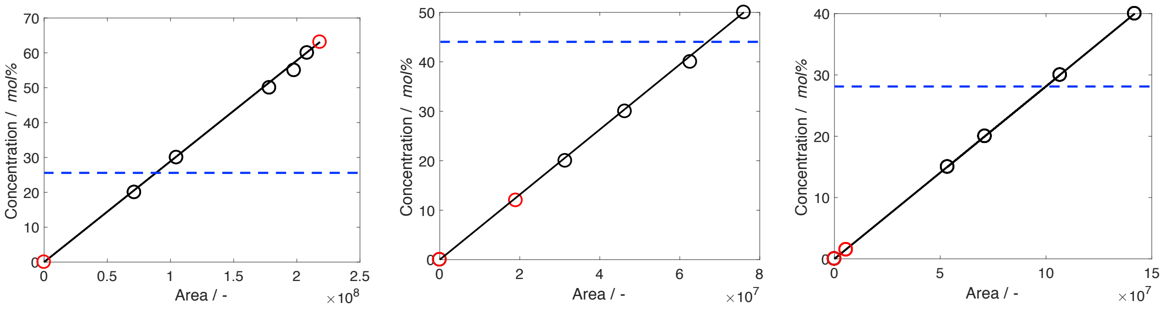

(a) N_2 calibration line. (b) H_2 calibration line. (c) CO calibration line.

Figure 6.16 The calibration lines for N_2, H_2 and CO (—) obtained from the extended calibration mixtures (○). The initial calibration points determined from the Refinery Gas mixture did not cover the steady state FT concentration range (- - -), except for N_2.

6.5 Collaboration with Shell Technology Centre Amsterdam

As the research described in this thesis is done in collaboration with Gas Conversion scientists at STCA in Amsterdam, the Netherlands, many opportunities arose throughout the doctorate whereby both parties could learn from one another. To facilitate this knowledge transfer, in total ten weeks were spent at STCA during the PhD spread over four different trips.

These visits were very useful to learn about (i) reaction operation, (ii) catalyst preparation, (iii) using LabVIEW and EZChrome for GC analysis and (iv) product analysis via Soxhlet extraction.

In the Sections below, these findings are discussed in more detail. Furthermore, access to other characterisation techniques or commercial samples was given by Shell. In addition, a week was spent at Zeton B.V. in Enschede, the Netherlands, for the FAT of the new rig.

6.5.1 Reactor Handling and Suggestions

Several examples can be given that summarise the knowledge transfer between Shell and the MRRC. Firstly, the collaborators at Shell taught us the practices of operating a pilot-scale rig safely and assisted in developing the SOP. Secondly, STCA suggested to purchase restriction devices to limit the outflow of gas in case of a pipe rupture. Furthermore, Shell also helped in designing a Y-shaped, customised part that Zeton B.V. manufactured, enabling a thermocouple to reach the reactor and at the same time allowing products to leave the reactor bed. In addition, the post-reaction catalyst analysis done via Soxhlet extraction which was first encountered at STCA, is now adopted and applied at the MRRC.

Finally, thanks to Shell, the catalyst bed was designed in several layers, as will be described in more detail in Section 7.2. As FTS is an extremely exothermic process, hotspot formation and temperature overshooting are a real threat, especially if the FT rig does not have any external cooling mechanism and only relies on convection and irradiation for cooling. Hence, Shell suggested to design the catalyst bed in three separate layers and dilute the catalyst extrudates with inert material. This common approach can prevent a large energy production that could lead to a temperature run-away.

6.5.2 Catalyst Impregnation

The experiments performed at Shell were intended to serve primarily as training in microreactor operation using FT catalysts. However, for completeness the collaborators also offered training in how to prepare the catalysts as well as test them. Some of the catalysis work done at the Shell laboratories in Amsterdam involved cobalt catalysts. Their supports are extrudates made of TiO_2 which are impregnated. The supports have a known pore volume of 0.3 mL g^{-1} and were impregnated with cobalt(II) nitrate hexa-hydrate. Promoters, like manganese(II) nitrate, can be added to increase the dispersion factor of the Co and therefore enhance the catalyst selectivity. These were the steps involved during the incipient wetness impregnation done at STCA:

1. Weigh 3.5 g of $Co(II)Ni \cdot 6 \cdot H_2O$ (corresponds to 2 mL)
2. Weigh 10 g of TiO_2 extrudates

3. Add 1 mL of deionised water to $Co(II)Ni \cdot 6 \cdot H_2O$
4. Add the $Co(II)Ni \cdot 6 \cdot H_2O$ solution to the extrudates using a pipette
5. Use a rolling device to ensure equal distribution of impregnation solution in the pellets
6. Dry the catalysts (at 120 °C for 2 h followed by another 2 h at 300 °C)

The roller device is used to ensure that the impregnation solution is distributed homogeneously over all the extrudates particles. These pellets should only be mixed for 10 minutes maximum. As the impregnation process weakens the wet extrudates, their mechanical strength can be compromised if rolled too extensively. The final step in the impregnation process is the drying. The temperature is increased by 3 °C minute^{-1} to 120 °C. The pellets are kept at this temperature for two hours before the temperature is further ramped up to 300 °C in 60 minutes. This final temperature is kept for two hours before cooling the pellets down to ambient temperature.

(a) Cobalt catalyst 0.1wt%. *(b) Cobalt catalyst 0.5wt%.*

(c) Cobalt catalyst 1wt%. *(d) Cobalt catalyst 2wt%.*

Figure 6.17 The different cobalt catalysts impregnated on TiO_2 supports, with increasing Co loadings ranging from 0.1wt% to 2wt%. The green cobalt titanate can clearly be seen for the samples (a) and (b) with lowest concentrations of Co.

The results for the cobalt impregnation of 0.1wt%, 0.5wt%, 1wt% and 2wt% on TiO_2 supports can be seen in Figures 6.17a - 6.17d respectively. The supports impregnated with 0.1wt% and

0.5wt% cobalt solution do not have the typical black colour but instead these samples turned out to be partially green. Cobalt titanate is known to have a green colour and therefore the low loadings cause the impregnated particles to interact very strongly with the support to eventually form cobalt titanate. This is not reducible at 350 °C and therefore low loadings in this state are not readily usable in FTS.

6.5.3 Passivation

The process of passivation is typically performed to enhance the stability of transition metal catalysts highly sensitive to air. Passivating catalysts is reported to suppress rapid, exothermic oxidation reactions with air, which may result in phase changes and local temperature hotspots. The objective is to preserve and protect reduced or spent catalysts superficially from further oxidation which allows reduced samples to be transferred to characterisation equipment. Passivation thus allows characterisation of catalysts in a state which resembles the activated state as the changes in the catalyst properties are minimised. Furthermore, passivated samples can be safely stored under ambient conditions [260]. In the early days, refineries performed an *in situ* regeneration or passivation of the catalyst by heating with N_2/air under controlled conditions [261].

The bench-top passivation units at Shell can feed between 25 - 90 NL h^{-1} of H_2, N_2 or air. Using a 1-inch reactor tube, 10 - 100 mL of catalyst can be loaded and the unit can operate up to 10 bar. Using glass wool at the bottom of the tube, the catalyst is kept in place. On both sides of the reactor, two sets of five heaters are used to heat up the catalyst tube. The maximum heating temperature is about 500 °C and the off gas is analysed by a GC. Also this rig is operated by LabVIEW via pre-loaded sequences, which include all the different steps required to complete a reduction or a passivation process. A possible reduction plan could be:

1. Heat up the oven to 150 °C under N_2
2. Dry the catalyst overnight
3. Increase the temperature to 280 °C and maintain this for 15 hours
4. Close the N_2 feed and switch to H_2 at 10 bar and keep this flowing for 72 hours
5. Cool down to 150 °C
6. Close the H_2 feed and switch to N_2

6.5.4 Reduction

Many catalysts undergo a pre-treatment where they get reduced under a reductive environment, often in the presence of H_2, in order to “activate” them. The materials are reduced to make the metals present in the catalyst pellets electronically more rich. The reduction process in the presence of H_2 can activate the pellets by partially reducing the oxide species on the catalyst which can then migrate onto the metal particles to destroy large ensembles of the active metal site. This can increase the interfacial region between the active metal and support [262]. The reduction process also facilitates the phase transition of TiO_2 from the anatase- to rutile-type which reduces the deactivation and coking of the catalyst [263].

Prior to that, one needs to find the optimal reduction temperature of the metal via temperature programmed reduction (TPR) experiments, to deduce at which temperature the metal gets reduced best [264]. The pilot-scale TPR unit at STCA is used to screen various reduction conditions for multiple catalysts before performing large scale reduction treatments. The rig is placed inside a GC oven to have better temperature control and therefore only minute quantities can be loaded at the same time (maximum 20 mg). Using H_2 as reactant, the temperature is ramped up to 450 °C with a 4 °C min^{-1} heating rate which is maintained for two hours. A gas chromatography - mass spectrometer (GC-MS) tracks the H_2 consumption and H_2O production to monitor the progress of the reduction. Prior to any experiments, leak testing is performed at atmospheric pressure by feeding a 30% flow of H_2.

6.5.5 Soxhlet

A typical post-reaction catalyst characterisation method is the soxhlet extraction, see Figure 6.18 for a schematic [265]. This setup can be used to obtain the waxy products that are produced during FTS and remain stuck in the intra-pellet regions of the catalyst. Using GC analysis, these extracted, waxy, long-chain hydrocarbons can be further analysed [266].

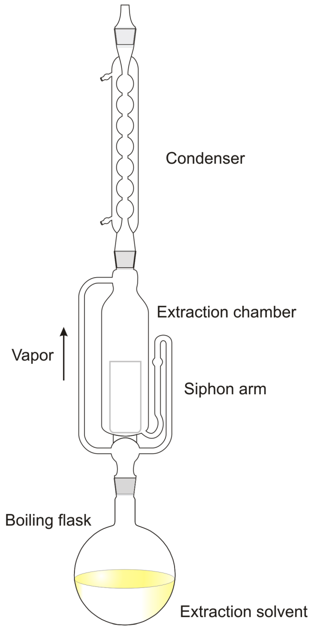

Figure 6.18 Soxhlet used to extract products after FTS from the catalyst pores. Reproduced from [265].

Typically 2 - 3 g of catalysts can be loaded in a filter, which is folded and subsequently stapled on the top to close. A Soxhlet extraction can be done overnight at atmospheric pressure. Toluene is the most commonly used extraction fluid when working in the oil and gas industry [267]. For this set up, no vacuum pump or N_2 purging is needed during the operation.

6.6 Influence of Feed Gas Composition on Catalytic Performance of Cobalt Catalyst

6.6.1 Introduction and Background

In the summer of 2016, two months were spent at STCA to perform preliminary experiments and to obtain some experience and further training in running a pilot-scale FT rig under real conditions. The scientific objective of this study was to understand the consequence of varying the H_2:CO feed ratio and analysing the effect of surface coverage [30, 268]. It is generally accepted that varying the feed composition will have an impact on the activity and selectivity of the catalyst but in the literature scientists still debate why many deviations exist from the theoretical ASF predictions [269].

These deviations could be caused by secondary reactions, such as growing surface chains that can terminate as paraffins or olefins. Readsorbed olefins can be further polymerised and hydrogenated, hence reducing the termination probability and increasing the chain-growth probability [99]. The extent of hydrogenation depends on many parameters, one of which is the partial pressure of CO and H_2 (P_{CO} and P_{H_2}). If an olefin chemisorbs onto the surface of the catalyst, this olefin has to compete for a vacant site. During normal FT reaction conditions, such an empty spot is very rare, as many different product species also compete with H_2 and CO to gain access to the active site on the metal catalyst. Therefore, changing the feed composition is thought to have an impact on the catalyst selectivity and product distribution [99].

6.6.2 Experimental

A glass reactor tube of a SSITKA machine was loaded with 0.1 g of FT cobalt catalyst powder. Using an on-line GC, the product stream (CO, CO_2, O_2, H_2 and C_1-C_{10+}) was analysed and quantified. More details on the catalyst were not provided by Shell due to confidentiality. The experimental reaction conditions were set at 3 bar and 220 °C.

Prior to all experiments, the catalyst was reduced and passivated at 350 °C and subsequently exposed to synthesis gas (mixture of H_2 and CO) for 72 hours to reach a steady state condition with stable activity. Typically, the feed ratio of H_2:CO during FTS is about 2:1. During these experiments P_{H_2} or P_{CO} was changed whereas the partial pressure of the second reactant was kept constant. Argon was co-fed to reach the reactor pressure balance of 3 bar.

6.6.3 Results and Discussion

In Figure 6.19, the product concentration is plotted against carbon number on a semi-log scale. The first experiments consisted of varying P_{CO} between 0.1 - 1.5 bar with a constant P_{H_2} of 0.5 bar, see Figure 6.19a. This results in relative amounts of CO ranging between 3 - 67% and a H_2:CO between 0.3 - 5.0. In the second set of experiments, the P_{H_2} was varied between 0.2 - 2.6 bar with a constant P_{CO} of 0.3 bar, see Figure 6.19b. This results in relative amounts of H_2 ranging between 7 - 89% and a H_2:CO between 0.7-8.7.

From Figure 6.19a, one can observe an increase in carbon number N as the P_{CO} increases, which suggests a strong, negative order in CO for $N > 6$. This figure also shows that the chain-growth probability, α, decreases with increasing H_2:CO ratio. ASF and the α were previously introduced in Section 2.2 on Page 6. This behaviour has been previously reported in the literature, whereby product selectivity and carbon number distribution of Co-catalysed FTS depends strongly on the H_2:CO ratio. This is in line with results published by both Mims *et al.* ([270]) and Weststrate *et al.* ([271]), and can be explained by a simple surface crowding model. Higher partial pressures of CO (P_{CO}) lead to increased concentrations of carbon species on the catalyst surface, which facilitate long-chain product formation [272]. Moreover, if the catalyst surface has higher coverage of carbon species, the selectivity towards methane is lower. However, for long TOS, this advantage comes at a cost as high CO partial pressures are reported to increase the production of carbonaceous deposits, which are linked to catalyst deactivation due to fouling [93].

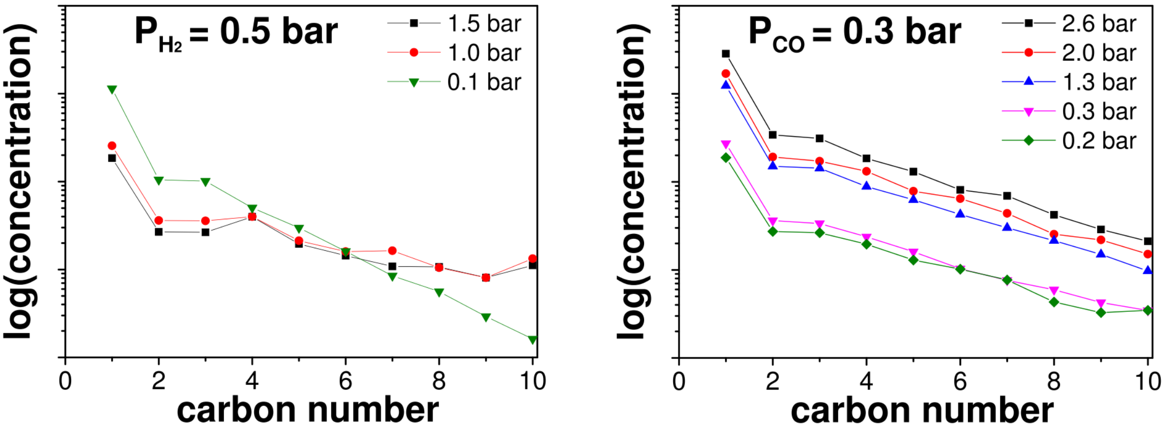

(a) The positive effect of increasing the P_{CO} on the carbon number at a fixed P_{H_2} of 0.5.

(b) The product distribution remains unchanged if the P_{H_2} is increased at a fixed P_{CO} of 0.3.

Figure 6.19 The influence of changing the feed gas composition on cobalt powder during FTS in a SSITKA apparatus.

A decreasing chain growth probability α facilitates the production of short-chain hydrocarbons [273]. In addition, the production of CH_4 increases with H_2:CO. This is in exact accordance with results published by Kuijpers *et al.* from STCA in 1994 where at constant P_{H_2}, the methane concentration decreases with increasing CO pressure [269]. However, in Figure 6.19b, the product distribution does not seem to be affected by the increase of P_{H_2}, as there is a first order dependence in H_2 for this specific reaction.

6.7 Commissioning the Cambridge Fischer-Tropsch Reactor

6.7.1 Reduction

The first experiments performed on the Zeton B.V. FT rig were done at 250 °C and 2 barg for 30 hours. The goal of this investigation was to reduce *in situ* the Ru/TiO_2 catalyst pellets using forming gas (5% H_2 in N_2) and measure the H_2 uptake using the GC. These first series of experiments were an excellent opportunity to test whether the reactor was working well and whether the commissioning was done appropriately.

The reduction process was initiated as soon as the N_2 was replaced by an initial flow of 10 NL h^{-1} of forming gas. These reduction conditions were maintained for 30 hours during which the forming gas flow was increased to 30 NL h^{-1}. All the reaction conditions are tabulated below in Table 6.3.

Table 6.3 Reaction conditions used during the initial pressure testing and reduction on the Ru/TiO_2 extrudates.

Description	Gas	Flow Rate [NL h^{-1}]	Pressure [barg]	Temperature [°C]	Time [h]
1. Cold, low pressure test	N_2	30	5	20	1
2. Cold, high pressure test	N_2	30	45	20	1
3. Hot, high pressure test	N_2	30	45	250	1
4. Reduction	5% H_2/N_2	10 - 30	2	250	0.5
5. Reduction	5% H_2/N_2	30	2	250	30
6. Cooling down	N_2	30	2	20	10

Furthermore, successful pressure and temperature tests were done on the FT rig. As a result, it was concluded that the GC unit was successfully integrated with the magnet, rig and reactor system. All trace heating were able to heat rapidly to high temperatures and maintain within ±0.2 °C at reaction level. A stable N_2 pressure was recorded using the Equilibar® in the reactor with no detectable pressure (<0.2 barg overnight) from 50 barg. This all confirmed the reactor was ready and set up safely to operate real FTS.

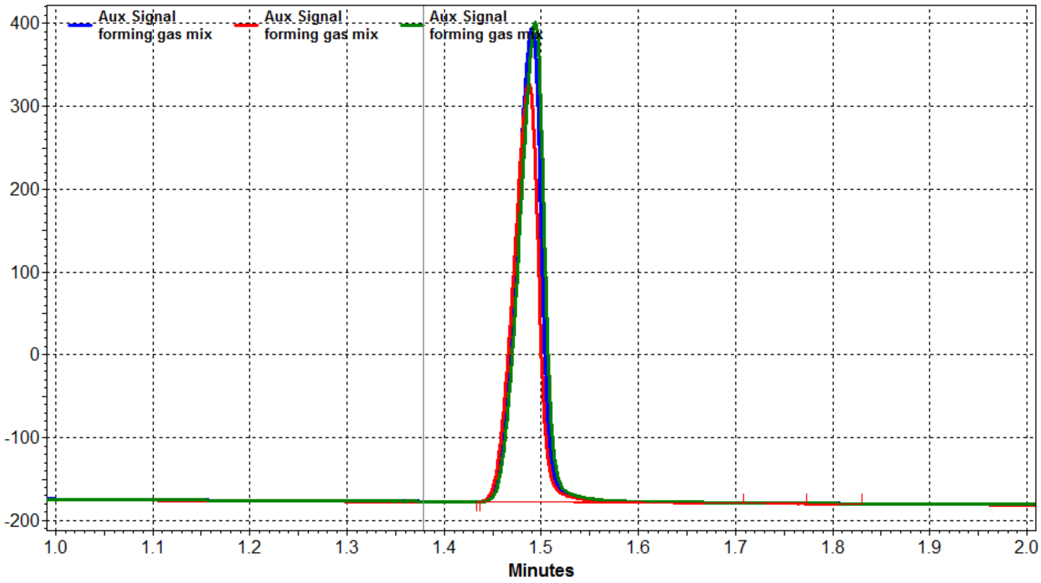

Figure 6.20 The TCD signal for H_2 *before (— / step 4), during (— / step 5) and after (— / step 6) reduction of Ru/*TiO_2 *extrudates took place. These correspond to steps 4 - 6 in Table 6.3.*

Finally, the uptake and consumption of H_2 was tracked with the GC during the reduction process, see Figure 6.20. The TCD signal for H_2 can be seen before, during and right after the reduction procedure (at 250 °C, 2 barg and 30 NL h^{-1} of forming gas) occured. The signal of H_2 during reduction decreased whereas the very comparable signals before and after the process indicate that the reduction process completed as no further H_2 was consumed.

6.7.2 Modifications to the Rig

During the commissioning and testing phase, the operators encountered some room for improvement. The two biggest modifications are described below, which enhanced pressure control and safety of the rig.

Pressure and Needle Valve Changes

In the final section of the rig, downstream of the control valve (PCV-250), a major modification was implemented to obtain better control over the pressure and minimise leak risks. PCV-250 allows the reactor pressure to be decreased from operating pressure down to 0.5 barg. Downstream of PCV-250, all lines and components encounter this 0.5 barg overpressure, which is required to create a pressure gradient enabling the products to leave the reactor into the vent. Also, the product return lines that were installed from the product collection bottles to the main product line, had 0.5 barg overpressure. These lines were placed to revert back any product gas potentially escaping to the WGFM and GC for analysis

Originally, a needle valve was installed right before the WGFM which controlled the pressure fed to the GC. Some overpressure is always required for the GC to operate normally and for the off-gas to reach the GC due to a pressure drop created over the lines. However, the product return lines connecting the collection bottles did not have a strong enough seal to withstand 0.5 barg. These glass jars were at atmospheric pressure and thus any leak would allow CO or H_2 to escape.

Figure 6.21 shows the final position of the needle valve and entrance to the GC. The modification allowed to change the position of the needle valve more upstream, thus only keeping the GC feed line under 0.5 barg pressure. Therefore the product return lines were kept at atmospheric pressure, thus reducing the leak rate and enhancing the pressure control.

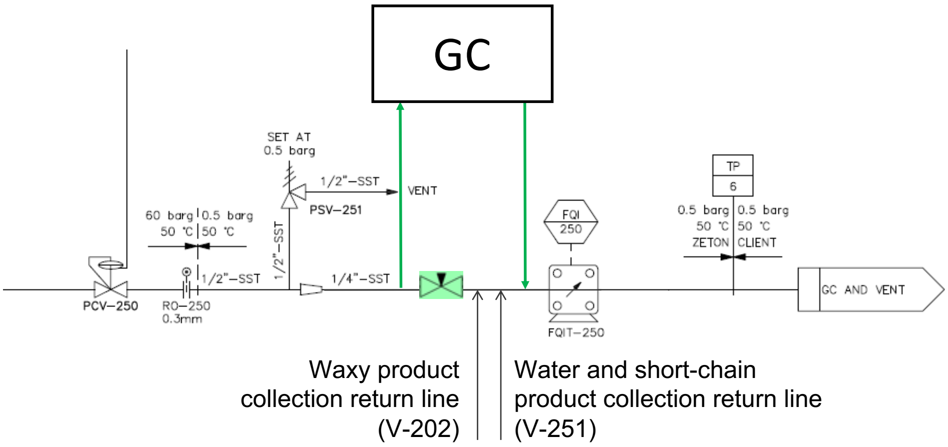

Figure 6.21 Modification implemented with the new position for the needle valve.

Restriction Orifice

A restriction orifice (RO) was placed on the H_2 and CO gas cylinders between the gas cylinder and the primary pressure reducer. The RO is installed in case of an emergency to limit the escaping gas. For example when a pipe ruptures and/or regulators fails, it reduces the maximum outlet flow rate of the gas to escape. Shell recommended the installation of the RO and their design and safety engineers assisted in calculating the actual maximum orifice diameter able to deliver the required feed flow rates and pressures. Shell also suggested that the distance between the cylinder and reducer should be as short as possible (maximum 20 cm) to minimise the gas volume that can escape. A technical drawing of the RO can be seen in Figure 6.22.

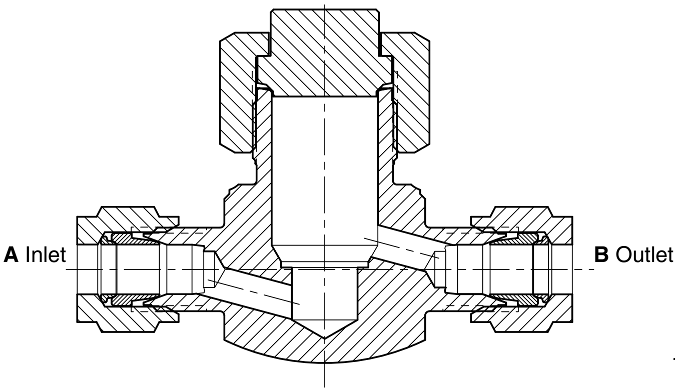

Figure 6.22 Restriction orifice from Hoke (6320 Series).

The RO holder is supplied by Hoke (serial number: 6320F4Y), is rated up to 5000 psi (±345 bar) and has a Viton® 7µ filter. The actual orifice is made of diamond and has an opening diameter of 0.03 mm for H_2 and 0.05 mm for CO. Since the installation of the orifices onto the FT rig, which had to be approved by several senior Safety Officers of the University, two other research groups in the Department of Chemical Engineering and Biotechnology have implemented the same safety precaution on their instruments to maximise gas safety.

6.8 Conclusions

This Chapter presents an overview of the customised Zeton FT reactor. This Chapter lays out the design and description of the new *in situ* NMR pilot-plant used to study FTS at elevated temperatures (up to 300 °C) and pressures (up to 50 bar). This setup provides our research group with a toolkit to perform cutting-edge measurements, which thus far have only been modelled or simply had to be approximated. The challenges of designing a pilot-plant that is compatible with NMR, therefore limiting the choice of building materials available, are discussed. Subsequently, a detailed description is giving of the FT reactor, which was designed, constructed, commissioned and tested in collaboration with STCA and Zeton B.V. Due to the high risk operation, significant attention is given to the safety features (C&E matrix, SOP and LabVIEW) making this an inherently safer pilot-plant to operate.

Furthermore, during the PhD important skills were acquired during knowledge transfers, exchanges and internships at STCA in the Netherlands, required to ensure the best operation of the FT rig. Basic catalysis engineering techniques were taught by Shell on how to modify and characterise catalysts for FTS. In addition, reactor design suggestions given by Shell are discussed in detail. A surface coverage study done by varying the H_2:CO feed ratio was performed as preliminary experiment to best prepare for real FT experiments in Cambridge. The following Chapters will present the scientific studies that could have only been done on the new reactor at the MRRC.

Chapter 7

Fischer-Tropsch - *Operando* MR Studies of Catalysis in GTL

7.1 Introduction

Within the gas conversion industry, FT plays a central role in the GTL business. Today, still many researchers debate the exact science behind FTS and therefore this process receives significant international attention [274, 275]. However, characterising the reactor-scale hydrodynamics and the pore-scale catalyst behaviour in real-life time under relevant conditions remains a very challenging experiment. This is mainly due to its harsh reaction conditions such as high pressure and temperature [276–278]. Due to several major hindrances, very few research groups have the required capabilities in-house to study this conversion. These obstacles vary from (i) the technical complexity, (ii) financial burden and (iii) the limited choice of relevant characterisation techniques.

At the MRRC, the Zeton FT reactor, described in Chapter 6, enables us to study the FTS process *in situ* with commercially relevant catalysts at 220 °C and 36 barg using NMR. This is the world's first GTL reactor positioned inside a superconducting magnet and this Chapter reports the first *operando* application of MR measurements to a FT system operating in a pilot scale trickle-bed reactor. These novel *operando* MR measurements consist of spatially-resolved product distribution evolution mapping, molecular diffusometry, relaxometry and high resolution 2D and 3D MR imaging. This information will be used to better understand the transport phenomena occurring in heterogeneous catalysis and hence optimise catalyst design and reaction operation.

The experiments described in this Chapter had a total TOS of more than 850 h. However, mostly data for the first 160 h is shown, as the most significant trends occur in that time period. Thereafter, the liquid product signal intensity plateaus indicating that steady state was reached for the reaction. Also, the results in this Chapter focus on the liquid products. The signal obtained during the measurements is dominated by the signal of the liquid products due to the low density of the gas phase products. The NMR data acquisition for the experiments discussed below was done in collaboration with Dr. Qingyuan Zheng, who also assisted during the data analysis.

7.2 Experimental

7.2.1 Reactor and Experimental Setup

This experiment was carried out in a pilot-scale fixed-bed reactor with an internal diameter (ID) of 20 mm using top-down continuous flow. This reactor has a design limit of T_{max} = 300 °C and P_{max} = 60 barg and was placed inside a SWB 300.14 MHz Bruker spectrometer, see Figure 7.1 for a reactor schematic. The reactor setup was previously discussed in Section 6.2.1.

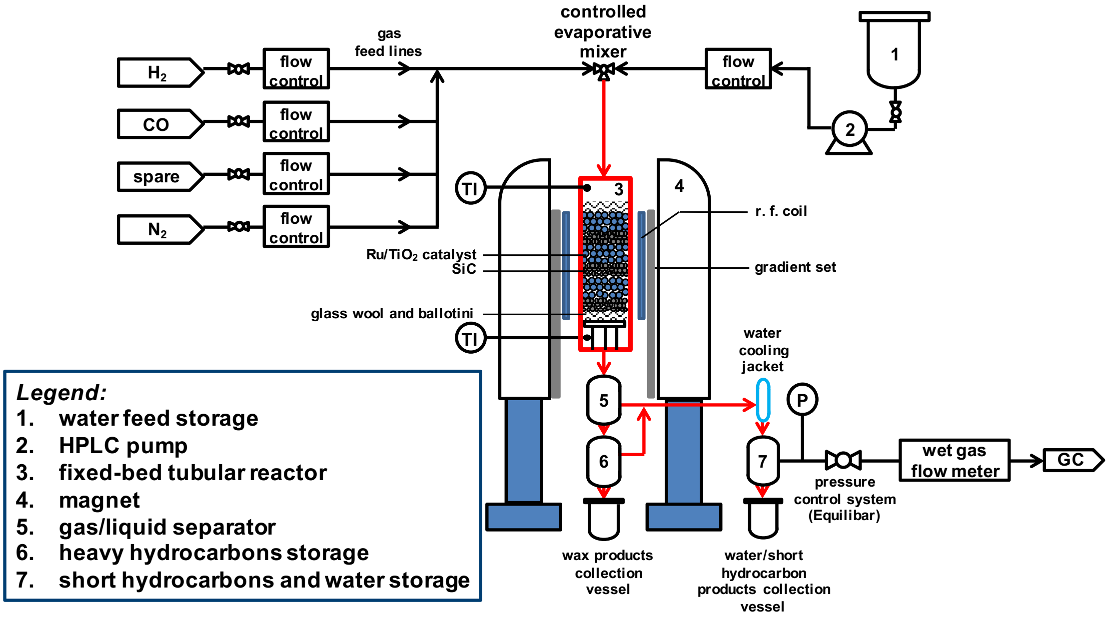

Figure 7.1 Reactor schematic of the high pressure and temperature FT pilot-scale rig. The parts of the rig equipped with trace heating are highlighted in red.

The reactor bed consisted of extrudate pellets of 1 wt% Ru/TiO_2 of 1 - 4 mm in length, supplied by the collaborators at Shell. The catalyst pellets have a BET surface area of 44.8 m^2 g^{-1} and a BJH average pore size of 28.6 nm measured by N_2 physisorption. These catalyst particles were packed in the reactor in 3 distinct layers, each of approximate 3 mm in height, see Figure 7.2. Due to the very high exothermicity of FTS, the catalyst bed was diluted and the catalyst layers were therefore all separated by inert silicon carbide (SiC) to prevent hotspot formation [279, 280]. This was done in line with reactor operation guidelines obtained from STCA.

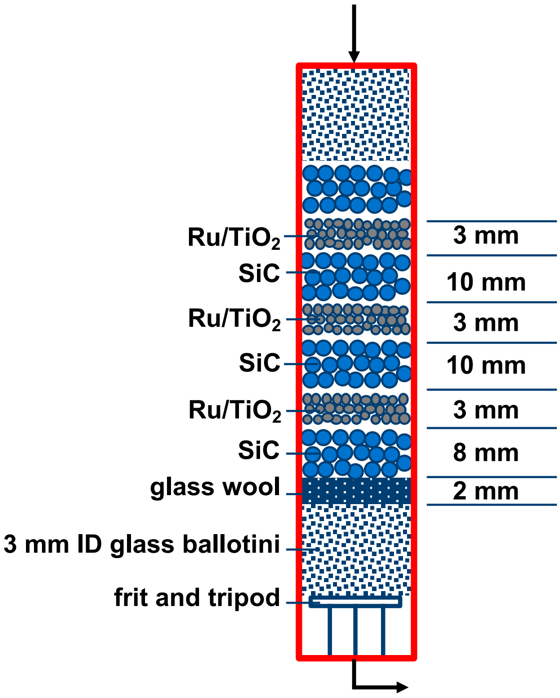

Figure 7.2 Schematic of the structure of the catalyst bed in the FT tubular reactor. It consists of 3 individual layers of Ru/TiO_2 catalyst separated by inert SiC.

The Ru/TiO_2 catalysts had previously been passivated by Shell. However, prior to every fresh FT experimental run, the catalyst bed was reduced *in situ* using H_2 at 250 °C and 2 barg for 30 h. Using both NMR and a GC, the reduction process was tracked by observing the H_2 signal intensity and concentration. Within the 30 h, the H_2 concentration plateaued, which is indicative that the reduction completed. Subsequently, the reactor temperature was dropped to 160 °C and pressurised to 36 barg under a H_2 (30 NL h^{-1}) and N_2 (9 NL h^{-1}) atmosphere. Once the desired pressure was reached, CO was introduced (3 NL h^{-1}) resulting in a molar syngas feed composition of H_2:CO:N_2 = 6:3:1.8 and a weight hourly space velocity (WHSV) of 3.6 NL h^{-1} $g_{cat}{}^{-1}$. To reach the desired FT operating temperature of 220 °C, the reactor temperature was ramped up at 1 °C min^{-1}. The moment the reactor reached 220 °C was marked at TOS = 0. The reactor off-gas (CO, CO_2, N_2, H_2, light hydrocarbons (C_1-C_5)) was analysed using an on-line GC. The measurement error of the GC was found to be of ±3% for the concentrations.

In summary, an overview of the materials, components and their properties are given in Table 7.1 and Table 7.2 below.

Table 7.1 The reaction conditions and parameters for the operando FT reaction.

Material	**Description**	**Unit**	**Value**
Catalyst	1 wt% Ru/TiO_2 in 3 layers of 3 mm height	[mm]	1 - 4
TOS	Time-on-Stream	[h]	> 800
T	Temperature	[°C]	220
P	Pressure	[barg]	36
WHSV	Weight Hourly Space velocity	[NL h^{-1} g_{cat}^{-1}]	3.6
Syngas	Molar feed composition H_2:CO:N_2	[-]	6:3:1.8

Table 7.2 List of components, materials and machines used in this FT experimental study.

Component	**Description**	**Supplier**
Ru/TiO_2	1 wt% FT catalyst	Shell Global Solutions
SiC	silicon carbide diluent	Shell Global Solutions
H_2	hydrogen 99.999%	AirLiquide
CO	carbon monoxide 99.97%	AirLiquide
N_2	nitrogen 99%	AirLiquide
glass wool	glass wool used a plug	MRRC
GC	gas chromatogram 7890B RGA	Agilent
FT reactor	FT rig	Zeton

In order to evaluate the reaction, the conversion X (%) of the reactants CO or H_2 is defined in Equation 7.1. The inlet and outlet flow rates of either CO or H_2 (mol h^{-1}) are represented by $F_{\text{reactant, in}}$ and $F_{\text{reactant, out}}$ respectively.

To quantify the product selectivities, S_{C_N} (%) represents the selectivity towards the hydrocarbon products with carbon number N (with $1 \leqslant N \leqslant 5$) and F_{C_N} (mol h^{-1}) is the respective molar flow rate, see Equation 7.2. Finally, $S_{C_{6+}}$ (%) in Equation 7.3 gives the selectivity towards C_{6+} products.

$$X_{\text{reactant}} = \frac{F_{\text{reactant, in}} - F_{\text{reactant, out}}}{F_{\text{reactant, in}}} \times 100 \tag{7.1}$$

$$S_{C_N} = \frac{N \times F_{C_N}}{F_{\text{CO, in}} - F_{\text{CO, out}}} \times 100 \tag{7.2}$$

$$S_{C_{6+}} = 100 - \sum_{N=1}^{5} S_{C_N} \tag{7.3}$$

7.2.2 NMR and MRI

A Bruker AV 300 spectrometer equipped with a SWB 7.1 T superconducting magnet was used for all of the NMR measurements. The gradient set (in x, y and z directions) has a maximum gradient strength of 0.83 T m^{-1} in each direction. The RF coil has an ID of 66 mm and it was tuned to a resonance frequency of 300.14 MHz for ^{1}H. The types of experiments and pulse programs used for this Chapter are:

1. 1-dimensional (1D) z-profile
2. z-T_1
3. z-D
4. 2D and 3D RARE imaging
5. 2D z-D diffusometry experiments

Throughout the experiments, information about (i) the liquid product built-up, (ii) mobility and (iii) transport properties of the molecules produced during FT was extracted. In any z-profile result discussed below, the top of the reactor is defined as $z = 5$ mm and following the flow direction the z values increase accordingly. The regions in the axial position between $z = 25$ - 30 mm, $z = 37$ - 42 mm and $z = 50$ - 55 mm are defined as the top, middle and bottom catalyst layers respectively. The glass wool layer extends between $z = 62$ - 68 mm.

Prior to performing the real FTS experiment, a z-profile of the catalyst bed was acquired without any ongoing reaction but at reaction temperature of 220 °C simply under inert N_2 atmosphere. This ‘background’ z-profile was subtracted from all subsequent acquisitions during processing of the reaction results. Therefore, the background signal associated with the (i) packing elements, (ii) reactor walls and (iii) insulation was removed. This processing step was applied during the analysis of the z-D and z-T_1 data. The background signal was considered to be negligible in the MR measurements (experiments 3. - 5. listed above) because of the transverse relaxation effect for the background signal in those measurements.

z-profile

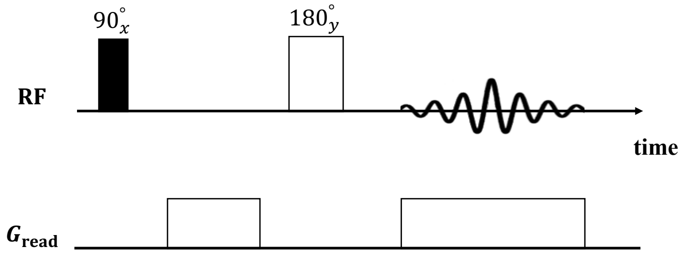

Figure 7.3 The pulse sequence used for the ^{1}H NMR z-profile experiments.

In order to track the amount of liquid species produced during operation, 1D profile images were acquired with a spin echo sequence and a frequency-encoding gradient applied along the axial direction (z-axis) of the reactor, see Figure 7.3. The z-profile has a FOV of 80 mm which results in a spatial resolution of 313 µm with the dephase and refocus gradient strength set at 11.7 G cm^{-1}. See Table 7.3 for all parameters.

Table 7.3 Pulse parameters and delays used in the z-profile NMR experiments during FTS.

Variable	**Description**	**Unit**	**Value**
AQ	Acquisition time	[s]	162
P1	90° high power pulse	[µs]	60
	Repetition time	[s]	40
NS	Number of scans	[-]	4
FOV	Field of view	[mm]	80
	Spatial resolution	[µm]	313
GPZ	Dephase and refocus gradients	[G cm^{-1}]	11.7

z-T_1

The spatially-resolved z-T_1 relaxation time experiment was carried out using a saturation recovery sequence in combination with 1D profile imaging with frequency encoding along the z-axis, see Figure 7.4. The T_1 encoding had a relaxation variable delay list ranging from 1 ms to 40 s of 16 time points. The setup for the 1D profile imaging in the z-T_1 measurement is the same as that for the z-D experiment. See Table 7.4 for all parameters.

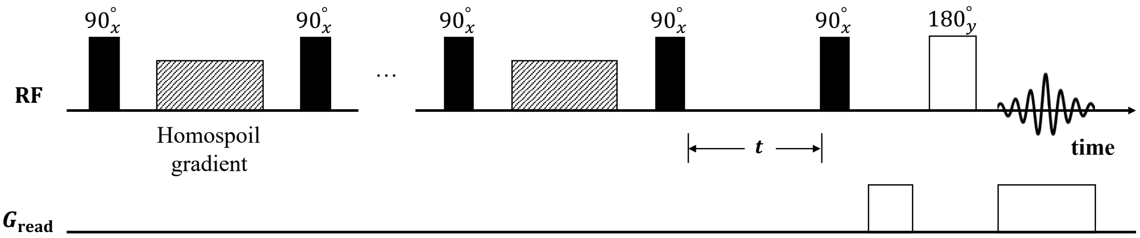

Figure 7.4 The pulse sequence used for the ^1H NMR z-T_1 experiments.

The data processing for z-T_1 data was similar to the z-D results. At each relaxation delay t, a T_1-weighted z-profile was obtained. As mentioned previously, a background T_1-weighted z-profile was acquired from the catalyst bed in the absence of any reaction under N_2 flow at the reaction temperature of 220 °C. This z-profile background data was subtracted from the T_1-weighted z-profile acquired during the data processing. The signal obtained of the 3 individual catalyst layers in these background-corrected T_1-weighted z-profiles was integrated to give the T_1 results for the 3 layers. These were fitted with a Tikhonov regularisation algorithm, see Section 5.4.4 [248], to produce T_1 distributions of all the liquid product produced during the reaction down the reactor. For this algorithm a smooth parameter of 0.1 was used.

Table 7.4 Pulse parameters and delays used in the z-T_1 NMR experiments during FTS.

Variable	Description	Unit	Value
AQ	Acquisition time	[min]	28.7
P1	90° high power pulse	[µs]	60
	Repetition time	[ms]	3000
NS	Number of scans	[-]	8
VD	Variable delay list	[-]	1 ms - 40 s
FOV	Field of view	[mm]	80
	Spatial resolution	[µm]	313
GPZ	Dephase gradients	[G cm^{-1}]	12.7
GPZ	Refocus gradients	[G cm^{-1}]	11.7

z-D

The spatially-resolved diffusion *z-D* measurements were measured with a 13-interval APGSTE pulse sequence combined with 1D profile imaging with frequency encoding along the z-axis, see Figure 7.5. The RF pulse spacing time τ was 2.1 ms, the diffusion observation time $\Delta = 20$ ms, the pulsed gradient duration $\delta = 4$ ms. The pulsed gradient strength increased linearly in 64 steps to 75 G cm^{-1} with a gradient stabilisation time of 1 ms. The 1D profile imaging in the *z-D* measurements had a FOV of 80 mm and a spatial resolution of 313 µm with the dephase and refocus gradient strength set at 12.7 and 11.7 G cm^{-1} respectively. See Table 7.5 for all parameters.

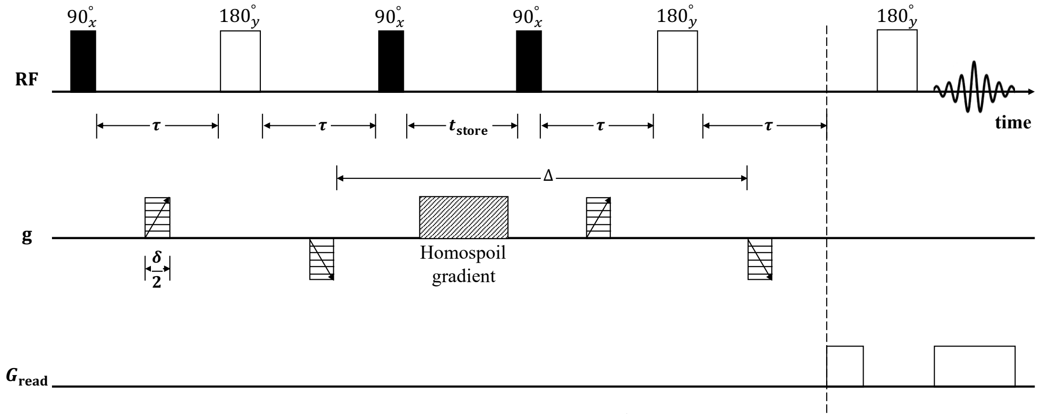

Figure 7.5 The pulse sequence used for the ^{1}H NMR z-D experiments.

During the *z-D* acquisitions, at each gradient step $\boldsymbol{g}$, a diffusion-weighted z-profile was obtained. At each $\boldsymbol{g}$ value, the signal of each of the three catalyst layers was integrated over their respective region to obtain the top, middle and bottom diffusion distribution. This diffusion data per layer was processed with a 1D Laplace inversion method which fits the data using a Tikhonov regularisation algorithm, see Section 5.4.4 [248]. The smooth parameter used in the regularisation was optimised to 1 using a L-curve method [247].

Table 7.5 Pulse parameters and delays used in the z-D NMR experiments during FTS.

Variable	Description	Unit	Value
AQ	Acquisition time	[min]	20.8
P1	90° high power pulse	[µs]	60
	Repetition time	[ms]	3000
τ	Pulse spacing time	[ms]	2.1
	Gradient pulse stabilisation time	[ms]	1
Δ	Observation time	[ms]	20
δ	Gradient pulse duration	[ms]	4
NS	Number of scans	[-]	4
	Number of gradient steps	[-]	64
	Pulsed-field gradient strength range	[G cm^{-1}]	0.1 - 75
FOV	Field of view	[mm]	80
	Spatial resolution	[µm]	313
GPZ	Dephase gradients	[G cm^{-1}]	12.7
GPZ	Refocus gradients	[G cm^{-1}]	11.7

2D and 3D MR Images

2D and 3D images were acquired using a RARE sequence, see Figure 7.6. This pulse sequence is used to provide information on the liquid product distribution in the reactor. The 3D image had a FOV of 25 mm × 25 mm × 80 mm in the x, y and z directions respectively. The spatial resolution was 195 µm × 195 µm × 313 µm in the three Cartesian coordinates. The 3D image was acquired with 8 scans, a recycle time of 8 s and a RARE factor of 16, giving a total acquisition time of the 18.2 h.

2D images were obtained to gather spatially-resolved information from within the reactor. During the measurements, a slice selected pulse of 512 µs in length was applied to image a vertical slice (3 mm slice thickness) of the reactor. The spatial resolution of the 2D vertical image is 172 µm × 625 µm with a FOV of 22 mm × 80 mm in the x and z directions respectively. The spatial resolution of the 2D transverse image is 172 µm × 172 µm with a FOV of 22 mm × 22 mm in the x and y directions respectively. The 2D images were

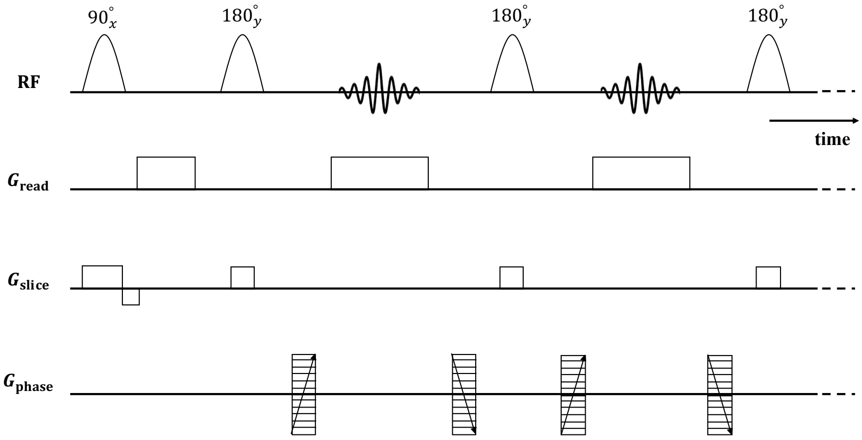

Figure 7.6 The pulse sequence used for the ^1H NMR 2D RARE experiments.

acquired with 8 scans, a recycle time of 8 s and a RARE factor of 16, resulting in a total data acquisition time of 2.8 min. See Table 7.6 for all parameters.

Table 7.6 Pulse parameters and delays used in the 2D and 3D MRI experiments during FTS.

Variable	Description	Unit	Value 2D Image	Value 3D Image
AQ	Acquisition time	[-]	2.8 min	18.2 h
P1	90° high power pulse	[µs]	60	60
	Slice selected pulse	[µs]	512	-
	Slice thickness	[mm]	3	-
	Repetition time	[ms]	8000	8000
NS	Number of scans	[-]	8	8
RARE	RARE-factor	[-]	16	16
FOV	Field of view	[mm]	22×80 (x×z) 22×22 (x×y)	25×25×80 (x×y×z)
	Resolution	[µm]	172×625 (x×z) 172×172 (x×y)	195×195×313 (x×y×z)

2D Diffusion Measurements

To study the diffusion behaviour of inter- and intra-pellet species under *operando* FTS conditions, 2D diffusion measurements were performed. Spatial resolution was obtain on the 3 individual catalyst layers in the transverse directions (x and y). The 2D diffusion measurement was set up using Paravision 6.0.1 software with a PGSTE sequence for the diffusion encoding. During the measurement, the observation time $\Delta = 20$ ms and the pulsed gradient duration δ was fixed at 4 ms. In addition, the gradient strength increased from 0.1 to 75 G cm^{-1} in 16 steps spaced equally.

For the 2D diffusion data, similar to the z-D data, a diffusion-weighted 2D image was acquired at each pulsed gradient strength $\boldsymbol{g}$. For each pixel of the 2D image, the diffusion data was processed using the 1D Laplace inversion as mentioned before with a smooth parameter of 1 to produce a diffusion distribution. The average diffusion value at each image pixel was calculated from the distributions and for the three catalyst layers, 2D diffusion maps were produced. The individual pixels associated with inter- and intra-pellet spaces were added up to obtain the diffusion data and average D distributions for both product environments separately.

During the processing of the 2D diffusion data, the first step consisted of masking the regions outside the catalyst bed by applying a binary, circular map. The centre point of the circle and the radius pixels (24.5 pixels) were set manually. All the intensity values outside the circular ring were put to 0. Subsequently, for the three different layers, gating levels were chosen to distinguish what signal was obtained from inter-pellet or intra-pellet regions. As most signal in the three layers is attributed to pixels from within catalyst pellets, all pixels with intensity above 30% of $I_{\mathrm{max.}}$ (maximum signal intensity of the image) were considered intra-pellet pixels. Thereafter, all the pixels with signal intensity between 13% and 30% of $I_{\mathrm{max.}}$ were associated with inter-pellet space. Finally, all pixels with intensity below 13% of $I_{\mathrm{max.}}$ were considered as noise level. This 2D masking methodology was applied to discriminate between the various regions and is based on previous work developed at the MRRC [281].

Table 7.7 Pulse parameters and delays used in the 2D z-D NMR experiments during FTS.

Variable	Description	Unit	Value
AQ	Acquisition time	[h]	4.6
	Slice thickness	[mm]	3
	Slice selected pulse	[µs]	512
P1	90° high power pulse	[µs]	60
	Repetition time	[ms]	8000
τ	Pulse spacing time	[ms]	2.1
	Gradient pulse stabilisation time	[ms]	1
Δ	Observation time	[ms]	20
δ	Gradient pulse duration	[ms]	4
NS	Number of scans	[-]	8
	Number of gradient steps	[-]	16
	Pulsed-field gradient strength range	[G cm^{-1}]	0.1 - 75
FOV	Field of view	[mm]	22 × 22 (x×y)
	Spatial resolution	[µm]	344 × 344 (x×y)

During the 2D imaging experiment, a pulse of 512 µs in duration was applied to select each of the 3 catalyst layers with a slice thickness of 3 mm. The 2D images have a spatial resolution of 344 µm × 344 µm in the transverse plane (x-y directions) for each of the catalyst layer with a FOV of 22 mm × 22 mm. The 2D diffusion measurement had 8 scans and a recycle time of 8 s, resulting in a total of 4.6 h for the data acquisition per catalyst layer. See Table 7.7 for all parameters.

7.3 Results and Discussion

7.3.1 Product Selectivity and Conversions

The FT reaction was operated for a total TOS of over 850 h, resulting in an overall CO conversion of approximately 21% and 25% for H_2. Furthermore, the selectivities towards the various N carbon number products are given in Figure 7.7 and Table 7.8.

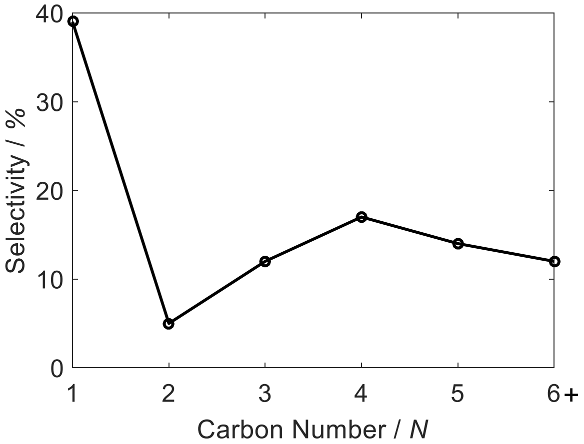

Figure 7.7 Selectivities S_{C_N} towards hydrocarbon products with carbon number N at X_{H_2} of 25%.

Parameter	Value [%]
$X_{\mathrm{H_2}}$	25
X_{CO}	21
$S_{\mathrm{C_1}}$	39
$S_{\mathrm{C_2}}$	5
$S_{\mathrm{C_3}}$	12
$S_{\mathrm{C_4}}$	17
$S_{\mathrm{C_5}}$	14
$S_{\mathrm{C_{6+}}}$	12

Table 7.8 Steady state conversion and selectivities obtained for the operando FT reaction.

During the start-up period of FTS, the catalyst pores fill up with long-chain paraffins (C_{6+}) and other liquid-phase hydrocarbon products. This filling rate is dependent on the formation of hydrocarbons and the outflow of products from the pore system. As more and more liquid, waxy products accumulate in the pores, the effective CO consumption rate tends to decrease due to the internal mass transfer limitations. This is even more pronounced at steady state, when catalyst pores are completely filled with liquid for LT-FT according to literature. It has been shown that the transport behaviour of the reactants, CO and H_2, is simply lower in the liquid phase compared to the diffusivity in the gas phase [273]. This internal mass transport limitation causes the H_2:CO ratio to increase, therefore decreasing the α towards the centre of the catalyst pellets. The very high selectivity towards CH_4 is in line with other studies, as a lower α severely favours the selectivity for CH_4 [282].

7.3.2 Liquid Production Distribution and Build-Up

The intensities in the 3 catalyst layers were integrated and plotted against TOS in Figure 7.8. This Figure shows that the signal intensities in the 3 catalyst layers first increase rapidly with TOS at the start-up of the reaction (TOS < 110 h) before reaching a plateau where the reaction is considered to reach steady state. The signal intensity after the start-up period levels off and this plateauing indicates reaching a steady state condition. The TOS < 35 h corresponds to intra-porous filling time whereas the time period 35 - 110 h corresponds to inter-porous space filling. This is consistent with the literature, where the initial period of pore filling by waxes is assumed to be in the order of a couple of days [282].

In Figure 7.8, there is a slight decrease of the signal intensities in the 3 catalyst layers over time after reaching the steady state, indicating a very minor deactivation (<10% decrease) of the catalyst. Between time period 300 - 500 h, no experiments were performed to measure the product signal intensity. Also, the pore-filling rate is the greatest at the bottom, followed by the middle and finally the top. This is in line with literature pore filling rate predictions during FTS, published by Hurt *et al.* [283]. In the literature it has regularly been described that fixed-bed reactors can have irregular voids or flow paths in which liquid-phase products formed from the FT reaction could be trapped [284]. In addition, capillary forces can prevent the trapped liquids to be flushed away by convective forces from the voids, reactor walls or the catalyst surface. As a consequence, the molecules present in those stagnant layers can react further in secondary reaction, to form even longer hydrocarbon chains and waxes.

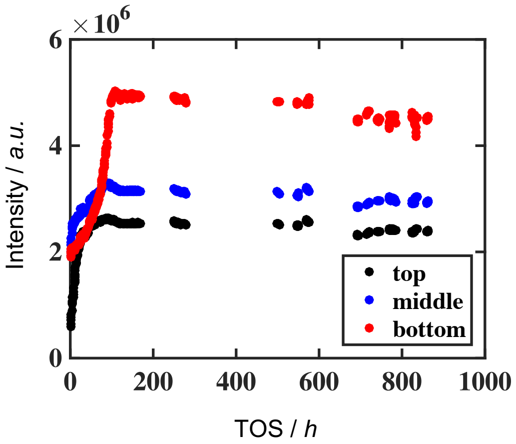

Figure 7.8 Product built-up for the three catalyst layers as a function of TOS, up to 875 h.

The 1D images and signal intensities in the three regions were integrated to give the amount of liquid product in the 3 catalyst layers at 3 different TOS, see Figure 7.9. It can be observed that the signal intensities in the 3 catalyst layers increase with longer TOS. The signal intensity is proportional to the ^{1}H spin density in the system, therefore the signal increase in Figure 7.9 indicates catalyst pore filling and accumulation of the liquid products over time.

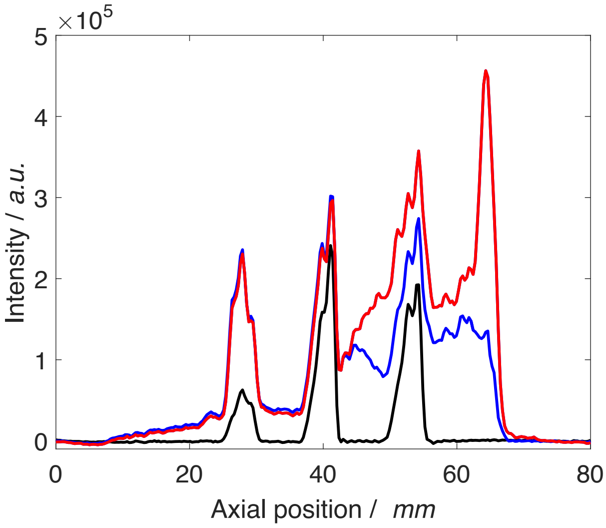

Figure 7.9 Amount of liquid products down the bed is tracked as a function of TOS with 2 h (——), 80 h (——) and 160 h (——) TOS.

In both Figures 7.9 and 7.10, one can notice the signal arising from the three catalyst layers and the glass wool. This additional layer is only detected from TOS > 100 h. In addition, due to product accumulation in the SiC particles, significant signal is detected between layers 2-3 and 3-glass wool.

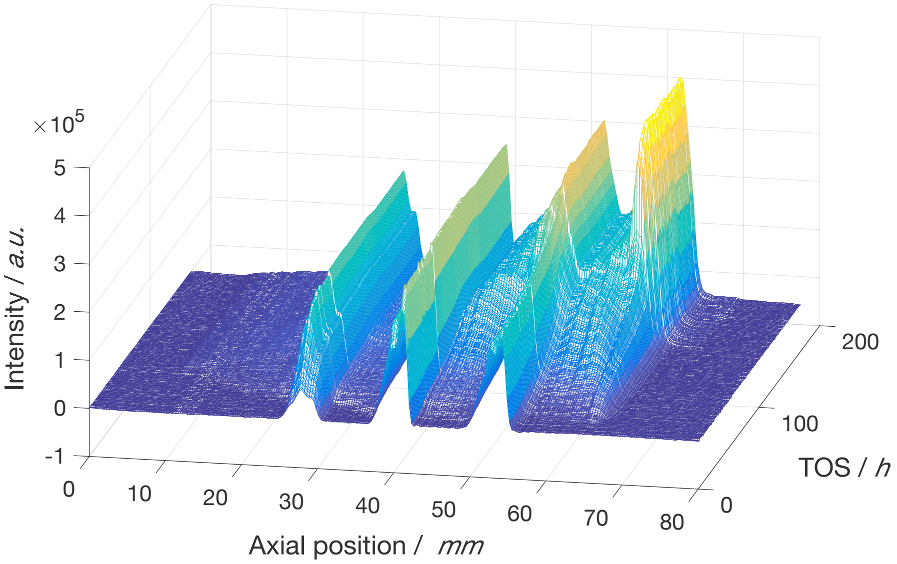

Figure 7.10 Spatially-resolved profiles down the bed and as a function of operating time. The three individual layers and the glass wool layer can be clearly identified.

Visually, Figure 7.10 is very valuable to understand the liquid product accumulation and hold-up spatially-resolved over time. Results published by Förtsch *et al.* revealed a similar condensation effect for FT products. A two-phase flow of reactants and products was observed with accumulation of liquid products through the reactor [27]. In addition, based on mathematical analyses of FTS presented by Huff *et al.*, it was suggested that liquid product oozes out of the catalyst pores before trickling down to the reactor exit [283].

2D Imaging

Figures 7.11 and 7.12 show the ^{1}H 2D images of the catalyst layers with TOS = 5 h and 160 h. The top, middle and bottom layers are shown with the signal derived from the liquid products (both intra- and inter-pellet) down the reactor. Firstly, the cylindrically shaped catalyst particles are clearly noticeable due to this high-resolution 2D image with a 172 µm × 172 µm resolution.

Secondly, most of the signal intensity is detected from within the catalyst pellets. The inter-particle regions remain mostly black after 5 h of operation. At 160 h of TOS, there is a significant proportion of the signal in the lowest layer occurring between the particles due to high volumes of accumulated product between the catalyst pellets up until the reactor wall. Moreover, in the top layer, the signal intensity increased, as more products are produced in the pellets.

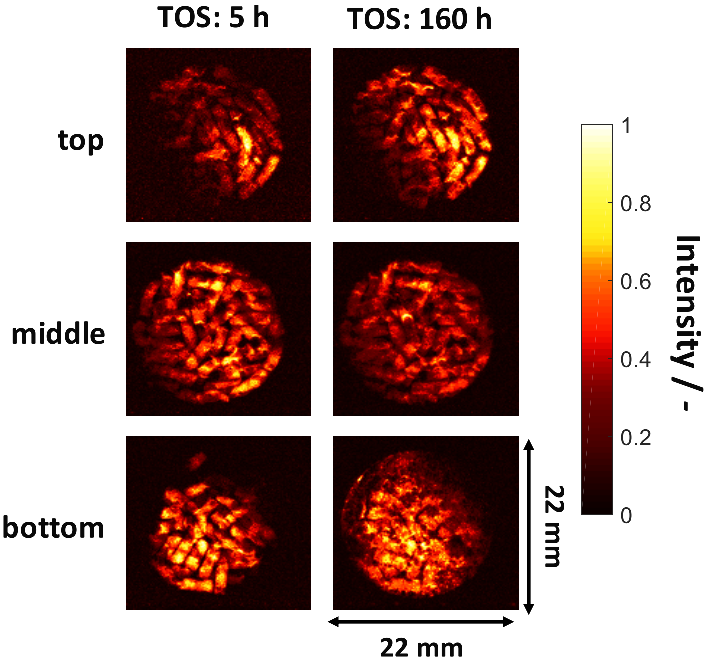

Figure 7.11 ^{1}H 2D cross-sectional imaging under operando FT conditions at TOS = 5 h and at steady state, 3 mm slice thickness with 172 µm × 172 µm resolution.

In Figure 7.12 at 160 h of TOS, the glass wool layer appears, with very strong signal intensity due to the product accumulation. Some signal from products trapped in the intermediate SiC layers can also be observed.

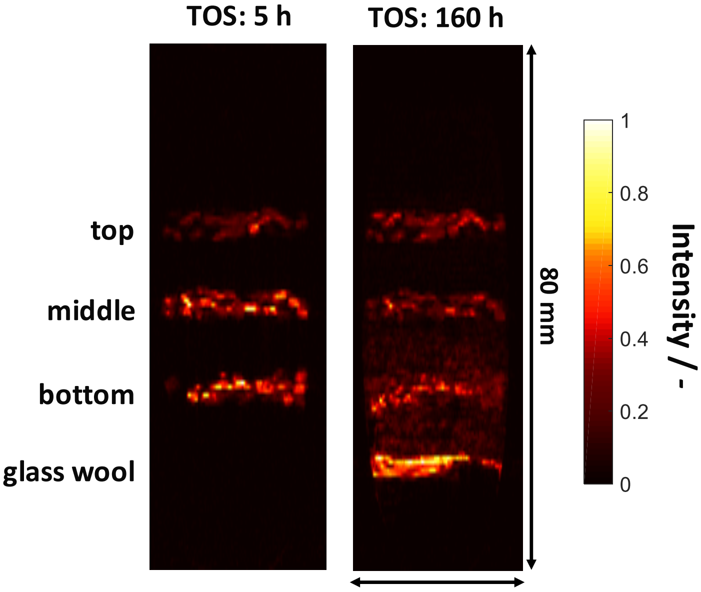

Figure 7.12 ^1H *2D longitudinal imaging under operando FT conditions at TOS = 5 h and at steady state, 3 mm slice thickness with 625* µm × *172* µm *resolution.*

3D RARE Images

Several studies were aimed at studying FT *in situ*, for example the time-resolved synchrotron µ-XRD-CT by Senecal *et al.* studying a single catalyst pellet of Co/γ-Al_2O_3 during reduction and the initial stages of FTS. This was done to gain insight into the solid-state changes [285]. Many studies are focussed at understanding the phase transformations occurring during different stages of Co-based FT [286–289]. Thus far, novel and improved *operando* investigations remain very challenging to study FTS [290, 291].

Using the 3D RARE imaging technique, the 3D image in Figure 7.13 was acquired which show the catalyst packing and the product signal clearly. Visually this is a very powerful technique to quantitatively observe where inside the reactor most of the liquid products accumulated. Starting from the top, the first two layers have the majority of the product contained inside the 3 mm catalyst layers within the intra-pore space of the catalyst pellets.

Between layers 2-3 and layers 3-glass wool, the amount of inter-pellet liquid product starts to increase significantly. Due to both the flow rate and gravity, the accumulation of inter-pellet products becomes especially noticeable at the bottom, where the glass wool layer acts like a plug hindering products to flow to the product collection vessels.

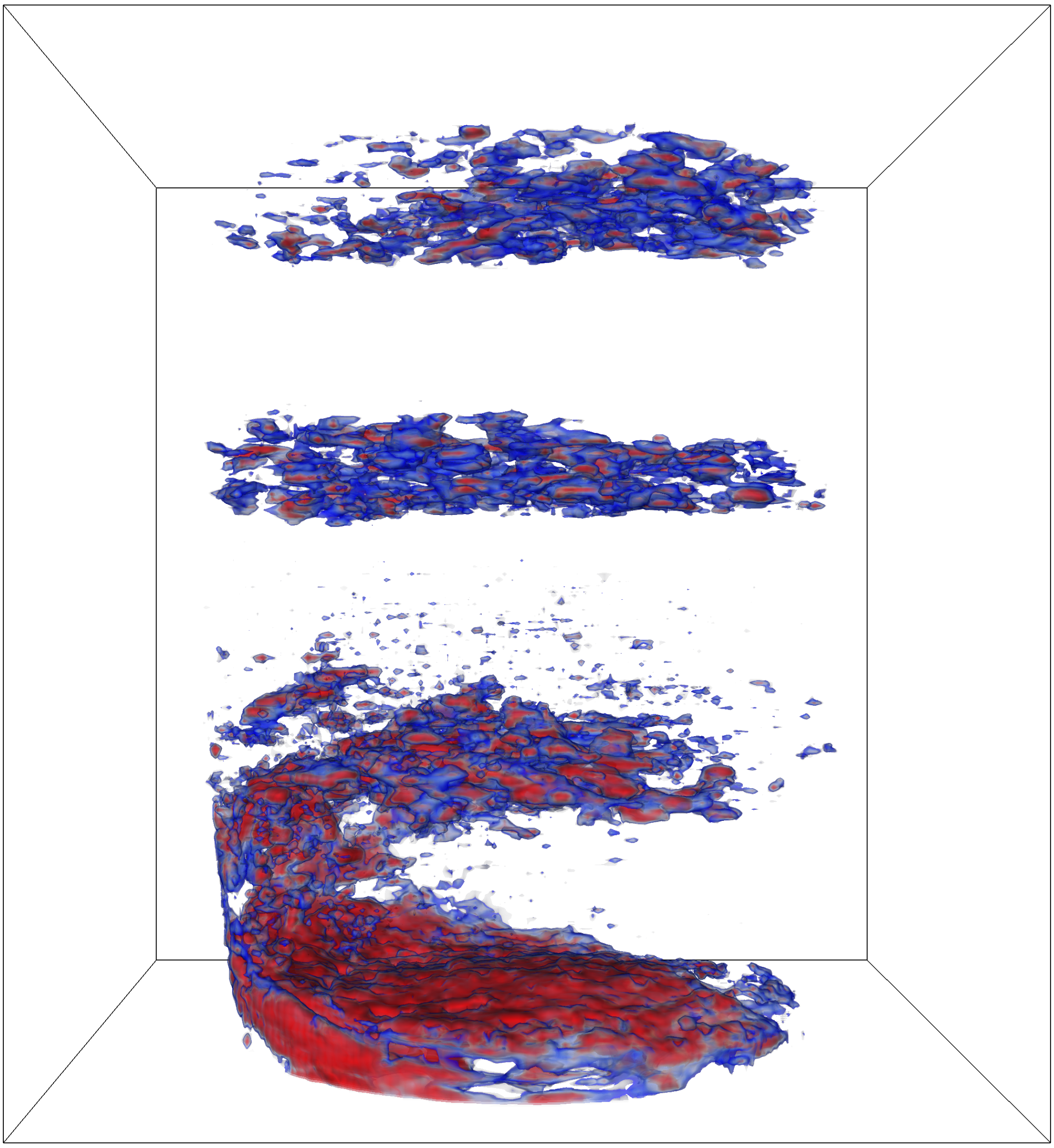

Figure 7.13 3D high resolution RARE image of the FT reactor at TOS of 250 h.

In Figure 7.14, four cross-sectional slices (x-y plane) down the reactor bed are shown, the top, middle and bottom catalyst layers with the final glass wool layer. The growth in signal intensity is associated with the accumulation of liquid product down the bed in each layer.

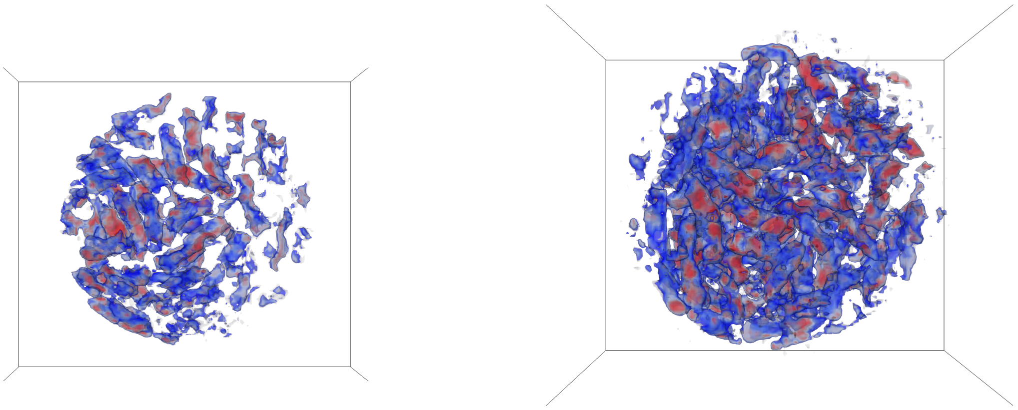

(a) Top catalyst layer *(b) Middle catalyst layer*

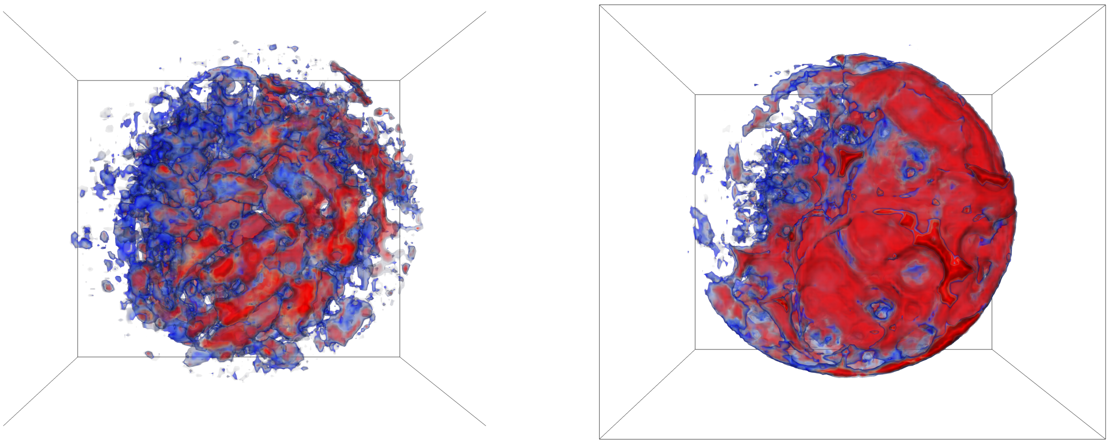

(c) Bottom catalyst layer *(d) Glass wool layer*

Figure 7.14 Cross-sectional slices down the reactor bed, indicating the signal intensity growth associated with the accumulation of liquid product.

7.3.3 Molecular Mobility with 1D Spatially-Resolved T_1 Experiments

The T_1 distributions of the relaxation times of the liquid products in the top, middle and bottom catalyst layers are obtained from the z-T_1 measurement themselves. These distributions represent both the intra- and inter-pellet products in the reactor bed. At steady state, the results were averaged for TOS = 80 - 160 h. As can be seen in Figure 7.15a, the areas of the distributions are all normalised to one. The overall T_1 value averages of the 3 catalyst layers can be calculated from the corresponding T_1 distributions, see Figure 7.15b. In this Figure, the start-up period is shown for TOS = 0 - 160 h.

The T_1 value is directly correlated with molecular mobility and it increases down the bed [292]. Between TOS = 0 - 50 h, all T_1 values increase consistently and converge to a stable relaxation value of around 5.5 s. As the NMR T_1 relaxation time is related to molecular dynamics, species that have a large T_1 indicating fast dynamics and vice versa. Until the reaction reaches steady state, the T_1 fluctuations can be attributed to reaction dynamics such as pore filling [293]. In addition, many different types of products being produced can cause the fluctuations in the T_1 evolution. This is in line with studies reported in the literature whereby the product composition in the catalyst pores varies with TOS until all pores are completely filled, i.e. steady state is reached [282].

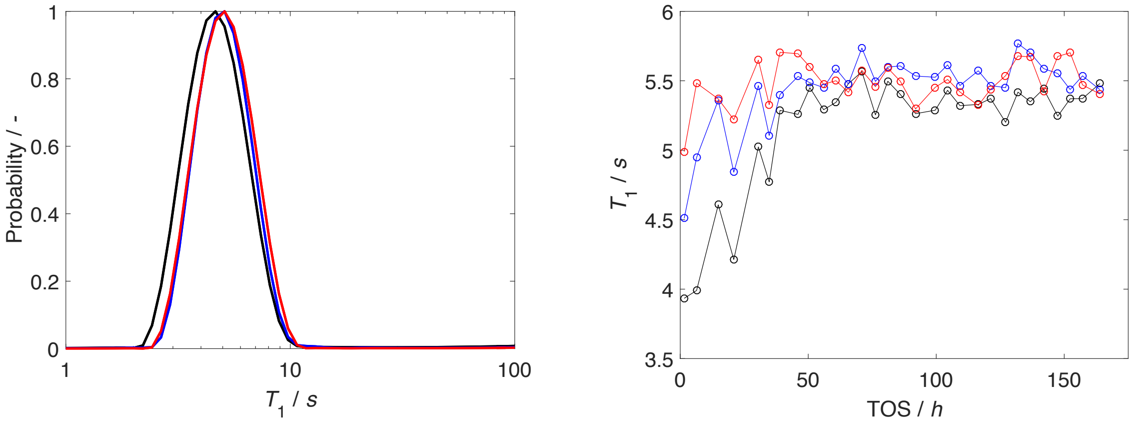

(a) T_1 distribution at steady state averaged for TOS between 80 - 160 h.

(b) T_1 increases over time during operation until it reaches a stable value of 5.5 s.

Figure 7.15 Spatially-resolved measurements of the T_1 relaxation time with the top (——), middle (——) and bottom (——) layers.

7.3.4 Molecular Diffusivity with 1D Spatially-Resolved Experiments

The distributions, seen in Figure 7.16a, represent the diffusion behaviours of the liquid products (found in both the intra- and inter-particle regions) produced in the top, middle and bottom catalyst layers. The distributions are extracted from the data obtained from the z-D measurement at steady state by averaging the results acquired at TOS = 80 - 160 h. As can be seen in Figure 7.16a, the areas of the distributions are all normalised to one. The overall D value for each of the three individual catalyst layers can be calculated from the corresponding D distributions. These values are plotted against TOS and can be seen in Figure 7.16b. Similar to the T_1 relaxation time, the D coefficient is correlated to molecular dynamics. Hence, the same type of fluctuations can be seen in Figure 7.16b as for the T_1 variation trends.

Four interesting insights can be drawn from the graphs in Figure 7.16. Firstly, throughout the whole 160 h, the D values for the top catalyst layers are consistently 20 % lower than the values extracted for the middle and bottom layer. This can occur due to the fact that more bulkier molecules are found at the top of the reactor inside the catalyst pellets and there the lighter products from the gas phase are more likely to condense to the liquid phase. In a typical LT-FT reactor, the concentration of liquid products increases with higher carbon numbers in the low carbon number range ($<C_{20}$), as the vapour pressure rapidly decreases with increasing carbon number [294]. This is in line with previous reported studies that molecules in liquid-filled pores have limited mobility and the heavier the hydrocarbon, the more severe the internal diffusion limitation is [295].

Secondly, only the top layer has a very significant drop for the first 25 h of operation, until the diffusivity value settles at 5.5 × 10^{-10} m^2 s^{-1}. This is believed to be caused by accumulation of liquid species inside the catalyst particles of the top layer. The liquid products partially fill the catalyst pores and due to tortuosity, the diffusion is restricted and thus limited. This is only relevant for the top layer, as for the middle and bottom layer, the D values are obtained from signal from both the liquid species inside and in the inter-particle space. Moving down the bed, there is a bigger contribution of inter-particle signal. In the lower section, the molecules can diffuse more freely as they experience much less restriction from the pore space. This leads to the higher D for the middle and bottom compared to the top layer.

Thirdly, overall the diffusivity behaviours increase slightly down the bed, which is similar to the T_1 trends reported above. Over time, more and more liquid is accumulated outside the catalyst pellets, leading to a slight increase in D as well. Ultimately, in Figure 7.16b, the fluctuation of D over time is associated with the pore filling, in line with the previously reported T_1 behaviour.

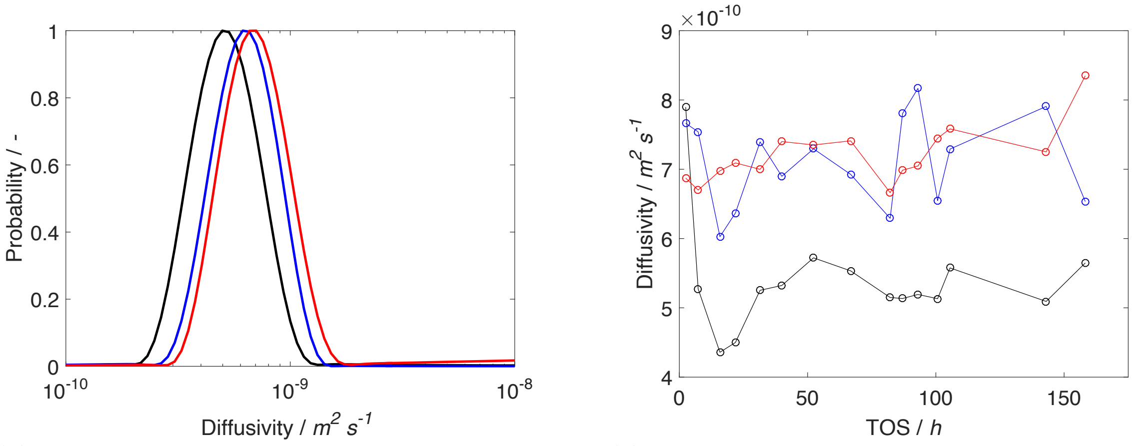

(a) Average diffusivity distribution for products formed inside the reactor bed at steady state, with the bottom layer having lower average D.

(b) Average D values. During start-up, there is a slight decrease of D in the first 20 h of operation. Subsequently, the diffusion plateaus.

Figure 7.16 1D spatial-resolved D down the catalyst bed with the top (—), middle (—) and bottom (—) layers.

In Figure 7.17a, a 1D vertical projection of a diffusivity measurement is shown for a TOS of 80 h. The signal very clearly shows the three individual layers and its evenly distributed signal intensities over the three regions. In this Figure, the accumulation of products between the final layer and the glass wool starts to become apparent. The diffusion decays stacked together in Figure 7.17b show that at steady state (TOS $>$ 160 h), there are quasi 4 layers, with noteworthy amount of product collected in between the layers in the bottom region of the reactor.

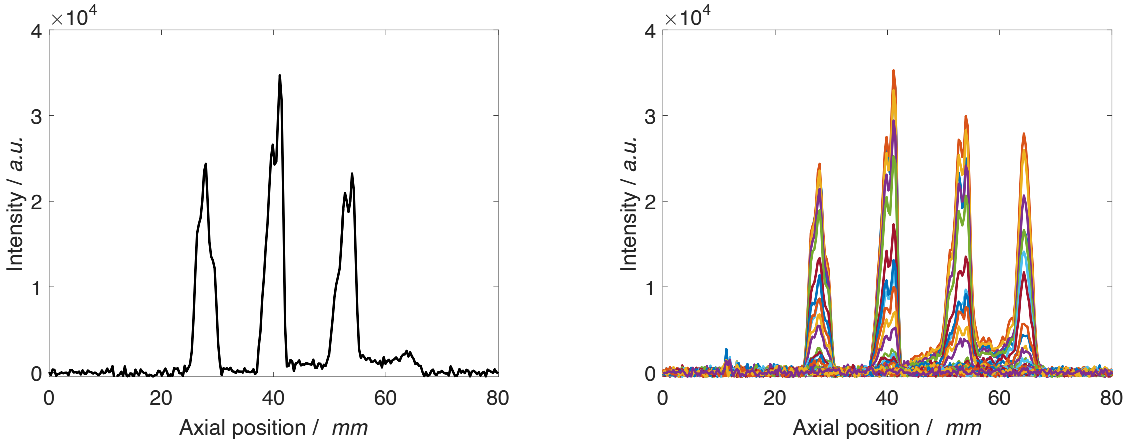

(a) 1D vertical projection of diffusion measurement at 80 h TOS.

(b) Diffusion decay for the whole catalyst bed at steady state at 160 h TOS.

Figure 7.17 Diffusion measurements spatially resolved down the catalyst bed.

7.3.5 2D Spatially-Resolved Diffusion Images

In order to get greater understanding of the exact diffusion behaviour within the catalyst bed, 2D images were used to extract 2D spatially-resolved diffusivity, see Figure 7.18. This method significantly increases the precision and resolution with which the transport behaviour of the reactor under *operando* conditions can be characterised. Figure 7.18 shows such a 2D D image for the middle catalyst layer with TOS of 880 h. With each step of increasing $\gamma^2 g^2 \delta^2$, the attenuation is observed in Figure 7.18 for each 2D D image.

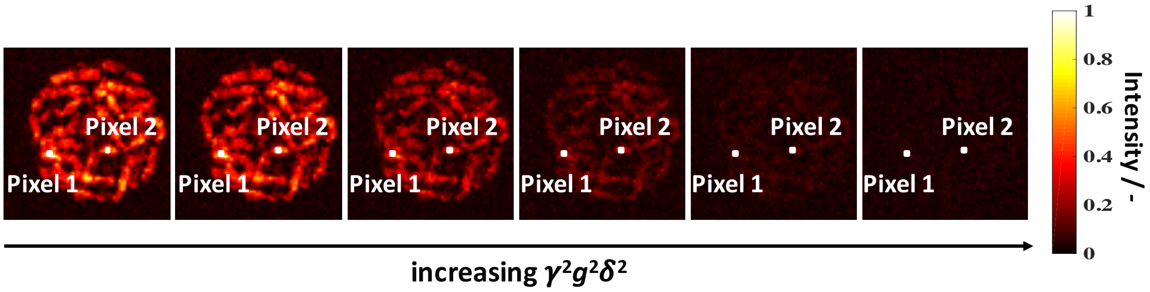

Figure 7.18 2D images used to extract 2D spatially-resolved diffusivity of products located in the middle catalyst layer, with TOS of 880 h.

As can be observed from Figure 7.18, most of the signal from the liquid products exists inside the intra-porous regions as they accumulate in that pore space. Therefore, an intensity contrast occurs between the inter- and intra-pellet liquid signal, with the strongest signal intensity arising from intra-pellet species. Using the intensity contrast between the two environments, a binary 2D image can be extracted of either intra-pellet or inter-pellet pixels. Using this technique, 2D diffusion measurements give an overall D distribution and a specific D value at each pixel. In Figure 7.18, from Pixels 1 and 2, the diffusion distributions were obtained, normalised and plotted in Figure 7.19. This can be done for all the various pixels for both intra- and inter-pellet image pixels.

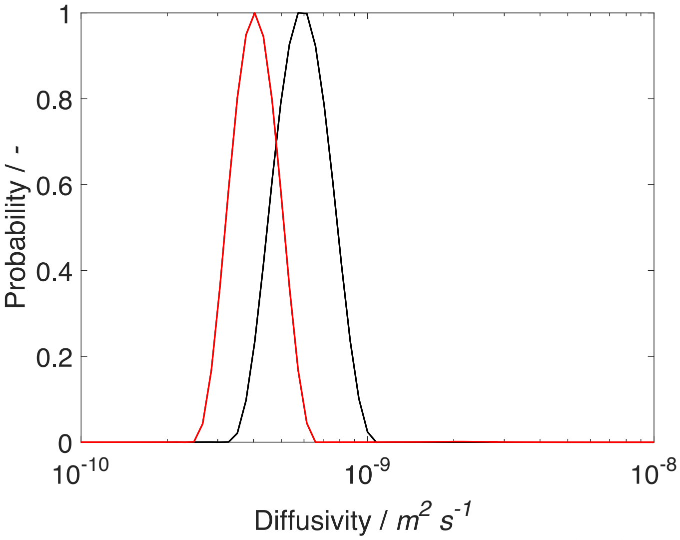

Figure 7.19 Diffusivity distribution for the overall products in Pixel 1 (—) and Pixel 2 (—) shown in Figure 7.18.

Figure 7.20 gives an overview of all the 2D D capabilities. The same 2D intensity images used to obtain the diffusivity spatially-resolved for both the intra- and inter-pellet products for each layer are shown in Figure 7.20a. These images are subsequently used to extract spatially-resolved binary images of either intra-pellet or inter-pellet pixels, see Figures 7.20b and 7.20c respectively. These two binary images are used to discriminate which pixels and its associated signal are inside the catalyst pellets or outside. Finally, Figures 7.20d and 7.20e are obtained by combining the first three Figures to obtain spatially-resolved maps of diffusivity D for intra-and inter-pellet products separately, see the colour bar for indication of the diffusion coefficients.

Observing the overall colour scale of the inter-pellet products D maps (Figure 7.20e), one notices that generally the diffusion coefficients are higher than in the intra-pellet D map (Figure 7.20d). Within the catalyst mesopores (intra-pellet environment), the longer chain products are formed and these heavy liquid products could remain trapped which results in lower diffusion coefficients. However, in the voids between the catalyst pellets (inter-pellet region), the products diffuse faster as they are less restricted and encounter negligible tortuosity. Tortuosity plays a role in slowing down the molecules. Therefore, for the three catalyst layers, the D values for the inter-pellet liquid are generally higher than those for the intra-pellet liquid. In addition, from the D maps it can be concluded that the D values vary significantly within the different catalyst pellets. This variation is even more pronounced across the catalyst layers which could reflect reaction heterogeneity across the bed. Differences in the pore geometry, the pore network or even metal dispersion could lead to this diffusion heterogeneity.

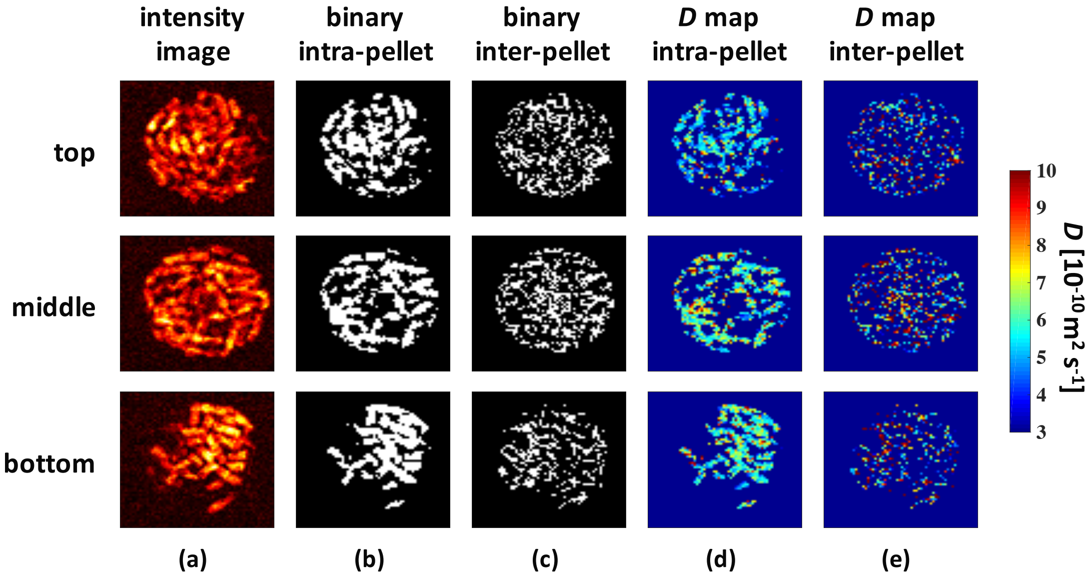

Figure 7.20 2D maps of diffusivity spatially-resolved for both the intra- and inter-pellet products derived from the 2D intensity images. (a) signal intensity maps, (b) intra-pellet pixels, (c) inter-pellet pixels, (d) diffusivity map of intra-pellet products and (e) diffusivity map of inter-pellet product.

The average D distributions for intra- and inter-pellet liquid products were obtained from the overall diffusion data acquired from the 2D image pixels associated with the two environments. The 2D masking method described in the Experimental Section above was applied to obtain the 2D diffusion maps of the inter- and intra-pellet product. The diffusion data for the pixels associated with the inter- and intra-pellet regions were summed up and this allowed to obtain diffusion data corresponding to each individual region per layer. This data was processed resulting in average diffusion distributions for the inter- and intra-pellet liquid. The results for the top, middle and bottom catalyst layers are presented in Figure 7.21. It can be concluded that the D distributions extend over one order of magnitude for both intra- and inter-pellet liquid products. Moreover, the inter-pellet products have larger population of species with $D > 10^{-9}$ m^2 s^{-1} compared to intra-pellet products. Finally, in the top layer, the inter- and intra-pellet product distributions are closely aligned compared to the bottom layer. Moving down the bed, the discrepancy between the inter- and intra-pellet product distributions increases.

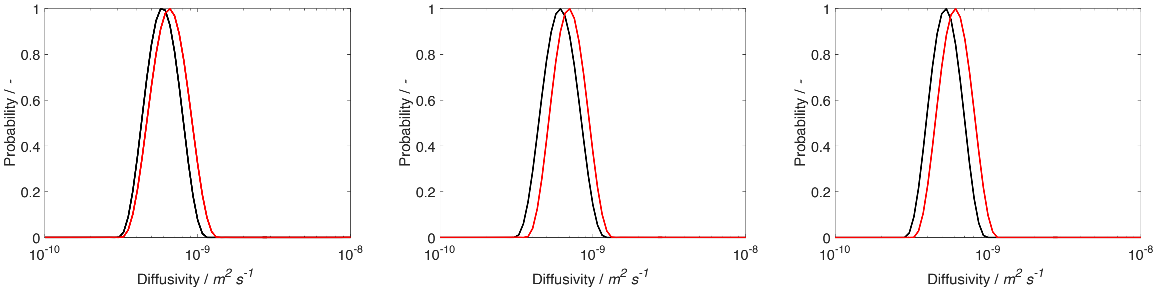

(a) Top catalyst layer. *(b) Middle catalyst layer* *(c) Bottom catalyst layer.*

Figure 7.21 Diffusivity distribution of all intra-pellet (——) and inter-pellet (——) products in the three catalyst layers.

7.4 Conclusions

The experiments described in this Chapter report the first ever *in situ* study of the FT process under real operating conditions with a TOS > 850 h. This resulted in spatially-resolved MRI measurements of the diffusion coefficients and product distributions within a fixed-bed pilot-scale reactor and single catalyst pellets.

These methods can be used to validate numerical reactor model simulations and further optimise new catalyst development. For our collaborators at STCA, they can finally verify their model inputs and link these with real, analytical measurements.

Firstly, spatially-resolved measurements of molecular diffusion and NMR spectroscopy can be made with a ~500 µm resolution from within Ru/TiO_2 catalyst pellets at realistic reaction operating conditions.

Secondly, PFG NMR diffusion data were acquired for each pixel of the 2D images of the three catalyst layers. The pixels in the images corresponding to the intra- and inter-pellet space of the catalyst bed can be observed. This 2D diffusion measurement is used to extract a D distribution and a D value at each pixel for the intra- and inter-pellet species. Using this information, spatially-resolved maps of diffusivity D were obtained for intra- and inter-pellet products separately. The results quantitatively reveal reaction and diffusion heterogeneity at both the pore- and reactor-scales.

Thirdly, moving down the bed, the signal intensities at the three catalyst layers increase with increasing TOS. It is observed that the liquid products mainly exist inside the catalyst pellets at the top and middle catalyst layers whereas significant accumulation of the inter-pellet liquid products is observed at the bottom catalyst layer. This is in line with earlier results reported by Hurt *et al.* [283]. There, the molecules can diffuse more freely as they experience less restriction from the pore space. This leads to the higher D for the middle and bottom compared to the top layer. Overall the diffusivity behaviours increase slightly down the bed, which is similar to the T_1 trends.

Finally, in the *operando* imaging of the FT reaction occurring with a TOS > 850 h, the cylindrically shaped catalyst particles are clearly noticeable due to the high-resolution 2D images with a 172 µm × 172 µm resolution. Also, high-resolution 3D RARE images were acquired from the reactor bed. The spatial resolutions obtained are in excellent agreement with spatial resolutions of conventional MRI discussed by Lysova *et al.* [154].

Chapter 8

Fischer-Tropsch: ***In Situ*** MR Studies of Emulsions post-FT

8.1 Introduction and Background

This final Results Chapter presents the preliminary study of feeding water at increasing water vapour pressures (P_{H_2}) post-FTS leading to emulsion formation in the porous catalysts. This Chapter is a continuation of previous two sets of Chapters:

- Chapters 4 and 5:
  Detection of spontaneous emulsion formation in θ-Al_2O_3, Q-silica beads and Ru/TiO_2 in a binary system of water and dodecane, with quantitative results on the droplet size.
- Chapters 6 and 7:
  Using the Zeton B.V. rig to study *operando* FTS at 220 °C and 36 barg.

This Chapter is a further investigation of the initial Chapter 4 with the same scientific objective of identifying oil-in-water liquid pocket formation in porous media but under a representative reaction environment. The scope of this work is to combine all the capabilities and in-house developed techniques to use spatially-resolved PFG diffusometry and T_1 relaxometry NMR experiments to study phase behaviour *in situ* at elevated pressure and temperature on real FTS catalyst and products post-synthesis. Post-FTS is defined as a system under the same reaction conditions as during FT, with the exception of feeding syngas. The aim is to elucidate how the condensation of water affects transport phenomena during FT.

The diffusion coefficients of CO and H_2 are approximately three times faster in water than in a typical FT hydrocarbon liquid product layer [13]. Iglesia *et al.* already hypothesised in

1996 that due to capillary effects, a separate water phase should condense inside the pores of the catalyst [13]. It was even suggested that the formation of wax-in-water emulsions could occur, stabilised by minor oxygenate by-products, at concentrations well below the saturation vapour pressure of water under FTS reaction conditions. The nanoporous catalyst support does not require high water concentrations to form a water-rich liquid phase, which makes intra-pellet regions better accessible to reactants. For supports with a greater pore size distribution, the emulsions would only form at high water partial pressures, as the bigger pores experience weaker capillary condensation effects. Furthermore, according to Iglesia's preliminary simulations, the presence of this separate water phase layer inside the intra-pellet voids increases the FT reaction rates and the selectivities towards both C_{5+} and olefins [12, 13]. See Section 2.7 for the discussion on the water effect and its phase behaviour and Section 5.2 for the discussion regarding emulsion formation related to FT.

8.2 Experimental

8.2.1 Reactor and Experimental Setup

During this preliminary investigation, the setup and experimental procedures are very similar to the z-T_1 and z-D acquisitions described in Section 7.2. The FT study was carried out on the same pilot-scale fixed-bed reactor which was placed inside a SWB 300.14 MHz Bruker spectrometer. In addition, water was fed using the HPLC liquid feed pump, and vaporised by the CEM at either 180 or 220 °C to operate at the same temperature conditions as the previous FT experiments. As this work was performed post-FT, no CO or H_2 were fed but only water and N_2 were mixed to pressurise the rig.

Table 8.1 The conditions and parameters for the emulsion detection post-FTS work.

Material	Description	Unit	Value
Catalyst	1 wt% Ru/TiO_2 in 3 layers of 3 mm height	[mm]	1 - 4
T	Temperature	[°C]	180 or 220 ±3
P_{reactor}	Pressure	[barg]	3.7 - 39.7 ±0.3
$P_{\mathrm{H_2O}}$	Partial vapour pressures of water (P/P_0)	[-]	0.3 - 0.95 ±0.04
$F_{\mathrm{H_2O}}$	Feed flow rate of water	[g h^{-1}]	10
$F_{\mathrm{N_2}}$	Feed flow rate of nitrogen	[NL h^{-1}]	10

The partial pressures of water $P_{\mathrm{H_2O}}$ were set at: 0.3, 0.5, 0.8, 0.9 and 0.95 ±0.04. These are P/P_0 points, where P_0 refers to the actual saturation vapour pressure of water. The P_0 for water at 180 and 220 °C is 10.03 and 23.20 barg respectively [296]. In order to achieve these partial pressure set-points, three input parameters were set: (i) the ambient N_2 feed flow rate at 10 NL h^{-1}, (ii) the ambient liquid flow rate of water of 10 g h^{-1} and (iii) the reactor temperature. This allowed to calculate the $P_{\mathrm{H_2O}}$ and $P_{\mathrm{N_2}}$ which add up to P_{reactor}. In summary, an overview of the conditions, materials, components and their properties is given in Tables 8.1 and Table 8.2.

Table 8.2 List of components, materials and machines used in this post-FT experimental study.

Component	**Description**	**Supplier**
Ru/TiO_2	1 wt% FT catalyst	Shell Global Solutions
SiC	silicon carbide diluent	Shell Global Solutions
N_2	nitrogen 99%	AirLiquide
H_2O	deionised water	MRRC
glass wool	glass wool used a plug	MRRC
FT reactor	FT rig	Zeton

8.2.2 NMR and MRI

z-T_1

Table 8.3 Pulse parameters and delays used in the z-T_1 NMR experiments during the water feeding study.

Variable	**Description**	**Unit**	**Value**
AQ	Acquisition time	[min]	23.1
P1	90° high power pulse	[µs]	75
	Repetition time	[ms]	3000
NS	Number of scans	[-]	8
VD	Variable delay list	[-]	1 ms - 30 s
	Number of gradient steps	[-]	16
FOV	Field of view	[mm]	80
	Spatial resolution	[µm]	313
GPZ	Dephase gradients	[G cm^{-1}]	12.7
GPZ	Refocus gradients	[G cm^{-1}]	11.7

The spatially-resolved z-T_1 relaxation time experiment was carried out using a saturation recovery sequence in combination with 1D profile imaging with frequency encoding along the z-axis. The T_1 encoding had a relaxation variable delay list ranging from 1 ms to 30 s of 16 time points. The setup for the 1D profile imaging in the z-T_1 measurement is the same as that for the z-D experiment. See Table 8.3 for all parameters.

The data processing for z-T_1 data was similar to the z-D results. At each relaxation delay t, a T_1-weighted z-profile was obtained. The signal obtained of the 3 individual catalyst layers in the T_1-weighted z-profiles was integrated to give the T_1 results for the 3 layers. These were fitted with a Tikhonov regularisation algorithm, see Section 5.4.4 [248], to produce T_1 distributions of all the condensed water and FT liquid products down the reactor. For this algorithm a smooth parameter of 1 was used.

z-D

The spatially-resolved diffusion z-D measurements were measured with a 13-interval APGSTE pulse sequence combined with 1D profile imaging with frequency encoding along the z-axis. The diffusion observation time Δ was varied between 20 - 500 ms, the pulsed gradient duration δ was varied between 1 - 4 ms. The pulsed gradient strength increased linearly in 32 steps to 75 G cm^{-1} with a gradient stabilisation time of 1 ms. The 1D profile imaging in the z-D measurements had a FOV of 80 mm and a spatial resolution of 313 µm with the dephase and refocus gradient strength set at 12.7 and 11.7 G cm^{-1} respectively. See Table 8.4 for all parameters.

Table 8.4 Pulse parameters and delays used in the z-D NMR experiments during the water feeding study.

Variable	**Description**	**Unit**	**Value**
AQ	Acquisition time	[min]	22.8
P1	90° high power pulse	[µs]	75
	Repetition time	[ms]	3000
τ	Pulse spacing time	[ms]	2.4
	Gradient pulse stabilisation time	[ms]	1
Δ	Observation time	[ms]	20 - 500
δ	Gradient pulse duration	[ms]	1 - 4
NS	Number of scans	[-]	8
	Number of gradient steps	[-]	32
	Pulsed-field gradient strength range	[G cm^{-1}]	0.1 - 75
FOV	Field of view	[mm]	80
	Spatial resolution	[µm]	313
GPZ	Dephase gradients	[G cm^{-1}]	12.7
GPZ	Refocus gradients	[G cm^{-1}]	11.7

Similar to the z-D acquisitions discussed in Chapter 7, at each gradient step $\boldsymbol{g}$, a diffusion-weighted z-profile was obtained. At each $\boldsymbol{g}$ value, the signal of each of the catalyst layers was integrated over their respective region to obtain the top, middle and bottom diffusion distribution. This diffusion data per layer was processed with a 1D Laplace inversion method which fits the data using a Tikhonov regularisation algorithm, see Section 5.4.4 [248]. The smooth parameter used in the regularisation was optimised to 5 [247].

8.3 Results and Discussion

8.3.1 Data Analysis

The diffusion results post-FTS for water and wax produced in Ru/TiO_2 catalyst pellets are mostly discussed in this Chapter using diffusion distributions. Only three sets of ST signal attenuation plots are shown: (i) to illustrate the fit to the regularisation algorithm and (ii) signal attenuation for freely diffusion wax at 220 °C for increasing observation time Δ. However, diffusion distributions or ST decays are two closely related methods of presenting the data since the signal is acquired using the same pulse sequence and therefore can be analysed in the same manner. In Chapter 4, excellent spectral resolution was obtained for dodecane and water. In this Chapter, the SNR of water is too low to distinguish its signal independently. Therefore diffusion distributions are used instead in this Chapter to analyse the diffusion behaviours. Furthermore, the diffusion decays are not utilised to extract DSD of emulsions, but the diffusion distributions are rather used to understand how the mass transport properties are effected by feeding water at increasing partial pressures post-FTS. The scientific objective was to employ the methodology developed thus far to detect spontaneous emulsion formation in porous media but under *operando* FT conditions without syngas flow. This Section will first cover the results obtained at 180 °C and subsequently discuss those obtained at 220 °C.

This study was not a model system with pure liquids, but was done at high pressure and temperature under N_2 and water flow conditions. At higher water partial pressures, bulk condensation could be observed in the top catalyst layer, which affected the pressure and temperature control. As a result, a pressure gradient established across the reactor bed. The pressure in the middle catalyst layer showed the most consistent pressure control, hence the pressure remained closest to the target partial pressure. All diffusion distributions were spatially acquired for the top, middle and bottom catalyst layers, however, only diffusion distributions for the middle catalyst layers are shown for clarity.

In Figure 8.1, the signal decays for water (Figure 8.1a) and wax (Figure 8.1b with increasing Δ) and their fits to the regularisation algorithms are shown. Only one set of signal decays and fits are shown as these are consistent and repeatable. The b-value for the wax experiment is two orders of magnitude larger than the water experiment, as both the Δ and δ are significantly higher during the experiments. No background data was subtracted from the data obtained at $\Delta = 20$ (—) ms and $\delta = 1$ ms to maximise the water signal in Figure 8.1a. In Figure 8.1b, a background profile was subtracted from the wax signal. This background profile was obtained by averaging the final 5 points in the 1D profile which correspond to the bottom part of the reactor containing inert SiC particles.

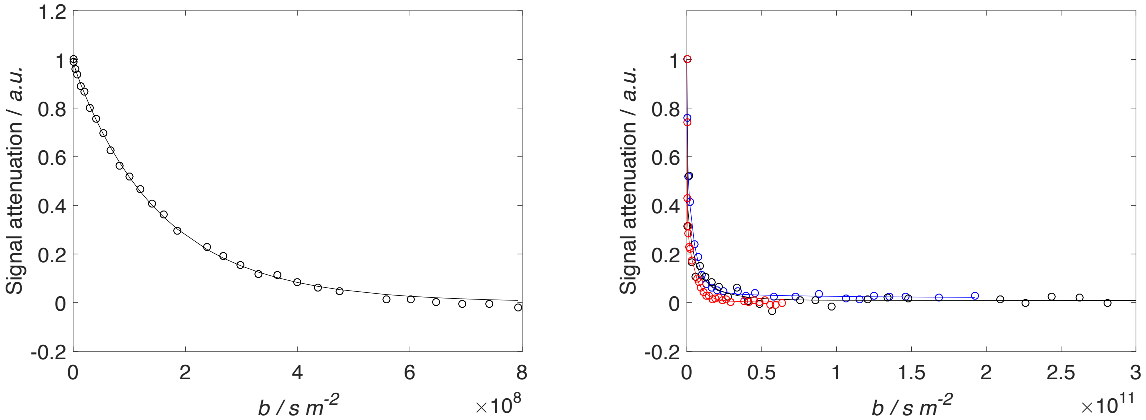

(a) Water signal decay and fit acquired at Δ *= 20 (—) ms and* δ *= 1 ms.*

(b) Wax signal decay and fit at Δ *= 100 (—), 300 (—) and 500 (—) ms and* δ *= 4 ms.*

Figure 8.1 Signal decay for (a) water and (b) wax in Ru/TiO$_2$ *catalyst pellets post-FTS, acquired at 180 °C and* $P/P_0 = 0.95$ *in the middle catalyst layer.*

8.3.2 Emulsion Detection at 180 °C

Figure 8.2 helps to understand what happens when the water partial pressure increases from 0.3 to 0.8 at 180 °C inside the Ru/TiO$_2$ catalyst pellets. Firstly, no water signal was observed as: (i) there was no spectral resolution allowing to distinguish the water and wax NMR peak during the diffusion experiments at low partial pressure. Most of the signal was governed by the wax species. And (ii), as the SNR was too low, not sufficient water signal attenuation was detected to extract a diffusion distribution. For increasing P/P_0, slight peak broadening can be observed for all layers across the catalyst bed. A single component wax diffusion distribution with a maximum apparent diffusion coefficient of 1.7×10^{-10} m^2 s^{-1} at $P/P_0 = 0.3$ was measured. The wax diffusion slightly increased to 2.2×10^{-10} m^2 s^{-1} at $P/P_0 = 0.8$. According to Wilke-Chang's theoretical prediction of bulk *n*-octacosane ($C_{28}H_{58}$), the bulk diffusion coefficient at 180 °C is about 3.6×10^{-10} m^2 s^{-1} [297]. Octacosane is chosen in this work to mimic the FT wax produced and is representative of the wax products according to the GC analyses [298, 299].

These diffusion behaviours are consistent across the three layers, except for the top layer at $P/P_0 = 0.8$, whereby capillary condensation of water inside pores can be observed. The peak with a maximum at 6.1×10^{-9} m^2 s^{-1} can be identified as water. The theoretical prediction by Wilke-Chang of bulk water diffusion at this temperature is 1.6×10^{-8} m^2 s^{-1}. Taking into account a tortuosity factor of 1.7, as established in Chapters 4 and 5, the effective diffusion coefficient of water should be approximately 9.5×10^{-9} m^2 s^{-1}, which is close to the value observed [300].

However, the apparent diffusion of water remains below the theoretical value as water could be restricted between the catalyst surface and the wax layer. This is in line with results published in the literature, whereby the diffusivity of the surface-wetting phase is slower closer to the pore surface. In addition, the presence of wax species will further slow down the water molecules [301, 302]. All the experiments described in Figure 8.2 were acquried with a $\Delta = 100$ ms and $\delta = 4$ ms.

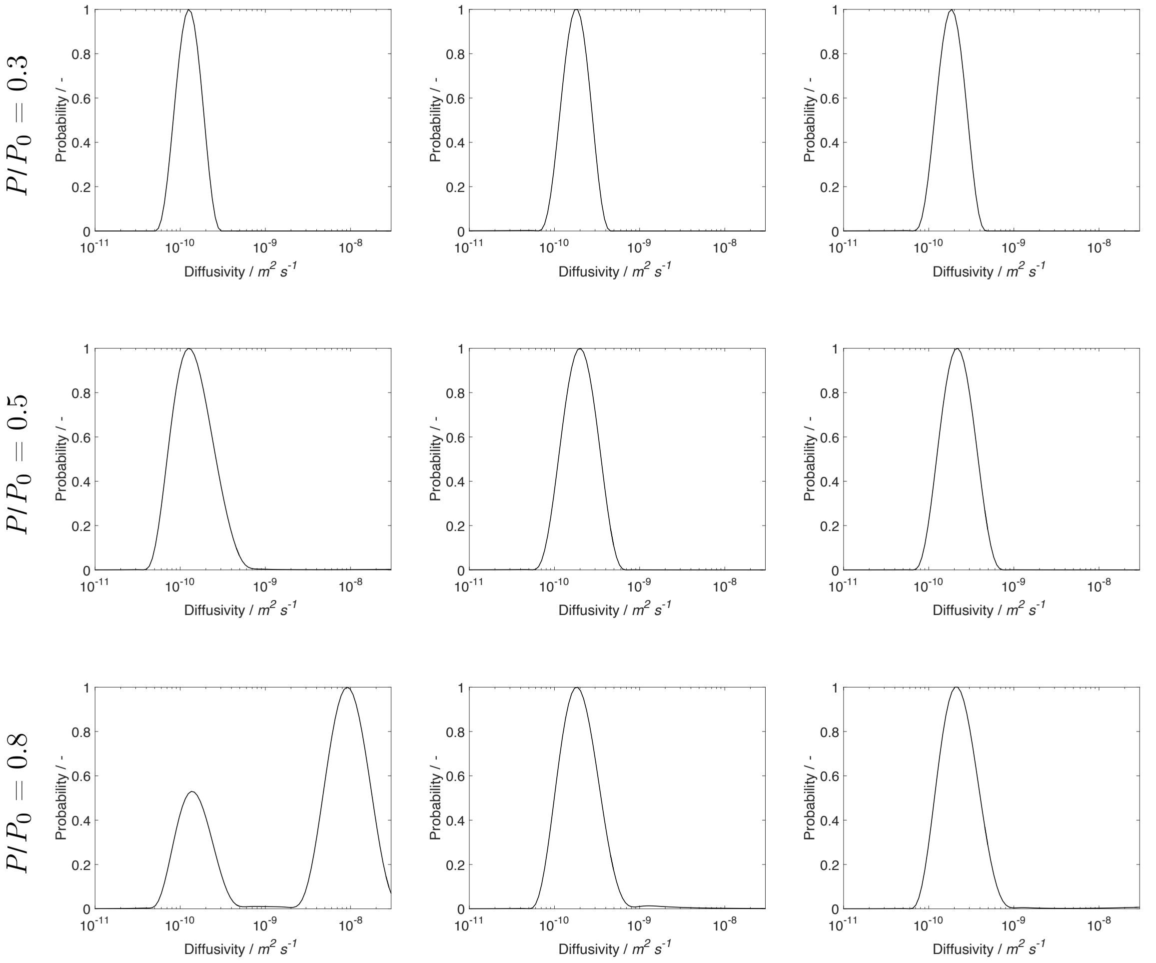

Top layer *Middle layer* *Bottom layer*

Figure 8.2 Diffusion distribution for FT wax products in Ru/TiO$_2$ catalyst pellets post-FTS, acquired at 180 °C, with Δ = 100 ms and δ = 4 ms. The distributions occurring in the top, middle and bottom catalyst layers at increasing water partial pressures P/P_0 between 0.3 - 0.8 are shown.

For the acquisitions depicted in Figure 8.3a, the water signal is observed at $P/P_0 = 0.9$ as sufficient water is present in the system. The maximum of the water diffusion distribution is at 6.5×10^{-9} m^2 s^{-1}, which can be observed for experiments with $\Delta = 20$ and $\delta = 1$ ms and with $\Delta = 100$ ms and $\delta = 4$ ms in the middle catalyst layer. For the experiment set up to detect water (at $\Delta = 20$ and $\delta = 1$ ms), the wax signal only decays 13% of initial signal and can be assumed constant. Again, as reported above, the confinement effect of the water layer trapped in between the wax-rich layer and the catalyst pore surface leads to lower than expected apparent diffusion coefficients for water [303].

For the experiments with the longest observation time Δ, the wax has the same uniform diffusion distribution with a maximum at around 2.8×10^{-10} m^2 s^{-1}. At $\Delta = 500$ ms, an additional peak at 1.5×10^{-11} m^2 s^{-1} is detected, which may be the first sign of restricted wax inside the system.

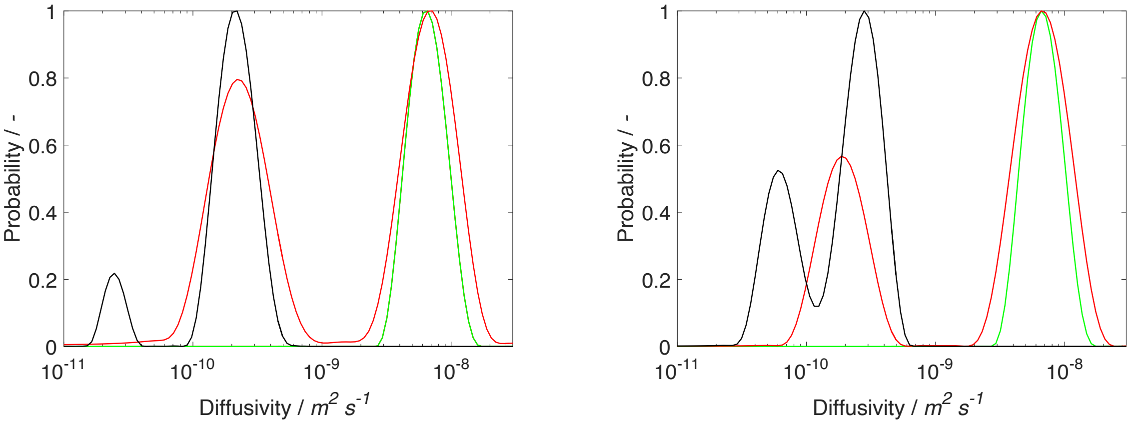

(a) $P/P_0 = 0.9$

(b) $P/P_0 = 0.95$

Figure 8.3 Diffusion distribution for FT products in Ru/TiO_2 catalyst pellets post-FTS, acquired at 180 °C and $P/P_0 = 0.9$ and 0.95, with $\Delta = 20$ (——) ms and $\delta = 1$ ms and with $\Delta = 100$ (——) and 500 (——) ms and $\delta = 4$ ms in the middle catalyst layer.

Similar to the experiment at $P/P_0 = 0.9$, in Figure 8.3b the water diffusion distribution can be observed at 7.1×10^{-9} m^2 s^{-1}, for experiments with $\Delta = 20$ and $\delta = 1$ ms and with $\Delta = 100$ ms and $\delta = 4$ ms. The wax diffusion distribution acquired at $\Delta = 500$ ms and $\delta = 4$ ms has two distinct distributions: the first with a fast component at 1.5×10^{-10} m^2 s^{-1}, partially overlapping with the result obtained at $\Delta = 100$ ms, and a slow component 5.5×10^{-11} m^2 s^{-1}. The wax diffusion behaviour decreases for increasing observation time Δ, which is indicative for emulsions which are detected at the highest partial pressure of water of 0.95. This is in line with the previous results of dodecane-in-water liquid pockets formed spontaneously if enough water is present in the pores. The decreasing diffusion behaviour at increasing Δ is indicative of this phenomenon.

In these high water content systems, it is likely that pockets arise where a mix occurs between wax-in-water emulsions and freely diffusion wax. It is very important to better understand the phase behaviour as this significantly influences the transport phenomena of molecules during FTS. This is in line with the previously stated hypothesis of Iglesia *et al.* that due to capillary effects, a separate water phase layer could condense inside the pores, giving rise to the formation of wax-in-water emulsions [13].

8.3.3 Emulsion Detection at 220 °C

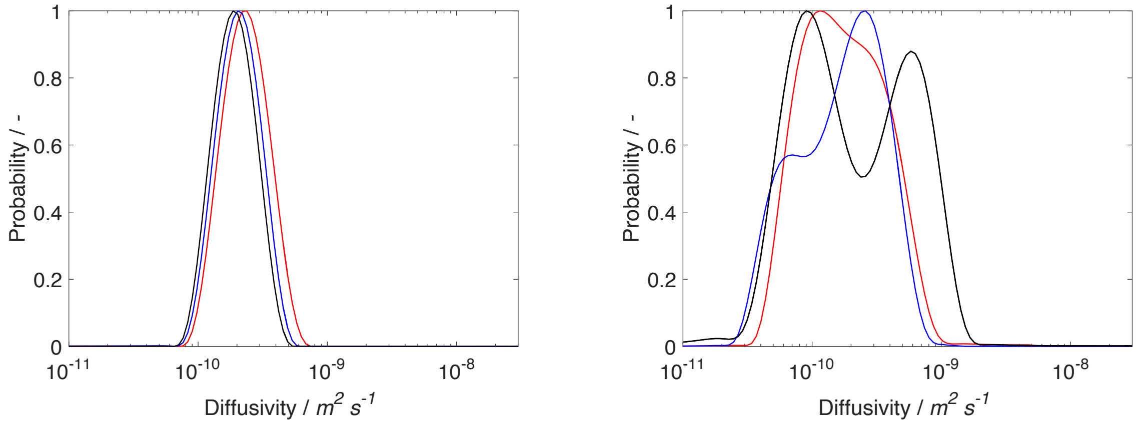

(a) P/P_0 = 0.3 (b) P/P_0 = 0.8

Figure 8.4 Diffusion distribution for FT products in Ru/TiO$_2$ *catalyst pellets post-FTS, acquired at 220 °C and* P/P_0 = *0.3 and 0.8, with* Δ = *100 (—), 300 (—) and 500 (—) ms and* δ = *4 ms in the middle catalyst layer.*

The diffusion distributions illustrated in Figure 8.4 are for FT wax at 220 °C and P/P_0 =0.3 and 0.8 respectively. Figure 8.4a shows narrow, single component distributions for wax with a maximum at 2.3×10^{-10} m^2 s^{-1}. This is in agreement with Wilke-Chang's prediction of bulk n-octacosane at this temperature of 3.6×10^{-10} m^2 s^{-1}. A very similar behaviour is seen for increasing observation times ranging from 100 to 500 ms. This is indicative that the wax species do not undergo restricted diffusion and therefore no spontaneous emulsion formation is observed. Relating to the experiments at 180 °C, more water should be present in the system for emulsion formation to take place. Again, no water distribution was observed for these partial pressure points due to the low SNR of water. Not sufficient water signal attenuation was recorded to extract a diffusion distribution as the wax signal was dominant.

Even at P/P_0 = 0.8 in Figure 8.4b, still no water was detected. However, a broad, single distribution was observed for wax at Δ of 100 ms. For the experiments at Δ = 300 and 500 ms and δ = 4 ms, the wax diffusion distribution has two components, with the fast component at around 3×10^{-10} m^2 s^{-1} and the slow component at about 9×10^{-11} m^2 s^{-1}. The faster component could correspond to wax freely diffusing inside the pores, as this value is in line with the prediction of Wilke-Chang. Finally, the slower component could represent a region containing a mixture of emulsions alongside freely diffusing wax. This would result in a broad distribution with two main peaks.

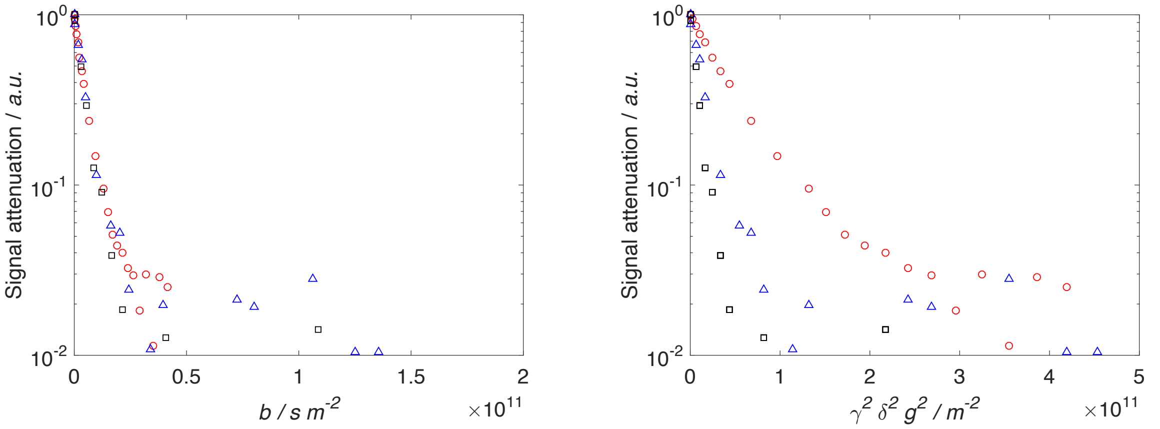

(a) ST plot for FT wax in Ru/TiO$_2$ at 220 °C, with Δ = 100 (○), 300 (△) and 500 (□) ms and δ = 4 ms at P/P_0 = 0.3.

(b) The same data plotted as in Figure (a) but as function of $\gamma^2\delta^2 g^2$, with Δ = 100 (○), 300 (△) and 500 (□) ms and δ = 4 ms.

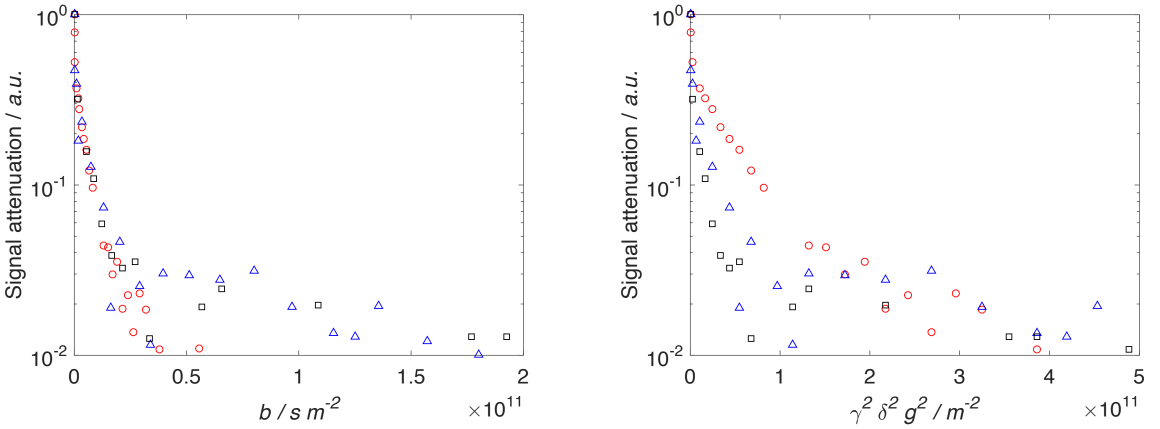

(c) ST plot for FT wax in Ru/TiO$_2$ at 220 °C, with Δ = 100 (○), 300 (△) and 500 (□) ms and δ = 4 ms at P/P_0 = 0.8.

(d) The same data plotted as in Figure (c) but as function of $\gamma^2\delta^2 g^2$, with Δ = 100 (○), 300 (△) and 500 (□) ms and δ = 4 ms.

Figure 8.5 ST plots for FT wax imbibed in Ru/TiO$_2$ catalyst pellets, at 220 °C at increasing P/P_0.

In Figure 8.5, the ST signal decays of FT wax are presented at 220 °C for $P/P_0 = 0.3$ and 0.8. In Figures 8.5a and 8.5c, the signal attenuations show similar trends as reported in Chapter 5 for unrestricted diffusion. For increasing observation times Δ ranging between 100 and 500 ms, the data points lie on a straight line and overlap. The displacement of wax molecules by the presence of water causes the curvature in the attenuation plots.

In Figures 8.5b and 8.5d, the same data is plotted without the time dependence. The signal decays for increasing observation times exhibit a steeper slope, corresponding to a greater RMSD which is characteristic for unrestricted diffusion. If the molecules are allowed to diffuse for a longer time, a bigger random walk distance can be covered, hence the faster decay. From Figure 8.5, it can be concluded that the FT wax is not fully restricted between P/P_0 of 0.3 and 0.8 at 220 °C, in line with the conclusions drawn from Figure 8.4b.

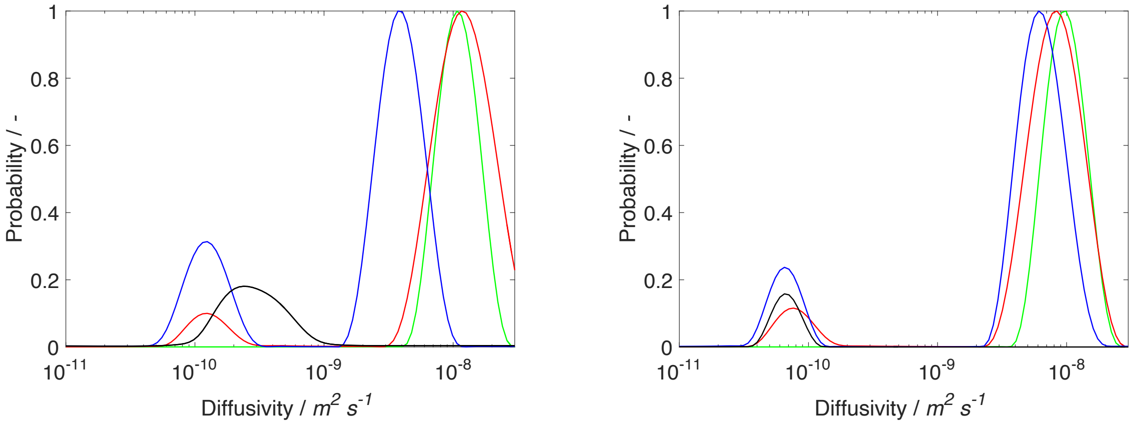

(a) $P/P_0 = 0.9$

(b) $P/P_0 = 0.95$

Figure 8.6 Diffusion distribution for FT products in Ru/TiO_2 catalyst pellets post-FTS, acquired at 220 °C and $P/P_0 = 0.9$ and 0.95, with $\Delta = 20$ (—) ms and $\delta = 1$ ms and with $\Delta = 100$ (—), 300 (—) and 500 (—) ms and $\delta = 4$ ms in the middle catalyst layer.

At $P/P_0 = 0.9$, see Figure 8.6a, higher quantities of water present in the system allow for detection of the water diffusion component for experiments with $\Delta = 20$ ms and $\delta = 1$ ms and with $\Delta = 100$ and 300 ms and $\delta = 4$ ms. The water signal is not detected for the longest observation time of $\Delta = 500$ ms due to relaxation effects. Also, at $\Delta = 300$ ms, the water diffusion distribution is shifted to lower diffusion values due to the influence of the wax signal. The water diffusion value is about 9.0×10^{-9} m^2 s^{-1} as capillary condensation of water takes place. The water diffusion value is close to Wilke-Chang's theoretical prediction of bulk water at 220 °C of 1.9×10^{-8} m^2 s^{-1}, which with the tortuosity factor of 1.7 becomes 1.1×10^{-8} m^2 s^{-1}. The pore confinement effect on water is noticeable, similarly published by Milischuk *et al.* who found that water forms two distinct molecular layers at the interface. At the pore surface, the water exhibits uniform, but somewhat lower than bulk liquid, density in the core region [304].

When increasing the observation time Δ at high P/P_0, most of the signal is derived from the water population while wax is displaced. Hence the decrease in the wax populations and lower wax diffusion distribution intensities. The wax exhibits a single component distribution, with a small population around 1.2×10^{-10} m^2 s^{-1}, which is slower than bulk wax seen at $P/P_0 = 0.3$.

At the highest P/P_0 of 0.95, the same effects are observed as in Figure 8.6a. Firstly, significant water is present in the catalyst bed and therefore the diffusion distributions can be obtained for water up to an observation time Δ of 300 ms. The maximum of the water distribution is around 9.5×10^{-9} m^2 s^{-1}. The diffusion of the wax species is $< 1 \times 10^{-10}$ m^2 s^{-1}, see Figure 8.6b. This value is far below the freely diffusion coefficient and indicates that the wax is restricted.

8.3.4 T_1 and D for increasing P/P_0

Studying the T_1 processes can reveal insights in the chemical environments of the probed molecules. The T_1 relaxation time can be correlated to the surface interaction strength of the species, whereby a low T_1 value indicates a strong interaction and vice versa [305]. Figure 8.7 shows the T_1 at 180 and 220 °C for both wax and water. At small P/P_0 (0.3 - 0.8), the low T_1 values for water indicate that it became the surface-wetting phase due to its strong interaction with the Ru/TiO$_2$ catalyst pellets. In the lower pressure point range, little changes occur as no significant water is condensing inside the pore space. The slow increase of T_1 correlates to the slow growth of the adsorbed water layer thickness.

The T_1 values for water increase for $P/P_0 > 0.8$ as capillary condensation occurs. This leads to a reduction of the surface interaction strength reflected by higher T_1 values. As more water accumulates inside the pores, water moves to more central regions in the pore space, hence an increase in T_1 values is noted. As more water condenses, the wax molecules undergo displacement, which is reflected by the sudden surge in the wax T_1 values.

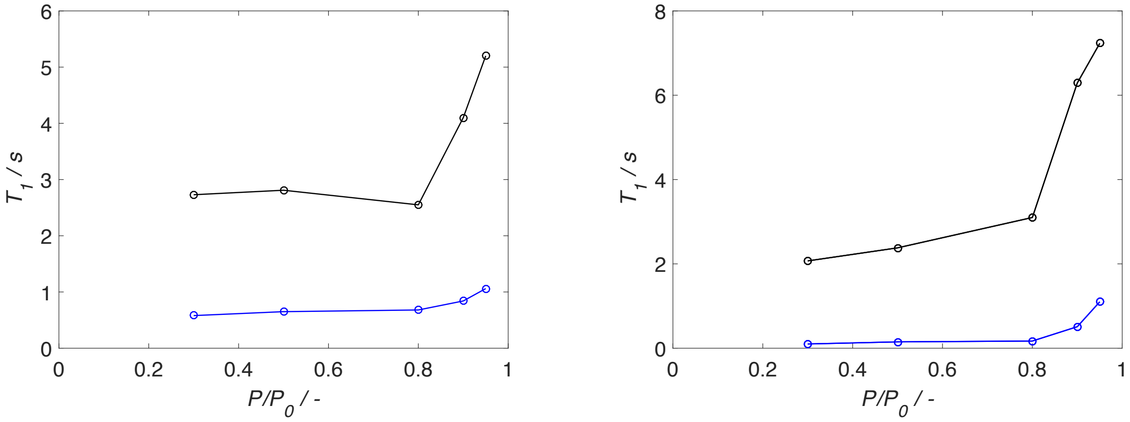

(a) 180 °C *(b) 220 °C*

Figure 8.7 T_1 values as a function of water relative pressure P/P_0 between 0.3 and 0.95 for FT products in Ru/TiO$_2$ catalyst pellets post-FTS, acquired at 180 and 220 °C, with wax (—) and water (—) in the middle catalyst layer.

In Figure 8.8, the diffusion of water for increasing partial pressures is consistent with the T_1 trend. At 180 °C and $P/P_0 > 0.8$, the diffusion of water is around 7.1×10^{-9} m^2 s^{-1}, which is below the bulk diffusion coefficient predicted by Wilke-Chang. Capillary condensation occurs without bulk condensation in the inter-particle space.

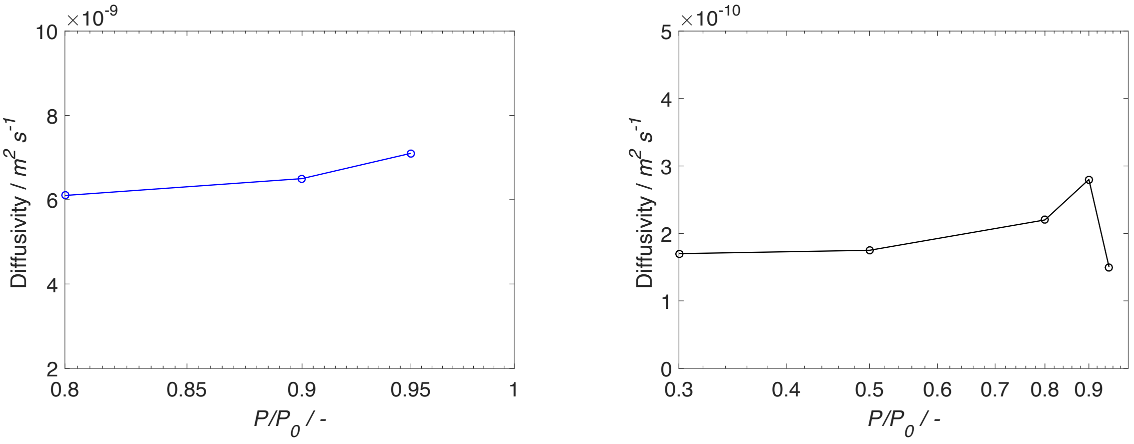

(a) water (—)

(b) wax (—)

Figure 8.8 Diffusivity of water (—) and wax (—) as a function of water relative pressure P/P_0 between 0.3 and 0.95 at 180 °C. Experiments acquired at $\Delta = 20$ ms an $\delta = 1$ ms for water and at $\Delta = 300$ ms and $\delta = 4$ ms for wax.

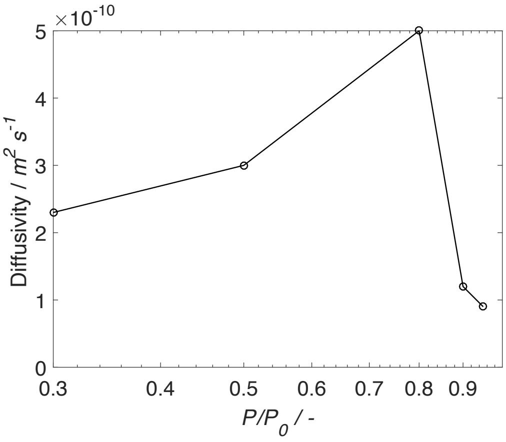

Figure 8.9 Diffusivity of wax (—) as a function of water relative pressure P/P_0 between 0.3 and 0.95 at 220 °C. Experiments acquired at $\Delta = 300$ ms and $\delta = 4$ ms for wax.

The wax molecules have an increasing diffusion dependency which is in line with the water up to $P/P_0 = 0.8$ as until that point, no spontaneous emulsions are formed. The increase in mobility for the wax molecules is reflected by the increase in both D and T_1, which is consistent behaviour for wax being displaced from the catalyst surface. This is in line with results published for spin-lattice relaxation and PFG NMR data published for wax-water behaviours in porous silica spheres at 195 °C [305]. For $P/P_0 > 0.8$, the onset of capillary condensation occurs. Sufficient condensed water is present in the system to have emulsification of wax-in-water. Due to the restrictive environment, the diffusion coefficient of wax plunges. These trends are consistent for both temperatures, see both Figure 8.8b and Figure 8.9. At 220 °C, this effect is more pronounced with faster diffusion behaviours at elevated temperatures.

Moreover, the experiments at 180 °C were performed prior to the measurements at 220 °C. Due to the nature of this study at elevated pressure and temperature with N_2 and water flow, it is expected that some of the wax products would have been flushed through to the production collection vessels. Hence, for later experiments, the quantity of wax in the system decreased due to convection and evaporation. This would suggest that at the final 220 °C experiments at $P/P_0 > 0.8$, the condensation of water would be easier as more void space would be available for the water to condense. Hence the shift to a lower P/P_0 for the drop in diffusion between 180 and 220 °C.

8.4 Conclusions

This Chapter presents the findings of an *in situ* emulsion detection study in 1 wt% Ru/TiO_2 FT catalysts at both 180 and 220 °C. This study used PFG and T_1 NMR techniques and was performed by feeding water to the system post-FTS by slowly increasing the water partial pressure between 0.3 - 0.95 P/P_0. This work is the final Chapter as it links the work discussed in the previous Chapters and achieves the scientific goal: using an unique pilot-scale reactor to study *operando* FTS and gain a better understanding of the phase behaviour and transport properties of FT products in porous media.

At $P/P_0 \leq 0.5$, both the water and wax diffuse freely without any bulk or capillary condensation of water being observed, confirmed by the low spin-lattice relaxation values. However, at $P/P_0 \geq 0.8$, capillary condensation of water inside the catalyst pores was reported. This is in agreement with capillary effects observed by Claeys *et al.*, where in small pore supports, a water phase could be formed at low water partial pressures [82]. The formation of the water-rich phase caused the wax species to be displaced from the surface and was found to be located in between the pore surface and the wax layer. The displaced wax species became isolated from the pore space, which caused both the T_1 and D values to surge. This phenomenon has also been identified by Zheng *et al.* [305]. The pore confinement effect caused the effective diffusion coefficient of water to be lower than the theoretical value predicted by Wilke-Chang [297]. This is in line with simulation results published by Papavasileiou *et al.*, where the reduced mobility of water lead to slower diffusion behaviours for the surface-wetting, water-rich layer which is adjacent to the pore surface in TiO_2 pellets. Youngs *et al.* also reported a slow increase in diffusivity with increasing distance from the interface, leading to the bulk value in the central region of the pore. The first two layers interacting with the surface have a decelerated diffusion behaviour because of the confinement effect [303, 306].

For high water partial pressure $P/P_0 \geq 0.9$, a system is reached where wax-in-water liquid pockets spontaneously form. This was concluded from the sudden drop in the diffusion behaviour for wax. At these high partial pressures, sufficient water was present in the system for emulsification to take place. The restrictive environment leads to the significant decrease in diffusion behaviour and further increase in T_1 time. This was already hypothesised by Iglesia *et al.* ([13]), who suggested that the condensed water phase in presence of FT wax could lead to the formation of hydrocarbon-in-water emulsions, which would be stabilised by oxygenates formed as a by-product. In addition, the presence of this separate water-rich layer inside the intra-pellet voids could increase the FT reaction rates and the selectivities towards both C_{5+} and olefins [12]. This work suggests that these liquid pockets can form naturally inside porous media, which is crucial information. The formation of large emulsions during FTS will especially have a significant impact on the way in which heat and mass transfer are modelled as emulsions can significantly hinder molecular diffusion of reactants in and products out of the catalyst pores.

Chapter 9

Conclusions and Future Work

9.1 Conclusions

This PhD thesis investigated the complex multiphase behaviour of aqueous and hydrocarbon liquids saturated in porous media, relevant to FTS. A PFG NMR technique was developed and implemented to address the goal of this thesis: investigate emulsion formation and mass transfer phenomena relevant to heterogeneous GTL catalysis. NMR relaxometry, diffusometry and MRI techniques were subsequently applied *in situ* to elucidate the phase behaviour of the FTS process under industrially-relevant conditions in a purposely built fixed-bed tubular reactor.

Chapter 4 confirmed that NMR relaxometry and PFG experiments can be applied to probe and identify spontaneous ganglia formation in porous media. Measurements on a model system were done at ambient conditions on immiscible mixtures of bulk water and dodecane imbibed in θ-alumina, with a pore size of 16 nm. Dodecane and water in this preliminary study were used as model compounds simulating the main FT products: linear hydrocarbons and an aqueous water phase. The relaxation results indicated that in the binary mixture, water was the surface-wetting phase and dodecane became isolated from the pore surface. Due to confinement effects, dodecane experienced restrictive diffusion, which confirmed the spontaneous formation of liquids pockets of dodecane-in-water.

Chapter 5 reported that PFG NMR methods were employed to study a variety of effects on the formation of ganglia of dodecane-in-water imbibed in both CARiACT Q-silica spherical beads and Ru/TiO_2 FT catalysts, with an average pore size of 28.6 nm. The emulsion formation behaviour was consistent across both types of support. The diffusometry data was used to extract information regarding the DSD of the confined emulsions. Firstly, the effect of temperature (20, 40 and 60 °C) on the stability and size of emulsions was investigated.

Secondly, the pore size distribution was varied (15 and 50 nm) for the Q-silica beads. For the ranges studied, very little effect was found on the DSD. However, the dodecane liquid pockets were identified to be in the order of 1 µm in size, thereby extending over several pore lengths and present in the shape of ganglia.

Subsequently, the addition of longer chain surfactants to the binary mixture, which reduced the surface tension, lead to a small increase in droplet size. However, when fatty acids, like stearic acid, were added to the system, it was found that the surface could be chemically modified to become hydrophobic. As a consequence, the spontaneous emulsion formation was no longer detected.

Chapter 6 presented the NMR compatible, *in situ*, fixed-bed tubular pilot-plant designed, built and commissioned in collaboration with STCA and Zeton B.V. This equipment provides the capability (up to 300 °C and 50 bar) to explore FTS and provide quantitative *operando* MR measurements of heterogeneous catalysis in a fixed-bed reactor. During the PhD and Shell collaboration, numerous reactor optimisations were implemented. Throughout the PhD, several visits were made to STCA, which facilitated knowledge transfers between STCA and the MRRC.

During the internship at Shell, a preliminary surface coverage study was performed by varying the feed ratio of H_2:CO. It was concluded that an increase in carbon number N was observed for increasing P_{CO}, which suggested a strong, negative order in CO for $N > 6$. Moreover, it was shown that the chain-growth probability, α, decreased with increasing H_2:CO ratio. However, the product distribution was not affected by the increase of P_{H_2}, as there was a first order dependence in H_2.

Chapter 7 reported the first ever *in situ* investigation into FTS under real operating conditions, which resulted in a TOS $>$ 850 h. In order to characterise heterogeneous catalytic systems, spatially-resolved MRI measurements of diffusion and product distributions from within both the pilot-scale reactor and a single catalyst pellet were performed. Spatially-resolved NMR spectroscopy allowed to obtain a resolution of ~500 µm for diffusion measurements inside the Ru/TiO_2 catalyst pellets under real reaction operating conditions.

PFG NMR diffusion data was also acquired per pixel (corresponding to the intra- and inter-pellet space) of 2D images of the three catalyst layers. This 2D diffusion measurement was used to extract a D distribution and a D value at each pixel for the intra- and inter-pellet species. Ultimately, spatially-resolved maps of diffusivity were created for intra-and inter-pellet products separately.

During FTS, the liquid product hold-up was proportional to the signal intensities in the three catalyst layers, which increased with increasing TOS. It was observed that the liquid products mainly existed inside the catalyst pellets in the top and middle catalyst layers whereas significant accumulation of the inter-pellet liquid products was identified in the bottom catalyst layer. Finally, high-resolution 2D images with a 172 µm × 172 µm resolution and additional high-resolution 3D RARE images were acquired from the reactor bed.

Chapter 8 focussed on the *in situ* emulsion detection study in 1 wt% Ru/TiO_2 FT catalysts at both 180 and 220 °C. Water was fed to the system post-FTS by slowly increasing the water partial pressure between 0.3 - 0.95 P/P_0. At $P/P_0 \leq 0.5$, the water and wax phases were able to diffuse freely and no capillary condensation of water was observed. This was confirmed by the low spin-lattice relaxation values. However, at $P/P_0 \geq 0.8$, capillary condensation of water inside the catalyst pores was reported. A water-rich phase was formed and this caused the FT wax to be displaced from the surface. The displaced wax species became isolated from the pore space, which caused both the T_1 and D values to surge. At the same time the water experienced confinement effects as it became located in between the pore surface and the wax layer, which lead to a lower effective diffusion coefficient for water than the theoretical value predicted by Wilke-Chang.

At high water partial pressure $P/P_0 \geq 0.9$, a system was established where wax-in-water pockets spontaneously formed, similar to the phenomena described in Chapters 4 and 5. This was concluded from the sudden drop in the diffusion behaviour for wax, especially at 220 °C. The restrictive environment of the ganglia lead to a significant decrease in diffusion behaviour and further increase in T_1 time.

This final Chapter addressed the main scientific goal of this thesis: to use an unique purposely-built NMR pilot-scale reactor to study *operando* FTS. This was done to gain a better understanding of the phase behaviour and transport properties of confined FT liquid products in porous media. It was shown that NMR can be applied to investigate mass transport behaviours in FTS-relevant systems, thereby demonstrating the ability to characterise heterogeneous catalytic systems. The formation of wax-in-water emulsions will have implications on the heat- and mass transport properties of both the reactants and products. This in turn will further influence the reaction rates and kinetics, the conversion, catalyst lifetime and product selectivity of the reaction. Ultimately, improving the fundamental understanding of the phase behaviour is necessary to validate and optimise hydrodynamics simulations of FTS.

9.2 Future Work

The newly developed capabilities of using the *in situ* NMR reactor opens up all sorts of opportunities for future *operando* heterogeneous catalysis studies, building up on the work presented in this thesis. Further questions that arise that can be addressed are listed below.

9.2.1 Droplet Detection during *operando* FT

The work presented in Chapter 8 on the emulsions formation was done post-FTS. It should be possible to apply the same methodology to identify *operando* spontaneous emulsion formation during FT under flow of syngas. Rytter *et al.* raised that so far no studies were performed where water was deliberately condensed in a fixed-bed to investigate the consequences on the performance of FTS [73]. Therefore, it is desirable that similar PFG NMR measurements are performed at realistic reaction conditions during FTS reactions to observe the phase behaviour. In addition, catalyst samples with varying pore size distribution could be analysed to further study the effect of water pore condensation. This could be linked to a full analysis on product selectivity and conversion.

9.2.2 FT Experiments with Catalyst Modified with Stearic Acid

This future work suggestion is building up from the previous statement. This is to further validate the findings of Chapter 5, whereby catalysts were impregnated with stearic acid, inhibiting droplet formation. The same type of catalysts modification could be implemented to understand whether similar inhibition effects can be observed under realistic FT conditions. This would indicate the effect of high levels of oxygenates could cause on the phase behaviour of fluids confined in the porous system.

9.2.3 Vary the Temperature and H_2:CO Feed Ratio during FTS

The effects of temperature and H_2:CO feed ratio on the catalyst lifetime and selectivity have often been addressed in the literature. However, regularly opposing arguments and conclusions were proposed justifying the various effects of varying the reaction parameters. The Zeton FT reactor is designed to study *operando* FT where commercially relevant operating conditions can easily be modified. These would be representative for Shell GTL Pearl Qatar operating conditions. In addition, the NMR reactor can also be used to screen various catalysts and compare their catalytic performance under different P and T.

9.2.4 Critical Time for Detecting Emulsion Formation

As observed in Chapters 4 and 5, the dodecane diffusion signal decay data points did not overlap for increasing observation times Δ, which was indicative for the restricted diffusion.

However, these experiments were acquired at relatively long observations times ranging between 150 and 500 ms as the dodecane signal decayed very slowly. If the diffusion were to be observed for very short times, the dodecane molecules would not be given enough time to experience the restrictive boundaries of the droplets. Hence, the hypothesis is that dodecane molecules would seem to initially be behaving like freely diffusing, unrestricted species. This would suggest that a critical time can be detected whereby the dodecane molecules start encountering the emulsion walls and become restricted. A significant change in diffusion behaviour would indicate this critical time.

9.2.5 Understand Deactivation

Finally, the FT reaction reported in Chapter 7 had an operating time of roughly 850 h. During this period, a slight catalyst deactivation could be noted due to the product signal decrease. However, as discussed in Chapter 2, the formation of coke can have a severe impact on the catalyst lifetime and product selectivity. Coking mechanisms and the influence of reaction selectivities could be studied if FT was performed for operating times nearing 2000 h. Similar studies were reported by Nakhaei Pour *et al.* [307], where syngas conversion dropped significantly by ±25% at 1700 h.

Bibliography

[1] J. Gorimbo, "Use of stability diagrams to predict catalyst speciation during Fischer Tropsch reduction stage: A mini-review," *Catalysis Science and Technology*, vol. 8, no. 8, pp. 2022–2029, 2018.

[2] A. Y. Krylova, "Products of the Fischer-Tropsch synthesis (A Review)," *Solid Fuel Chemistry*, vol. 48, pp. 22–35, jan 2014.

[3] H. Gruber, P. Groß, R. Rauch, A. Reichhold, R. Zweiler, C. Aichernig, S. Müller, N. Ataimisch, and H. Hofbauer, "Fischer-Tropsch products from biomass-derived syngas and renewable hydrogen," *Biomass Conversion and Biorefinery*, 2019.

[4] S. S. Ail and S. Dasappa, "Biomass to liquid transportation fuel via Fischer Tropsch synthesis - Technology review and current scenario," may 2016.

[5] I. L. Pykett, J. H. Newhouse, F. S. Buonanno, T. J. Brady, M. R. Goldman, J. P. Kistler, and G. M. Pohost, "Principles of nuclear magnetic resonance imaging.," *Radiology*, vol. 143, pp. 157–168, apr 1982.

[6] G. A. G. A. Webb and A. E. Aliev, *Nuclear magnetic resonance. Vol. 37, A review of the literature published between June 2006 and May 2007*. Royal Society of Chemistry, 2008.

[7] D. Glasser, D. Hildebrandt, X. Liu, X. Lu, and C. M. Masuku, "Recent advances in understanding the Fischer–Tropsch synthesis (FTS) reaction," *Current Opinion in Chemical Engineering*, vol. 1, pp. 296–302, aug 2012.

[8] C. M. Masuku, D. Hildebrandt, and D. Glasser, "The role of vapour–liquid equilibrium in Fischer–Tropsch product distribution," *Chemical Engineering Science*, vol. 66, pp. 6254–6263, dec 2011.

[9] Z. Yang and N. L. Abbott, "Spontaneous Formation of Water Droplets at Oil-Solid Interfaces," *Langmuir*, vol. 26, no. 17, pp. 13797–13804, 2010.

[10] V. S. Ermolaev, V. Z. Mordkovich, and I. G. Solomonik, "Influence of capillary condensation on heat and mass transfer in the grain of a Fischer-Tropsch synthesis catalyst," *Theoretical Foundations of Chemical Engineering*, vol. 44, no. 5, pp. 660–664, 2010.

[11] S. T. Roberts, M. P. Renshaw, M. Lutecki, J. McGregor, A. J. Sederman, M. D. Mantle, and L. F. Gladden, "Operando magnetic resonance: monitoring the evolution of conversion and product distribution during the heterogeneous catalytic ethene oligomerisation reaction.," *Chemical communications (Cambridge, England)*, vol. 49, pp. 10519–21, nov 2013.

[12] S. Dukalski, M., Harting, J., Huinink, H., Kako Joibari, F., Onderwaater, W., van der Bijl, E., van Oort, B., Wijts, G., Zhang, "The physics of water and wax in the

pores of a working Gas-to-Liquids catalyst Citation for published version (APA)," in *Proceedings Physics with Industry 2012*, (Leiden), pp. 81–98, Lorentz Center Leiden, Leiden University, 2012.

[13] E. Iglesia, "Design, synthesis, and use of cobalt-based Fischer-Tropsch synthesis catalysts," *Applied Catalysis A: General*, vol. 161, pp. 59–78, nov 1997.

[14] C. K. Rofer-DePoorter, "A comprehensive mechanism for the Fischer-Tropsch synthesis," *Chemical Reviews*, vol. 81, pp. 447–474, oct 1981.

[15] O. O. James, B. Chowdhury, M. A. Mesubi, and S. Maity, "Reflections on the chemistry of the Fischer–Tropsch synthesis," *RSC Advances*, vol. 2, p. 7347, aug 2012.

[16] M. E. Dry, "Catalytic aspects of industrial Fischer-Tropsch synthesis," *Journal of Molecular Catalysis*, vol. 17, no. 2-3, pp. 133–144, 1982.

[17] P. M. Maitlis and A. de Klerk, *Greener Fischer-Tropsch Processes for Fuels and Feedstocks.* 2013.

[18] S. Bezergianni and A. Dimitriadis, "Comparison between different types of renewable diesel," 2013.

[19] M. D. André Steynberg, *Fischer-Tropsch Technology.* Elsevier Science, 1st ed., 2004.

[20] S. Sartipi, M. Makkee, F. Kapteijn, and J. Gascon, "Catalysis engineering of bifunctional solids for the one-step synthesis of liquid fuels from syngas: a review," *Catalysis Science & Technology*, vol. 4, p. 893, mar 2014.

[21] R. Guettel, U. Kunz, and T. Turek, "Reactors for Fischer-Tropsch Synthesis," *Chemical Engineering & Technology*, vol. 31, pp. 746–754, may 2008.

[22] B. H. Davis and M. L. Occelli, *Advances in Fischer-Tropsch synthesis, catalysts, and catalysis.* CRC Press, 2009.

[23] L. M. Tau, H. Dabbagh, S. Bao, and B. H. Davis, "Fischer-Tropsch synthesis. Evidence for two chain growth mechanisms," *Catalysis Letters*, vol. 7, no. 1, pp. 127–140, 1990.

[24] C. H. Bartholomew, "Recent technological developments in Fischer-Tropsch catalysis," *Catalysis Letters*, vol. 7, no. 1, pp. 303–315, 1990.

[25] G. L. Bezemer, J. H. Bitter, H. P. C. E. Kuipers, H. Oosterbeek, J. E. Holewijn, X. Xu, F. Kapteijn, A. J. van Dillen, and K. P. de Jong, "Cobalt particle size effects in the Fischer-Tropsch reaction studied with carbon nanofiber supported catalysts.," *Journal of the American Chemical Society*, vol. 128, pp. 3956–64, mar 2006.

[26] R. Yang, L. Zhou, J. Gao, X. Hao, B. Wu, Y. Yang, and Y. Li, "Effects of experimental operations on the Fischer-Tropsch product distribution," *Catalysis Today*, vol. 298, pp. 77–88, dec 2017.

[27] D. Förtsch, K. Pabst, and E. Groß-Hardt, "The product distribution in Fischer-Tropsch synthesis: An extension of the ASF model to describe common deviations," 2015.

[28] M. F. M. Post, A. C. Van't Hoog, J. K. Minderhoud, and S. T. Sie, "Diffusion limitations in fischer-tropsch catalysts," *AIChE Journal*, vol. 35, pp. 1107–1114, jul 1989.

[29] A. A. Muleja, Y. Yao, D. Glasser, and D. Hildebrandt, "A study of Fischer-Tropsch synthesis: Product distribution of the light hydrocarbons," *Applied Catalysis A: General*, vol. 517, 2016.

[30] E. Iglesia, S. C. Reyes, and R. J. Madon, "Transport-enhanced α-olefin readsorption pathways in Ru-catalyzed hydrocarbon synthesis," *Journal of Catalysis*, vol. 129, no. 1, pp. 238–256, 1991.

[31] G. A. Hadjigeorghiou and J. T. Richardson, "FISCHER-TROPSCH SELECTIVITY OF Ni/Al203 CATALYSTS," tech. rep.

[32] G. Henrici Olive, "The Fischer-Tropsch Synthesis: Molecular Weight Distribution of Primary Products and Reaction Mechanism," *Angewandte Chemie International Edition in English*, vol. 15, no. 3, pp. 136–141, 1976.

[33] B. W. Wojciechowski, "The Kinetics of the Fischer-Tropsch Synthesis," *Catalysis Reviews*, vol. 30, pp. 629–702, dec 1988.

[34] N. O. Egiebor, W. C. Cooper, and B. W. Wojciechowski, "Carbon number distribution of Fischer - Tropsch CO-hydrogenation products from precipitated iron catalysts," *The Canadian Journal of Chemical Engineering*, vol. 63, no. 5, pp. 826–834, 1985.

[35] T. J. Donnelly, I. C. Yates, and C. N. Satterfield, "Analysis and Prediction of Product Distributions of the Fischer-Tropsch Synthesis," *Energy and Fuels*, vol. 2, pp. 734–739, nov 1988.

[36] E. Kuipers, C. Scheper, J. Wilson, I. Vinkenburg, and H. Oosterbeek, "Non-ASF Product Distributions Due to Secondary Reactions during Fischer–Tropsch Synthesis," *Journal of Catalysis*, vol. 158, pp. 288–300, jan 1996.

[37] N. Moazami, H. Mahmoudi, K. Rahbar, P. Panahifar, A. Tsolakis, and M. L. Wyszynski, "Catalytic performance of cobalt-silica catalyst for Fischer-Tropsch synthesis: Effects of reaction rates on efficiency of liquid synthesis," *Chemical Engineering Science*, vol. 134, 2015.

[38] F. Fischer, H. T. B. Chem, and undefined 1926, "Die Erdölsynthese bei gewöhnlichem Druck aus den Vergasungsprodukten der Kohlen,"

[39] Q. Zhang, J. Kang, and Y. Wang, "Development of Novel Catalysts for Fischer-Tropsch Synthesis: Tuning the Product Selectivity," *ChemCatChem*, vol. 2, pp. 1030–1058, sep 2010.

[40] M. A. Vannice, "The catalytic synthesis of hydrocarbons from H2 CO mixtures over the group VIII metals. IV. The kinetic behavior of CO hydrogenation over Ni catalysts," *Journal of Catalysis*, vol. 44, no. 1, pp. 152–162, 1976.

[41] R. Krishna, "A Scale-up Strategy for a Commercial Scale Bubble Column Slurry Reactor for Fischer-Tropsch Synthesis," *Oil and Gas Science and Technology*, vol. 55, no. 4, pp. 359–393, 2000.

[42] D. L. King, "A Fischer-Tropsch study of supported ruthenium catalysts," *Journal of Catalysis*, vol. 51, pp. 386–397, mar 1978.

[43] N. E. Tsakoumis, M. Rønning, Ø. Borg, E. Rytter, and A. Holmen, "Deactivation of cobalt based Fischer–Tropsch catalysts: A review," *Catalysis Today*, vol. 154, pp. 162–182, sep 2010.

[44] D. D. Hibbitts, B. T. Loveless, M. Neurock, and E. Iglesia, "Mechanistic role of water on the rate and selectivity of fischer-tropsch synthesis on ruthenium catalysts," *Angewandte Chemie - International Edition*, vol. 52, pp. 12273–12278, nov 2013.

[45] Y.-N. Wang, W.-P. Ma, Y.-J. Lu, J. Yang, Y.-Y. Xu, H.-W. Xiang, Y.-W. Li, Y.-L. Zhao, and B.-J. Zhang, "Kinetics modelling of Fischer–Tropsch synthesis over an industrial Fe–Cu–K catalyst," *Fuel*, vol. 82, pp. 195–213, jan 2003.

[46] R. Dictor, A. B. J. of Catalysis, and undefined 1986, "Fischer-Tropsch synthesis over reduced and unreduced iron oxide catalysts," *Elsevier*.

[47] G. P. van der Laan and A. A. C. M. Beenackers, "Kinetics and Selectivity of the Fischer–Tropsch Synthesis: A Literature Review," *Catalysis Reviews*, nov 2011.

[48] J. Matthey and U. K. Billingham, "A robust and precious metal-free high performance cobalt Fischer–Tropsch catalyst," 1929.

[49] B. D. F. P. Technology and undefined 2001, "Fischer–Tropsch synthesis: current mechanism and futuristic needs," *Elsevier*.

[50] A. Nakhaei Pour and M. R. Housaindokht, "The olefin to paraffin ratio as a function of catalyst particle size in Fischer–Tropsch synthesis by iron catalyst," *Journal of Natural Gas Science and Engineering*, vol. 14, pp. 204–210, sep 2013.

[51] J. Patzlaff, Y. Liu, C. Graffmann, J. G. C. Today, and undefined 2002, "Interpretation and kinetic modeling of product distributions of cobalt catalyzed Fischer–Tropsch synthesis," *Elsevier*.

[52] S. T. Roberts, *NMR Relaxometry and Diffusometry Techniques for Exploring Heterogeneous Catalysis*. PhD thesis, University of Cambridge, 2012.

[53] J. A. Moulijn, A. E. Van Diepen, and F. Kapteijn, "Catalyst deactivation: Is it predictable? What to do?," *Applied Catalysis A: General*, vol. 212, pp. 3–16, apr 2001.

[54] M. Argyle and C. Bartholomew, "Heterogeneous Catalyst Deactivation and Regeneration: A Review," *Catalysts*, vol. 5, no. 1, 2015.

[55] P. Biloen and W. M. Sachtler, "Mechanism of Hydrocarbon Synthesis over Fischer-Tropsch Catalysts," *Advances in Catalysis*, vol. 30, pp. 165–216, jan 1981.

[56] E. Rytter and A. Holmen, "Deactivation and regeneration of commercial type fischer-tropsch co-catalysts—A mini-review," mar 2015.

[57] H. S. Fogler, *Essentials of chemical reaction engineering*. Prentice Hall, 2011.

[58] L. Biegler, I. Grossmann, and A. Westerberg, "Systematic methods for chemical process design," dec 1997.

[59] M. E. Davis, R. J. Davis, B. Burr Ridge, I. Dubuque, I. Madison, and W. New York San Francisco St Louis Bangkok Bogota Caracas Kuala Lumpur Lisbon London Madrid Mexico City Milan Montreal New Delhi Santiago Seoul Singapore Sydney Taipei Toronto, "Fundal1entals of Chel1ical Reaction Engineering," tech. rep., 2003.

[60] J. E. Bailey, "Periodic Operation Of Chemical Reactors: A Review," *Chemical Engineering Communications*, vol. 1, no. 3, pp. 111–124, 1974.

[61] F. Berruti, T. S. Pugsley, L. Godfroy, J. Chaouki, and G. S. Patience, "Hydrodynamics of circulating fluidized bed risers: A review," *The Canadian Journal of Chemical Engineering*, 1995.

[62] J. Ruud Van Ommen and R. F. Mudde, "Measuring the Gas-Solids Distribution in Fluidized Beds-A Review," tech. rep.

[63] A. C. Rees, J. F. Davidson, J. S. Dennis, P. S Fennell, L. F. Gladden, A. N. Hayhurst, M. D. Mantle, C. R. Müller, and A. J. Sederman, "The nature of the flow just above the perforated plate distributor of a gas-fluidised bed, as imaged using magnetic resonance," *Chemical Engineering Science*, 2006.

[64] M. T. Kreutzer, F. Kapteijn, J. A. Moulijn, and J. J. Heiszwolf, "Multiphase monolith reactors: Chemical reaction engineering of segmented flow in microchannels," *Chemical Engineering Science*, vol. 60, no. 22, pp. 5895–5916, 2005.

[65] J. X. Zhu, Z. Q. Yu, Y. Jin, J. R. Grace, and A. Issangya, "Cocurrent downflow circulating fluidized bed (downer) reactors - A state of the art review," 1995.

[66] A. Mahecha-Botero, J. R. Grace, S. S. Elnashaie, and C. J. Lim, "Advances in modeling of fluidized-bed catalytic reactors: A comprehensive review," 2009.

[67] "Gas-to-liquids (GTL): A review of an industry offering several routes for monetizing natural gas," *Journal of Natural Gas Science and Engineering*, vol. 9, pp. 196–208, nov 2012.

[68] A. Brown, "QATAR INVESTOR VISIT 2009," tech. rep., 2009.

[69] B. Todić, V. V. Ordomsky, N. M. Nikačević, A. Y. Khodakov, and D. B. Bukur, "Opportunities for intensification of Fischer–Tropsch synthesis through reduced formation of methane over cobalt catalysts in microreactors," *Catal. Sci. Technol.*, vol. 5, pp. 1400–1411, feb 2015.

[70] D. J. Vermeer and R. Krishna, "Hydrodynamics and Mass Transfer in Bubble Columns Operating in the Churn-Turbulent Regime," *Industrial and Engineering Chemistry Process Design and Development*, vol. 20, pp. 475–482, jul 1981.

[71] G. Haarlemmer and T. Bensabath, "Comprehensive Fischer–Tropsch reactor model with non-ideal plug flow and detailed reaction kinetics," *Computers & Chemical Engineering*, vol. 84, pp. 281–289, jan 2016.

[72] J. H. Crowell, H. E. Benson, J. H. Field, and H. H. Storch, "PILOT PLANTS. Fischer-Tropsch Oil Circulation Processes," *Industrial & Engineering Chemistry*, vol. 42, pp. 2376–2384, nov 1950.

[73] E. Rytter and A. Holmen, "Perspectives on the Effect of Water in Cobalt Fischer-Tropsch Synthesis,"

[74] P. Azadi, "Microkinetic Modeling of the Fischer-Tropsch Synthesis over Cobalt Catalysts," *ChemCatChem*, vol. 7, no. 1, pp. 137–143, 2015.

[75] A. Bordet, L.-M. Lacroix, K. Soulantica, and B. Chaudret, "A New Approach to the Mechanism of Fischer-Tropsch Syntheses Arising from Gas Phase NMR and Mass Spectrometry," *ChemCatChem*, vol. 8, pp. 1727–1731, may 2016.

[76] R. M. De Deugd, *Fischer-Tropsch Synthesis Revisited; Efficiency and Selectivity Benefits from Imposing Temporal and/or Spatial Structure in the Reactor.* PhD thesis, Univerity of Technology Delft, 2004.

[77] R. J. Kokes, W. K. Hall, and P. H. Emmett, "Fischer-tropsch synthesis mechanism studies. the addition of radioactive ethanol to the synthesis gas," *Journal of the American Chemical Society*, vol. 79, no. 12, pp. 2989–2996, 1957.

[78] R. C. Brady and R. Pettit, "Mechanism of the Fischer-Tropsch reaction. The chain propagation step," *Journal of the American Chemical Society*, vol. 103, pp. 1287–1289, mar 1981.

[79] R. B. Anderson, H. Kolbel, and M. Ralek, *The Fischer-Tropsch synthesis.* Academic Press, 1984.

[80] A. Deluzarche, R. Kieffer, and A. Muth, "Reactions CO, H2 - synthese du methanol sur chromite de zinc etude d'especes chimisorbees a la surface du catalyseur schemas reactionnels possibles," *Tetrahedron Letters*, vol. 18, no. 38, pp. 3357–3360, 1977.

[81] W. H. Zimmerman, J. A. Rossin, and D. B. Bukur, “Effect of particle size on the activity of a fused iron Fischer-Tropsch catalyst,” *Industrial & Engineering Chemistry Research*, vol. 28, no. 4, pp. 406–413, 1989.

[82] M. Claeys and E. van Steen, “On the effect of water during Fischer–Tropsch synthesis with a ruthenium catalyst,” *Catalysis Today*, vol. 71, pp. 419–427, jan 2002.

[83] H. H. Nijs and P. A. Jacobs, “New evidence for the mechanism of the fischer-tropsch synthesis of hydrocarbons,” *Journal of Catalysis*, vol. 66, no. 2, pp. 401–411, 1980.

[84] P. A. Jacobs and D. Van Wouwe, “Selective synthesis of hydrocarbons via heterogeneous Fischer-Tropsch chemistry,” *Journal of Molecular Catalysis*, vol. 17, no. 2-3, pp. 145–160, 1982.

[85] H. H. Nijs and P. A. Jacobs, “Metal particle size distributions and Fischer-Tropsch selectivity. An extended Schulz-Flory model,” *Journal of Catalysis*, vol. 65, no. 2, pp. 328–334, 1980.

[86] H. Schulz, E. vein Steen, and M. Claeys, “Selectivity and mechanism of Fischer-Tropsch synthesis with iron and cobalt catalysts,” *Studies in Surface Science and Catalysis*, vol. 81, pp. 455–460, jan 1994.

[87] H. Pichler, “Twenty-five Years of Synthesis of Gasoline by Catalytic Conversion of Carbon Monoxide and Hydrogen,” *Advances in Catalysis*, vol. 4, no. C, pp. 271–341, 1952.

[88] Ø. Borg, S. Storsæter, S. Eri, H. Wigum, E. Rytter, and A. Holmen, “The effect of water on the activity and selectivity for γ-alumina supported cobalt Fischer-Tropsch catalysts with different pore sizes,” *Catalysis Letters*, vol. 107, pp. 95–102, feb 2006.

[89] F. G. Botes, “Influences of water and syngas partial pressure on the kinetics of a commercial alumina-supported cobalt Fischer-Tropsch catalyst,” *Industrial and Engineering Chemistry Research*, vol. 48, pp. 1859–1865, feb 2009.

[90] J. van de Loosdrecht, B. Balzhinimaev, J. A. Dalmon, J. W. Niemantsverdriet, S. V. Tsybulya, A. M. Saib, P. J. van Berge, and J. L. Visagie, “Cobalt Fischer-Tropsch synthesis: Deactivation by oxidation?,” *Catalysis Today*, vol. 123, pp. 293–302, may 2007.

[91] A. Kogelbauer, J. C. Weber, and J. G. Goodwin, “The formation of cobalt silicates on Co/SiO2 under hydrothermal conditions,” *Catalysis Letters*, vol. 34, pp. 259–267, sep 1995.

[92] G. Kiss, C. E. Kliewer, G. J. DeMartin, C. C. Culross, and J. E. Baumgartner, “Hydrothermal deactivation of silica-supported cobalt catalysts in Fischer-Tropsch synthesis,” *Journal of Catalysis*, vol. 217, pp. 127–140, jul 2003.

[93] C. J. Bertole, G. Kiss, and C. A. Mims, “The effect of surface-active carbon on hydrocarbon selectivity in the cobalt-catalyzed Fischer-Tropsch synthesis,” *Journal of Catalysis*, vol. 223, pp. 309–318, apr 2004.

[94] C. J. Bertole, C. A. Mims, and G. Kiss, “The effect of water on the cobalt-catalyzed Fischer-Tropsch synthesis,” *Journal of Catalysis*, vol. 210, no. 1, pp. 84–96, 2002.

[95] C. J. Bertole, C. A. Mims, and G. Kiss, “Support and rhenium effects on the intrinsic site activity and methane selectivity of cobalt Fischer-Tropsch catalysts,” *Journal of Catalysis*, vol. 221, pp. 191–203, jan 2004.

[96] C. M. Lok, “Novel highly dispersed cobalt catalysts for improved Fischer-Tropsch productivity,” in *Natural Gas Conversion VIIProceedings of the 7th Natural Gas Conversion Symposium* (X. Bao and Y. Xu, eds.), vol. 147 of *Studies in Surface Science and Catalysis*, pp. 283–288, Elsevier, 2004.

[97] I. Fernández-Morales, A. Guerrero-Ruiz, F. J. López-Garzón, I. Rodríguez-Ramos, and C. Moreno-Castilla, "Hydrogenolysis of n-butane and hydrogenation of carbon monoxide on Ni and Co catalysts supported on saran carbons," *Applied Catalysis*, vol. 14, pp. 159–172, 1985.

[98] E. Iglesia, S. L. Soled, R. A. Fiato, and G. H. Via, "Dispersion, support, and bimetallic effects in Fischer-Tropsch synthesis on cobalt catalysts," in *Natural Gas Conversion IIProceedings of the Third Natural Gas Conversion Symposium* (H. E. Curry-Hyde and R. F. Howe, eds.), vol. 81 of *Studies in Surface Science and Catalysis*, pp. 433–442, Elsevier, 1994.

[99] E. Iglesia, S. L. Soled, and R. A. Fiato, "Fischer-Tropsch synthesis on cobalt and ruthenium. Metal dispersion and support effects on reaction rate and selectivity," *Journal of Catalysis*, vol. 137, no. 1, pp. 212–224, 1992.

[100] L. Shi, J. Chen, K. Fang, and Y. Sun, "Effect of water on the deactivation of coprecipitated Co-ZrO2 catalyst for fischer-tropsch synthesis," *Studies in Surface Science and Catalysis*, vol. 167, pp. 97–102, 2007.

[101] Z. A. Makrodimitri, D. J. M. Unruh, and I. G. Economou, "Molecular simulation of diffusion of hydrogen, carbon monoxide, and water in heavy n-alkanes.," *The journal of physical chemistry. B*, vol. 115, pp. 1429–39, feb 2011.

[102] Z. A. Makrodimitri, D. J. M. Unruh, and I. G. Economou, "Molecular simulation and macroscopic modeling of the diffusion of hydrogen, carbon monoxide and water in heavy n-alkane mixtures.," *Physical chemistry chemical physics : PCCP*, vol. 14, pp. 4133–41, mar 2012.

[103] I. Makrodimitri Z, Economou, "Molecular Simulation of Diffusion and Solubility of Hydrogen, Carbon Monoxide and Water in Heavy n-Alkanes," tech. rep., Shell Global Solutions International B.V., 2010.

[104] B. M. Weckhuysen, "Preface: recent advances in the in-situ characterization of heterogeneous catalysts," *Chemical Society Reviews*, vol. 39, p. 4557, nov 2010.

[105] B. H. Davis, "Fischer-Tropsch Synthesis: Comparison of Performances of Iron and Cobalt Catalysts," 2007.

[106] H. Karaca, O. V. Safonova, S. Chambrey, P. Fongarland, P. Roussel, A. Griboval-Constant, M. Lacroix, and A. Y. Khodakov, "Structure and catalytic performance of Pt-promoted alumina-supported cobalt catalysts under realistic conditions of Fischer-Tropsch synthesis," *Journal of Catalysis*, 2011.

[107] F. C. Meunier, "The design and testing of kinetically-appropriate operando spectroscopic cells for investigating heterogeneous catalytic reactions," *Chemical Society Reviews*, vol. 39, p. 4602, nov 2010.

[108] "Phase changes studied under in situ conditions—A novel cell," *Catalysis Today*, vol. 275, pp. 149–154, oct 2016.

[109] A. Rochet, V. Moizan, C. Pichon, F. Diehl, A. Berliet, and V. Briois, "In situ and operando structural characterisation of a Fischer–Tropsch supported cobalt catalyst," *Catalysis Today*, vol. 171, pp. 186–191, aug 2011.

[110] B. M. Weckhuysen, "Snapshots of a working catalyst: Possibilities and limitations of in situ spectroscopy in the field of heterogeneous catalysis," *Chemical Communications*, 2002.

[111] B. M. Weckhuysen, *In-situ spectroscopy of catalysts.* American Scientific Publishers, 2004.

[112] B. M. Weckhuysen, “Preface: recent advances in the in-situ characterization of heterogeneous catalysts,” *Chemical Society Reviews*, vol. 39, p. 4557, nov 2010.

[113] M. A. Bañares, “Operando methodology: combination of in situ spectroscopy and simultaneous activity measurements under catalytic reaction conditions,” *Catalysis Today*, vol. 100, pp. 71–77, feb 2005.

[114] G. Leofanti, G. Tozzola, M. Padovan, G. Petrini, S. Bordiga, and A. Zecchina, “Catalyst characterization: characterization techniques,” tech. rep., 1997.

[115] M. E. Ali, M. M. Rahman, S. M. Sarkar, and S. B. A. Hamid, “Heterogeneous metal catalysts for oxidation reactions,” *Journal of Nanomaterials*, 2014.

[116] T. Blasco, “Insights into reaction mechanisms in heterogeneous catalysis revealed by in situ NMR spectroscopy,” *Chemical Society Reviews*, vol. 39, p. 4685, nov 2010.

[117] H. Topsøe, “Developments in operando studies and in situ characterization of heterogeneous catalysts,” *Journal of Catalysis*, vol. 216, pp. 155–164, may 2003.

[118] S. W. Price, D. J. Martin, A. D. Parsons, W. A. Sławiński, A. Vamvakeros, S. J. Keylock, A. M. Beale, and J. F. W. Mosselmans, “Chemical imaging of Fischer-Tropsch catalysts under operating conditions,” *Science Advances*, vol. 3, no. 3, 2017.

[119] P. T. Callaghan, *Principles of Nuclear Magnetic Resonance Microscopy.* Clarendon Press, 1993.

[120] J. Keeler, *Understanding NMR Spectroscopy.* John Wiley & Sons, 2011.

[121] M. H. Levitt, *Spin Dynamics: Basics of Nuclear Magnetic Resonance*, vol. 6. John Wiley & Sons, 2001.

[122] L. F. Gladden and P. Alexander, “Applications of nuclear magnetic resonance imaging in process engineering,” *Measurement Science and Technology*, vol. 7, no. 3, pp. 423–435, 1996.

[123] Horst Friebolin, *Basic One- and Two-Dimensional NMR Spectroscopy.* Wiley, 2nd ed., 2010.

[124] E. M. Purcell, H. C. Torrey, and R. V. Pound, “Resonance absorption by nuclear magnetic moments in a solid [7],” 1946.

[125] F. Bloch, W. W. Hansen, and M. Packard, “The nuclear induction experiment,” *Physical Review*, vol. 70, no. 7-8, pp. 474–485, 1946.

[126] M. Unser, “Sampling - 50 years after Shannon,” *Proceedings of the IEEE*, vol. 88, pp. 569–587, apr 2000.

[127] P. B. Kingsley, “Product operators, coherence pathways, and phase cycling. Part III: phase cycling,” *Concepts in Magnetic Resonance*, vol. 7, no. 3, pp. 167–192, 1995.

[128] A. B. Tayler, *Experimental Characterisation of Bubbly Flow using MRI.* PhD thesis, University of Cambridge, 2011.

[129] R. W. Brown, Y.-C. N. Cheng, E. M. Haacke, M. R. Thompson, and R. Venkatesan, *Magnetic resonance imaging : physical principles and sequence design.*

[130] J. Cavanagh, W. J. Fairbrother, A. G. Palmer, N. J. Skelton, and M. Rance, *Protein NMR Spectroscopy.* Elsevier Inc., 2007.

[131] T. D. Claridge, *High-Resolution NMR Techniques in Organic Chemistry: Third Edition.* Elsevier Inc., may 2016.

[132] E. Hahn, “Spin Echoes,” *Physical Review*, vol. 80, pp. 580–594, nov 1950.

[133] H. Carr and E. Purcell, “Effects of Diffusion on Free Precession in Nuclear Magnetic Resonance Experiments,” *Physical Review*, vol. 94, pp. 630–638, may 1954.

[134] N. Bloembergen, E. M. Purcell, and R. V. Pound, “Relaxation effects in nuclear magnetic resonance absorption,” *Physical Review*, vol. 73, no. 7, pp. 679–712, 1948.

[135] C. Johnson, “Diffusion ordered nuclear magnetic resonance spectroscopy: principles and applications,” *Progress in Nuclear Magnetic Resonance Spectroscopy*, vol. 34, pp. 203–256, may 1999.

[136] E. O. Stejskal and J. E. Tanner, “Spin Diffusion Measurements: Spin Echoes in the Presence of a Time-Dependent Field Gradient,” *The Journal of Chemical Physics*, vol. 42, p. 288, jul 1965.

[137] J.-F. Kuntz, P. Palmas, and D. Canet, “Diffusive diffraction measurements in porous media: Effect of structural disorder and internal magnetic field gradients,” *Journal of Magnetic Resonance*, vol. 188, no. 2, pp. 322–329, 2007.

[138] M. A. Isaacs, N. Robinson, B. Barbero, L. J. Durndell, J. C. Manayil, C. M. A. Parlett, C. D’Agostino, K. Wilson, and A. F. Lee, “Unravelling mass transport in hierarchically porous catalysts,” *Journal of Materials Chemistry A*, vol. 7, no. 19, pp. 11814–11825, 2019.

[139] S. E. Mailhiot, S. L. Codd, J. R. Brown, J. D. Seymour, and R. K. June, “Pulsed gradient stimulated echo (PGStE) NMR shows spatial dependence of fluid diffusion in human stage IV osteoarthritic cartilage,” *Magnetic Resonance in Medicine*, vol. 80, pp. 1170–1177, sep 2018.

[140] R. Cotts, M. Hoch, T. Sun, and J. Markert, “Pulsed field gradient stimulated echo methods for improved NMR diffusion measurements in heterogeneous systems,” *Journal of Magnetic Resonance (1969)*, vol. 83, pp. 252–266, jun 1989.

[141] P. Mansfield and P. K. Grannell, “Nmr ‘diffraction’ in solids?,” nov 1973.

[142] P. Mansfield, “Proton spin imaging by nuclear magnetic resonance,” *Contemporary Physics*, vol. 17, no. 6, pp. 553–576, 1976.

[143] P. Mansfield, “Multi-planar image formation using NMR spin echoes,” *Journal of Physics C: Solid State Physics*, vol. 10, no. 3, 1977.

[144] S. Ljunggren, “A simple graphical representation of fourier-based imaging methods,” *Journal of Magnetic Resonance (1969)*, vol. 54, no. 2, pp. 338–343, 1983.

[145] D. B. Twieg, “The k trajectory formulation of the NMR imaging process with applications in analysis and synthesis of imaging methods,” *Medical Physics*, vol. 10, no. 5, pp. 610–621, 1983.

[146] T. T. M. Nguyen, A. J. Sederman, M. D. Mantle, and L. F. Gladden, “Radial and axial segregation in horizontal rotating cylinders studied by Magnetic Resonance Imaging (MRI),” dec 2006.

[147] J. Hennig, A. Nauerth, and H. Friedburg, “RARE imaging: A fast imaging method for clinical MR,” *Magnetic Resonance in Medicine*, vol. 3, pp. 823–833, dec 1986.

[148] N. P. Ramskill, I. Bush, A. J. Sederman, M. D. Mantle, M. Benning, B. C. Anger, M. Appel, and L. F. Gladden, “Fast imaging of laboratory core floods using 3D compressed sensing RARE MRI,” 2016.

[149] M. A. Bernstein, K. F. King, and X. J. Zhou, *Handbook of MRI pulse sequences*. Academic Press, 2004.

[150] U. Bentrup, “Combining in situ characterization methods in one set-up: looking with more eyes into the intricate chemistry of the synthesis and working of heterogeneous catalystsw,” *This journal is c The Royal Society of Chemistry*, vol. 39, pp. 4718–4730, 2010.

[151] L. F. Gladden, “Applications of in situ magnetic resonance techniques in chemical reaction engineering,” *Topics in Catalysis*, vol. 8, no. 1, pp. 87–95, 1999.

[152] K. J. Packer, “Reflections on applications of NMR in heterogeneous catalysis and surface chemistry,” tech. rep., 1996.

[153] T. Xu and J. F. Haw, “The development and applications of CAVERN methods for in situ NMR studies of reactions on solid acids,” *Topics in Catalysis*, vol. 4, no. 1, pp. 109–118, 1997.

[154] A. A. Lysova and I. V. Koptyug, “Magnetic resonance imaging methods for in situ studies in heterogeneous catalysis,” *Chemical Society Reviews*, vol. 39, p. 4585, nov 2010.

[155] L. F. Gladden, “Magnetic resonance in reaction engineering: Beyond spectroscopy,” 2013.

[156] M. Hunger and J. Weitkamp, “In situ IR, NMR, EPR, and UV/Vis Spectroscopy: Tools for New Insight into the Mechanisms of Heterogeneous Catalysis,” *Angewandte Chemie International Edition*, vol. 40, pp. 2954–2971, aug 2001.

[157] L. Qi, R. Alamillo, W. A. Elliott, A. Andersen, D. W. Hoyt, E. D. Walter, K. S. Han, N. M. Washton, R. M. Rioux, J. A. Dumesic, and S. L. Scott, “Operando Solid-State NMR Observation of Solvent-Mediated Adsorption-Reaction of Carbohydrates in Zeolites,” *ACS Catalysis*, 2017.

[158] C. D’Agostino, G. L. Brett, P. J. Miedziak, D. W. Knight, G. J. Hutchings, L. F. Gladden, and M. D. Mantle, “Understanding the solvent effect on the catalytic oxidation of 1,4-butanediol in methanol over Au/TiO 2 catalyst: NMR diffusion and relaxation studies,” *Chemistry - A European Journal*, 2012.

[159] L. Baker, M. Renshaw, M. Mantle, A. Sederman, A. Wain, and L. Gladden, “Operando magnetic resonance studies of phase behaviour and oligomer accumulation within catalyst pores during heterogeneous catalytic ethene oligomerization,” *Applied Catalysis A: General*, vol. 557, pp. 125–134, may 2018.

[160] Q. Zheng, F. J. Russo-Abegao, A. J. Sederman, and L. F. Gladden, “Operando determination of the liquid-solid mass transfer coefficient during 1-octene hydrogenation,” *Chemical Engineering Science*, vol. 171, pp. 614–624, nov 2017.

[161] A. A. Lysova, I. V. Koptyug, A. V. Kulikov, V. A. Kirillov, and R. Z. Sagdeev, “An NMR Imaging Study of Steady-State and Periodic Operation Modes of a Trickle Bed Reactor,” *Topics in Catalysis*, vol. 52, pp. 1371–1380, sep 2009.

[162] L.-S. Bouchard, K. Kovtunov, S. Burt, M. Anwar, I. Koptyug, R. Sagdeev, and A. Pines, “Para-Hydrogen-Enhanced Hyperpolarized Gas-Phase Magnetic Resonance Imaging,” *Angewandte Chemie International Edition*, vol. 46, pp. 4064–4068, may 2007.

[163] K. V. Kovtunov, D. Lebedev, A. Svyatova, E. V. Pokochueva, I. P. Prosvirin, E. Y. Gerasimov, V. I. Bukhtiyarov, C. R. Müller, A. Fedorov, and I. V. Koptyug, “Robust In Situ Magnetic Resonance Imaging of Heterogeneous Catalytic Hydrogenation with and without Hyperpolarization,” *ChemCatChem*, vol. 11, p. cctc.201801820, dec 2018.

[164] R. Katakey and T. Patel, “Big oil’s plan to become big gas,” *Bloomberg Businessweek*, 2015.

[165] M. Johns, “NMR studies of emulsions,” *Current Opinion in Colloid & Interface Science*, vol. 14, no. 3, pp. 178–183, 2009.

[166] I. Lönnqvist, A. Khan, and O. Söderman, “Characterization of emulsions by NMR methods,” *Journal of Colloid and Interface Science*, vol. 144, pp. 401–411, jul 1991.

[167] R. V. Petersen, “Emulsion science. Edited by Philip Sherman. Academic Press, Inc., Ltd., Berkeley Square House, Berkeley Square, London, W.1. U. S. Academic Press, Inc., 111 Fifth Avenue, New York, NY 10003, 1968. 16 × 23.5cm. × + 496pp. Price 115s $21.00,” *Journal of Pharmaceutical Sciences*, vol. 57, pp. 1453–1454, aug 1968.

[168] K. Packer and C. Rees, “Pulsed NMR studies of restricted diffusion. I. Droplet size distributions in emulsions,” *Journal of Colloid and Interface Science*, vol. 40, no. 2, pp. 206–218, 1972.

[169] R. B. Bird, W. E. Stewart, and E. N. Lightfoot, *Transport phenomena.* J. Wiley, 2007.

[170] K. Hollingsworth and M. Johns, “Measurement of emulsion droplet sizes using PFG NMR and regularization methods,” *Journal of Colloid and Interface Science*, vol. 258, no. 2, pp. 383–389, 2003.

[171] K. Hollingsworth, A. Sederman, C. Buckley, L. Gladden, and M. Johns, “Fast emulsion droplet sizing using NMR self-diffusion measurements,” *Journal of Colloid and Interface Science*, vol. 274, no. 1, pp. 244–250, 2004.

[172] J. Van Den Enden, D. Waddington, H. Van Aalst, C. Van Kralingen, and K. Packer, “Rapid determination of water droplet size distributions by PFG-NMR,” *Journal of Colloid and Interface Science*, vol. 140, no. 1, pp. 105–113, 1990.

[173] S. A. Creber, T. R. Pintelon, and M. L. Johns, “Quantification of the velocity acceleration factor for colloidal transport in porous media using NMR,” *Journal of Colloid and Interface Science*, vol. 339, pp. 168–174, nov 2009.

[174] K. Hollingsworth and M. Johns, “Droplet migration in emulsion systems measured using MR methods,” *Journal of Colloid and Interface Science*, vol. 296, pp. 700–709, apr 2006.

[175] M. Johns and L. Gladden, “Sizing of Emulsion Droplets under Flow Using Flow-Compensating NMR-PFG Techniques,” *Journal of Magnetic Resonance*, vol. 154, pp. 142–145, jan 2002.

[176] P. J. McDonald, E. Ciampi, J. L. Keddie, M. Heidenreich, and R. Kimmich, “Magnetic-resonance determination of the spatial dependence of the droplet size distribution in the cream layer of oil-in-water emulsions: Evidence for the effects of depletion flocculation,” *Phys. Rev. E*, vol. 59, pp. 874–884, Jan 1999.

[177] G. Goudappel, J. van Duynhoven, and M. Mooren, “Measurement of Oil Droplet Size Distributions in Food Oil/Water Emulsions by Time Domain Pulsed Field Gradient NMR,” *Journal of Colloid and Interface Science*, vol. 239, no. 2, pp. 535–542, 2001.

[178] S. Godefroy and P. Callaghan, “2D relaxation/diffusion correlations in porous media,” 2003.

[179] J. P. M. van Duynhoven, G. J. W. Goudappel, G. van Dalen, P. C. van Bruggen, J. C. G. Blonk, and A. P. A. M. Eijkelenboom, “Scope of droplet size measurements in food emulsions by pulsed field gradient NMR at low field,” *Magnetic Resonance in Chemistry*, vol. 40, pp. S51–S59, dec 2002.

[180] J. Mitchell and M. L. Johns, "Rapid measurements of diffusion using pfg: Developments and applications of the difftrain pulse sequence," *Concepts in magnetic resonance.*, vol. 34A, no. 1, pp. 1–15, 2009.

[181] D. Bernin and D. Topgaard, "NMR diffusion and relaxation correlation methods: New insights in heterogeneous materials," *Current Opinion in Colloid & Interface Science*, vol. 18, pp. 166–172, jun 2013.

[182] W. S. Price, "Pulsed-field gradient nuclear magnetic resonance as a tool for studying translational diffusion: Part 1. basic theory," *Concepts in Magnetic Resonance*, vol. 9, no. 5, pp. 299–336.

[183] G. Froment, K. Bischoff, and J. de Wilde, *Chemical Reactor Analysis and Design*. Wiley, 3rd editio ed., 2011.

[184] X. Li, W. Zhang, X. Li, S. Liu, H. Huang, X. Han, L. Xu, and X. Bao, "Insights into the Deactivation Mechanism of Heterogeneous Mo/Hβ-Al 2 O 3 Catalysts for Olefin Metathesis," *The Journal of Physical Chemistry C*, vol. 113, pp. 8228–8233, may 2009.

[185] M. P. Hollewand and L. F. Gladden, "Transport heterogeneity in porous pellets—I. PGSE NMR studies," *Chemical Engineering Science*, vol. 50, pp. 309–326, jan 1995.

[186] M. Holz, S. R. Heil, and A. Sacco, "Temperature-dependent self-diffusion coefficients of water and six selected molecular liquids for calibration in accurate 1H NMR PFG measurements," *Physical Chemistry Chemical Physics*, vol. 2, pp. 4740–4742, jan 2000.

[187] C. D'Agostino, J. Mitchell, L. F. Gladden, and M. D. Mantle, "Hydrogen bonding network disruption in mesoporous catalyst supports probed by pfg-nmr diffusometry and nmr relaxometry," *The Journal of Physical Chemistry C*, vol. 116, no. 16, pp. 8975–8982, 2012.

[188] A. Perazzo, G. Tomaiuolo, V. Preziosi, and S. Guido, "Emulsions in porous media: From single droplet behavior to applications for oil recovery," jun 2018.

[189] C. Solans, D. Morales, and M. Homs, "Spontaneous emulsification," apr 2016.

[190] A. Cortis and T. A. Ghezzehei, "On the transport of emulsions in porous media," *Journal of Colloid and Interface Science*, vol. 313, pp. 1–4, sep 2007.

[191] H. Soo and C. J. Radke, "A filtration model for the flow of dilute, stable emulsions in porous media-I. Theory," *Chemical Engineering Science*, vol. 41, no. 2, pp. 263–272, 1986.

[192] M. I. Romero, M. S. Carvalho, and V. Alvarado, "Experiments and network model of flow of oil-water emulsion in porous media," *Physical Review E - Statistical, Nonlinear, and Soft Matter Physics*, vol. 84, oct 2011.

[193] M. Moradi, M. Kazempour, J. T. French, and V. Alvarado, "Dynamic flow response of crude oil-in-water emulsion during flow through porous media," *Fuel*, vol. 135, pp. 38–45, nov 2014.

[194] A. Mandal and A. Bera, "Modeling of flow of oil-in-water emulsions through porous media," *Petroleum Science*, vol. 12, pp. 273–281, jun 2015.

[195] S. Cobos, M. S. Carvalho, and V. Alvarado, "Flow of oil-water emulsions through a constricted capillary," *International Journal of Multiphase Flow*, vol. 35, pp. 507–515, jun 2009.

[196] A. R. Tehrani-Bagha, A. Viladot, K. Holmberg, and L. Nordstierna, "An Ouzo emulsion of toluene in water characterized by NMR diffusometry and static multiple light scattering," *Colloids and Surfaces A: Physicochemical and Engineering Aspects*, vol. 494, pp. 81–86, apr 2016.

[197] S. C. Ayirala and D. N. Rao, "Multiphase flow and wettability effects of surfactants in porous media," in *Colloids and Surfaces A: Physicochemical and Engineering Aspects*, vol. 241, pp. 313–322, Elsevier, jul 2004.

[198] A. C. Payatakes, "Dynamics of Oil Ganglia During Immiscible Displacement in Water-Wet Porous Media," *Annual Review of Fluid Mechanics*, vol. 14, pp. 365–393, jan 1982.

[199] R. Pal, "Techniques for measuring the composition (oil and water content) of emulsions - a state of the art review," may 1994.

[200] S. F. Wong, J. S. Lim, and S. S. Dol, "Crude oil emulsion: A review on formation, classification and stability of water-in-oil emulsions," *Journal of Petroleum Science and Engineering*, vol. 135, pp. 498–504, nov 2015.

[201] V. B. Menon and D. T. Wasan, "Characterization of oil-water interfaces containing finely divided solids with applications to the coalescence of water-in-oil Emulsions: A review," *Colloids and Surfaces*, vol. 29, no. 1, pp. 7–27, 1988.

[202] T. Tadros, P. Izquierdo, J. Esquena, and C. Solans, "Formation and stability of nano-emulsions," *Advances in Colloid and Interface Science*, vol. 108-109, pp. 303–318, may 2004.

[203] S. L. Deore and S. N. Kale, "Emulsion Micro Emulsion and Nano Emulsion: A Review," *Systematic Reviews in Pharmacy*, vol. 8.

[204] Y. Ouyang, R. S. Mansell, and R. D. Rhue, "Emulsion-mediated transport of nonaqueous-phase liquid in porous media: A review," *Critical Reviews in Environmental Science and Technology*, vol. 25, no. 3, pp. 269–290, 1995.

[205] D. E. Resasco, "Carbon nanohybrids used as catalysts and emulsifiers for reactions in biphasic aqueous/organic systems," *Chinese Journal of Catalysis*, vol. 35, pp. 798–806, jun 2014.

[206] C. D. McAuliffe, "Oil-in-Water Emulsions and Their Flow Properties in Porous Media," *Journal of Petroleum Technology*, vol. 25, pp. 727–733, jun 1973.

[207] S. L. Kokal, B. B. Maini, and R. Woo, "Flow of Emulsions in Porous Media," pp. 219–262, may 1992.

[208] R. Raghavan and S. Marsden, "Theoretical Aspects of Emulsification in Porous Media," *Society of Petroleum Engineers Journal*, vol. 11, pp. 153–161, jun 1971.

[209] A. Y. Khodakov, W. Chu, and P. Fongarland, "Advances in the development of novel cobalt Fischer-Tropsch catalysts for synthesis of long-chain hydrocarbons and clean fuels.," *Chemical reviews*, vol. 107, pp. 1692–744, may 2007.

[210] J. Strassner, "Effect of pH on Interfacial Films and Stability of Crude Oil-Water Emulsions," *Journal of Petroleum Technology*, vol. 20, pp. 303–312, mar 1968.

[211] R. Cash, J. Cayias, M. Hayes, D. MacAllister, T. Schares, R. Schechter, and W. Wade, "Spontaneous Emulsification-A Possible Mechanism for Enhanced Oil Recovery," in *Fall Meeting of the Society of Petroleum Engineers of AIME*, Society of Petroleum Engineers, apr 1975.

[212] E. Peake and G. W. Hodgson, "Alkanes in aqueous systems. I. Exploratory investigations on the accommodation of C_{20} - C_{33} n-alkanes in distilled water and occurrence in natural water systems," *Journal of the American Oil Chemists' Society*, vol. 43, pp. 215–222, apr 1966.

[213] J. Abou-Kassem and S. F. Ali, "Modeling of Emulsion Flow In Porous Media," *Journal of Canadian Petroleum Technology*, vol. 34, jun 1995.

[214] H. Soo and C. J. Radke, "The Flow Mechanism of Dilute, Stable Emulsions in Porous Media," *Ind. Eng. Chem. Fundam*, vol. 23, pp. 342–347, 1984.

[215] K. J. Ruschak and C. A. Miller, "Spontaneous Emulsification in Ternary Systems with Mass Transfer,"

[216] B. P. Binks and S. O. Lumsdon, "Catastrophic Phase Inversion of Water-in-Oil Emulsions Stabilized by Hydrophobic Silica,"

[217] M.-J. Rang and C. A. Miller, "Spontaneous Emulsification of Oils Containing Hydrocarbon, Nonionic Surfactant, and Oleyl Alcohol," *Journal of Colloid and Interface Science*, vol. 209, pp. 179–192, jan 1999.

[218] K. Fukuda, J. B. Lindman, and K. ShinodaI, "Microemulsions Formed by Alkyl Polyglucosides and an Alkyl Glycerol Ether," *Langmuir*, vol. 9, pp. 2921–2925, 1993.

[219] W. Warisnoicharoen, A. Lansley, and M. Lawrence, "Nonionic oil-in-water microemulsions: the effect of oil type on phase behaviour," *International Journal of Pharmaceutics*, vol. 198, pp. 7–27, mar 2000.

[220] D. Attwood, C. Mallon, and C. J. Taylor, "Phase studies on oil-in-water phospholipid microemulsions," *Internutional Journal of Pharmaceutics*, vol. 84, 1992.

[221] M. Kahlweit and R. Strey, "Phase Behavior of Ternary Systems of the Type H_2O-Oil-Nonionic Amphiphile (Microemulsions)," *Angewandte Chemie International Edition in English*, vol. 24, pp. 654–668, aug 1985.

[222] B. P. Binks and C. P. Whitby, "Nanoparticle silica-stabilised oil-in-water emulsions: improving emulsion stability," *Aspects*, vol. 253, pp. 105–115, 2005.

[223] M. Shen and D. E. Resasco, "Emulsions Stabilized by Carbon Nanotube-Silica Nanohybrids," *Langmuir*, vol. 25, no. 18, pp. 10843–10851, 2009.

[224] M. Kahlweit, R. Strey, P. Firman, D. Haase, J. Jen, and R. Schomacker, "General Patterns of the Phase Behavior of Mixtures of H_2O, Nonpolar Solvents, Amphiphiles, and Electrolytes. 1,"

[225] B. P. B. And and C. P. Whitby, "Silica Particle-Stabilized Emulsions of Silicone Oil and Water: Aspects of Emulsification," 2004.

[226] M. Kahlweit, R. Strey, R. Schomacker, and D. Haase, "General Patterns of the Phase Behavior of Mixtures of H_2O, Nonpolar Solvents, Amphiphiles, and Electrolytes. 2," *Langmuir*, vol. 5, pp. 305–315, 1989.

[227] . Noushine Shahidzadeh, , Daniel Bonn, J. Meunier, Minou Nabavi, , Marc Airiau, and M. Morvan, "Dynamics of Spontaneous Emulsification for Fabrication of Oil in Water Emulsions," 2000.

[228] J. C. López-Montilla, P. E. Herrera-Morales, S. Pandey, and D. O. Shah, "Spontaneous Emulsification: Mechanisms, Physicochemical Aspects, Modeling, and Applications," *Journal of Dispersion Science and Technology*, vol. 23, pp. 219–268, jan 2002.

[229] T. Förster, W. Von Rybinski, and A. Wadle, "Influence of microemulsion phases on the preparation of fine-disperse emulsions," *Advances in Colloid and Interface Science*, vol. 58, pp. 119–149, jul 1995.

[230] T. Sottmann, K. Kluge, R. Strey, J. Reimer, and O. Söderman, "General Patterns of the Phase Behavior of Mixtures of H_2O, Alkanes, Alkyl Glucosides, and Cosurfactants,"

[231] Y. Cheng, M. Qiao, and B. Zong, "Fischer-Tropsch Synthesis," in *Encyclopedia of Sustainable Technologies*, 2017.

[232] C. Bouchy, G. Hastoy, E. Guillon, and J. A. Martens, "Fischer-Tropsch Waxes Upgrading via Hydrocracking and Selective Hydroisomerization," *Oil & Gas Science and Technology – Rev. IFP*, vol. 64, no. 1, pp. 91–112, 2009.

[233] J. J. Spivey and K. P. De Jong, "Catalysis in the Refining of Fischer–Tropsch Syncrude Titles in the Series: 1: Carbons and Carbon Supported Catalysts in Hydroprocessing 2: Chiral Sulfur Ligands: Asymmetric Catalysis 3: Recent Developments in Asymmetric Organocatalysis 4: Catalysis in the Refining of Fischer–Tropsch Syncrude,"

[234] R. Klimkiewicz, "Upgrading oxygenated Fischer-Tropsch derivatives and one-step direct synthesis of ethyl acetate from ethanol - examples of the desirability of research on simple chemical compounds transformations.," *Chemistry Central journal*, vol. 8, no. 1, p. 77, 2014.

[235] A. de. Klerk and E. Furimsky, *Catalysis in the refining of Fischer-Tropsch syncrude.* RSC Pub, 2010.

[236] D. Leckel, "Selectivity Effect of Oxygenates in Hydrocracking of Fischer-Tropsch Waxes," 2007.

[237] D. Shi, J. A. Faria, A. A. Rownaghi, R. L. Huhnke, and D. E. Resasco, "Fischer–Tropsch Synthesis Catalyzed by Solid Nanoparticles at the Water/Oil Interface in an Emulsion System," *Energy & Fuels*, vol. 27, pp. 6118–6124, oct 2013.

[238] D. E. Resasco, "Carbon nanohybrids used as catalysts and emulsifiers for reactions in biphasic aqueous/organic systems," *Chinese Journal of Catalysis*, vol. 35, pp. 798–806, jun 2014.

[239] D. Shi, J. Faria, T. N. Pham, and D. E. Resasco, "Enhanced Activity and Selectivity of Fischer-Tropsch Synthesis Catalysts in Water/Oil Emulsions," *ACS Catalysis*, vol. 4, pp. 1944–1952, jun 2014.

[240] P. A. Zapata, J. Faria, M. P. Ruiz, and D. E. Resasco, "Condensation/Hydrogenation of Biomass-Derived Oxygenates in Water/Oil Emulsions Stabilized by Nanohybrid Catalysts," 2012.

[241] S. H. Yalkowsky, Y. He, P. Jain, Y. He, and P. Jain, *Handbook of Aqueous Solubility Data.* CRC Press, apr 2016.

[242] J. S. Murday and R. M. Cotts, "Self-Diffusion Coefficient of Liquid Lithium," *The Journal of Chemical Physics*, vol. 48, no. 11, p. 4938, 1968.

[243] P. V. Hemmingsen, A. Silset, A. Hannisdal, and J. Sjöblom, "Emulsions of Heavy Crude Oils. I: Influence of Viscosity, Temperature, and Dilution," *Journal of Dispersion Science and Technology*, vol. 26, pp. 615–627, sep 2005.

[244] M. Johns and K. Hollingsworth, "Characterisation of emulsion systems using NMR and MRI," *Progress in Nuclear Magnetic Resonance Spectroscopy*, vol. 50, pp. 51–70, mar 2007.

[245] B. Balinov, B. Jonsson, P. Linse, and O. Soderman, "The NMR Self-Diffusion Method Applied to Restricted Diffusion. Simulation of Echo Attenuation from Molecules in Spheres and between Planes," *Journal of Magnetic Resonance, Series A*, vol. 104, no. 1, pp. 17–25, 1993.

[246] X. Li, J. C. Cox, and R. W. Flumerfelt, "Determination of emulsion size distribution by NMR restricted diffusion measurement," *AIChE Journal*, vol. 38, pp. 1671–1674, oct 1992.

[247] I. J. Day, "On the inversion of diffusion NMR data: Tikhonov regularization and optimal choice of the regularization parameter," *Journal of Magnetic Resonance*, vol. 211, pp. 178–185, aug 2011.

[248] A. Reci, A. Sederman, and L. Gladden, "Retaining both discrete and smooth features in 1D and 2D NMR relaxation and diffusion experiments," *Journal of Magnetic Resonance*, vol. 284, pp. 39–47, nov 2017.

[249] M. Holz, S. R. Heil, and A. Sacco, "Temperature-dependent self-diffusion coefficients of water and six selected molecular liquids for calibration in accurate 1h nmr pfg measurements," *Phys. Chem. Chem. Phys.*, vol. 2, pp. 4740–4742, 2000.

[250] S. L. Ee, X. Duan, J. Liew, and Q. Dzuy Nguyen, "Droplet size and stability of nano-emulsions produced by the temperature phase inversion method," *Chemical Engineering Journal*, vol. 140, pp. 626–631, 2008.

[251] H. Chen, E. Dong, J. Li, and H. A. Stone, "Adhesion of moving droplets in microchannels," *Applied Physics Letters*, vol. 103, sep 2013.

[252] H. Soot and C. J. Radke, "The Flow Mechanism of Dilute, Stable Emulsions in Porous Media," *Ind. Eng. Chem. Fundam*, vol. 23, pp. 342–347, 1984.

[253] H. Soo, M. C. Williams, and C. J. Radke, "A filtration model for the flow of dilute, stable emulsions in porous media-II. Parameter evaluation and estimation," *Chemical Engineering Science*, vol. 41, no. 2, pp. 273–281, 1986.

[254] P. Radstake, J. den Breejen, G. Bezemer, J. Bitter, K. de Jong, V. Frøseth, and A. Holmen, "On the origin of the cobalt particle size effect in the fischer-tropsch synthesis," *Studies in Surface Science and Catalysis*, vol. 167, pp. 85–90, jan 2007.

[255] J. P. Den Breejen, P. B. Radstake, G. Leendert Bezemer, V. Frøseth, A. Holmen, J. H. Bitter, and K. P. De Jong, "A SSITKA study to understand the cobalt particle size effect in Fischer-Tropsch catalysis," tech. rep.

[256] DuPont™, "Chemical Resistance Guides: Elastomers Chemical Resistance Guide and Kalrez® - Application Guide," tech. rep., 2008.

[257] J.-W. Noordermeer, "Temperature Guide Book," tech. rep.

[258] A. Technologies, *Fundamentals of Gas Chromatography.* first edit ed., 2002.

[259] C. Wang, "Parallel GC for Complete Refinery Gas Analysis," *Agilent Technologies.*

[260] M. Wolf, "Effectiveness of catalyst passivation techniques studied in situ with a magnetometer," *Catalysis Today*, vol. 275, pp. 135–140, oct 2016.

[261] A. Gil, A. Diaz, and M. Montes, "Passivation and Reactivation of Nickel Catalysts," Tech. Rep. 5, 1991.

[262] K. Takanabe, K. Nagaoka, K. Nariai, and K. I. Aika, "Influence of reduction temperature on the catalytic behavior of Co/TiO 2 catalysts for CH4/CO2 reforming and its relation with titania bulk crystal structure," *Journal of Catalysis*, 2005.

[263] A. Wahyu Budiman, S.-H. Song, T.-S. Chang, C.-H. Shin, and M.-J. Choi, "Dry Reforming of Methane Over Cobalt Catalysts: A Literature Review of Catalyst Development,"

[264] N. Pernicone and F. Traina, "Catalyst Activation by Reduction," *Studies in Surface Science and Catalysis*, vol. 3, pp. 321–351, jan 1979.

[265] E. Generalic, "Soxhlet extractor," 2018.

[266] S. B. Hawthorne, C. B. Grabanski, E. Martin, and D. J. Miller, "Comparisons of Soxhlet extraction, pressurized liquid extraction, supercritical fluid extraction and subcritical water extraction for environmental solids: recovery, selectivity and effects on sample matrix," *Journal of Chromatography A*, vol. 892, pp. 421–433, sep 2000.

[267] M. Luque de Castro and F. Priego-Capote, "Soxhlet extraction: Past and present panacea," *Journal of Chromatography A*, vol. 1217, pp. 2383–2389, apr 2010.

[268] T. Bhatelia, C. Li, Y. Sun, P. Hazewinkel, N. Burke, and V. Sage, "Chain length dependent olefin re-adsorption model for Fischer-Tropsch synthesis over Co-Al2O3 catalyst," *Fuel Processing Technology*, vol. 125, 2014.

[269] E. Kuipers, "Chain Length Dependence of α-Olefin Readsorption in Fischer-Tropsch Synthesis," *Journal of Catalysis*, vol. 152, pp. 137–146, mar 1995.

[270] C. Mims and C. Bertole, "Surface carbon coverage and selectivity in FT synthesis: a simple model for selectivity correlations," pp. 375–380, 2001.

[271] C. J. Weststrate and J. W. Niemantsverdriet, "Understanding FTS selectivity: The crucial role of surface hydrogen," *Faraday Discussions*, vol. 197, 2017.

[272] A. Lillebø, E. Rytter, E. A. Blekkan, and A. Holmen, "Fischer-Tropsch Synthesis at High Conversions on Al2O3-Supported Co Catalysts with Different H2/CO Levels," *Industrial and Engineering Chemistry Research*, vol. 56, pp. 13281–13286, nov 2017.

[273] M. E. Dry, "The Fischer-Tropsch process: 1950-2000," in *Catalysis Today*, 2002.

[274] B. H. Davis, "Overview of reactors for liquid phase Fischer-Tropsch synthesis," in *Catalysis Today*, 2002.

[275] F. Diehl and A. Y. Khodakov, "Promotion of Cobalt Fischer-Tropsch Catalysts with Noble Metals: a Review," *Oil & Gas Science and Technology-Rev. IFP*, vol. 64, no. 1, pp. 11–24, 2009.

[276] B. H. Davis and M. L. Occelli, "Fischer-Tropsch synthesis, catalysts and catalysis: advances and applications," in *Fischer-Tropsch synthesis, catalysts and catalysis: advances and applications*, 206.

[277] A. K. Dalai and B. H. Davis, "Fischer-Tropsch synthesis: A review of water effects on the performances of unsupported and supported Co catalysts," 2008.

[278] A. T. Bell, "Catalytic Synthesis of Hydrocarbons over Group VIII Metals. A Discussion of the Reaction Mechanism," *Catalysis Reviews*, 1981.

[279] E. Iglesia, J. J. Spivey, and T. H. T. H. Fleisch, *Natural gas conversion VI : proceedings of the 6th Natural Gas Conversion Symposium, June 17-22, 2001, Alaska, USA*. Elsevier, 2001.

[280] M. E. Dry, "The fischer-tropsch process - commercial aspects," *Catalysis Today*, vol. 6, pp. 183–206, jan 1990.

[281] M. H. M. Lim, "Magnetic resonance imaging studies of single and multiphase flow in packed beds," 2004.

[282] F. Pöhlmann, C. Kern, S. Rößler, and A. Jess, "Accumulation of liquid hydrocarbons in catalyst pores during cobalt-catalyzed Fischer–Tropsch synthesis," *Catalysis Science & Technology*, vol. 6, no. 17, pp. 6593–6604, 2016.

[283] G. A. Hurt and C. N. Satterfield, "Liquid Accumulation in Catalyst Pores in a Fischer-Tropsch Fixed-Bed Reactor," tech. rep., 1985.

[284] W. Liu, J. Hu, and Y. Wang, "Fischer-Tropsch synthesis on ceramic monolith-structured catalysts," *Catalysis Today*, 2009.

[285] P. Senecal, S. D. Jacques, M. Di Michiel, S. A. Kimber, A. Vamvakeros, Y. Odarchenko, I. Lezcano-Gonzalez, J. Paterson, E. Ferguson, and A. M. Beale, "Real-Time Scattering-Contrast Imaging of a Supported Cobalt-Based Catalyst Body during Activation and Fischer-Tropsch Synthesis Revealing Spatial Dependence of Particle Size and Phase on Catalytic Properties," *ACS Catalysis*, vol. 7, pp. 2284–2293, apr 2017.

[286] N. E. Tsakoumis, R. Dehghan, R. E. Johnsen, A. Voronov, W. Van Beek, J. C. Walmsley, Ø. Borg, E. Rytter, D. Chen, M. Rønning, and A. Holmen, "A combined in situ XAS-XRPD-Raman study of Fischer-Tropsch synthesis over a carbon supported Co catalyst," *Catalysis Today*, vol. 205, pp. 86–93, apr 2013.

[287] M. Rønning, N. E. Tsakoumis, A. Voronov, R. E. Johnsen, P. Norby, W. Van Beek, Ø. Borg, E. Rytter, and A. Holmen, "Combined XRD and XANES studies of a Re-promoted Co/γ-Al 2O3 catalyst at Fischer-Tropsch synthesis conditions," *Catalysis Today*, vol. 155, pp. 289–295, oct 2010.

[288] A. Voronov, N. E. Tsakoumis, N. Hammer, W. Van Beek, H. Emerich, and M. Rønning, "The state and location of Re in Co-Re/Al2O3 catalysts during Fischer-Tropsch synthesis: Exploring high-energy XAFS for in situ catalysts characterisation," in *Catalysis Today*, vol. 229, pp. 23–33, Elsevier, jun 2014.

[289] N. E. Tsakoumis, A. P. York, D. Chen, and M. Rønning, "Catalyst characterisation techniques and reaction cells operating at realistic conditions; towards acquisition of kinetically relevant information," jul 2015.

[290] A. V. Puga, "On the nature of active phases and sites in CO and CO2 hydrogenation catalysts," *Catalysis Science and Technology*, vol. 8, no. 22, pp. 5681–5707, 2018.

[291] K. Morgan, J. Touitou, J. S. Choi, C. Coney, C. Hardacre, J. A. Pihl, C. E. Stere, M. Y. Kim, C. Stewart, A. Goguet, and W. P. Partridge, "Evolution and Enabling Capabilities of Spatially Resolved Techniques for the Characterization of Heterogeneously Catalyzed Reactions," *ACS Catalysis*, vol. 6, pp. 1356–1381, feb 2016.

[292] T. F. Child, "Pulsed n.m.r. study of molecular motion and environment of sorbed water on cellulose," *Polymer*, 1972.

[293] F. Pöhlmann and A. Jess, "Interplay of reaction and pore diffusion during cobalt-catalyzed Fischer–Tropsch synthesis with CO2-rich syngas," *Catalysis Today*, 2016.

[294] X. Zhan and B. H. Davis, "Assessment of internal diffusion limitation on Fischer-Tropsch product distribution," tech. rep., 2002.

[295] J. J. Geerlings, J. H. Wilson, G. J. Kramer, H. P. Kuipers, A. Hoek, and H. M. Huisman, "Fischer-Tropsch technology - From active site to commercial process," *Applied Catalysis A: General*, 1999.

[296] W. Wagner and A. Pruss, “The IAPWS formulation 1995 for the thermodynamic properties of ordinary water substance for general and scientific use,” *J. Phys. Chem. Ref. Data*, vol. 31, no. 2, pp. 387–535, 2002.

[297] C. R. Wilke and P. Chang, “Correlation of diffusion coefficients in dilute solutions,” *AIChE Journal*, vol. 1, no. 2, pp. 264–270, 1955.

[298] J. J. Marano and G. D. Holder, “Characterization of Fischer-Tropsch liquids for vapor-liquid equilibria calculations,” *Fluid Phase Equilibria*, vol. 138, pp. 1–21, nov 1997.

[299] E. Reverchon, P. Russo, and A. Stassi, “Solubilities of Solid Octacosane and Triacontane in Supercritical Carbon Dioxide,” *Journal of Chemical and Engineering Data*, vol. 38, no. 3, pp. 458–460, 1993.

[300] J. A. Schramke, S. F. Murphy, W. J. Doucette, and W. D. Hintze, “Prediction of aqueous diffusion coefficients for organic compounds at 25°C,” *Chemosphere*, vol. 38, pp. 2381–2406, apr 1999.

[301] I. C. Bourg and C. I. Steefel, “Molecular dynamics simulations of water structure and diffusion in silica nanopores,” *Journal of Physical Chemistry C*, vol. 116, pp. 11556–11564, may 2012.

[302] A. Pajzderska, M. A. Gonzalez, J. Mielcarek, and J. Wąsicki, “Water behavior in MCM-41 as a function of pore filling and temperature studied by NMR and molecular dynamics simulations,” *Journal of Physical Chemistry C*, vol. 118, pp. 23701–23710, oct 2014.

[303] T. G. Youngs, D. Weber, L. F. Gladden, and C. Hardacre, “Liquid structure and dynamics of aqueous isopropanol over γ-alumina,” *Journal of Physical Chemistry C*, vol. 113, no. 51, pp. 21342–21352, 2009.

[304] A. A. Milischuk and B. M. Ladanyi, “Structure and dynamics of water confined in silica nanopores,” *Journal of Chemical Physics*, vol. 135, nov 2011.

[305] Q. Zheng, J. L. Brown, M. D. Mantle, A. J. Sederman, T. A. Baart, C. M. Guédon, and L. F. Gladden, “Water-wax behaviour in porous silica at low temperature Fischer-Tropsch conditions,” *Applied Catalysis A: General*, 2019.

[306] S. Takahara, N. Sumiyama, S. Kittaka, T. Yamaguchi, and M. C. Bellissent-Funel, “Neutron scattering study on dynamics of water molecules in MCM-41. 2. Determination of translational diffusion coefficient,” *Journal of Physical Chemistry B*, vol. 109, pp. 11231–11239, jun 2005.

[307] A. Nakhaei Pour, S. M. K. Shahri, Y. Zamani, M. Irani, and S. Tehrani, “Deactivation studies of bifunctional Fe-HZSM5 catalyst in Fischer-Tropsch process,” *Journal of Natural Gas Chemistry*, vol. 17, pp. 242–248, sep 2008.

Appendix A

Zeton B.V. Reactor Documentation

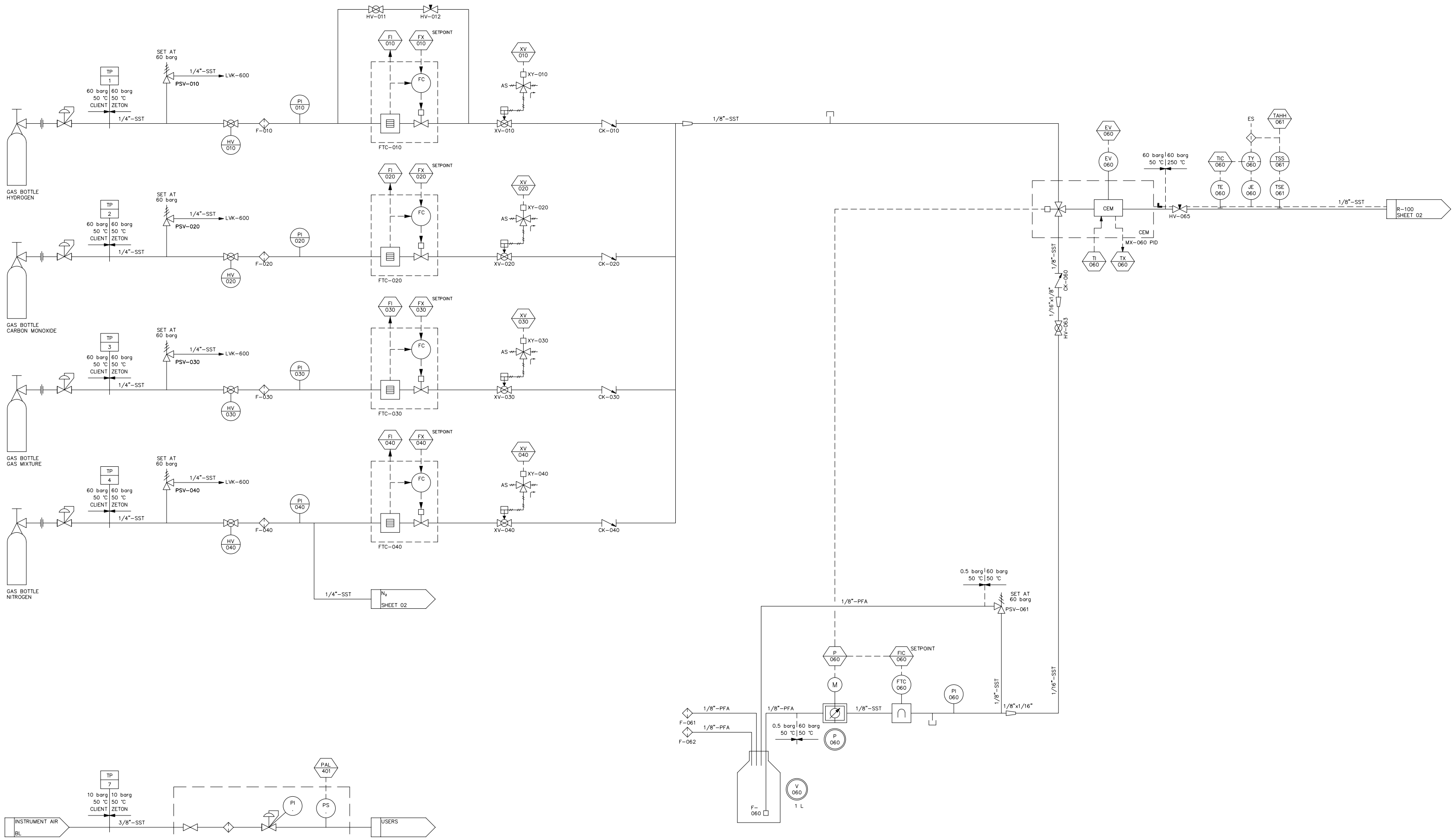

Figure A.1 First part of the P&ID drawing, which shows the four feed lines, the liquid feed and pressure control. Supplied by Zeton B.V.

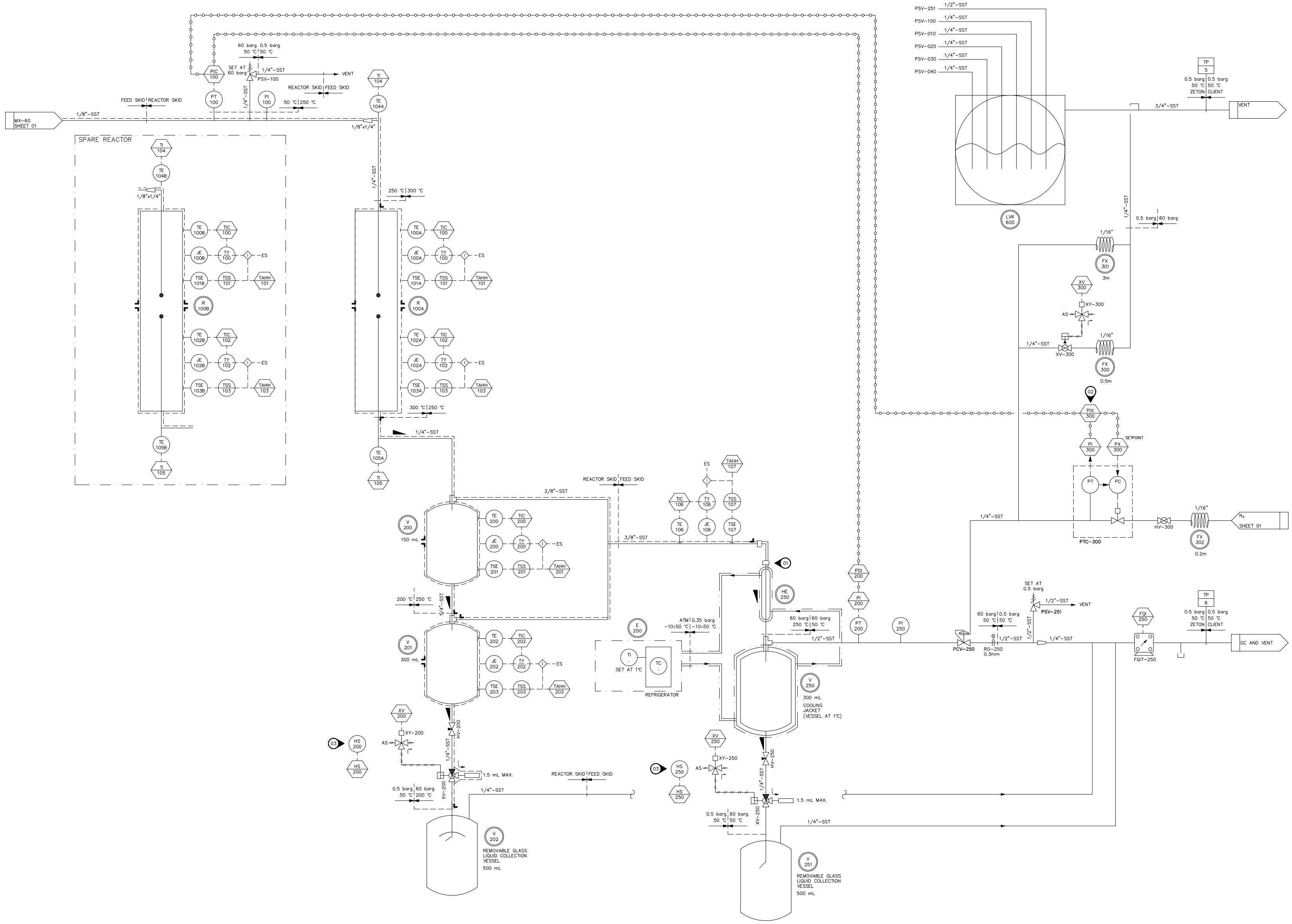

Figure A.2 Second part of the P&ID drawing, which shows the main reactor body with trace heating, all the product collection vessels, the leak detecting vessel and the GC. Supplied by Zeton B.V.

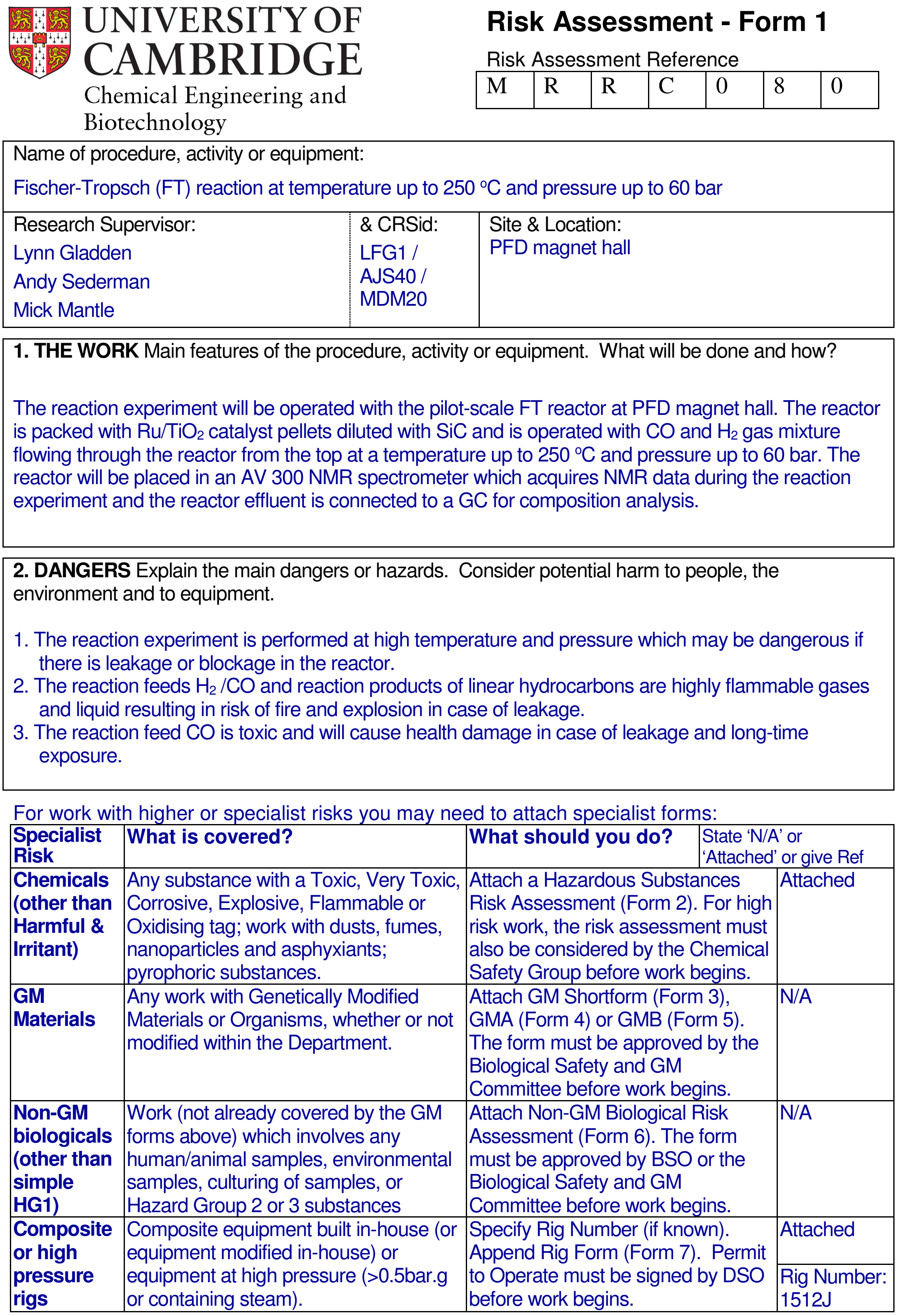

UNIVERSITY OF CAMBRIDGE
Chemical Engineering and Biotechnology

Risk Assessment - Form 1

Risk Assessment Reference

M	R	R	C	0	8	0

Name of procedure, activity or equipment: Fischer-Tropsch (FT) reaction at temperature up to 250 °C and pressure up to 60 bar		
Research Supervisor: Lynn Gladden Andy Sederman Mick Mantle	& CRSid: LFG1 / AJS40 / MDM20	Site & Location: PFD magnet hall

1. THE WORK Main features of the procedure, activity or equipment. What will be done and how?

The reaction experiment will be operated with the pilot-scale FT reactor at PFD magnet hall. The reactor is packed with Ru/TiO_2 catalyst pellets diluted with SiC and is operated with CO and H_2 gas mixture flowing through the reactor from the top at a temperature up to 250 °C and pressure up to 60 bar. The reactor will be placed in an AV 300 NMR spectrometer which acquires NMR data during the reaction experiment and the reactor effluent is connected to a GC for composition analysis.

2. DANGERS Explain the main dangers or hazards. Consider potential harm to people, the environment and to equipment.

1. The reaction experiment is performed at high temperature and pressure which may be dangerous if there is leakage or blockage in the reactor.
2. The reaction feeds H_2 /CO and reaction products of linear hydrocarbons are highly flammable gases and liquid resulting in risk of fire and explosion in case of leakage.
3. The reaction feed CO is toxic and will cause health damage in case of leakage and long-time exposure.

For work with higher or specialist risks you may need to attach specialist forms:

Specialist Risk	**What is covered?**	**What should you do?**	State 'N/A' or 'Attached' or give Ref
Chemicals (other than Harmful & Irritant)	Any substance with a Toxic, Very Toxic, Corrosive, Explosive, Flammable or Oxidising tag; work with dusts, fumes, nanoparticles and asphyxiants; pyrophoric substances.	Attach a Hazardous Substances Risk Assessment (Form 2). For high risk work, the risk assessment must also be considered by the Chemical Safety Group before work begins.	Attached
GM Materials	Any work with Genetically Modified Materials or Organisms, whether or not modified within the Department.	Attach GM Shortform (Form 3), GMA (Form 4) or GMB (Form 5). The form must be approved by the Biological Safety and GM Committee before work begins.	N/A
Non-GM biologicals (other than simple HG1)	Work (not already covered by the GM forms above) which involves any human/animal samples, environmental samples, culturing of samples, or Hazard Group 2 or 3 substances	Attach Non-GM Biological Risk Assessment (Form 6). The form must be approved by BSO or the Biological Safety and GM Committee before work begins.	N/A
Composite or high pressure rigs	Composite equipment built in-house (or equipment modified in-house) or equipment at high pressure (>0.5bar.g or containing steam).	Specify Rig Number (if known). Append Rig Form (Form 7). Permit to Operate must be signed by DSO before work begins.	Attached Rig Number: 1512J

Figure A.3 Rig Risk Assessment - Form 1. This is snapshot of the official risk assessment of the Department of Chemical Engineering and Biotechnology describing the general experiments, chemicals used and associated risks.

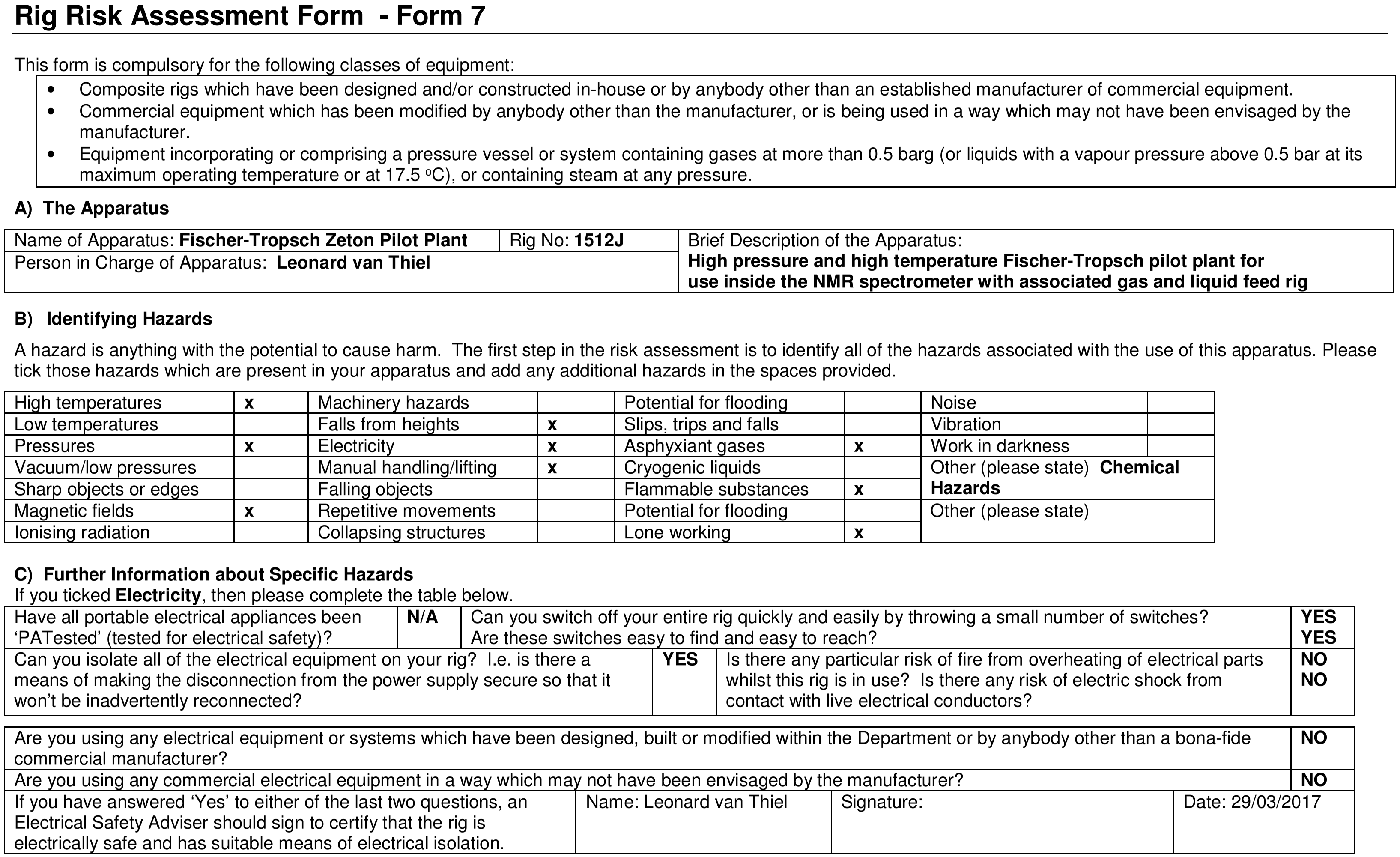

Rig Risk Assessment Form - Form 7

This form is compulsory for the following classes of equipment:

- Composite rigs which have been designed and/or constructed in-house or by anybody other than an established manufacturer of commercial equipment.
- Commercial equipment which has been modified by anybody other than the manufacturer, or is being used in a way which may not have been envisaged by the manufacturer.
- Equipment incorporating or comprising a pressure vessel or system containing gases at more than 0.5 barg (or liquids with a vapour pressure above 0.5 bar at its maximum operating temperature or at 17.5 °C), or containing steam at any pressure.

A) The Apparatus

Name of Apparatus: **Fischer-Tropsch Zeton Pilot Plant**	Rig No: **1512J**	Brief Description of the Apparatus: **High pressure and high temperature Fischer-Tropsch pilot plant for use inside the NMR spectrometer with associated gas and liquid feed rig**
Person in Charge of Apparatus: **Leonard van Thiel**		

B) Identifying Hazards

A hazard is anything with the potential to cause harm. The first step in the risk assessment is to identify all of the hazards associated with the use of this apparatus. Please tick those hazards which are present in your apparatus and add any additional hazards in the spaces provided.

High temperatures	x	Machinery hazards		Potential for flooding		Noise	
Low temperatures		Falls from heights	x	Slips, trips and falls		Vibration	
Pressures	x	Electricity	x	Asphyxiant gases	x	Work in darkness	
Vacuum/low pressures		Manual handling/lifting	x	Cryogenic liquids		Other (please state) **Chemical Hazards**	
Sharp objects or edges		Falling objects		Flammable substances	x		
Magnetic fields	x	Repetitive movements		Potential for flooding		Other (please state)	
Ionising radiation		Collapsing structures		Lone working	x		

C) Further Information about Specific Hazards

If you ticked **Electricity**, then please complete the table below.

Have all portable electrical appliances been 'PATested' (tested for electrical safety)?	**N/A**	Can you switch off your entire rig quickly and easily by throwing a small number of switches? Are these switches easy to find and easy to reach?	**YES** **YES**
Can you isolate all of the electrical equipment on your rig? I.e. is there a means of making the disconnection from the power supply secure so that it won't be inadvertently reconnected?	**YES**	Is there any particular risk of fire from overheating of electrical parts whilst this rig is in use? Is there any risk of electric shock from contact with live electrical conductors?	**NO** **NO**

Are you using any electrical equipment or systems which have been designed, built or modified within the Department or by anybody other than a bona-fide commercial manufacturer?			**NO**
Are you using any commercial electrical equipment in a way which may not have been envisaged by the manufacturer?			**NO**
If you have answered 'Yes' to either of the last two questions, an Electrical Safety Adviser should sign to certify that the rig is electrically safe and has suitable means of electrical isolation.	Name: Leonard van Thiel	Signature:	Date: 29/03/2017

Figure A.4 Rig Risk Assessment - Form 7. This is snapshot of the official risk assessment of the Department of Chemical Engineering and Biotechnology focussed on identifying the laboratory equipment and its main risks.

Appendix B

Schematic of the Gas Chromatograph Optimised for Fischer-Tropsch Product Analysis

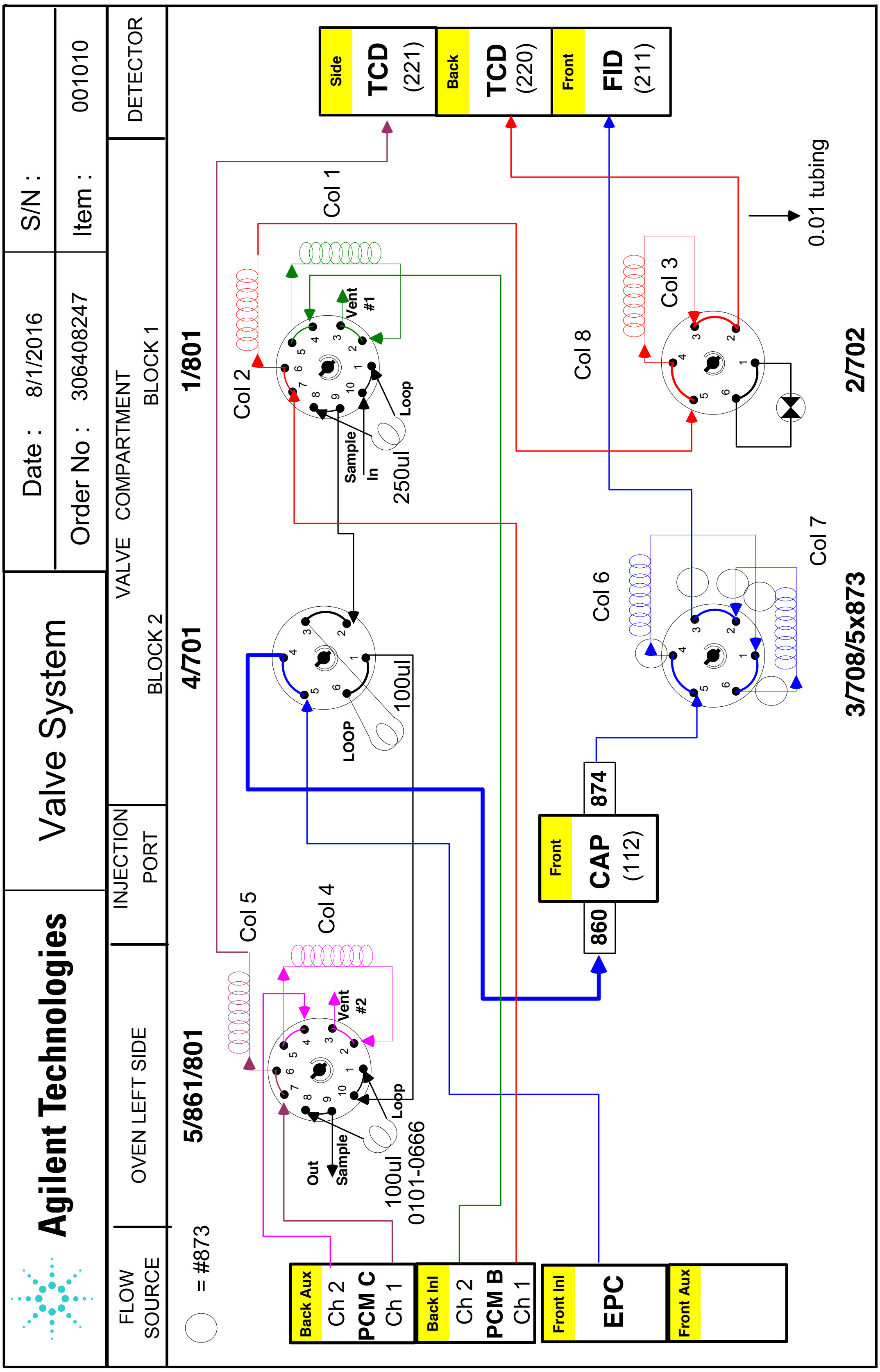

Figure B.1 The valves system of the Agilent GC with the three detectors.